PRODUCT PROPERTIES PREDICTION AFTER FORMING PROCESS SEQUENCE

A THESIS SUBMITTED TO
THE GRADUATE SCHOOL OF NATURAL AND APPLIED SCIENCES
OF
THE MIDDLE EAST TECHNICAL UNIVERSITY

BY

BAHADIR KOÇAKER

IN PARTIAL FULFILLMENT OF THE REQUIREMENTS FOR THE DEGREE OF
MASTER OF SCIENCE
IN
THE DEPARTMENT OF MECHANICAL ENGINEERING

JULY 2003

Approval of the Graduate School of Natural and Applied Sciences.

—————————————
Prof. Dr. Canan ÖZGEN
Director

I certify that this thesis satisfies all the requirements as a thesis for the degree of Master of Science.

—————————————
Prof. Dr. Eres SÖYLEMEZ
Head of the Department

This is to certify that we have read this thesis and that in our opinion it is fully adequate, in scope and quality, as a thesis for the degree of Master of Science.

—————————————
Prof. Dr. A. Erman TEKKAYA
Supervisor

Examining Committee in Charge:

Prof. Dr. Alp ESİN (Chairperson)   —————————————

Prof. Dr. A. Erman TEKKAYA (Supervisor)   —————————————

Dipl.-Ing. Guenter DOMANI   —————————————

Asst. Prof. Dr. Serkan DAĞ   —————————————

Assoc. Prof. Dr. C. Hakan GÜR   —————————————

ABSTRACT

**PRODUCTION PROPERTIES PREDICTION AFTER FORMING PROCESS
SEQUENCE**

Koçaker, M. Bahadır

M.S., Department of Mechanical Engineering

Supervisor: Prof. Dr.-Ing. A. Erman Tekkaya

July 2003, 184 pages

Cold metal forming processes have been widely used for manufacturing of their high production rates and increased yield strength after forming process. For the use in service, increased yield strength of the cold-formed products should be known. The new yield strength can be found by several methods. Mechanical tests such as compression or tensile test are direct methods to obtain new yield strength if the product shape is appropriate. Finite element simulations may be another way to get accurate results for new yield strength distribution. Also Vickers hardness number can be used for prediction of yield strengths by available conversion models. The aim of this study is to compare the results of all these methods. During the study two different materials (austenitic stainless steel and carbon steel) cold formed by drawing and extrusion are investigated. FE simulations have been conducted to predict product properties. For this purpose flow curves obtained from compression and tensile tests are used in FE-models based on elasto-plastic, isotropic hardening material. Results show that both materials are highly anisotropic and have much lower yield strength values than found in simulations. Similarly none of the models correlating Vickers hardness numbers and yield strengths are successful since they are designed for an isotropic hardening material. This study basically presents the deviation of a real material behavior from isotropic material behavior.

Keywords: Cold Forming, Flow Curves, Yield Strength, Drawing, Extrusion, Finite Element Analysis, Vickers Hardness Test and Test of Compression and Tension in Products

ÖZ

BİRBİRİNİ İZLEYEYEN ŞEKİLLENDİRME İŞLEMLERİNDEN SONRA ÜRÜN ÖZELLİKLERİ TAHMİNİ

Koçaker, M. Bahadır

M.S., Department of Mechanical Engineering

Supervisor: Prof. Dr.-Ing. A. Erman Tekkaya

July 2003, 184 pages

Soğuk metal şekillendirme işlemleri yüksek üretim hızı ve şekillendirme sonrası artan malzeme mukavemetleri gibi nedenlerden dolayı yaygın olarak kullanılan üretim işlemleridir. Bu yöntemle şekillendirilmiş ürünlerin kullanımlarında artan akma geriliminin bilinmesi gerekmektedir. Bu akma gerilimi çeşitli yollarla bulunabilir. Ürün şekli uygun ise basit basma ve çekme testleri artan akma gerilimini bulmak için direk yöntemlerdir. Yeni akma gerilimi dağılımını elde etmek için sonlu eleman simulasyonu diğer bir yol olabilir. Ayrıca Vickers sertlik ölçümleri hazır çevrim modelleri kullanılarak akma gerilimi tahmininde bulunabilir. Bu çalışmanın amacı butun bu yöntemlerin sonuçlarini karşılaştırmaktır. Çalışma boyunca ostenitik paslanmaz çelik ve karbon çeliği olmak üzere çekme ve ekstrüzyonla soğuk şekillendirilmiş iki malzeme üstünde çalışılmıştır. Sonlu eleman simulasyonları ürün özellikleri tahmininde kullanılmıştır. Bu amaçla basma ve çekme deneylerinden elde edilen akma eğrileri elasto-plastik ve eşyönel pekleşmeyi öngören sonlu eleman simulasyonlarında kullanılmıştır. Sonuçlar her iki malzemenin de eşyönel olmadığını ve simule edilenden cok daha düşük akma gerilimlerine sahip olduklarını göstermiştir. Benzer olarak eşyönel malzemeler için geliştirildiklerinden Vickers sertlik değerleri ile akma gerilimi arasındaki bağıntıların hiçbiri başarılı olamamışlardır. Bu calışma genel olarak gerçek bir malzemenin davranışının eşyönel malzeme davranışından sapmasını sunmaktadır.

Anahtar Kelimeler: Soğuk Şekillendirme, Akma Eğrileri, Akma Gerilimi, Çekme, Ekstrüzyon, Sonlu Eleman Analizi, Vickers Sertliği, Ürünlerde Basma ve Çekme Testleri

ACKNOWLEDGEMENT

TABLE OF CONTENTS

LIST OF TABLES

ix

LIST OF FIGURES

xiii

xvii

CHAPTER 1

INTRODUCTION

Among the metal forming processes, cold metal forming processes are the most advantageous due to low scrap, high production rates, and increased yield strength of cold-formed products after forming operation. In general, the costumer of these products requires the new increased yield strength distribution for design calculations. However, the cold-formed products may not be appropriate for standard material testing experiments such as simple tension, simple compression or simple torsion. Thus, usually either simplified analytical computations or finite element models are used to predict the new increased yield strength distribution. Also some researchers developed some relations between yield stress and Vickers hardness, which is an easy to apply mechanical test method. Both methods demand an accurate knowledge of data that describes the plastic material behavior.

In this thesis product properties after some cold forming processes used through out the production of anchors by HILTI will be investigated.

1.1   Materials and Forming Processes' Description

HILTI has a wide product range mainly on construction equipments. HILTI has products for positioning, drilling and demolition, diamond, cutting and sanding, screw fastening, direct fastening, installation, fire stop, and construction foams.

In this study cold-forming processes of two different types of anchors produced by HILTI will be investigated. Differences between the anchors are materials that they are made from and their dimensions. These materials that are initially annealed are totally cold formed to result an anchor. Materials are austenitic stainless steel and low carbon steel. Designations of the materials are given in DIN norms and American standards in Table 1.1. The compositions of these materials are also given in Table 1.2. Through out this study materials will be called as stainless steel and carbon steel.

Table 1.1 Materials investigated in the study

Materials	DIN	AISI
Austenitic Stainless Steel	X5CrNiMo18 10 (1.4401)	316
Low Carbon Steel	18MnV5	-

Table 1.2 Chemical compositions of materials

Chemical Composition % (max. unless noted)									
	C	**Mn**	**P**	**S**	**Si**	**Cr**	**Ni**	**Mo**	**V**
X5CrNiMo1810	0.08	2.00	0.045	0.030	1.000	16.00-18.00	10.00-14.00	2.00-3.00	-
18MnV5	0.15-0.25	1.60	0.035	0.035	0.40	-	-	-	0.12

Stainless steel and carbon steel is received in coil form as annealed and surface treated from material supplier. For stainless steel a lubricant surface Vicafil and Stearat (soap) are used and for carbon steel phosphate and Stearat are used for lubrication. After processes as rolling for straightening, wire drawing, extrusion, heading and rolling for thread forming the anchor is formed. Figure 1.1 illustrates these processes.
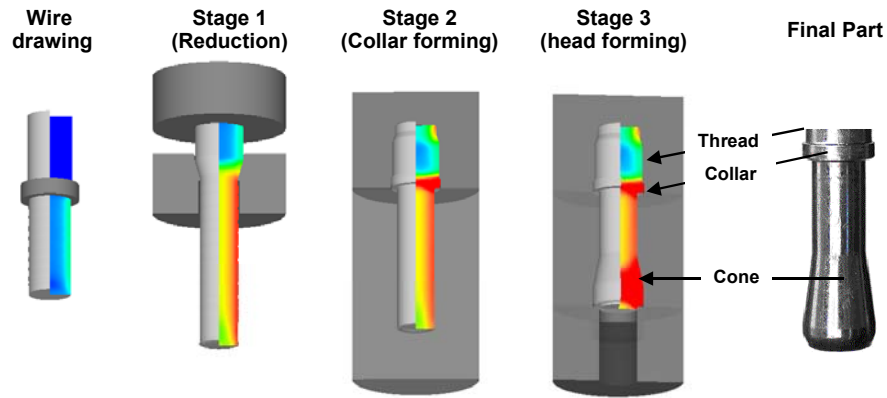
Figure 1.1 Illustration of forming processes to produce an anchor

1.2 Aim and Scope of the Study

Goal of the study is the determination of the final product (anchor) properties by means of FE simulations. Besides one motivation of this study has been the large difference between compression and tensile flow curves of stainless steel, obtained by HILTI. This difference is shown in the below graph.
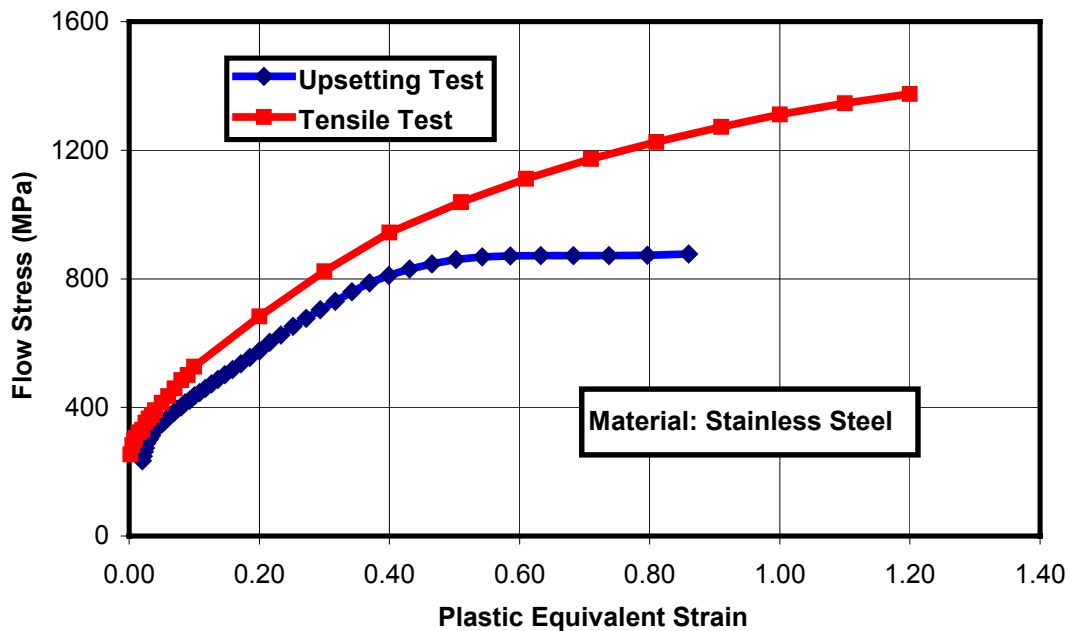
Figure 1.2 Compression and tension flow curves supplied by HILTI

Although small differences between compression and tension plastic behavior can be expectable, such a big difference was surprising. Flow curve variation in different directions makes it difficult to choose which curve to use in the FEM models.

In this study it is aimed first to obtain reliable results for materials plastic behavior. For this purpose tension and compression tests are repeated. These tests are also performed after drawing and extrusion which are two primary forming processes applied to rolled stainless and carbon steel. To see the Bauschinger effect (drop in the yield stress at stress reversals) some compression tests are done to workpieces pre-strained by tension. Some Vickers hardness measurements are also taken to see if there is a good match between calculated hardness values on the points where the strain is known with the known relations and obtained flow curves. The results and evaluation of these tests are presented in Chapter 3.

Finite element simulations of forming processes and experiments performed are made with isotropic material model. Through out the study only two cold forming processes (drawing and extrusion) are investigated. The experiment results compared with these simulations will provide deviations of a real material from complete isotropic material model. This comparison will be given in Chapter 4, 5 and 6.

CHAPTER 2

LITERATURE SURVEY

In this chapter literature on mechanical tests like compression test, tensile test and Vickers hardness tests are widely discussed. Correction methods for compression and tensile tests are also presented. Vickers hardness test is mainly mentioned with its correlations with yield stress.

Friction models are inseparable parts of FE simulations and forming processes. Hence friction models and parametric characterization of them are also presented. Plastic material models are briefly summarized to give general information on available yield criterion and hardening rules.

Literature on austenitic stainless steel and AISI 316 steel is presented. Some results reported in previous studies for similar behaviors in large strain load reversal experiments are given.

2.1   Mechanical Tests

Knowledge of both the stresses occurring in the plastic zone during a metal forming process and also of the resulting forces is a prerequisite for the design of metal forming tools and machines.

The stresses depend on the plastic properties of the workpiece material, on friction in the interface between workpiece and the tool and on the geometry of the system. These stresses can be calculated using the methods of the theory of plasticity if the hardening characteristic of the material is known. The hardening characteristic is quantitatively described by the flow curve. To determine the flow curve of material several mechanical experiments are available. Tensile test, compression test, torsion test, plane strain upsetting test are some of these mechanical experiments for bulk metal forming. Also some indentation (hardness) tests like Brinell, Rockwell, Vickers and Knoop are available to obtain some other useful mechanical properties (like yield strength).

In this section most frequently used experiments in both literature and industry will be presented.

2.1.1   Tensile Test

The tension test consists of elongating a sample of material under a tensile load until it breaks. The test specimen used may have either a circular or a rectangular cross section. The ends of tensile specimens are usually enlarged to provide extra area for gripping and to avoid having the sample break where it is being gripped (Figure 2.1).

The usual manner of conducting the test is to deform the specimen at a constant speed. Hence, distance h in Fig. 2.1 is varied so that

$$\frac{dh}{dt} = \dot{h} = constant \tag{2.1}$$

The load must be applied to enforce this displacement rate varies as the test proceeds. This load F may be divided by the initial cross-sectional area A_0 to obtain the engineering stress in the specimen at any time during the test.

$$\sigma_{eng} = \frac{P}{A_0} \qquad (2.2)$$
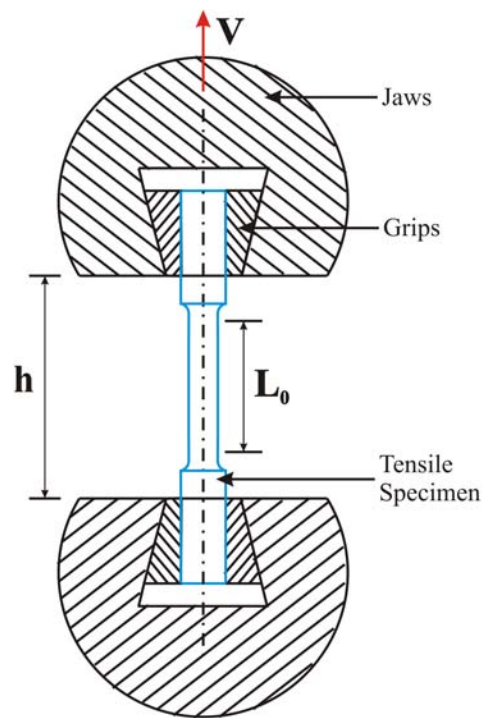
Figure 2.1 Typical grips for a tension test in a universal testing machine

Displacements on the specimen are measured within a straight central portion of constant cross section over a gage length L_0 as indicated in Figure 2.1. The engineering strain ε_{eng} may be computed from the change of this length, ΔL.

$$\varepsilon_{eng} = \frac{\Delta L}{L_0} \qquad (2.3)$$

It is sometimes reasonable to assume that all of the grip parts and the specimen ends are nearly rigid. In this case, virtually all of the change in crosshead motion is due to deformation within the straight section of the test specimen, so that ΔL is approximately the same as Δh, the change in h. Strain may therefore be estimated from

$$\varepsilon_{eng} = \frac{\Delta h}{L_i} \qquad (2.4)$$

Initial portions of stress-strain curves from tension tests exhibit a variety of different behaviors for different materials. There may be a well-defined initial straight line, as for many engineering materials, where the deformation is predominantly elastic. The *elastic modulus*, *E,* also called *Young's modulus*, may then be obtained from the stresses and strains at two points on this line, such as A and B in Figure 2.2.

$$E = \frac{\sigma_B - \sigma_A}{\varepsilon_B - \varepsilon_A} \qquad (2.5)$$

The ultimate tensile strength, σ_u, also called simply the *tensile strength*, is the highest engineering stress reached prior to fracture. If the behavior is brittle, the ultimate strength occurs at the point of fracture. However, in ductile metals, engineering stress reaches a maximum and then decreases prior to fracture. The highest load reached at any point during the test, P_{max}, is used to obtain the ultimate strength by dividing by the original cross-sectional area.

$$\sigma_u = \frac{P_{max}}{A_i} \qquad (2.6)$$
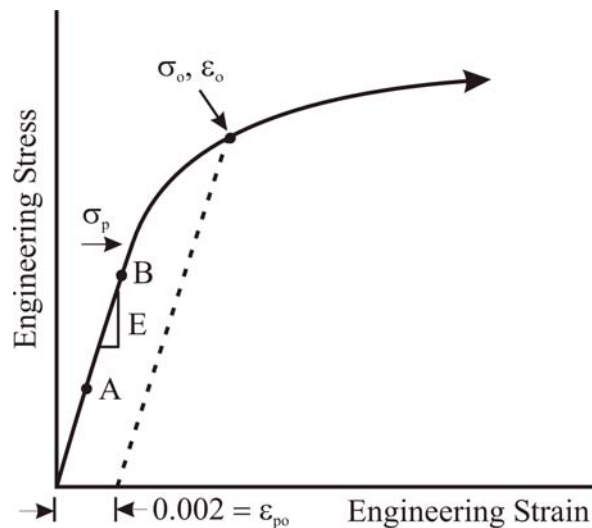
Figure 2.2 Initial portions of stress-strain curves for many metals and alloys

The engineering fracture strength, σ_f, is obtained from the load at fracture, P_f, even if this is not the highest load reached.

$$\sigma_f = \frac{P_f}{A_i} \qquad (2.7)$$

Hence, for brittle materials, $\sigma_u \approx \sigma_f$, whereas for ductile materials, σ_u may exceed σ_f.

The departure from linear-elastic behavior as in Figure 2.2 is called yielding. This is simply because stresses that cause yielding result in rapidly increasing deformation due to the contribution of plastic strain. The yielding event can be characterized by several methods. The simplest is to identify the stress where the first departure from linearity occurs. This is called the *proportional limit*, σ_p, and is illustrated in Figure 2.2. Some materials may exhibit a stress-strain curve with a gradually decreasing slope and no proportional limit. Even where there is a definite linear region, it is difficult to precisely locate where this ends. Hence, the value of proportional limit depends on judgment, so that this is a poorly defined quantity. Another quantity sometimes defined is the *elastic limit*, which is the highest stress that does not cause plastic deformation. Determination of this quantity is difficult, as periodic unloading to check for permanent deformation is necessary. A third approach is the *offset method*, which is illustrated by dashed lines in Figure 2.2. A straight line is drawn parallel to the elastic slope, E or E_t, but offset by an arbitrary amount. The intersection of this line with the engineering stress-strain curve is a well-defined point that is not affected by judgment. This is called the *offset yield strength*, σ_{f0}. The most widely used and standardized offset for engineering metals is a strain of 0.002, that is 0.2%, although other values are also used. Note that the offset strain is a plastic strain, such as $\varepsilon_{p0} = 0.002$, as unloading from σ_{f0} would follow a dashed line in Figure 2.2, and this ε_{p0} would be the uncovered strain.

True stress in a simple tension test is simply the load P divided by the current cross-sectional area A, rather than the original area A_i.

$$\sigma_{true} = \frac{P}{A} \tag{2.8}$$

Hence, true and engineering stress are related by

$$\sigma_{true} = \sigma_{eng}\left(\frac{A_i}{A}\right) \tag{2.9}$$

Total true strain can be defined with below integral.

$$\varepsilon_{true} = \int_{L_i}^{L} \frac{dL}{L} = \ln\frac{L}{L_i} \tag{2.10}$$

where $L = L_i + \Delta L$ is the final length. Noting that $\varepsilon_{eng} = \Delta L / L_i$ is the engineering strain leads to a relationship between ε_{eng} and ε_{true}.

$$\varepsilon_{true} = \ln\frac{L_i + \Delta L}{L_i} = \ln\left(1 + \frac{\Delta L}{L_i}\right) = \ln\left(1 + \varepsilon_{eng}\right) \tag{2.11}$$

For materials that behave in a ductile manner, once the strains have increased substantially beyond the yield region, most of the strain that has accumulated is inelastic strain. The volume change in a tension test is limited to the small change associated with elastic strains; plastic strains do not contribute to volume change. It is therefore reasonable to assume that the volume is constant.

$$A_i L_i = AL \tag{2.12}$$

This gives

$$\frac{A_i}{A} = \frac{L}{L_i} = \frac{L_i + \Delta L}{L_i} = 1 + \varepsilon_{eng} \tag{2.13}$$

Substitution of the above equation into Eqs. (2.10) and (2.11) gives two additional equations relating true and engineering stress and strain.

$$\sigma_{true} = \sigma_{eng}\left(1 + \varepsilon_{eng}\right) \qquad (2.14)$$

$$\sigma_{true} = \ln\left(\frac{A_i}{A}\right) \qquad (2.15)$$

For members with round cross sections of original diameter d_i and final diameter d, the last equation may be used in the form

$$\varepsilon_{true} = \ln\left(\frac{\dfrac{\pi d_i^{\,2}}{4}}{\dfrac{\pi d^2}{4}}\right) = 2\ln\frac{d_i}{d} \qquad (2.16)$$

If the behavior in a tension test is ductile, a phenomenon called *necking* usually occurs as illustrated in Figure 2.3. The deformation is uniform along the gage length early in the test, but later begins to concentrate in one region, resulting in the diameter there decreasing more than elsewhere. In ductile metals, necking begins at the ultimate strength point, and the decrease in load beyond this is a sequence of the cross-sectional area rapidly decreasing. Once necking begins, the longitudinal strain becomes non-uniform as illustrated in Fig. 2.4(c). The percent reduction in area is based on the minimum diameter at fracture and so is a measure of the highest strain along the gage length. In contrast, the percent elongation at fracture is an average over an arbitrarily chosen length. Its value varies with the ratio of gage length to diameter, L_i/d_i, increasing for smaller values of this ratio. As a consequence, it is necessary to standardize the gage lengths used. For example, $L_i/d_i=4$ is commonly used in the United States for specimens with round cross sections, but $L_i/d_i=5$ is specified in most international standards.

11
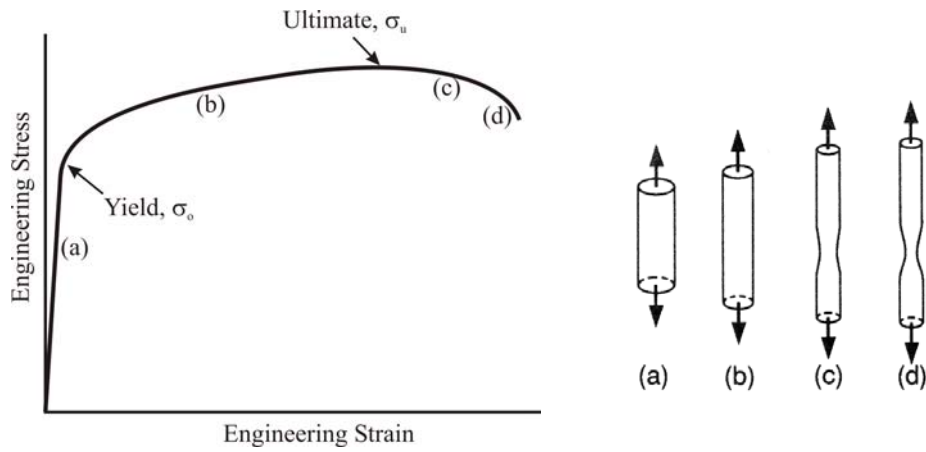
Figure 2.3 Schematic of the engineering stress-strain curve of a typical ductile metal that exhibits necking behavior

A complication arises in interpreting tensile results near the end of a test where there is a large amount of necking. As pointed out by Bridgman [9] in 1944, large amounts of necking result in a tensile hoop stress being generated around the circumference in the necked region. Thus, the state of stress in no longer uniaxial as assumed and the axial stress is increased above what it should be.

A correction can be made by using the factor $\left(1+2R/a\right)\ln\left(1+a/2R\right)$ that is given by Bridgman. The inverse of this factor, may be called "correction factor", since it is the factor by which the "uncorrected true stress" is to be multiplied to obtain the "corrected true stress". Also Siebel [8] has a similar factor $\left(1+a/4R\right)$ that is presented before Bridgman's. Both corrections depend on a single parameter, *a/R*, the ratio of the radius of the neck to the radius of curvature of the contour of the neck as illusturated in Figure 2.4. The "corrected true stresses" given by Bridgman's analysis are progressively larger than the "corrected true stresses" that is given by Siebel's formula.

Correction factor *B* is used as follows:

$$\tilde{\sigma}_B = B\tilde{\sigma} \qquad (2.17)$$
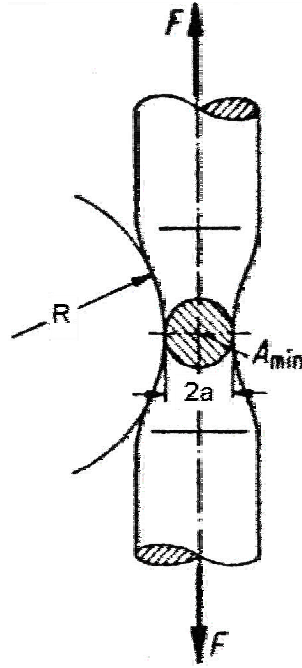
Figure 2.4 Schematic representation of *a* and *R* values

where, $\tilde{\sigma}$ is the uncorrected true stress and $\tilde{\sigma}_B$ is the corrected true stresses. $\tilde{\sigma}_B$ is the axial component of the triaxial stress state. The uncorrected true stress can be calculated as

$$\tilde{\sigma} = Load\big/\pi a^2 \qquad (2.18)$$

where $2a$ is the minimum diameter on the cross-sectional area along the neck region (Figure 2.5).

On the other hand the correction factor by Bridgman is

$$B = \frac{1}{\left(1+2\dfrac{R}{a}\right)\ln\left(1+\dfrac{1}{2}\dfrac{a}{R}\right)} \qquad (2.19)$$

The corresponding equivalent strain is given by

$$\bar{\varepsilon} = \ln(\frac{A_0}{A_{min}}) \qquad (2.20)$$

13

where A_{min} is the minimum cross-section in the necking zone at a given force (Figure 2.4). By this method the flow curve can be determined up to strains of the order of unity (ε=1).

Correction factors as a function of a/R is given in Figure 2.5.
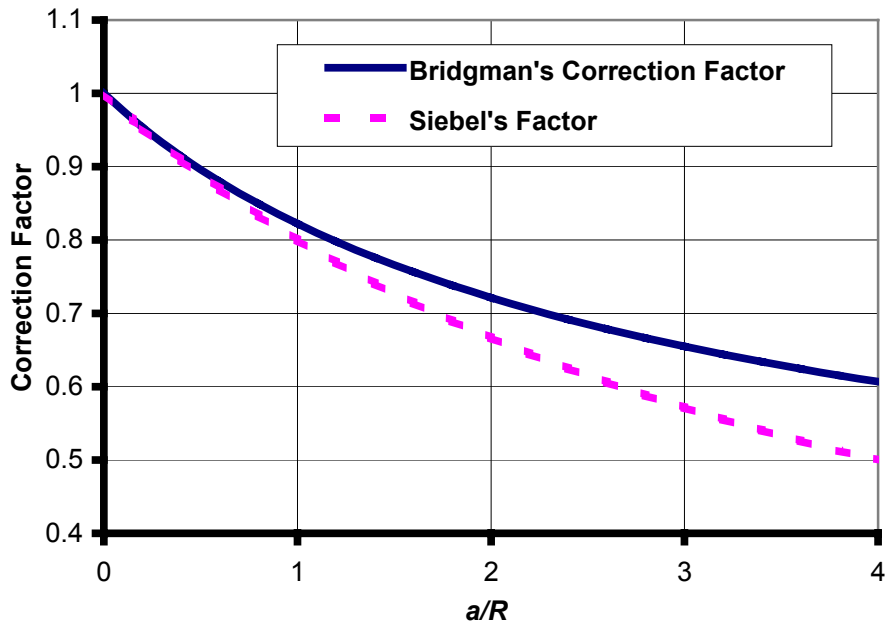
Figure 2.5 Bridgman's and Siebel's Correction factor as a function of a/R

Bridgman also showed that a/R is a function of the reduction of area after so many experiments on a variety of steels and heat treatments varying from annealed to quenched. Even in the extreme case the correction factor computed from the directly measured a/R does not differ by more than 4 percent for the factor from the median curve. By assuming a mean experimental connection between the shape of the contour of the neck and reduction of area, Figure 2.6 can be plotted.

Rather than using the curve, the correction factor may be estimated from the following equation [3]:

$$B = 0.83 - 0.186\log\tilde{\varepsilon} \quad \left(0.15 \leq \tilde{\varepsilon} \leq 3\right) \tag{2.21}$$

where the correction is not needed for $\tilde{\varepsilon} < 0.15$, and where log is the logarithm to the base 10. This equation closely represents Bridgman's curve, corresponding to the dashed line in Figure 2.7.
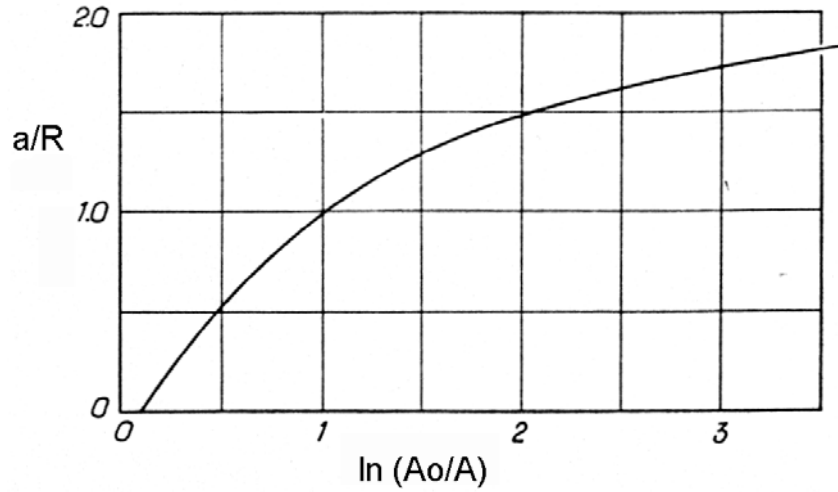
Figure 2.6 Average contour factor (*a/R*) as a function of the logarithmic strain at the neck [9]
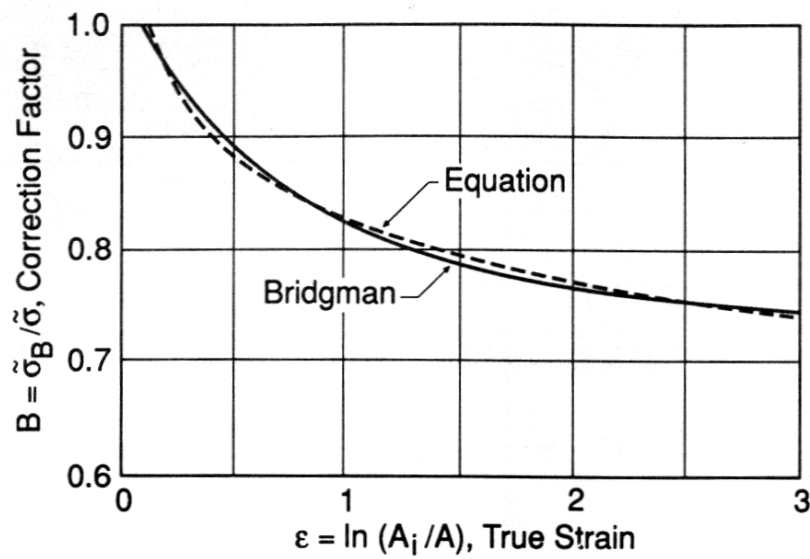
Figure 2.7 The curve of Bridgman [9] is shown along with the curve fitted on it

From the curve, note that a 10% correction ($B = 0.9$) corresponds to a true strain of about $\varepsilon = 0.4$. This corresponds to a ratio of initial to necked diameter of 1.22. Hence, fairly large strains must occur for the correction to be significant.

2.1.2 Compression Test

Since metals generally exhibit their lowest formability under tensile stress, upsetting is performed to attain higher strain values. If the flow curve shall only be determined for low strains the tensile test provides sufficient information. This test is even sufficient in cases where the flow curve determined for low strains can be extrapolated to higher ones. This is the case if the below equation can be presupposed because then only the constants C and n have to be determined. This equation is called Ludwik's equation.

$$\sigma_f = K\bar{\varepsilon}_{pl}{}^n \tag{2.22}$$

In this equation, K and n are specific constants of the material, n being the strain-hardening exponent.

Now it is assumed, however that Ludwik's equation cannot be presupposed – at least not exactly – and that the flow curve is to be determined up to high strains. Ludwik's equation should only be used for rough estimations.

The conventional upsetting test of circular cylinders can be described as compression of a cylindrical test piece between plane parallel dies with lubricated or dry surface (Figure 2.8).

The strain is obtained using the equation

$$\varepsilon(u) = \ln\frac{h(u)}{h_0} < 0 \tag{2.23}$$
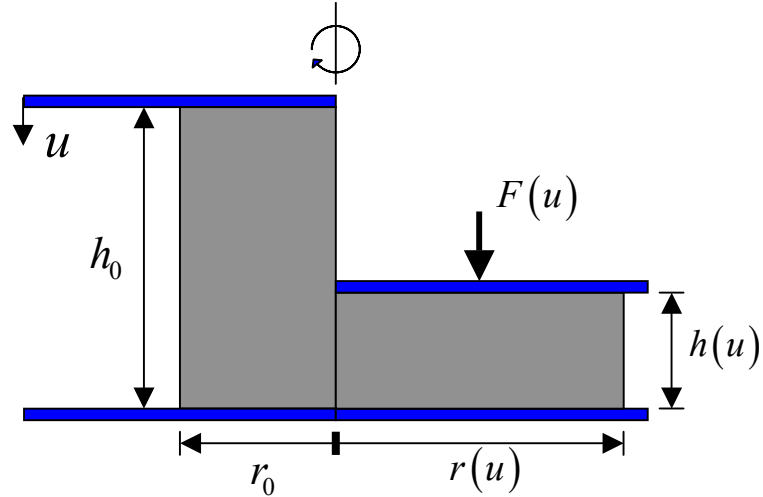
Figure 2.8 Schematic representation of compression test without any friction

In this equation *h(u)* is the actual height of the specimen at the force *F*. So it can be written that

$$h(u) = h_0 - u \qquad (2.24)$$

where u is the measured reduction of height.

Eq. (2.23) leads to

$$h(u) = h_0 e^{-\bar{\varepsilon}} \qquad (2.25)$$

Whereas the strain given by Eq. (2.23) is negative, the equivalent strain is positive by definition. The relation holds

$$\bar{\varepsilon} = -\varepsilon = \ln \frac{h_0}{h(u)} \qquad (2.26)$$

True stress value can be calculated from the measured force *F* and the reduction of height *u* of the specimen.

$$\sigma_f(u) \approx \frac{F(u)}{\pi r^2(u)} \qquad (2.27)$$

In this way the errors of measurement of both the force and the reduction of height are transferred into the obtained true stress while the equivalent strain obtained by Eq. (2.26) is only influenced by the error in the reduction of height.

For discussing the effect of experimental errors on the obtained stress-strain curve, the reduction of specimen height and the force are now written as functions of equivalent strain. Using Eqs.(2.23), (2.24), (2.26) one obtains

$$u(\bar{\varepsilon}) \approx h_0 \left(1 - e^{-\bar{\varepsilon}}\right) \qquad (2.28)$$

Since the force increases to a great extent during the test, considerable elastic deformation of the upsetting dies takes place. This may cause an additional error unless the reduction of height is measured directly at the specimen.

2.1.2.1 Effect of Friction:

Basically, it should be possible to determine flow curves for high strains in upsetting tests. However, in industrial use there are some sources of error that multiply with growing strain. Since the range of high strains is the main field of application of compression tests the amount of such errors should be reduced as much as possible.

One major source of error is the friction between the end faces of the specimen and the dies.

Friction has two effects:

1. An additional force is required for attaining a given strain. According to Siebel [11], Eq. (2.27) has to be replaced by

$$\frac{F(\bar{\varepsilon})}{\pi r^2(\bar{\varepsilon})} \approx \sigma(\bar{\varepsilon}) \left\{ 1 + \frac{2\mu r(\bar{\varepsilon})}{3h(\bar{\varepsilon})} \right\} \qquad (2.29)$$

where μ is the coefficient of friction (Coulomb friction assumed). In order to minimize the correction term in Eq. (2.29), which describes the influence of friction, the slenderness ratio (*r/h*) of the specimen should be as high as possible. However, because of the danger of instability (buckling), it has to be confined to certain limits.

Compression test can be solved also with upper bound method, and similar correction term can be found as

$$\frac{F(\bar{\varepsilon})}{\pi r^2(\bar{\varepsilon})} = \sigma(\bar{\varepsilon}) \left(1 + \frac{2}{3} \frac{m}{\sqrt{3}} \frac{r(\bar{\varepsilon})}{h(\bar{\varepsilon})} \right) \qquad (2.30)$$

where m is shear factor (constant friction factor assumed).

Siebel's correction term will be compared with other correction functions in Chapter 3.

2. Friction causes bulging (barreling) of the specimen that results in a triaxial state of stress. Thus, the strain to fracture is reduced because circumferential tensile stresses appear in the surface of the specimen, which are of the same order of magnitude as the axial compressive stress.

When determining the flow curves, the following problem generally arises. The correction term in Eq. (2.29) has to be determined. For this purpose the coefficient of friction must known. Furthermore the contour of barreling of the specimen has to be measured to correct the test results. Measurement of the contour of barreling causes another measurement error. For all these reasons friction is a very important source of errors, which can only be neglected at low strains in which barreling effect is relatively small.

Numerous modifications of the upsetting test have been described in many publications. They serve mainly to eliminate the effect of friction by after-testing evaluation. These modifications can be subdivided as follows:

- Suppressing barreling by using conical dies: this test was first proposed by Siebel and Pomp [11]. The end faces of the specimen and the upsetting dies are conical that the barreling of the specimens is eliminated for low strains (ε < 0.4). The frictional work, however, cannot be eliminated in this way.

- Upsetting under sticking friction conditions in order to avoid friction work: these conditions can be attained by using grooved anvils and no lubricant. In [13-15] it was shown that for some materials under sticking friction conditions the measured force-displacement curve deviates only slightly from the one obtained with lubricated specimens, see Figure 2.9. This can be explained by assuming that the increase of the resistance to deformation due to friction is compensated by the triaxial state of stress and the inhomogeneity of deformation. Therefore the test data can be treated formally like those measured with good lubrication when calculating the flow curve, using Eqs. (2.23) and (2.27). A disadvantage of upsetting under sticking friction conditions is the tensile stress on the surface of the specimen, which may cause an early initiation of fracture. In spite of this, however, according to [14] the method gives at least as good results as upsetting with good lubrication in the range $\bar{\varepsilon} \leq 0.9$; for higher strains, the measured curve deviates a great deal more from the one obtained with lubrication, see Figure 2.9.
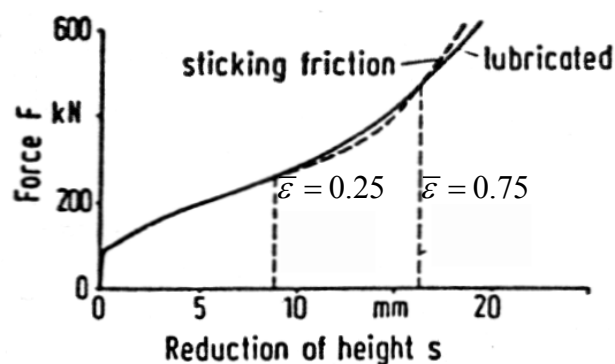
Figure 2.9 Measured curves for upsetting tests with lubrication and under sticking friction [13].

- Extrapolation to infinite slenderness ratio: in the extrapolation method according to Sachs [16] specimens of different slenderness ratios are compressed. The "friction-free" flow curve is obtained by extrapolating the test results to $r_0/h_0 = 0$. Theoretically for a cylinder of infinite length the end effects would be negligible, the barreling effect would therefore be absent (Eq 3.29), and the mean compressive pressure could be taken as the true stress in axial compression. This method has been studied recently by Sato and Takeyama [17]. The compression of at least two or three specimens is required. Furthermore the extrapolation can be inaccurate because of inhomogeneous deformation of the specimens.

- Reducing the friction work by interrupting the test and machining the specimen to its initial slenderness ratio [1,18] or by upsetting predeformed specimens [19].

- Trying to minimize friction: to obtain good lubrication the use of polished dies with a PTFE spray or MoS_2 paste is recommended. An effective lubrication can also be achieved by using PTFE foils, but in this case test results depend on the thickness of the foil; the test must be interrupted at some intervals to replace the foil since its thickness decreases during deformation. Another way to minimize friction can be achieved by using a lubricant together with the geometry proposed by Rastegaev [21]. This treatment will lead to a uniaxial stress state, which can be converted easily into a flow curve, even for high deformation of the sample. This method will be discussed in Section 2.1.2.2. At all cases, lubrication reduces friction, but does not completely eliminate it, and the effect of friction grows as the slenderness of the specimen decreases.

- Determining the coefficient of friction and eliminating the effect of friction by using the correction term for after-test evaluation: Siebel's correction function or correction function coming from upper bound solution of compression process is generally used to obtain friction free flow curve. For this calculation correction friction coefficient should be known. Ring

compression test is one of the standard tests that are used for this purpose. Another method for obtaining a friction free flow curve is using FEM in an iterative way [22, 23]. This method is summarized is Section 2.1.2.3.

2.1.2.2 Rastegaev Compression Test

Various modifications of the upsetting test have been described by which friction is either suppressed or eliminated through test evaluation in Section 2.1.2.1. The simplest way to of reducing friction is to use a proper lubricant. The best lubrication is obtained by using specimens according to Rastegaev [21], see Figure 2.10. For experiments at room temperature paraffine is filled into the end recesses of the test piece as a lubricant.
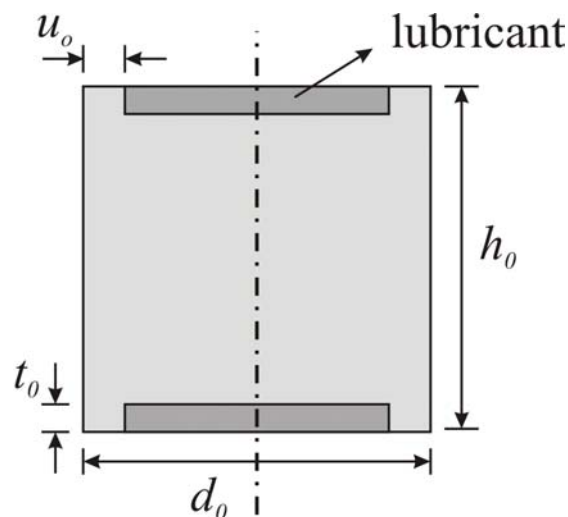
Figure 2.10 Schematic drawing of Rastegaev test specimen.

Figure 2.11 shows that Rastegaev specimens retain a cylindrical shape up to high strains. Unfortunately, compared to conventional specimens for Rastegaev specimens the reduction in height is measured with increased error since the walls surrounding the end faces are bent away and the end faces do not remain plane. From this, an error of both stress and strain results which increases exponentially with increasing strain. This error cannot be reduced by using test pieces of increased slenderness ratio, since the Rastegaev specimens would skew

laterally because of the perfect lubrication. As a rule, the following value of slenderness ratio for Rastegaev specimens are recommended:

$$h_0/d_0 \leq 1 \qquad (2.31)$$
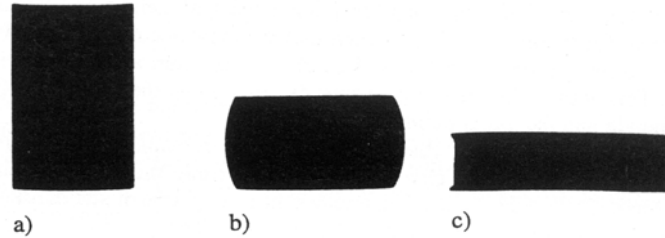
Figure 2.11 Cylindrical upsetting specimens (h_0 = 16 mm, d_0 = 10 mm) with and without end recesses; (a) before test, (b) without lubrication $\bar{\varepsilon} \approx 0.7$, (c) Rastegaev test specimen ($\bar{\varepsilon} \approx 1.3$) [2].

The results of Rastegaev tests depend on the dimensions of the walls surrounding the end faces of the specimens. [2] recommends below conditions for ring dimensions:

$$\frac{t_0}{u_0} > \mu \qquad (2.32)$$

$$\frac{t_0}{u_0} \approx 0.4 \qquad (2.33)$$

2.1.2.3 Iterative FEM Method to Correct Stress Strain Data

Using compression test to obtain flow curve, friction in the interface between the die and the specimen leads to a bulging of the sample and thereby to an inhomogeneous stress and strain state. The calculation of the flow stress from experimentally determined force–displacement curves implies a uniaxial stress state, but this will produce an error because of the above-mentioned bulging, when friction occurs. So to reduce the error caused by inhomogeneous deformation, a method combining compression tests with FEM simulations can

be used and this method will be summarized in this section. In literature this is generally named as inverse analysis.

If one can define a material as a temperature, strain rate, strain and process variables as friction coefficient and slenderness ratios (simply dimensions), the only unknown will be flow curve (stress strain data). Making initial guess of material flow data as experimental data, friction free flow curve can be obtained even in the first iteration with enough accuracy.

Parteder and Bünten [22] successfully applied this method to obtain flow curve from a compression test under sticking friction conditions and called this method as iterative finite-element procedure. In this work it is assumed that strain rate dependency is negligible and isothermal conditions are satisfied. Force-displacement curve is used to obtain force-plastic displacement curve by shifting the curve by u_{off}. Then the flow curve is obtained by Eqs. (2.26) and (2.27). The obtained flow curve is fit to the Ludwik's curve as seen in Figure 2.12. Correction function of FEM iterative method is defined as

$$c^i(u) = 1 - \frac{F_m(u)}{F_s^i(u)} \quad i = 0,1,2...$$
(2.34)

where $F_m(u)$ is measured force for that plastic displacement, $F_s^i(u)$ is simulated force for that plastic displacement and that iteration and $c^i(u)$ is correction function for that iteration.

To protect the solution from the effects of discretization, the relationship $c(u)$ will be fitted by a function of the form:

$$c_{fit}^0(u) = au^s e^{(-bu^s)} + du^t$$
(2.35)

for the zero-iteration. The parameters a, b, d, s and t can be evaluated by curve fitting. So new flow curve can be represented as

$$\sigma_y^{i+1}\left(\varepsilon_{pl}\right) = \frac{\sigma_y^i\left(\varepsilon_{pl}\right)}{1+c_{fit}^i\left(\varepsilon_{pl}\right)} \quad i = 0,1,2... \tag{2.36}$$
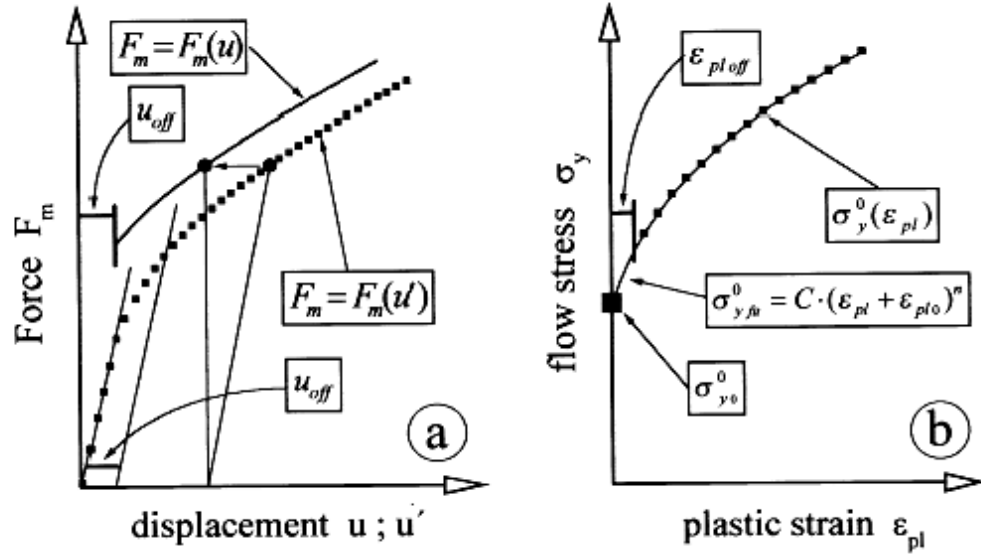
Figure 2.12 Schematic representation of: (a) the measured force-displacement relationship $F_m\left(u'\right)$ and filtering of the elastic deflection $F_m\left(u\right)$; and (b) determination of the flow curves $\sigma_y\left(\varepsilon_{pl}\right)$ with extrapolation of the initial flow stress σ_{y0}^0.

In this study obtained correction function for different slenderness ratios is compared with Siebel's correction function (Figure 2.13). The following equation represents the Siebel's correction function.

$$c_{siebel}\left(\varepsilon_{pl}\right) = \frac{\mu d_0 \sqrt{h_0}}{3\left(h_0 \exp\left(-\varepsilon_{pl}\right)\right)^{3/2}} \tag{2.37}$$

In Figure 2.13 Siebel's correction function is proposed for $\mu = 0.2$. It can be clearly seen that for relatively high slenderness ratios Siebel's correction function is much more higher than the correction function of FEM's. This is beacause Siebel's equation neglects barrelling.

Parteder and Bünten [22] concludes that this correction is almost independent of the temperature and the hardening behaviour of the material.
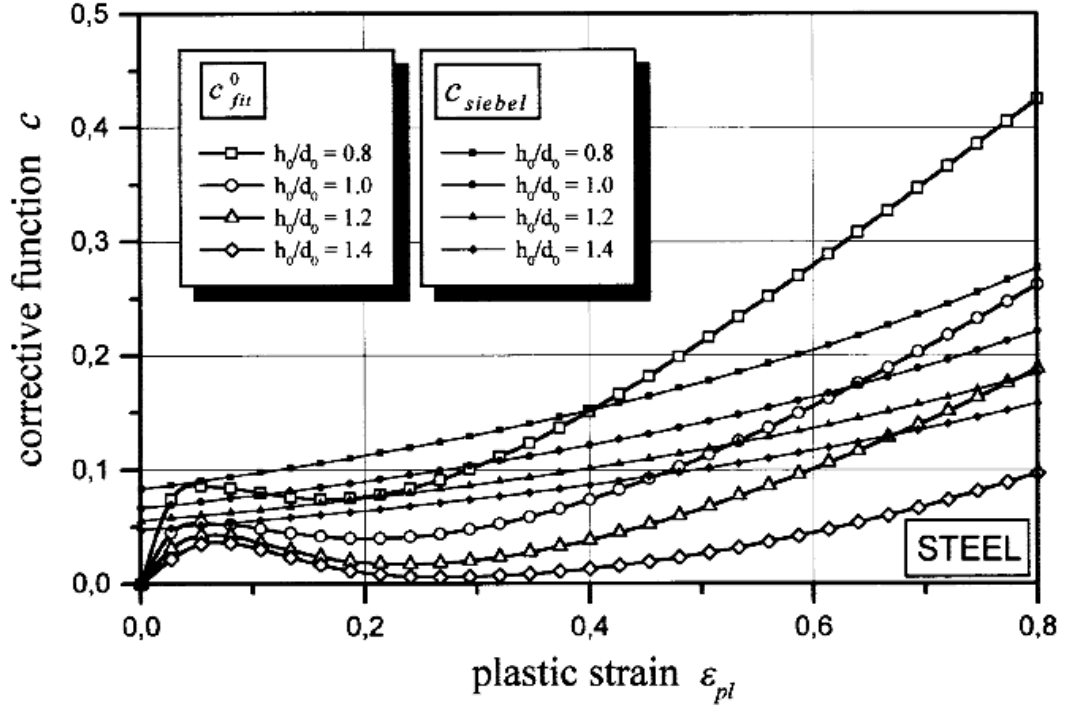
Figure 2.13 Correction function $c_{fit}^{0}\left(\varepsilon_{pl}\right)$ compared with the function proposed by Siebel $c_{siebel}\left(\varepsilon_{pl}\right)$ for different initial sample dimensions

Xinbo et al. [23] also used the same method to determine the metal material flow stress and called it 'method of C-FEM'. In this work elastic part of the strain is neglected, and correction function is defined as

$$\bar{\sigma} = f\left(x_1, x_2, ..., x_3\right)\sigma_{\exp} \tag{2.38}$$

Here, $x_1, x_2, ..., x_i$ are parameters related to conditions which cause inhomogeneous deformation. This method works similar to the iterative finite element procedure but uses different definition for correction function. In C-FEM method a target function is defined to use it as convergence criteria. Iterations are repeated until the target-function attains the required precision. This target function is constructed as follows:

26

During the metal forming process, the power w_0 caused by external force on a sample through dies is equal to the internal plastic deformation power w_p and heat power w_f caused by friction. The external power is calculated by a function

$$w_0 = \sum_{i=1}^{n} P_i v_i \tag{2.39}$$

Here, n is the number of moving dies, P_i the force on the moving die on No. i and v_i is its velocity component in the P_i direction. The internal plastic deformation power and heat power produced by friction on the interface are calculated, respectively, by functions below:

$$w_p = \int \overline{\sigma}\dot{\overline{\varepsilon}}\,dV = \int f\left(x_1, x_2, ..., x_i\right)\overline{\sigma}_{\exp}\dot{\overline{\varepsilon}}\,dV \tag{2.40}$$

$$w_f = \frac{m}{\sqrt{3}}\int \overline{\sigma}\left|\Delta u\right|dV = \frac{m}{\sqrt{3}}\int f\left(x_1, x_2, ..., x_i\right)\overline{\sigma}_{\exp}\left|\Delta u\right|dV \tag{2.41}$$

Here, Δu denotes the relative sliding velocity on the interface.

The total power consumed by a sample can also be calculated by a FEM method:

$$w_i^{FEM} = w_p + w_f \tag{2.42}$$

At any moment during the metal forming process, the equation below should hold

$$w_i^{FEM} = w_0 \tag{2.43}$$

Then, a target-function for C-FEM can be set up according to Eq. (2.43)

$$\Phi = \int \left(w_0 - w_i^{FEM}\right)^2 dt = 0 \tag{2.44}$$

In C-FEM, a correction function $f(x_1, x_2, ..., x_3)$ for $\bar{\sigma}$ is determined by optimizing the target-function, which makes $\bar{\sigma}$ in Eqs. (2.40) and (2.41) try to approach the true flow stress at any moment.

Assuming that L_0 and L_{FEM} denote the instantaneous external load from a compression test and FEM simulation, respectively, then there should be

$$L_{FEM} = L_0 \tag{2.45}$$

Therefore, the target-function for C-FEM can also be expressed as

$$\Phi = \int (L_0 - L_{FEM})^2 \, dt = 0 \tag{2.46}$$

Comparing with Eq. (2.44), the target-function of Eq. (2.46) does not need modification of the original FEM program code, and can be optimized directly by using FEM simulation results. As a result, the correction function $f(x_1, x_2, ..., x_3)$ for $\bar{\sigma}$ can be determined more conveniently.

In this work correction function is fitted to a second order polynomial.

2.1.3 Vickers Hardness and Its Relation with Yield Stress of Cold Formed Materials:

Hardness tests have for a long time been a standard method for material characterization as they provide an easy, inexpensive, non-destructive, and objective method of evaluating basic properties from small volume of materials. As well as resistance to plastic deformation; stiffness, strength of thin coatings, residual stresses near the surface, and the fracture toughness of the material are some basic properties that can be measured by the hardness tests. Hardness measurements are popular because of their flexibility where the products are not appropriate for standard material testing experiments such as simple tension, simple compression or simple torsion. In this study hardness data will be used to

28

supply new increased yield strength distribution of cold-formed products and verify or compare the data obtained by FEM simulations.

In the literature besides Brinell, Rockwell and Knoop hardness tests, Vickers hardness number (HV) has been the most popular in investigation of the relationship between hardness and the flow stress of the material because of two reasons. Firstly, its superior resolution as compared to spherical indenters. And secondly, the Vickers indenter is self-similar, through which the hardness is ideally independent of the indentation load and indentation depth. Therefore, in this study, Vickers indentation will be used as a hardness test.

In literature, various authors have investigated the relationship between Vickers hardness number and the yield stress of material and the yield stress of the material. A review of the first results is covered by Tabor in his standard work [24]. For non-strain hardening materials the Vickers hardness number HV defined as

$$HV = \frac{\text{indenter force in kg}}{\text{surface area of the imprint in mm}^2} \qquad (2.47)$$

is related to the constant yield stress Y by [24]:

$$HV = 2.9 \ Y \text{ to } 3.0 \ Y \qquad (2.48)$$

For strain hardening materials, Tabor [25] suggests a similar expression evaluated at a representative plastic strain:

$$HV = 2.9 \ Y \ \left(\text{at an eng. plastic strain of } 0.08 \right) \qquad (2.49)$$

To analyze the effect of work-hardening material, Tabor performed upsetting tests and measured the hardness values of these specimens and correlated these values to the yield stress of the specimen, which was assumed to be constant. This approach involves errors because the hardness and hence yield stress distribution of the upsetting specimen is rather inhomogeneous due to friction.

The relationship between hardness number and yield stress related to metal forming is investigated by Ramaekers [27], Wilhelm [28], Dannenman et al. [26], Kim et al. [29] and Srinivasan & Venugopal [30]. In all these studies, however, the error in correlation was around 20%.

Some modifications on Tabor's correlation have been performed by Tekkaya [31, 32] for the relationship between Vickers hardness number and the yield strength of the material. Tekkaya conducted Tabor's experiments numerically by means of the finite element method. Experimental uncertainties such as effects of friction, unknown strain and stresses, which altogether lead to diverging analytical models, are avoided by means of this approach. Following basic assumptions and simplifications were made in the simulation of the Vickers indentation test:

— The material behaviour is of elasto-plastic type;
— strain hardening is isotropic (anisotropic hardening behaviour is neglected);
— deformation during indentation is temperature and velocity independent;
— friction between indenter and the workpiece is neglected;
— prior work-hardening of the workpiece material is homogeneous in all directions;
— all the material flow curves used in simulations are Ludwik type of flow curves;
— three dimensional Vickers indentation process can be replaced by a cone indentation process in order to simplify the actual three-dimensional analysis to an axisymmetrical analysis. Hence, an indenter with a conical nose and an equivalent cone angle is used (Figure 2.14).

As a result of extensive simulations with 5 different materials at five different plastic strains, improved Tabor's equation is given as:

$$HV = 2.475\,Y \left(\text{at equivalent plastic strain of } 0.112\right) \qquad (2.50)$$
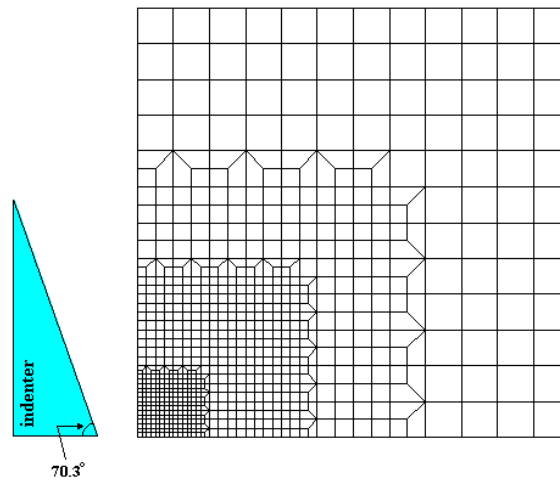
Figure 2.14 Used mesh in the analyses with 773 axisymmetrical elements; semi-cone angle of indenter is 70.3°

Tekkaya [31, 32] also gives a systematic procedure to find the equivalent yield stress of the cold-formed material in the following manner:

— obtain the flow curve of the workpiece material up to high plastic strains as accurately as possible;

— measure the Vickers hardness on the cold-formed workpiece at the required location. For statistical reasons, it is strongly recommended to use at least 10 measurements and take their average;

— compute the representative flow stress in MPa from the proposed formula as:

$$Y_{rep}\left(at\ \varepsilon_{pl}^{*}\right)=9.81\cdot HV/2.475 \qquad (2.51)$$

where ε_{pl}^{*} is offset equivalent plastic strain;

— from the flow curve of the workpiece material determine the value ε_{pl}^{*} corresponding to the representative yield stress Y_{rep}, Figure 2.16;

— the actual yield stress of the material is found from the flow curve by reading the yield stress at the strain $\varepsilon_{pl}^{*}=0.112$ (Figure 2.15).

31
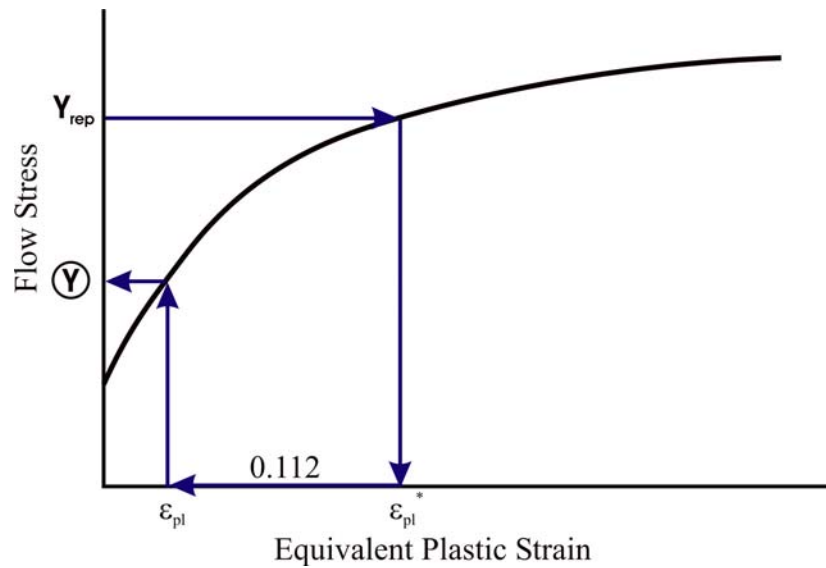
Figure 2.15 Determination of the yield stress of cold-formed parts using the flow curve

Tekkaya and Yavuz [33] repeated a similar work with 10 different materials to obtain the hardness numbers in the strain-hardened states. The hardness values for non-hardened case have been analyzed separately, and the below relation is given

$$HV = 3.04 \cdot Y \quad \textit{(at an offset strain of 0.03)} \qquad (2.52)$$

Linear approximation analysis for the test results obtained from the strain-hardened cases have been done by using different offset strains. Unlike the Tekkaya's relation, maximum regression is obtained with the offset strain of 0.120 and the new relation is observed as following:

$$HV = 2.527 \cdot Y \quad \textit{(at an offset strain of 0.120)} \qquad (2.53)$$

To understand the effects of the strain-hardened states on the correlation, the numerical results have been divided into to two parts such as the equivalent plastic strain in between 0.00 and 0.50, and, greater than 0.50. Following relations are obtained:

$$HV = 2.528 \cdot Y \text{ } \textit{(at an offset strain 0.130)} \quad \textbf{for } \textbf{0.00} < \varepsilon_{pl} < \textbf{0.50} \quad (2.54)$$

$$HV = 2.520 \cdot Y \text{ } \textit{(at an offset strain 0.230)} \quad \textbf{for } \varepsilon_{pl} \geq \textbf{0.50} \quad (2.55)$$

Another work has been done to analyze the influences of the strain-hardening exponent (*n*) in the Ludwik type representation of the flow curves by Tekkaya and Yavuz [33]. In this work, three relations were found for the given interval of n as followings:

$$HV = 2.50 \cdot Y \text{ } \textit{(at an offset strain 0.118)} \quad \textbf{for } \textbf{0.00} < \textbf{n} < \textbf{0.10} \quad (2.56)$$

$$HV = 2.52 \cdot Y \text{ } \textit{(at an offset strain 0.116)} \quad \textbf{for } \textbf{0.10} \leq \textbf{n} < \textbf{0.20} \quad (2.57)$$

$$HV = 2.54 \cdot Y \text{ } \textit{(at an offset strain 0.135)} \quad \textbf{for } \textbf{n} \geq \textbf{0.20} \quad (2.58)$$

Same analysis has been performed for the material constant *K* in the Ludwik's formula ($Y = K \cdot \varphi^n$) as following :

$$HV = 2.51 \cdot Y \text{ } \textit{(at an offset strain 0.140)} \quad \textbf{for } \textbf{K} < \textbf{800} \cdot \textbf{MPa} \quad (2.59)$$

$$HV = 2.51 \cdot Y \text{ } \textit{(at an offset strain 0.130)} \quad \textbf{for } \textbf{K} \geq \textbf{800} \cdot \textbf{MPa} \quad (2.60)$$

Given relations will be used to predict experimental Vickers hardness numbers by using the flow curves obtained for annealed state in Chapter 4.

2.2   Friction Models and Parameter Characterization

A friction model is one of the key input boundary conditions in finite element simulations. It is said that the friction models play an important role in controlling the accuracy of necessary output results. Among the various friction models, which one is of higher accuracy is still unknown and controversial. Frictional parameter values are determined by fitting data of friction area ratio

from finite element analyses to experimental results. The friction area ratio is expressed by:

$$F_r = \frac{A_{w0} - A_{10}}{A_{w0}} \qquad (2.61)$$

where A_{w0} is the final expanded original contact area deformed without friction, A_{10} the final expanded original contact area.

The importance of tribological considerations in bulk metal forming has been generally recognized as affecting: tool life, metal flow during forming, workpiece integrity and surface finish, the relationship of lubricant to machine elements, cost considerations and energy conservation. Although a great deal of effort has been expended in understanding the mechanisms of friction, the subject of friction still remains somewhat in its infancy because of the complex nature of the inter-relationships between the great variety of parameters involved.

Friction models normally applied in finite element analyses for bulk metal forming are:
1. Coulomb friction model:

$$\tau = \mu p \qquad (2.62)$$

2. The constant friction model:

$$\tau = mk \qquad (2.63)$$

3. The general friction model:

$$\tau = f \alpha k \qquad (2.64)$$

where τ is the friction stress, μ the coefficient of friction, p the normal pressure, k the shear flow stress, m the friction factor, f the friction factor expressing the friction in the real contact ($0 \leq f \leq 1$), and α the ratio of the real to the apparent contact area.

Previous friction modelling has been largely based on experimental observations. Distribution of the friction stress in metal forming was not measured until the 1960s. Unksov [46] developed the polarisation-optical method for measuring stresses at the tool/workpiece interface during the plane-strain upsetting of lead specimens. Van Rooyen and Backofen [48] first used a combination of two pins, one normal to the interface and one at an angle, to directly measure the friction stress and normal pressure in upsetting of circular cylindrical specimens. In total, the common points observed by various previous experimental results are:

1. friction stress at the neutral point is zero;

2. friction stress increases largely with increasing diameter/distance from the central/neutral point outwards; and

3. friction stress increases significantly with increasing reduction in height.

Table 2.1 Various friction models used in bulk metal forming (example: simple upsetting)

Friction Model	Friction stress distributions	Main assumptions and applications	Author(s), year
$\tau = \mu p$		Dry slipping occurs over the whole tool/workpiece interface. Friction stress τ is directly proportional to local normal pressure p. It is mainly used for cold metal forming due to its simplicity.	Von Karman, 1925 [36]; Kunogi, 1954 [37]; Kudo, 1960 [38]; Siebel, 1930 [39]
$\tau = mk$		Dry slipping occurs over the whole tool/workpiece interface. $k = \sigma_0/\sqrt{3}$ is the shear flow stress, and σ_0 is the yield stress. It is the most popular model since its simplicity and seemingly indicating the material feature of plastic deformation.	Siebel, 1930 [39]
$\tau = \dfrac{K}{2}$		Sticking occurs over the whole interface between tools and workpiece. $K = 1.15\sigma_0$. It is used for hot metal forming or unlubricated cold forming of "soft" materials.	Orowan, 1946 [40]; Sims, 1954 [41]; Alexander, 1955 [42]
$\tau = \eta \dfrac{d\upsilon_x}{dy}$		Viscous slipping friction proportional to relative velocity of slip,occurs over the whole interface between tools and workpiece. Due to its relative complexity, its applications are very limited.	Nadai, 1939 [43]

Table 2.1 (Continued)
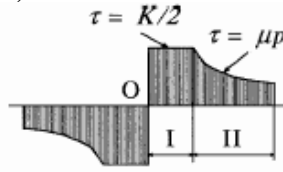
Area I: $\tau = \dfrac{K}{2}$ Area II: $\tau = \mu p$		The interface is divided into two zones: (I) sticking occurs at the central zone whose centre is the neutral point; (II) dry slipping occurs at the edge zone when frictional stress is less than yield stress in shear. It is used for rolling and forging.
		Orowan, 1943 [44]
Area I: $\tau = \tau_{II}\dfrac{r}{OA}$ Area II: $\tau = \dfrac{K}{2}$ Area III: $\tau = \mu p$		A zone of restricted plastic deformation exists in the middle of the sticking zone. The tool/workpiece interface is divided into three zones: (I) the stick zone, $0 \le r < OA$; (II) the drag zone, $OA \le r \le OB$; and (III) the slip zone, $OB \le r < R$, in which R is the contact radius. It is used for general metal forming.
		Tselikov, 1958 [45]; Unksov, 1961 [46]
Area I: $\tau = \tau_{II}\dfrac{r}{OA}$ Area II: $\tau = \dfrac{K}{2}$ Area III: $\tau = \mu p$		Three zones are similar to the model of Tselikov and Unksov: (I) the central sticking zone; (II) the sliding zone, $OA < r < OB$, $p/\sigma_0 \ge 1.5$; and (III) the homogeneous deformation zone, $r > OB$, $p/\sigma_0 < 1.5$. It is used for general metal forming
		Bay and Gerved, 1984 [47]
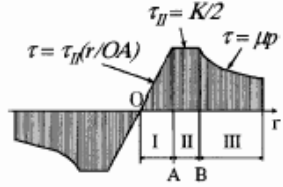
Based on experimental observations, a number of investigations have been carried out to model the friction stress as a function of deformation zone distance. A summary of the friction stress distribution in simple upsetting of a circular cylindrical workpiece as an example is shown in Table 2.1. The main difference between these theories is in the assumptions made with regard to the type of friction (slipping, viscous or sticking) and how the frictional stress is distributed at the tool/workpiece interface. Normally, a friction model can be expressed in terms of either the normal stress or the shear flow stress. It is noted that at the center point (neutral point), a discontinuous jump in friction stress usually appears due to the change of sliding direction, for some theories. Such a discontinuity at the neutral point has not yet been seen in previous experimental observations. Division of different friction zones with a continuous distribution of friction stress at the neutral point might be reasonable. In fact, current FEM codes hardly use these techniques, but apply globally a friction model to the whole contact zone at the tool/workpiece interface, and for the whole process (Table 2.2).

Table 2.2 Friction models normally applied in MSC/Superform

	General expression	Near the neutral point	Reference
Coloumb friction model	$\tau = \mu p$	$\tau_n = \mu p \left\{ \dfrac{2}{\pi} \arctan \left(\dfrac{|u_r|}{u_0} \right) \right\} \dfrac{u_r}{|u_r|}$	[49]
Constant friction model	$\tau = mk$	$\tau_n = mk \left\{ \dfrac{2}{\pi} \arctan \left(\dfrac{|u_r|}{u_0} \right) \right\} \dfrac{u_r}{|u_r|}$	[49]

For the forging process, the currently accepted technique of friction determination involves the deformation of a ring specimen of standard geometry. With good lubrication between the workpiece and platens, there is a general outward expansion of the entire specimen as seen in Figure 2.16. The diameter of the internal hole expands. With poor interfacial lubrication, however, the specimen surface tends to seize to the platens. The outer surface still expands, but the inner free surface now barrels inward and the internal hole diameter decreases.

original specimen

good lubrication

poor lubrication
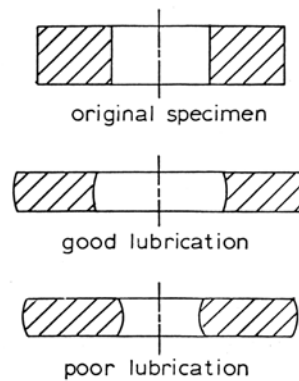
Figure 2.16 Ring profiles

The early approach was to couple experimental results with a supporting analysis of ring deformation based on the theory of plasticity. Early analysis of hollow ring deformation by the slab method was performed by Kunogi [37], and was followed by the upper-bound approach of Kudo [38] and Avitzur [12]. With the assumption of friction having a given model, the friction value is varied to

produce a family of calibration curves (Figure 2.17) relating internal diameter change to reduction.
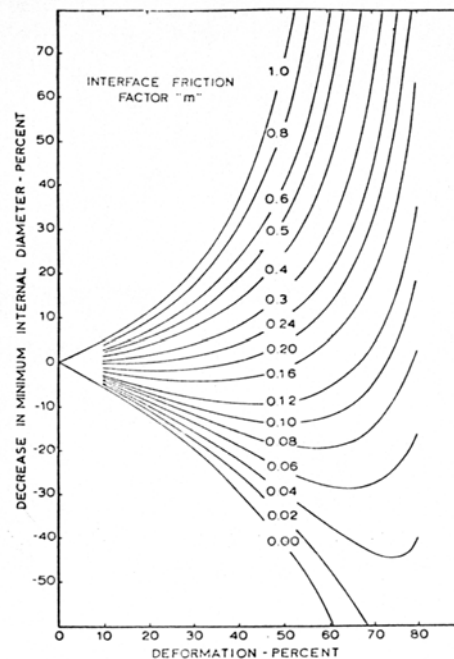
Figure 2.17 Calibration curves [34]

Although having already established its functional utility, the ring compression test for determining friction does have several areas of deficiency. First, it is indeed possible that friction values will vary as reduction in height proceeds. Secondly, ambiguities may arise when the specimen deforms with excessive barreling or bulging, or shows an out-of-roundness or eccentricity of the center hole.

The complexity that arises from the analysis of nonuniform deformation (barreling and folding), is tried to be solved by coupling the experimental results with a supporting analysis of FEM. Tan [35] performed some compression experiments and presented that calibration curves of the friction area ratio for all of the five chosen friction models used in the finite element simulations do fit the experimental results.

Another work is performed by Kocak [50]. He compared inner and outer diameter of contact surface and the barreled outer diameter with finite element simulations. Through out this study in FE simulations Coulomb friction will be

38

used. The coulomb friction coefficient is determined by ring compression tests by Kocak [50].

2.3 Plastic Material Behavior

In order to describe the plastic behaviour of a material in a general stress state, three elements are needed:

  – a yield criterion expressing the relationship between the stress components at the moments when plastic yielding occurs,
  – an associated flow rule expressing the relationship between the components of the strain-rate and stress,
  – a hardening rule describing the evalution of the initial yield stress during the forming process.

2.3.1 Yield Criterion

The transition from elastic to the plastic state occurs when the stress reaches the yield point of the material. In the one-dimensional tension-compression test, yielding takes place when the stress $\sigma = F/A$ reaches the value σ_f. This condition can be considered to be a yield criterion,

$$\left| \frac{F}{A} \right| = \sigma_f \qquad (2.65)$$

In case of a multiaxial stress it is more difficult to define a criterion for the transition from elastic to the plastic state. From many yield criteria, which have been proposed for an isotropic material, criterion of von Mises is one of the most popular one.

In terms if principal stresses, the von Mises criterion reads

$$\sigma_f = \sqrt{\frac{1}{2}\left[\left(\sigma_1 - \sigma_2\right)^2 + \left(\sigma_2 - \sigma_3\right)^2 + \left(\sigma_1 - \sigma_3\right)^2\right]} \qquad (2.66)$$

The start of the flow must depend on a combination of normal and shear stresses, which does not change its value when transformed from one coordinate system into another. Hence von Mises criterion can be written in a general way as follows:

$$\sigma_f = \sqrt{\frac{1}{2}\left[\left(\sigma_x - \sigma_y\right)^2 + \left(\sigma_y - \sigma_z\right)^2 + \left(\sigma_z - \sigma_x\right)^2 + 3\left(\tau_{xy}^2 + \tau_{yz}^2 + \tau_{zx}^2\right)\right]} \quad (2.67)$$

A physical interpretation of the von Mises rule shows that the right side of Eq. (2.67) is proportional to the energy which is stored in the elastically deformed material prior to yielding. This is the energy necessary for elastic volume change. The flow rule says that plastic flow starts when this elastic energy reaches a critical value. That is the why the von Mises rule is also called the "distortion energy criterion".

Such a relation is the mathematical description of a surface in the three dimensional space of the principal stresses usually called the "yield surface".
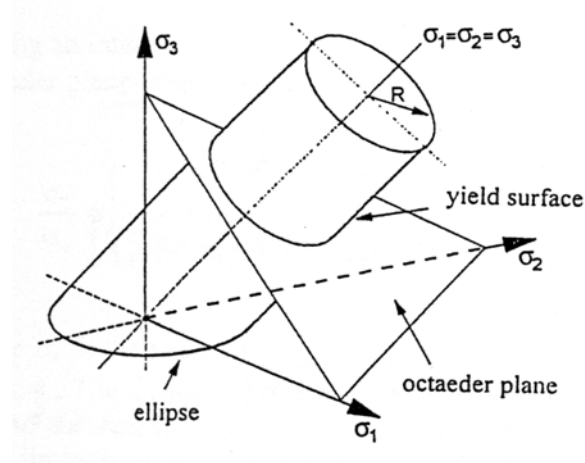
Figure 2.18 Mises yield surface in stress space.

The yield surface must be closed, smooth and convex. For incompressible materials it is a cylinder the cross section of which depends on the material. For the von Mises criterion it is a circular cylinder (Figure 2.18). All the points located in the inside of the surface are related to an elastic state of the material. The points belonging to the surface are related to the plastic state. Points outside have no physical meaning.

Eq. (2.67) was developed for isotropic materials. Many workhardened alloys, however, exhibit anisotropy in mechanical properties due to the crystallographic texture caused by the forming process. For an anisotropic material also there are various yield criteria existing (e.g. Hill [51], Hosford [52], Barlat [53], Karafillis-Boyce [54]), but Hill's quadratic yield criteria is one of the most popular one for steel type of metals because of its simplicity and easy implementation to FEM codes. In this model material is supposed to have an anisotropy with three orthogonal symmetry planes.

The yield criterion is expressed by a quadratic function of the following type

$$
\begin{aligned}
2f\left(\sigma_{ij}\right) \equiv F\left(\sigma_y - \sigma_z\right)^2 + G\left(\sigma_z - \sigma_x\right)^2 + H\left(\sigma_x - \sigma_y\right)^2 \\
+2L\tau_{yz}^2 + 2M\tau_{zx}^2 + 2N\tau_{xy}^2 = 1
\end{aligned}
\tag{2.68}
$$

Here f is the yield function; F, G, H, L, M and N are constants specific to the anisotropy state of material, and x, y, z are the principal anisotropic axes. It is assumed that there is no Bauschinger effect and that a hydrostatic stress does not influence yielding. Hence, linear terms are not included and only differences normal stress components appear in the yield criterion.

In the case of sheet metals x is usually parallel to the rolling direction, y in transverse and z in normal direction.

If the tensile yield stresses in the principal anisotropy directions are denoted by X, Y and Z, it can easily be shown that

$$\frac{1}{X^2} = G + H; \quad \frac{1}{Y^2} = H + F; \quad \frac{1}{Z^2} = F + G \qquad (2.69)$$

From this equation, by some simple mathematical calculations the coefficients F, G, and H are obtained as functions of the uniaxial yield stresses

$$2F = \frac{1}{Y^2} + \frac{1}{Z^2} - \frac{1}{X^2}; \quad 2G = \frac{1}{Z^2} + \frac{1}{X^2} - \frac{1}{Y^2}; \quad 2H = \frac{1}{X^2} + \frac{1}{Y^2} - \frac{1}{Z^2} \qquad (2.70)$$

If R, S and T are the shear yield stresses associated to the same directions, then

$$2L = \frac{1}{R^2}; \quad 2M = \frac{1}{S^2}; \quad 2N = \frac{1}{T^2} \qquad (2.71)$$

As a consequence, in order to give a complete description of the anisotropy of the material, six independent yield stresses (X, Y, Z, R, S and T) have to be known as the orientation of the principal anisotropy axes.

2.3.2 Work Hardening Rules

The term classical theory of plasticity is applied to the behavior of a solid which obeys von Mises yield criterion and the associated flow directed along the normal to the yield surface. The symmetry of the von Mises yield surface in deviatoric stress space requires symmetry in the associated plastic flow in uniaxial tension and compression. This type of material use isotropic hardening which assumes that the yield surface expands with work hardening while neglecting the distortion and movement of the center of the yield surface. Isotropic hardening can give a good approximation as long as the path of forward loading remains radial or proportional. Isotropic hardening is incorporated into plasticity theories with a parameter that usually depends on plastic strain. It follows that such a model cannot accommodate the Bauschinger effect which entails different behavior in tension and compression. A simple way to allow for this effect is to let the yield surface translate relative to the origin of the stress space. A shift of the center of the yield surface means that it is no longer

symmetric with respect to the origin. The shift is a feature of kinematic hardening. It is expressed in terms of shift tensor, also called back stress.

Most constitutive equations for plastic deformation of solids use either isotropic hardening, kinematic hardening, or a combination of both. Below sections give some brief description of these hardening rules.

2.3.2.1 Isotropic Hardening:

The isotropic workhardening rule assumes that the center of the yield surface remains stationary in the stress space, but that the size (radius) of the yield surface expands, due to workhardening. The change of the von Mises yield surface is plotted in Figure 2.19(b).
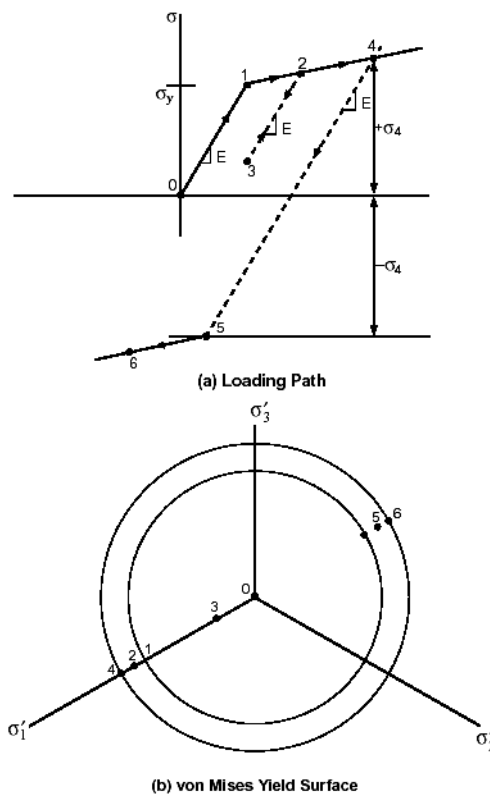
Figure 2.19 Schematic of isotropic hardening rule (uniaxial test)

A review of the load path of a uniaxial test that involves both the loading and unloading of a specimen will assist in describing the isotropic workhardening rule. The specimen is first loaded from stress free (point 0) to initial yield at point

1, as shown in Figure 2.19(a). It is then continuously loaded to point 2. Then, unloading from 2 to 3 following the elastic slope E (Young's modulus) and then elastic reloading from 3 to 2 takes place. Finally, the specimen is plastically loaded again from 2 to 4 and elastically unloaded from 4 to 5. Reverse plastic loading occurs between 5 and 6. It is obvious that the stress at 1 is equal to the initial yield stress and stresses at points 2 and 4 are larger than σ_y, due to workhardening. During unloading, the stress state can remain elastic (for example, point 3), or it can reach a subsequent (reversed) yield point (for example, point 5). The isotropic workhardening rule states that the reverse yield occurs at current stress level in the reversed direction. Let σ_4 be the stress level at point 4. Then, the reverse yield can only take place at a stress level of σ_4 (point 5).

For many materials, the isotropic workhardening model is inaccurate if unloading occurs (as in cyclic loading problems). For these problems, the kinematic hardening model or the combined hardening model represents the material better.

2.3.2.2 Kinematic Hardening

Under the kinematic hardening rule, the von Mises yield surface does not change in size or shape, but the center of the yield surface can move in stress space. Figure 2.20(b) illustrates this condition. Ziegler's law [56] is used to define the translation of the yield surface in the stress space.

The loading path of a uniaxial test is shown in Figure 2.20(a). The specimen is loaded in the following order: from stress free (point 0) to initial yield (point 1), 2 (loading), 3 (unloading), 2 (reloading), 4 (loading), 5 and 6 (unloading). As in isotropic hardening, stress at 1 is equal to the initial yield stress σ_y, and stresses at 2 and 4 are higher than σ_y, due to workhardening. Point 3 is elastic, and reverse yield takes place at point 5. Under the kinematic hardening rule, the reverse yield occurs at the level of $\sigma_5 = \left(\sigma_4 - 2\sigma_y\right)$, rather than at the stress level

of $-\sigma_4$. Similarly, if the specimen is loaded to a higher stress level σ_7 (point 7), and then unloaded to the subsequent yield point 8, the stress at point 8 is $\sigma_8 = (\sigma_7 - 2\sigma_y)$. If the specimen is unloaded from a (tensile) stress state (such as

(a) Loading Path

(b) von Mises Yield Surface

Figure 2.20 Schematic of kinematic hardening rule (uniaxial test)

point 4 and 7), the reverse yield can occur at a stress state in either the reverse (point 5) or the same (point 8) direction.

For many materials, the kinematic hardening model gives a better representation of loading/unloading behavior than the isotropic hardening model. For cyclic loading, however, the kinematic hardening model can represent neither cyclic hardening nor cyclic softening.

2.3.2.3 Combined Hardening:

Some load reversal experiments recently showed that neither isotropic hardening nor kinematic hardening can model this type of behavior (Figure 2.21).
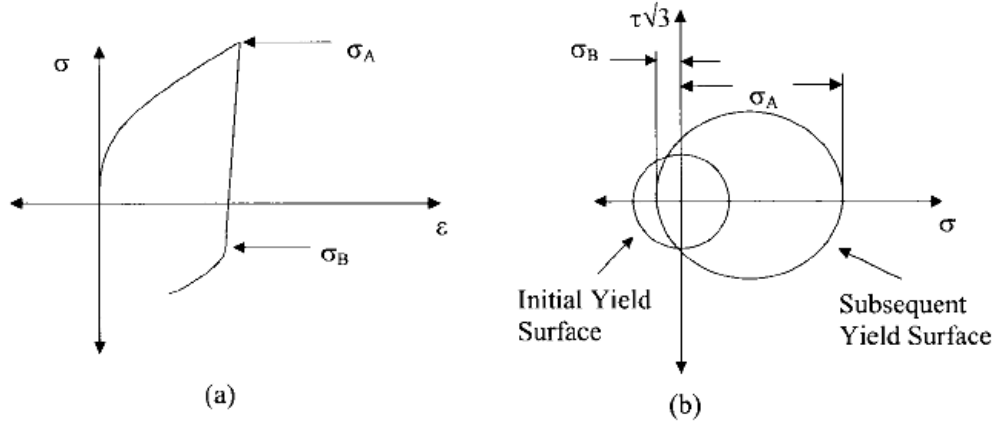
Figure 2.21 (a) Method of determining σ_A and σ_B (compression after tension); (b) representation of σ_A and σ_B on yield surfaces

Figure 2.22 shows a material with highly nonlinear hardening. Here, the initial hardening is assumed to be almost entirely isotropic, but after some plastic straining, the elastic range attains an essentially constant value (that is, pure kinematic hardening). The basic assumption of the combined hardening model is that such behavior is reasonably approximated by a classical constant kinematic hardening constraint, with the superposition of initial isotropic hardening. The isotropic hardening rate eventually decays to zero as a function of the equivalent plastic strain measured by

$$\overline{\varepsilon}^p = \int \dot{\overline{\varepsilon}}^p \, dt = \int \left(\frac{2}{3} \dot{\varepsilon}_{ij}^p \dot{\varepsilon}_{ij}^p \right)^{1/2} dt \qquad (2.72)$$

This implies a constant shift of the center of the elastic domain, with a growth of elastic domain around this center until pure kinematic hardening is attained. In this model, there is a variable proportion between the isotropic and kinematic

46

contributions that depends on the extent of plastic deformation (as measured by $\overline{\varepsilon}^p$).

The workhardening data at small strains governs the isotropic behavior, and the data at large strains governs the kinematic hardening behavior. If the last workhardening slope is zero, the behavior is the same as the isotropic hardening model.
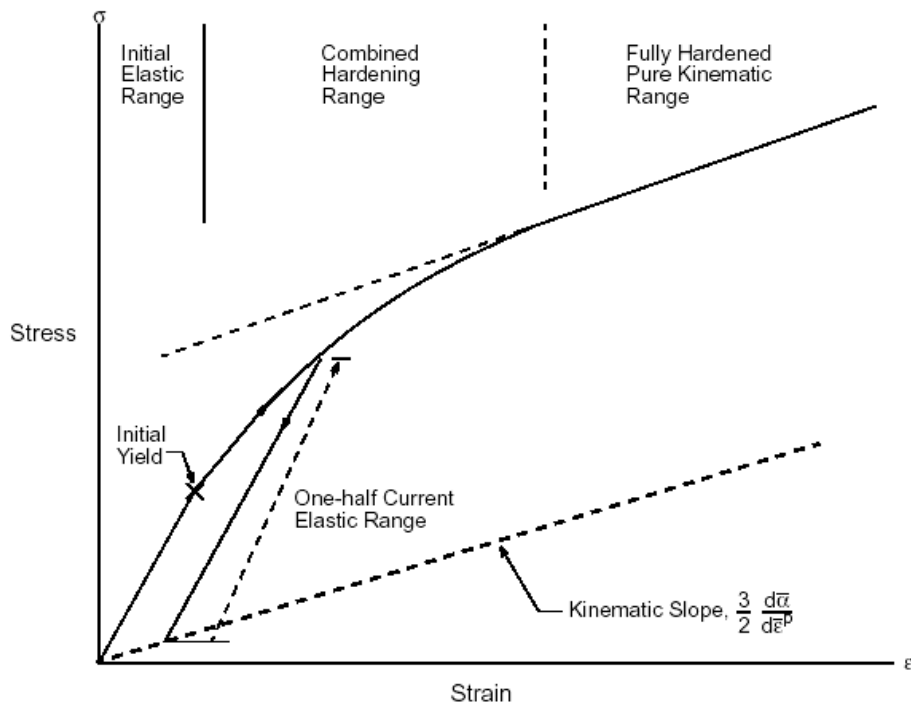
Figure 2.22 Basic uniaxial tension behavior of the combined hardening model

Non-linear kinematic hardening model can reproduce the shape of the stress-strain curve quite well, but is not able to predict certain features of the material behavior at points of loading reversal: it has been observed that for some materials, the response at the reversed yield point show a certain transient behavior [57,58,63-70]. It is well known that the above mentioned kinematic hardening rule cannot approximate such a transient. Recently Hu[68,69], Yoshida and Uemori [70] attempted to model this transient response.

47

2.3.3 Flow Rule

Yield stress and workhardening rules are two experimentally related phenomena that characterize plastic material behavior. The flow rule is also essential in establishing the incremental stress-strain relations for plastic material. The flow rule describes the differential changes in the plastic strain components $d\varepsilon^p$ as a function of the current stress state.

The Prandtl-Reuss representation of the flow rule in conjunction with the von Mises yield function can be represented as:

$$d\varepsilon_{ij}^p = d\overline{\varepsilon}^p \frac{\partial \overline{\sigma}}{\partial \sigma_{ij}'} \qquad (2.73)$$

where $d\overline{\varepsilon}^p$ and σ are equivalent plastic strain increment and equivalent stress, respectively.

The significance of this representation is illustrated in Figure 2.23. This figure illustrates the "stress-space" for the two-dimensional case. The solid curve gives the yield surface (locus of all stress states causing yield) as defined by the von Mises criterion.

Eq (2.73) expresses the condition that the direction of inelastic straining is normal to the yield surface. This condition is called either the normality condition or the associated flow rule.

If the von Mises yield surface is used, then the normal is equal to the deviatoric stress.
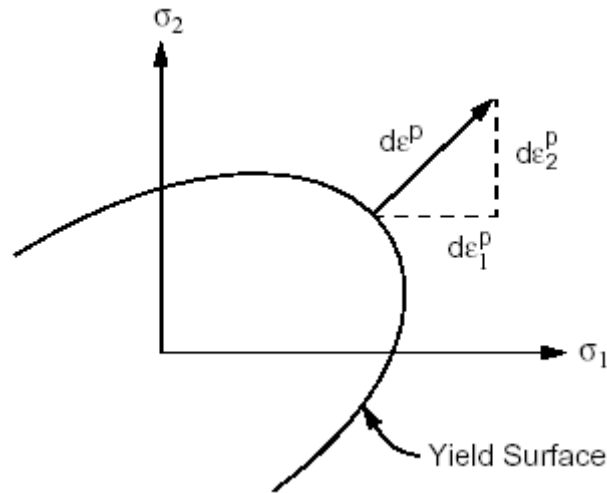
Figure 2.23 Yield surface and normality criterion 2-D stress space

2.4   Austenitic Stainless Steels

In this section a general information for austenitic stainless steels and especially for AISI 316 steel which is investigated in this study.

Austenitic stainless steels are used in the production of a wide variety of formed and drawn parts for architectural, automotive, industrial, and domestic applications. The most commonly used stainless steels are the austenitic grades, of which AISI 302 and 304 are the most popular. These grades contain 16% or more Cr, a ferrite-stabilizing element, and sufficient austenite stabilizing elements, such as carbon, nitrogen, nickel, and manganese, to render austenite stable at room temperature. The grades containing silicon, molybdenum, titanium, or niobium – AISI 302B, 316, 317, 321, and 347, for example – will sometimes include a minor amount of δ-ferrite because of ferrite-stabilizing influence of these elements. Alloys with substantial nickel are fully austenitic, for example, AISI 310 or 330.

Austenitic stainless steels can be classified as stable and metastable with respect to the stability of the austenite in them. Martensite can be formed, particularly in the leaner grades, by cooling specimens to very low temperatures or by extensive

deformation. Nonmagnetic, hexagonal close-packed (hcp) ε-martensite and magnetic, body-centered cubic (bcc) α'-martensite have been observed. Emprical relations have been developed to show how composition influences the resistance of such steel to deformation-induced martensite.

For many metals the flow curve is described empirically by the Ludwik's equation (Eq. (2.22)). Several researchers [59-62] have observed deviations of the flow curve from the Ludwik relation for stainless steels. Low and Garofalo [59] found that Ludwik relation was an inadequate description of the plastic flow behavior exhibited by an 18-8 stainless steel and suggested a strain induced decomposition of austenite to martensite was responsible for the exceptional behavior of this material.

To illustrate further the influence of the strain-induced transformation of austenite to martensite in metastable austenitic stainless steels, the flow curve of a sample of AISI type 301 steel is compared in Figure 2.24 with the flow curve of a deep-drawing carbon steel. The upper curve in this curve is for the type 301 steel, an example of a metastable austenitic stainless steel that exhibits a marked strain-induced transformation. The lower curve in this figure is for carbon steel, a material that undergoes no transformation and obeys the Eq. (2.23). The flow curve of the type 301 steel, in addition to lying at higher stresses than the flow curve for the carbon steel, exhibits a complex curvature that cannot be accounted for by Eq. (2.23).

Ludwigson and Berger [60] presented a new stress-strain relation for metastable austenitic stainless steels (like AISI 301 steel) by using volume fractions of remained austenite and newly formed martensite.
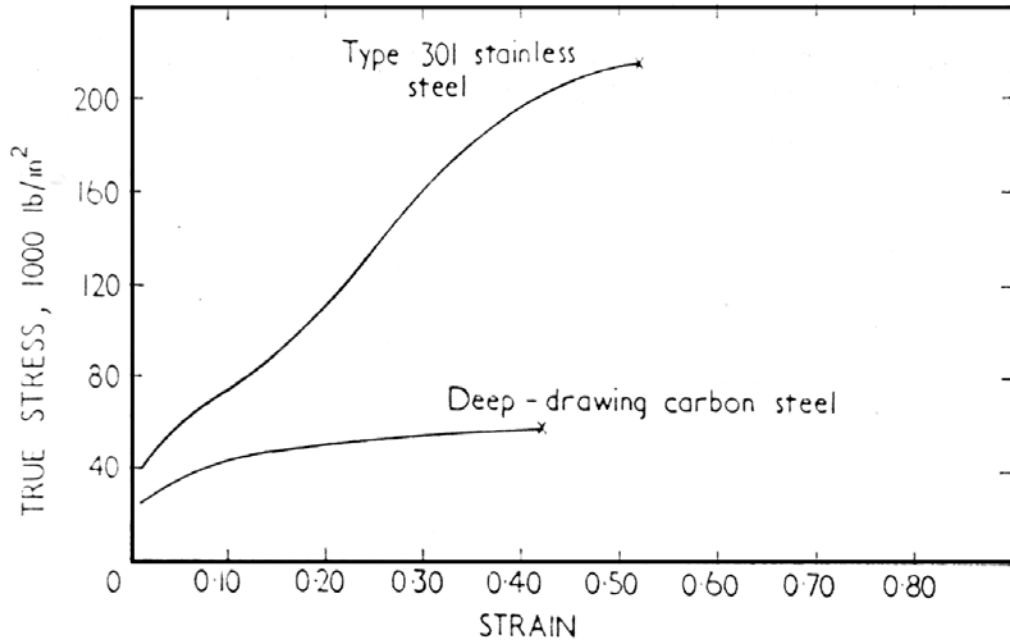
Figure 2.24 Difference in the plastic behavior of deep-drawing carbon steel and type 301 stainless steel in uniaxial tension test [60]

Then it is understood that this deviation of the flow curve is not unique to only metals that exhibit phase transformation. Ludwigson [61] latter developed a model for annealed stable austenitic (also a fcc structure) steel that doesn't exhibit any martensitic transformation and for some other fcc metals and alloys. This model can be summarized shortly for the stainless steel used in this study as follows:

As shown in Figure 2.25, the Ludwik relation fails to describe the plastic behavior of stainless steel at lower strains. The flow curve at low strains is concave up when plotted on logarithmic coordinates and lies at higher stresses than those represented by the Ludwik relation to low strains.

The difference between the observed true stress at low strains and the stress represented by the Ludwik relation extended to these low strains is termed Δ. In Figure 2.26 the logarithm of Δ was plotted against strain. This function can be represented as a linear function of strain:

$$\ln \Delta = K_2 + n_2 \varepsilon \qquad (2.74)$$

51
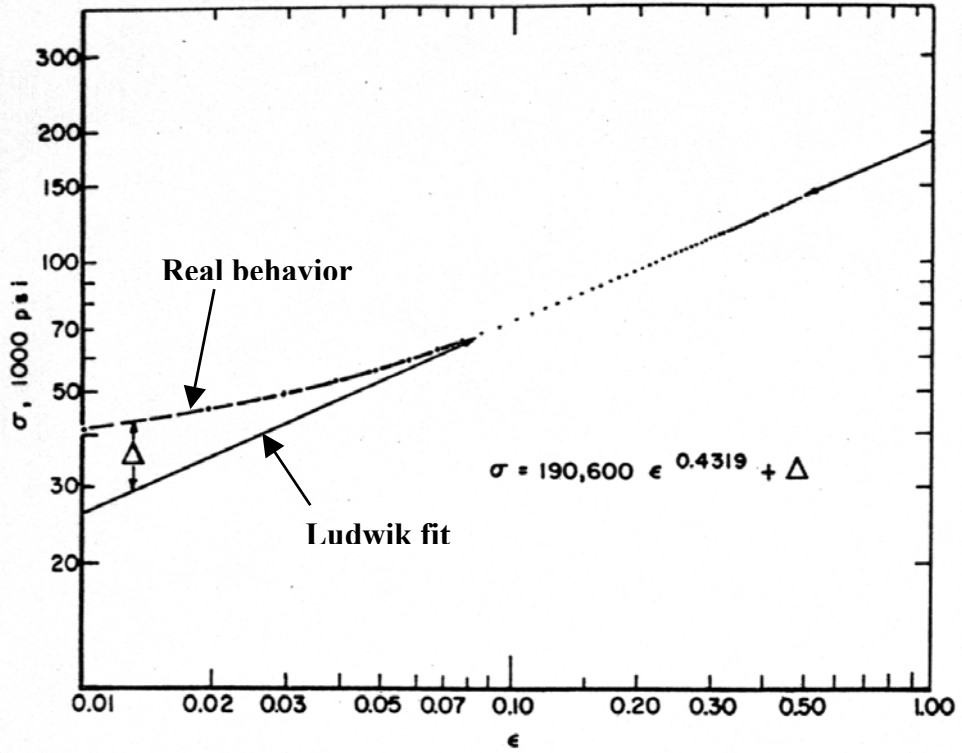
Figure 2.25 Example of a flow curve for a stable austenitic stainless steel

(logarithmic coordinates) [61]
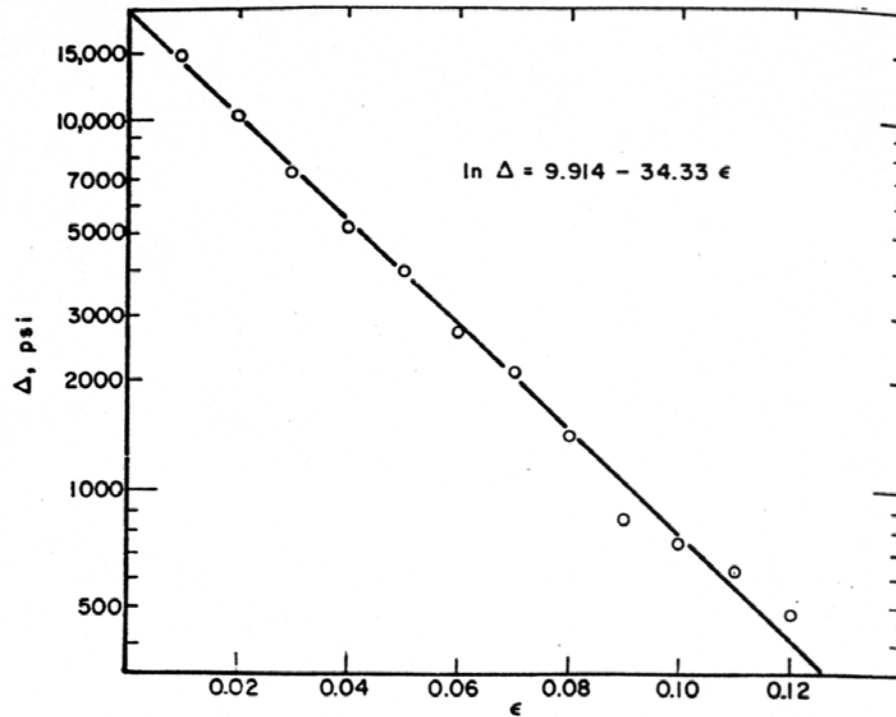
Figure 2.26 The relation between Δ (logarithmic coordinates) and true strain [61]

52

In this case K_2 and n_2 are constants. Modified Ludwik's relation now can be written as

$$\sigma = K_1 \varepsilon^{n_1} + \Delta \qquad (2.75)$$

where $\Delta = e^{(K_2 + n_2 \varepsilon)}$. Then mathematical model of Ludwigson can be written as

$$\sigma = K_1 \varepsilon^{n_1} + e^{K_2} \cdot e^{n_2 \varepsilon} \qquad (2.76)$$

where $K_1 = K$ and $n_1 = n$ which are constants of Ludwik's relation.

An additional parameter, ε_L, is defined by Ludwigson [61] as the minimum strain above which the unmodified Ludwik relation reasonably represents the data. The value of ε_L was evaluated by setting the ratio of the modification term, Δ, to the other term, $K_1 \varepsilon^{n_1}$, in Eq. (2.76) equal to some arbitrary small value r:

$$e^{(K_2 + n_2 \varepsilon_L)} \big/ K_1 \varepsilon_L^{n_1} = r \qquad (2.77)$$

In Ludwigson's work, a value of $r = 0.02$ is selected to evaluate ε_L.

The flow curve parameters derived for various fcc metallic structures in Ludwigson's work [61] are given in Table 2.3. The metals and alloys in this table are arranged in order of increasing stacking fault energy. The 17Cr-15 Mn-0.4 N steel, a stable austenitic stainless steel sample, and brass – structures with lowest stacking fault energies – exhibited the smallest negative values of n_2 and the largest values of ε_L. Structures with somewhat higher stacking fault energies – silver and copper – exhibited more negative values of n_2 and the lower values of ε_L. Aluminum and nickel, metals with high stacking fault energies, did not exhibit the departure from Ludwik behavior at low strains that was found to be the characteristic of the other fcc structures tested.

Table 2.3 Flow-curve parameters of fcc materials tested in bar form in air [61]

	K_1, ksi	n_1	K_2	$-n_2$	ε_L
17Cr-15 Mn-0.4 N	278.6	0.4778	10.637	24.27	0.124
Stainless Steel					
(T5482-1)	194.3	0.5067	9.996	17.47	0.154
Brass	78.8	0.1547	10.366	23.51	0.141
Silver	50.8	0.4354	7.839	70.25	0.034
Copper	68.6	0.4054	7.868	75.80	0.028
Aluminum	21.2	0.216	*	*	*
Nickel	151.8	0.357	*	*	*

Ludwigson concluded that deviation from Ludwik's relation is generic to low-stacking-fault fcc metallic structures. The initial transient positive departure from the Ludwik relation is thought to correspond to the planar glide of dislocations. However, as they are interdicted in this motion by their increasing density, dislocations tend to cross slip and create cells. The secondary state behavior, described adequately by the unmodified Ludwik relation, is thought to correspond to cross slip and its consequent cell formation and cell wall thickening. It is shown also by electron transmission examination that ε_L is the strain at which the transient behavior decays and the steady-state behavior becomes predominant. In materials with low stacking fault energy, the recombination of disassociated partial dislocations, required before cross slip can occur, is difficult. In such materials an extended transient region is expected. But is stacking fault energy is high, cross slip can occur more readily and a restricted range of transient behavior is expected.

Mannan et al. [62] investigated 316 stainless steel with different grain sizes in the range of 0.025 – 0.650 mm at room temperature at a nominal strain rate of 3×10^{-4} s^{-1} and used Ludwigson's equation to model the flow curve. In this study the absence of martensite was confirmed by examining the tested specimens

magnetically with a ferriscope as well as by x-ray diffraction. Table 2.4 gives comparison of values of constants for Ludwigson's equation that are evaluated by Mannan et al. [62].

Table 2.4 Summary of flow curve parameters of modified Ludwik relation (Ludwigson's equation) at 300 K for various grain sizes [62]

Grain diameter (mm)	K_1 (MPa)	n_1	K_2	$-n_2$	ε_L
0.025	1350	0.381	5.089	42.089	0.097
0.040	1230	0.398	4.911	34.877	0.114
0.060	1250	0.415	5.055	33.195	0.123
0.125	1240	0.456	5.052	30.509	0.136
0.270	1220	0.460	5.068	29.899	0.139
0.650	1090	0.464	5.056	29.303	0.145

Ulvan and Kousaris [63] also performed experiments on bulk formability and tensile properties of austenitic stainless steel types 304 and 316. They have observed that tensile specimens of steel 304 underwent a martensitic transformation during testing, which was evident from the magnetic nature if the specimens after testing. On the other hand specimens of steel 316 showed a lesser tendency to transform to martensite during tensile testing, but the necked region of these specimens exhibited weak magnetic properties. Being different from Ludwigson's work, they found that logarithmic plot of delta (Δ) against true strain values was better described by a second order equation. Hence, they presented the below equation:

$$\sigma = K_1 \varepsilon^{n_1} + \exp\left(M_1 \varepsilon^2 + M_2 \varepsilon + M_3\right) \quad (2.78)$$

The value of strain ε_L increased with increasing grain size in both steels 304 and 316. This is in agreement with the results of Mannan et al. [63] on steel type 316.

2.5   Large Strain Load Reversal Experiments

In metals which have been plastically deformed in one direction, the yield and flow stresses during unloading and reverse loading are lower than those in the same direction as that of prestaining. This phenomenon is widely known as the Bauschinger effect [64]. The degree of the effect has been estimated by several parameters, such as the drop in the yield stress or the proof stress at the stress reversal, the strain in the reversed direction (the Bauschinger strain) and the energy which may help the deformation at the time at the time of reversed load. The work-hardening behavior of a polycrystalline solid under Bauschinger and cyclic deformation has been investigated for some decades because of its importance for both understanding of fundamental mechanics of plastic deformation and industrial application. A significant progress has been achieved in the field of cyclic plasticity at small strains in explaining phenomena like cyclic hardening, stress-strain hysteresis, Masing relationship. For a complete understanding of the effect, the whole shape of the stress-strain curve in the reversed direction (the Bauschinger curve) must be taken account. As for experimental observations, only a limited number of papers have been published on large-strain cyclic plasticity, while there are many papers on reverse deformation experiments after large strains [57,58,65-72]. These papers are generally about large strain stress reversal on cell-forming metals and it is stated that the most common dislocation configuration in fcc metals developed during room-temperature deformation is the cell structure. In many materials, after a certain amount of monotonic loading, the dislocations are not randomly dispersed inside the material but tend to dispose themselves along certain patterns and form dislocation structures such as cells and walls that can be observed with the transmission electron microscope (TEM). Also it is mentioned that AISI 316 steel is stated as a stable austenitic stainless steel by several researchers [61,62] and the cell forming structure of this steel is reported.

Some researchers and the materials that were investigated by them are given in Table 2.5.

Table 2.5 Researcher investigated the effect of large strain load reversals on several materials

Materials	Tests Performed	Reference
Aluminum (fcc)	Tension – Compression Compression - Tension	Hasegawa and Yakou [65]
Copper (fcc)	Tension – Compression Compression - Tension	Christodoulou et al. [68]
Aluminum (fcc) Copper (fcc)	Tension – Compression	Hasegawa et al. [66]
Aliminum (fcc)	Torsion tests of thin-walled tube specimens	Takahashi and Shiono [67]
99.99 pct Al OFE copper 70:30 brass Al-1 pct Mg Al-2 pct Mg Al-0.17 pct Fe-0.07 pct Si Al-0.8 pct Mn two Al-Cu alloys	Torsion tests of thin-walled tube specimens	Stout and Rollett [69]
Aluminum-killed mild steel (0.036% carbon) (bcc)	Planar simple shear test	Hu et al. [70]

Hasegawa and Yakou [65] investigated the compressive flow beahaviour of polycrystalline aluminium pre-strained by tension at room temperature and 450^0C, in order to obtain information about the dislocation mechanism for the Bauschinger effect. The change in dislocation structures during compression was also examined by transmission electron microscopy.

The work-hardening rate was smaller at an early stage of compression than just before the stress reversal as seen from the Figure 2.27. This tendency became more marked with increasing temperature; at temperatures above 150^0C the plastic deformation proceeded at a constant flow stress at an early stage of compression. Hasegawa and Yakou [65] called this region "Region of Constant Flow Stress", and this region is shown bounded by two arrows in Figure (2.27).
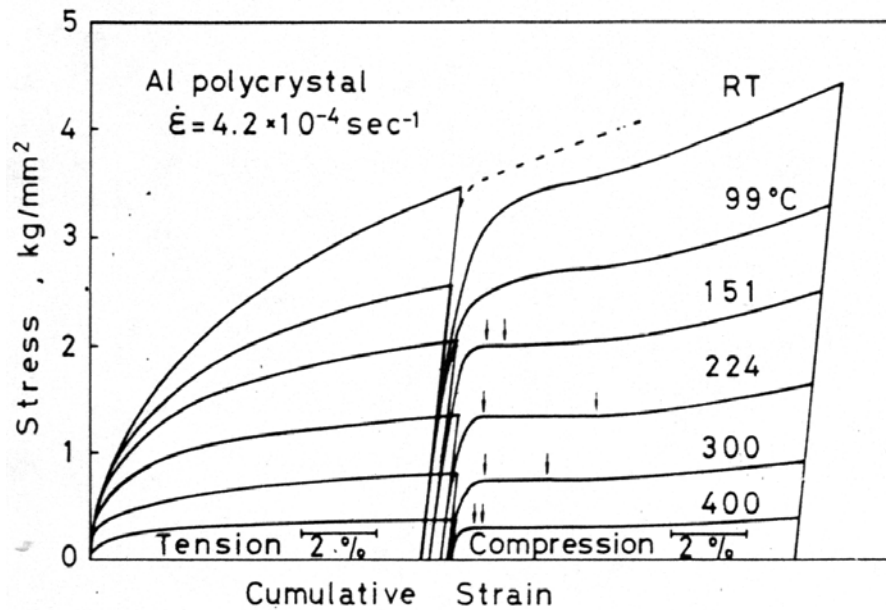
Figure 2.27 Stress-cumulative strain curves of aluminium in tension – compression test from the work of Hasegawa and Yakou [65]

The structural observations and some complementary experiments revealed that cell walls and sub-boundaries, which had been developed by pre-straining at low and high temperature respectively, were unstable against the stress reversal. This result implies that the dissolution and re-formation of cell walls and sub-boundaries occur during the reversed straining. Furthermore, it was found that, at both low and high temperatures, the total dislocation density decreased by about 16% at an early stage of the reversed straining. These structural changes are considered to be the origin of the work-hardening behavior mentioned above. It is also concluded that, in addition to the reversed motion of free isolated dislocations within cells or sub-grains, the dissolution of cell walls or sub-boundaries upon the stress reversal is closely related to the Bauschinger effect at least in metals in which cells or subgrains are formed during pre-straining.

Examples of dislocation structures are shown in Figure 2.28, which imply that, when compressive strains are subsequently given, the cell walls consisting of dislocation tangles developed during pre-straining by tension are dissolved and the overall distribution of dislocations becomes more uniform (Figure 2.28(b)

and (c)). After the strain increased to point D in the subsequent compression cell walls consisting of opposite sign dislocations are newly formed (Figure 2.28(d)), the cell size being approximately equal to that just before the stress reversal.
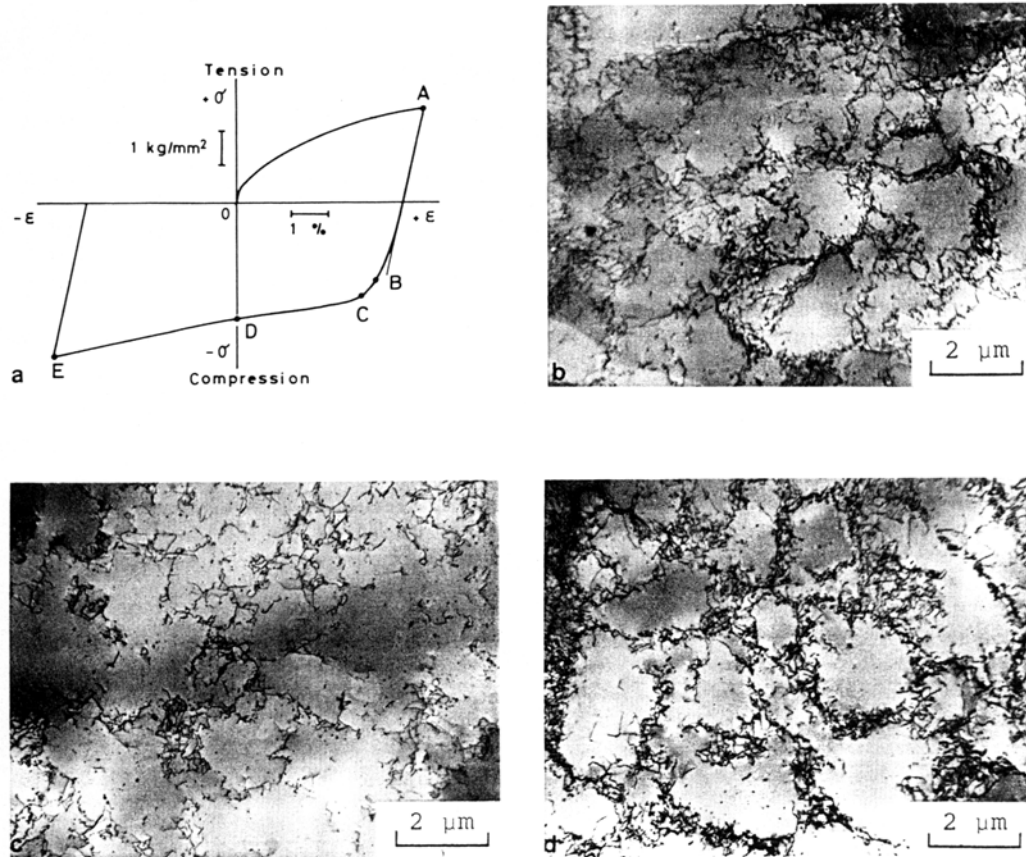
Figure 2.28 (a) Stress-strain curve of aluminium at room temperature. Thin foils for transmission electron microscopy were prepared from specimens subjected to deformation up to points A to E. Photographs (b), (c) and (d) show the typical structures at points A, C, and D, respectively [65]

Takahashi and Shiono [67] also investigated pure aluminum using thin-walled hollow cylinder specimen geometry. The prestrains in these experiments were up to a shear strain of 0.5. After the largest prestrains, upon reversing the stress direction, they found a region of very high work-hardening and then a plateau in the flow stress (Figure 3.29). Eventually, the work hardening resumed at a rate approximately equivalent to monotonic deformation.
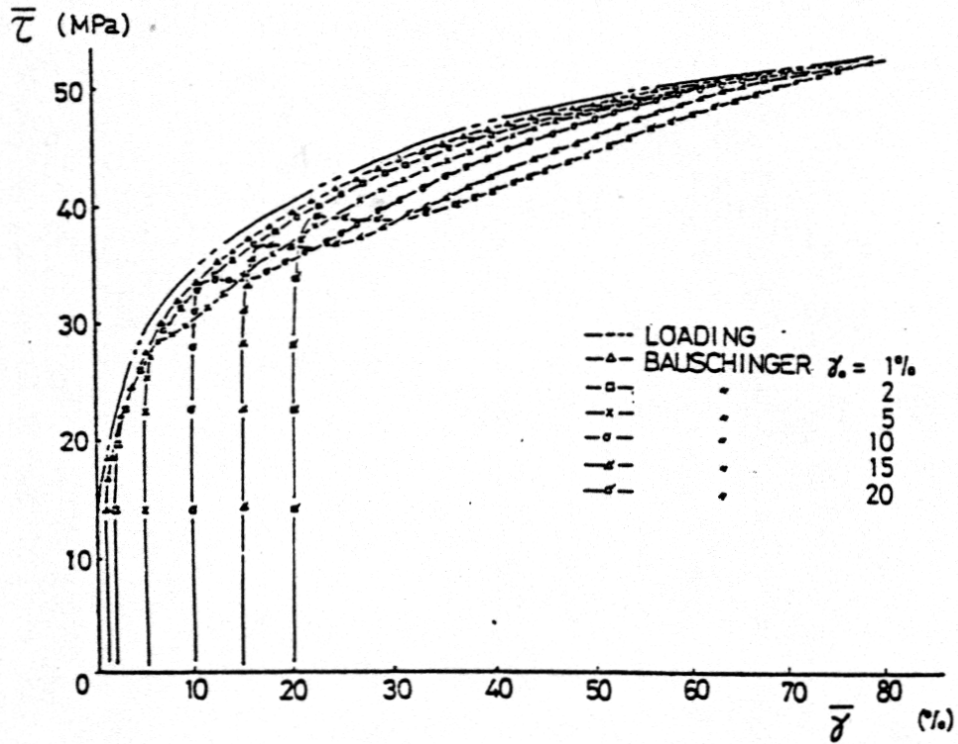
Figure 2.29 Bauschinger curves of aliminum obtained by Takahashi and Shiono [67]

A similar observation is done by Christodoulou et al. [68]. He determined the flow behavior of polycrystalline copper under conditions where the loading direction is reversed after increasing amounts of prestress (or prestrain) by tension-compression and compression-tension experiments (Figure 2.30).
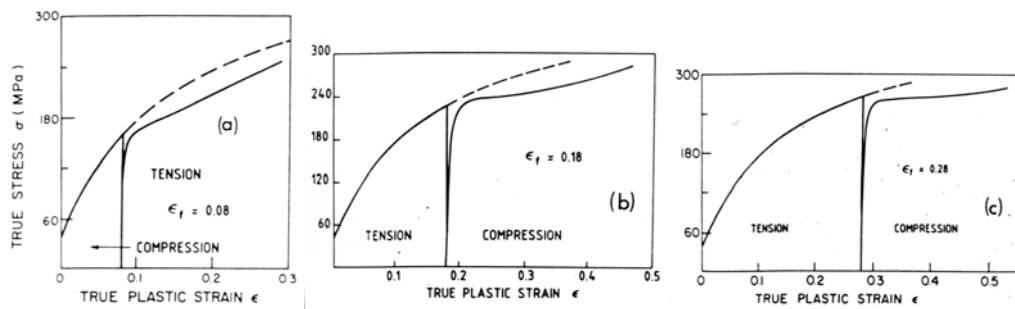
Figure 2.30 True stress versus accumulated plastic strain flow curves after (a) $\sigma_f = 156 MPa$ (in compression), (b) $\sigma_f = 227 MPa$ (in tension), and (c) $\sigma_f = 265 MPa$ (in tension) [68]

60

It is shown in Figure 2.31 that the Bauschinger effect (defined as the response during early stages of reverse flow) first increases and then saturates as the prestress is raised. If θ (f: forward, r: reverse) is defined as the slope of the flow curve, in the same stress range, the reverse work hardening rate, θ_r, is higher than that determined from a continuous test θ_f. Beyond this stage, θ_r becomes less than θ_f. The difference $\Delta\theta = \theta_f - \theta_r$ attains non-negligible values over an extended stress (strain) interval of reverse loading before it becomes equal to zero.
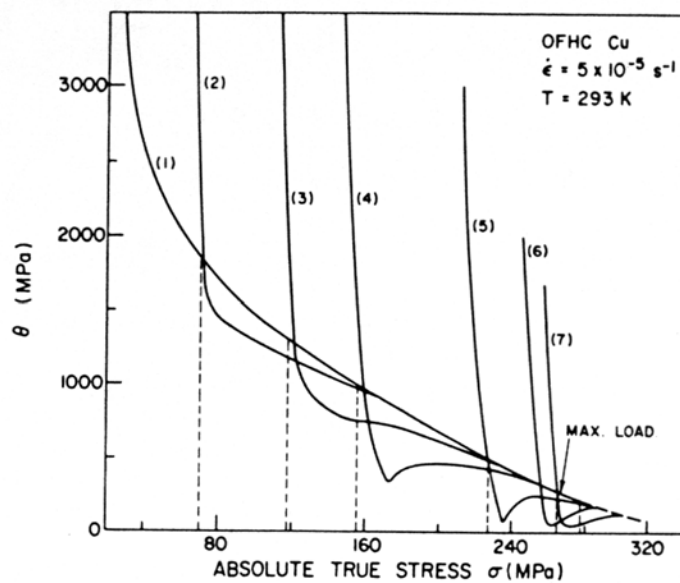
Figure 2.31 Dependence of plastic work hardening rate on absolute stress during forward (curve 1) and reverse flow, after (2) 70 MPa (comp.), (3) 118 MPa (comp.), (4) 156 MPa (comp.), (5) 227 MPa (tension), (6) 265 MPa (tension), and (7) 277 MPa (tension) [68]

Concurrently, the reverse flow stress σ_r tends to saturate before it begins to rise again. It is suggested that the region of "almost" constant flow stress and the lower θ_r coincide with the partial dissolution of dislocation tangles and cell-walls observed by TEM. The rearrangement of dislocation substructure that appears to take place in this stress (strain) interval, is treated by employing a two-component composite model.

61

Stout and Rollett [69] have also performed Bauschinger experiments on a variety of fcc metals and alloys (99.99 pct Al, OFE copper, 70:30 brass, Al-1 pct Mg, Al-2 pct Mg, Al-0.17 pct Fe-0.07 pct Si, Al-0.8 pct Mn, and two Al-Cu alloys), after large amounts of prestrain, using torsion and a short thin walled tube geometry. In this work it is stated that the behavior of these materials could be divided into two categories: those that deform by planar slip (those which have exceptionally low stacking fault energy) and those that form a "cell" structure and are characterized as having wavy slip. When the deformation was wavy in nature, the observed Bauschinger effects are attributed to be a result of the tangling of the "cells" formed during the prestrain.

Several phenomenological theories have been proposed to describe the strain-hardening behavior under reverse loading. Prager [1949] introduced the " back-stress" to explain the influence of predeformation on the reverse plastic loading. Ziegler [56] related the evolution of the back-stress to the plactic flow. More complex and accurate models, based on the evolution of the back-stress, have also been proposed (Mroz [73], Dafalias & Popov [74], Krieg [75], Chaboche & Rousselier [76], Mroz [77], Hu at al. [78]). However, despite the success of these models in describing cyclic hardening at small strain amplitude, they fail to describe the strain-hardening stagnation behavior. The main reason for this is that the back-stress cannot account for the polarity of persistent dislocation structures, such as dislocation walls, because no significant change in the absolute value of the flow stress occurs during the depolarization process. Hu et al. [71] presented a work to model the observed strain hardening stagnation by the evolution of structural parameters that characterize the formation, disintegration and reformation of persistent structures. Work-hardening behavior of aluminum killed mild steel under stress reversal at large strains is studied by Hu et al. [70,71] with planar simple shear test and compared with the model. Another model, is presented by Yoshida and Uemori [72] which can describe the work-hardening stagnation appearing under reverse deformation.

CHAPTER 3

PERFORMED EXPERIMENTS AND THEIR EVALUATIONS

In this chapter performed compression and tensile experiments are evaluated within each other. Comparison of the two tests is made as a conclusion. Hardness values are also presented to show the general hardness distribution within the specimens. The correlation of the hardness values with yield stress will be handled in the following chapter.

3.1   Performed Experiments
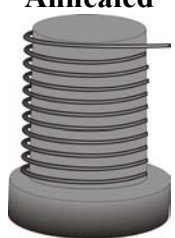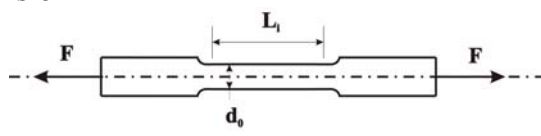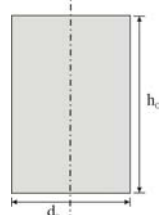
Majority of the experiments were performed in HILTI laboratories. These test are mechanical tests that include tensile, standard compression, Rastegaev compression, and Vickers hardness tests.

Forming process sequence contains three forming stages as rolling, drawing and extrusion. Rolling is done not for a diameter reduction purpose but rather for straightening of the rods. Hence, during the rolling process it is assumed that little plastic strain is induced in the workpiece. Test specimens can be classified with respect to their workhardening state as annealed, rolled, drawn and extruded. Simply the specimen is named with the last process performed on it. Because of the forming press configuration it is only possible to take specimen for stainless steel before the rolling operation and for carbon steel after the
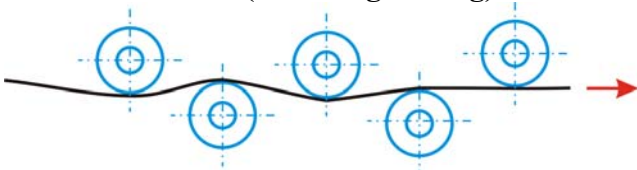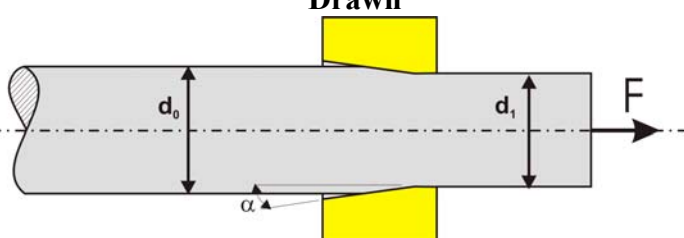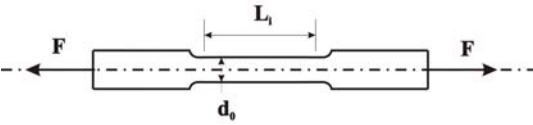
rolling operation. Standard compression, Rastegaev compression, and Vickers hardness tests were performed for all states. But tensile testing is done only for annealed and drawn states. This is because of the insufficient length of the extruded side. For each experiment at least three specimens were tested for more consistent results. Besides some tensile and compression (single direction deformation) tests, compression tests are also performed after the tensile tests t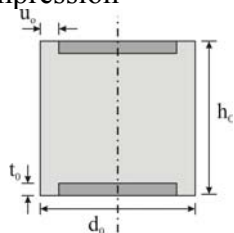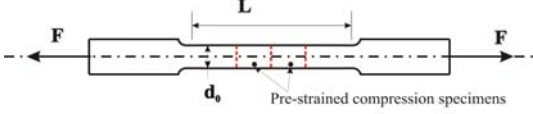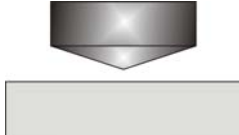o see the material characteristics under load reversals. Compression test specimens are machined from a pre-strained tensile specimen. Number of specimens and percentage of elongations before machining are given in Table 3.1. These tests can be called as large-strain reverse deformation experiments. As it is known that HILTI have more than one material supplier, test specimens were collected from the same lot (charge) of material.

Table 3.1 and Table 3.2 contain detailed schematic representations of states and experiments for stainless steel and carbon steel respectively as well as numbers and dimensions of the specimens.
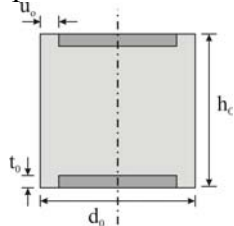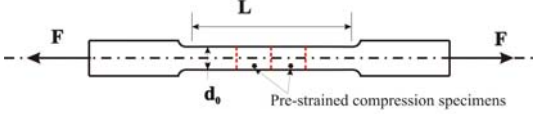
Table 3.1 Schematic representations of experiments performed in annealed, rolled, drawn and extruded state of stainless steel.

	Annealed	
State		d_0=11.44-11.50 (mm)
Experiments Performed	Tension	d_0=8 mm L_i=40 mm Strain rate: 1×10^{-4} s^{-1} # of experiments: 3
	Standard Compression	d_0=10 mm h_0=15 mm h_0/d_0=1.5 (kept constant) Strain rate: 2×10^{-2} s^{-1} # of experiments: 3

Table 3.1 (Continued)

Experiments Performed	Rastegaev Compression	d_0=10 mm h_0=10 mm u_0=0.50 mm t_0=0.20 mm Strain rate: 2×10^{-2} s^{-1} # of experiments: 6
	Standard Compression of Pre-strained Specimens	Geometry: Default tensile specimen Pre-strain: 10%, 20%, 36% # of experiments for each pre-strain: 2
	Vickers Hardness Measurements	HV 10 Vickers hardness measurements are done on axial and radial sections of the workpiece.
State	**Rolled (for straightening)**	
	No experiments were performed in this state for stainless steel.	
State	**Drawn**	Drawing: d_1=10.54 mm Measured: d_1=10.50 mm
Experiments Performed	Tension	d_0=8 mm L_i=40 mm Strain rate: 1×10^{-4} s^{-1} # of experiments: 3
	Standard Compression	d_0=10 mm h_0=15 mm h_0/d_0=1.5 (kept constant) Strain rate: 2×10^{-2} s^{-1} # of experiments: 4
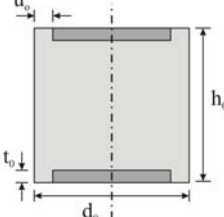
Table 3.1 (Continued)

Experiments Performed	Rastegaev Compression 	d_0=10 mm h_0=10 mm u_0=0.50 mm t_0=0.20 mm Strain rate: $2x10^{-2}$ s^{-1} # of experiments: 4
	Standard Compression Pre-strained Specimens 	Geometry: Default tensile specimen Pre-strain: 4% # of experiments for each pre-strain: 2
	Vickers Hardness Measurements 	HV 10 Vickers hardness measurements are done on axial and radial sections of the workpiece.
State	**Extruded** 	$\alpha = 13^o$ Drawing: d_0=10.59 mm d_1=8.32 mm Measured: d_0=10.53-10.63 mm d_1=8.33-8.35 mm
Experiments Performed	Standard Compression 	d_0=8.33 mm h_0=12.44 mm h_0/d_0≈1.5 (kept constant) Strain rate: $2x10^{-2}$ s^{-1} # of experiments: 3
	Rastegaev Compression 	d_0=8.33 mm h_0=8.28 mm u_0=0.50 mm t_0=0.20 mm Strain rate: $2x10^{-2}$ s^{-1} # of experiments: 3
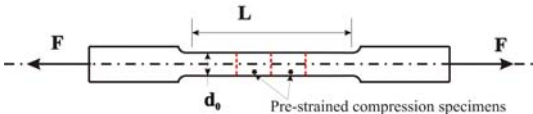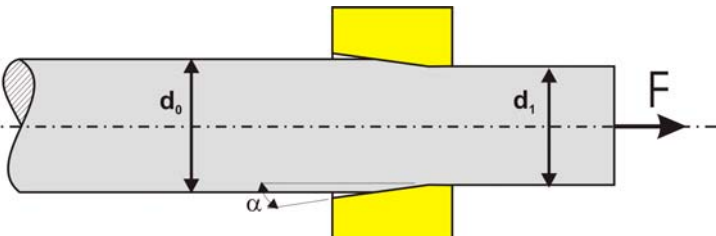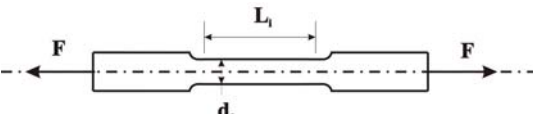
Table 3.1 (Continued)

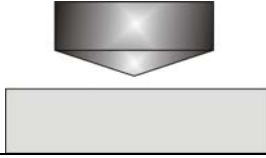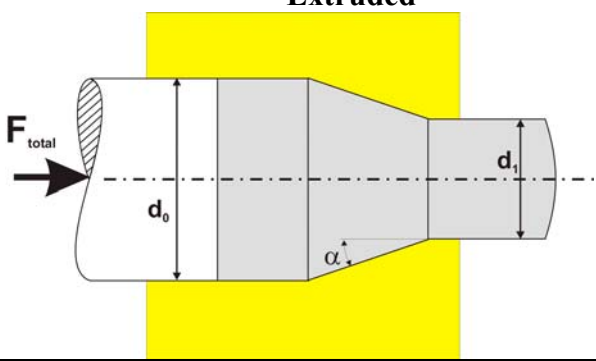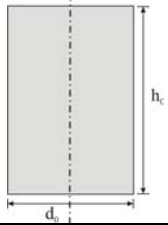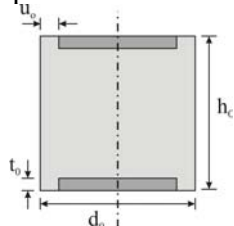|	Vickers Hardness Measurements	
		HV 10 Vickers hardness measurements are done on axial and radial sections of the workpiece.

Table 3.2 Schematic representations of experiments performed in annealed, rolled, drawn and extruded state of carbon steel.
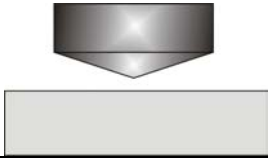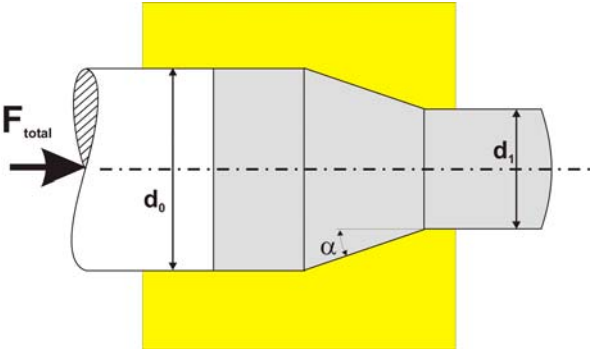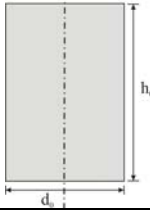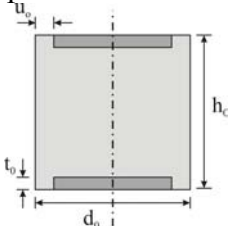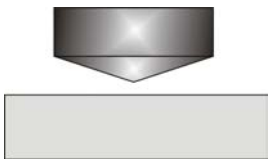
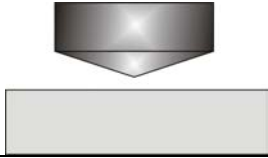|	**Annealed**	
State		
	No experiments were performed in this state for stainless steel.	
State	**Rolled (for straightening)** 	d_0=11.22-11.60 (mm)
Experiments Performed	Tension 	d_0=8 mm L_i=40 mm Strain rate: 1×10^{-4} s^{-1} # of experiments: 3
	Standard Compression 	d_0=10 mm h_0=15 mm h_0/d_0=1.5 (kept constant) Strain rate: 2×10^{-2} s^{-1} # of experiments: 3
	Rastegaev Compression 	d_0=10 mm h_0=10 mm u_0=0.50 mm t_0=0.20 mm Strain rate: 2×10^{-2} s^{-1} # of experiments: 4

Table 3.2 (Continued)

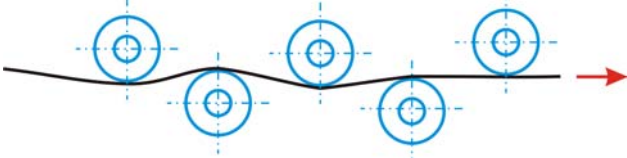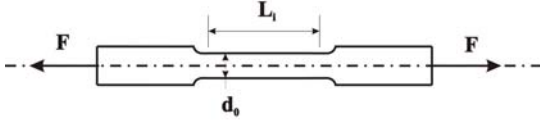|		
Experiments Performed	Standard Compression of Pre-strained Specimens	Geometry: Default tensile specimen Pre-strain: 11.2% # of experiments for each pre-strain: 2
	Vickers Hardness Measurements	HV 10 Vickers hardness measurements are done on axial and radial sections of the workpiece.
State	**Drawn**	Drawing: d_1=10.61 mm Measured: d_1=10.60-10.62 mm
Experiments Performed	Tension	d_0=8 mm L_i=40 mm Strain rate: 1×10^{-4} s^{-1} # of experiments: 3
	Standard Compression	d_0=10 mm h_0=15 mm h_0/d_0=1.5 (kept constant) Strain rate: 2×10^{-2} s^{-1} # of experiments: 3
	Rastegaev Compression	d_0=10 mm h_0=10 mm u_0=0.50 mm t_0=0.20 mm Strain rate: 2×10^{-2} s^{-1} # of experiments: 5
	Standard Compression Pre-strained Specimens	Geometry: Default tensile specimen Pre-strain: 1.9% # of experiments for each pre-strain: 2

Table 3.2 (Continued)

Vickers Hardness Measurements	HV 10 Vickers hardness measurements are done on axial and radial sections of the workpiece.

State

Extruded

$\alpha = 15^{\circ}$
Drawing:
d_0=10.61 mm
d_1=9.4 mm
Measured:
d_0=10.61-10.63 mm
d_1=9.42 mm

Experiments Performed

Standard Compression

d_0=9.42 mm
h_0=14.08 mm
$h_0/d_0 \approx 1.5$ (kept constant)
Strain rate: 2×10^{-2} s^{-1}
# of experiments: 3

Rastegaev Compression

d_0=9.42 mm
h_0=9.38 mm
u_0=0.50 mm
t_0=0.20 mm
Strain rate: 2×10^{-2} s^{-1}
# of experiments: 3

Vickers Hardness Measurements

HV 10 Vickers hardness measurements are done on axial and radial sections of the workpiece.

Experiments were performed on a Zwick Material Testing Machine with hydraulic drive that has a 200 kN load cell and extensometer for tensile testing. The output data contains displacement in mm, punch or lifting arm force in N, and time in seconds.

For hardness measurements Akashi AVK-C1 hardness tester is used. This computer controlled hardness tester has a servo-motor driven xy-table that facilitates circumferential and radial hardness measurements.

In order to compare results of annealed, drawn and extruded specimens, strains should be known. Logarithmic strains on center of the drawn and extruded specimens for stainless steel can be given as:

$$\varepsilon_{drawing} = 2\ln\frac{d_0}{d_1} = 2\ln\frac{11.5}{10.5} = 0.182 \tag{3.1}$$

$$\varepsilon_{extrusion} = 2\ln\frac{d_0}{d_1} = 2\ln\frac{11.5}{8.34} = 0.64 \tag{3.2}$$
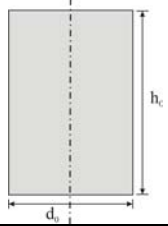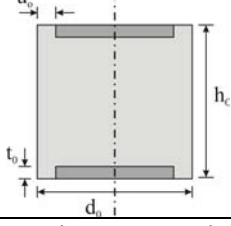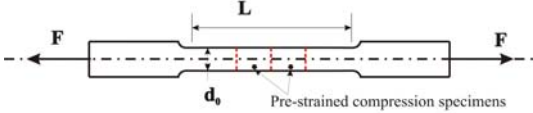
Logarithmic strains on center of the drawn and extruded specimens for stainless steel can be given as:

$$\varepsilon_{drawing} = 2\ln\frac{d_0}{d_1} = 2\ln\frac{11.50}{10.61} = 0.178 \tag{3.3}$$

$$\varepsilon_{extrusion} = 2\ln\frac{d_0}{d_1} = 2\ln\frac{11.5}{9.42} = 0.40 \tag{3.4}$$

3.2   Stainless Steel

In this section experiments performed, their results and evaluations will be presented in detail. Load reversal experiments are investigated in Section 3.2.2.

3.2.1   Tensile Test Results

Tension tests, in which round specimens of 8 mm diameter and 40 mm gauge length were employed, were performed at an average strain rate of 1×10^{-3} s^{-1}, using 200 kN Zwick hydraulic testing machine. Tests were repeated at least three times to obtain reliable results.

Load stroke data (Figure 3.1) can easily be converted to engineering stress – engineering strain data with the help of Eqs. (2.2), (2.3) and to true stress – true strain data with the help of Eqs. (2.12), (2.15). Maximum of engineering stress – strain curve gives the point where the necking starts and the ultimate tensile strength, σ_u as shown in Figure 3.3. For this stainless steel specimen ultimate tensile strength can be taken as $\sigma_u = 560MPa$, and necking strain as $\varepsilon_{eng}{}^{necking} = 0.383$.
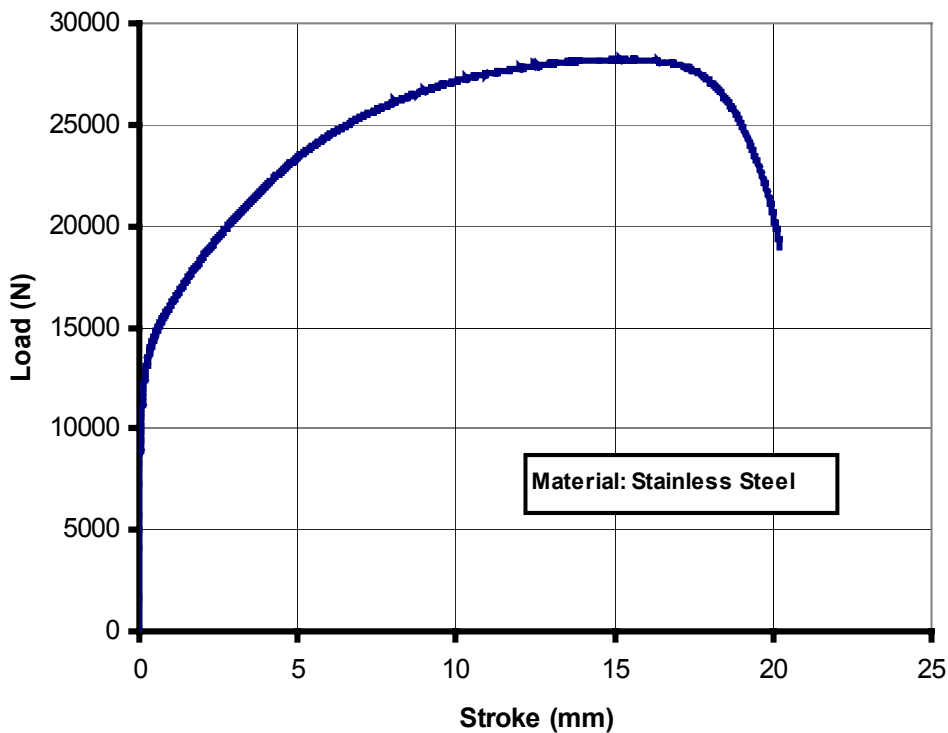
Figure 3.1 Load-stroke curve of stainless steel obtained from tension test

Yield stress is found by using 0.002 offset method. This method can simply be applied to the engineering stress strain data by choosing two arbitrary points that can be guessed to be in elastic region. After shifting the line formed by these two points by 0.002 strain, the intersection of the shifted line and engineering stress – strain curve gives the yield stress, σ_0 as illustrated in Figure 3.2. Slope of the line represented in Figure 3.2 is found to be 163000 MPa. This value is a little bit smaller than the expected value of 196000 MPa. This may be because of the measurement errors of the extensometer.

71
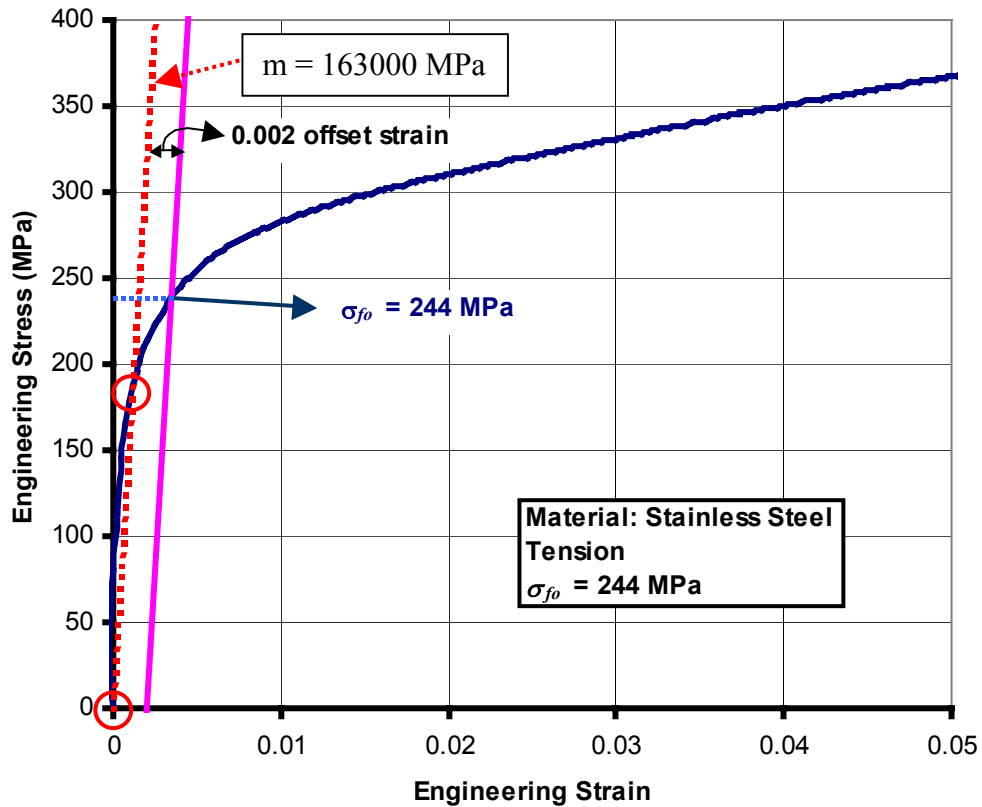
Figure 3.2 Yield point determination from engineering stress and strain curve of stainless steel obtained from tension test

From Figure 3.3 it can be seen that tension data is only available up to $\varepsilon_{true} = 0.324$. In Section 2.1.1 it is described how to use Bridgman and Siebel's correction factors in order to extend our stress - strain up to higher strains. But for this extension minimum radius and the radius of curvature at the neck is needed. During the experiment the data collected is force as N from the force transducer and displacement on the gage length as mm from the extansometer. Also for Bridgman correction some photos are taken by a stationary digital camera during test. Time synchronizing is done with electronic timer in order to match photos with the corresponding instant on the stress - strain curve. By the help of a java application [79] distance corresponding to a single pixel is found with the known diameter of holding section of tensile specimen. In Figure 3.4 it

can be seen that by using image processing needed dimensions can be found if distance per pixel is a known value.
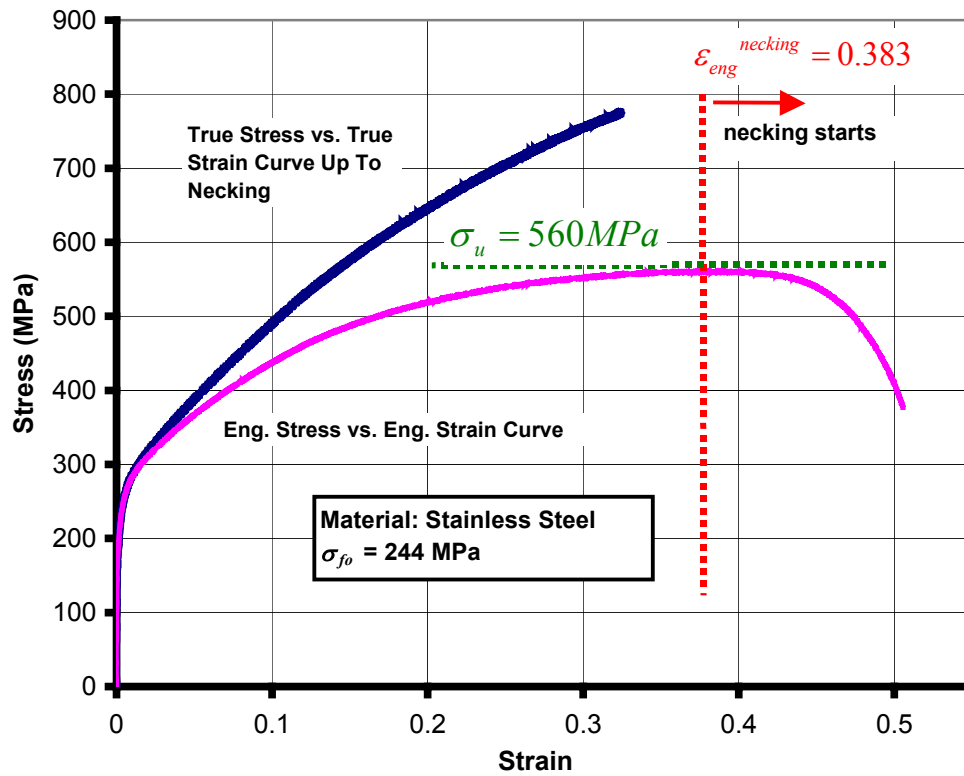
Figure 3.3 Stress and strain curve of stainless steel obtained from tension test
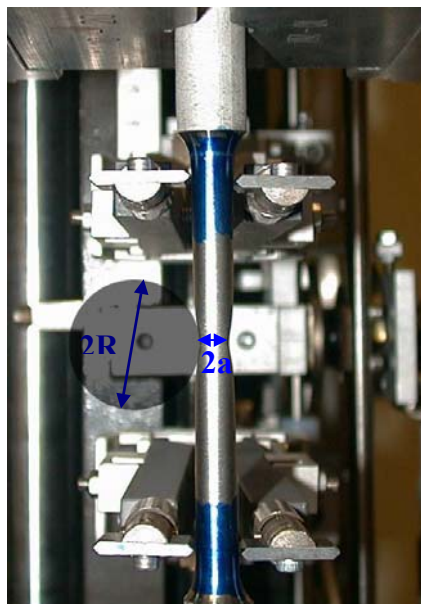
Figure 3.4 Measurement of radius of the neck and radius of curvature of the contour of the neck

73

Fractured parts are also measured for the last point on the stress - strain curve. They are digitized by scanning them in a flatbed scanner as can be seen from Figure 3.5.

Figure 3.5 Photo of the failed tensile specimen with circles fit to the neck section.
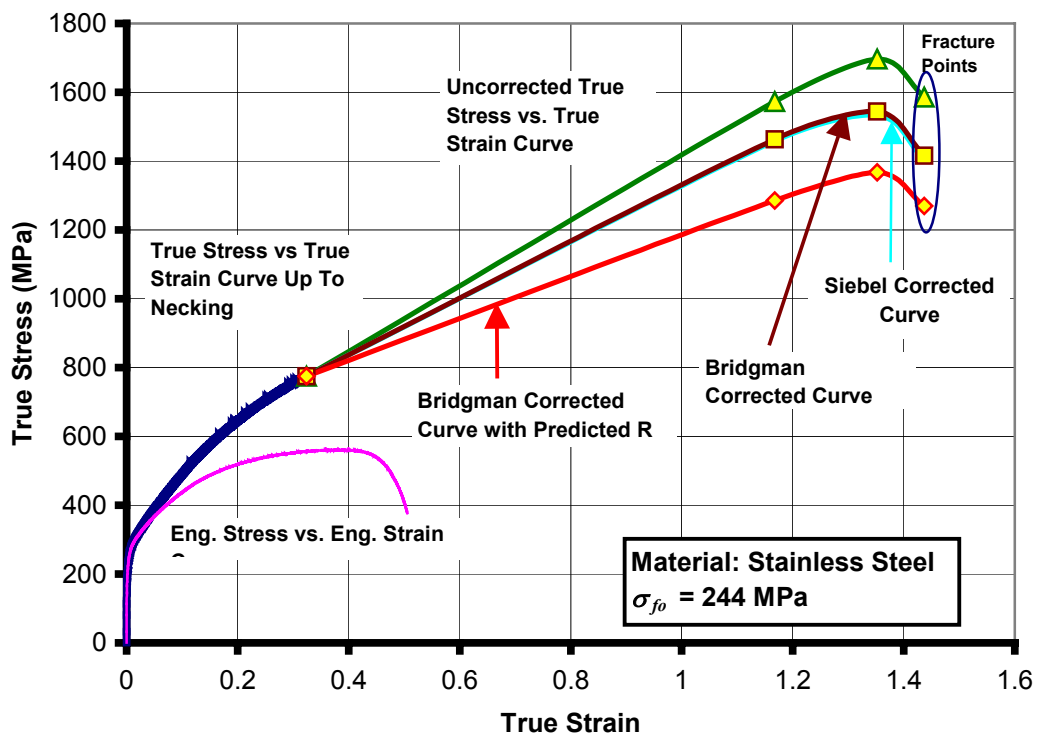
Figure 3.6 Corrected and uncorrected stress values calculated with dimensions obtained from digital photographs.

Bridgman correction factor can also be predicted with the known value of minimum area at the neck and using Eqs. (2.21) and (2.22). Trying to measure radius of curvature of the contour of the neck may lead some extra measuring errors. These predicted values are also plotted in Figure 3.6.

74

Flow curve can be obtained by plotting true stress values against equivalent true plastic strain values determined by the Eq. (3.5).

$$\varepsilon_{pl} = \varepsilon - \varepsilon_{el} = \varepsilon - \frac{\sigma_{f0}}{E} \qquad (3.5)$$

In this equation, ε_{pl} denotes the total equivalent plastic strain and ε_{el} is the total elastic strain at the point where σ_{f0} and E denotes the yield stress and modulus of elasticity. Figure 3.7 shows the flow curve of stainless steel obtained from tension test without any extrapolation.
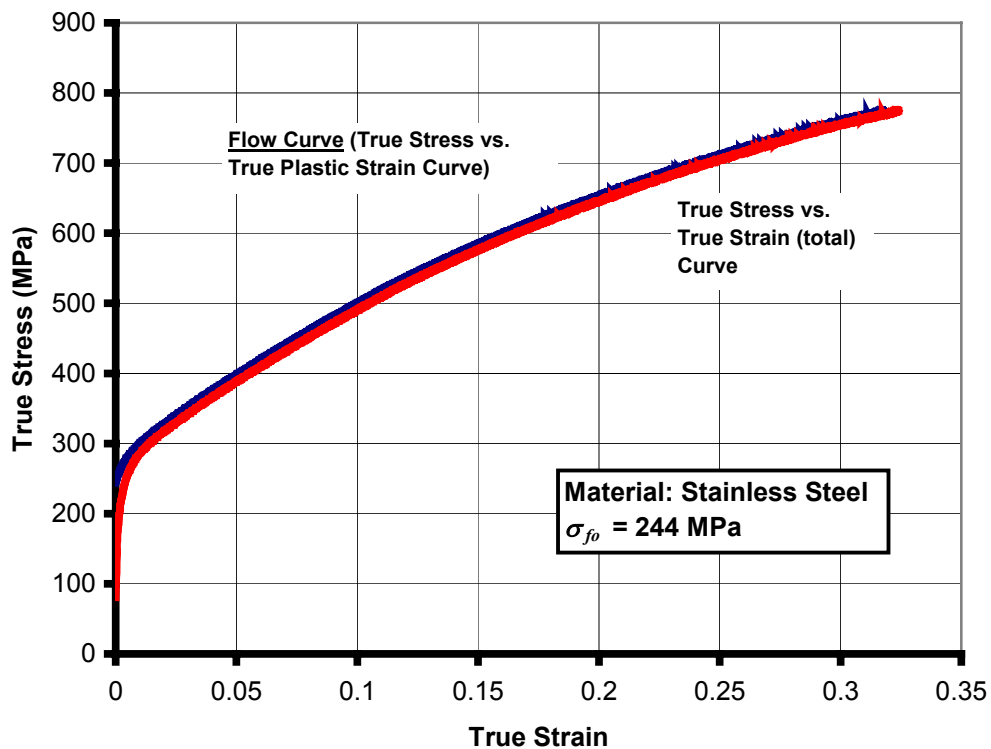
Figure 3.7 Flow curve and true stress – strain curve of stainless steel obtained from tension test

The yield stresses for the higher strain values can be obtained from the extrapolation of the experimental flow curves by using the power law, which is also known as Ludwik's equation shown in Eq.(3.6).

$$\sigma = K\varepsilon_{pl}{}^{n} \tag{3.6}$$

where n is called the strain hardening coefficient, and K is the strength coefficient. In order to find K and n, Eq. (3.6) can be written as

$$\ln(\sigma) = \ln(K) + n\ln(\varepsilon_{pl}) \tag{3.7}$$

which is a straight line on an x-y plot. This line can represented by the following equation

$$y = mx + b \tag{3.8}$$

From Eqs. (3.7) and (3.8) the following variables and constants can be defined:

$$y = \ln(\sigma) \tag{3.9}$$

$$x = \ln(\varepsilon_{pl}) \tag{3.10}$$
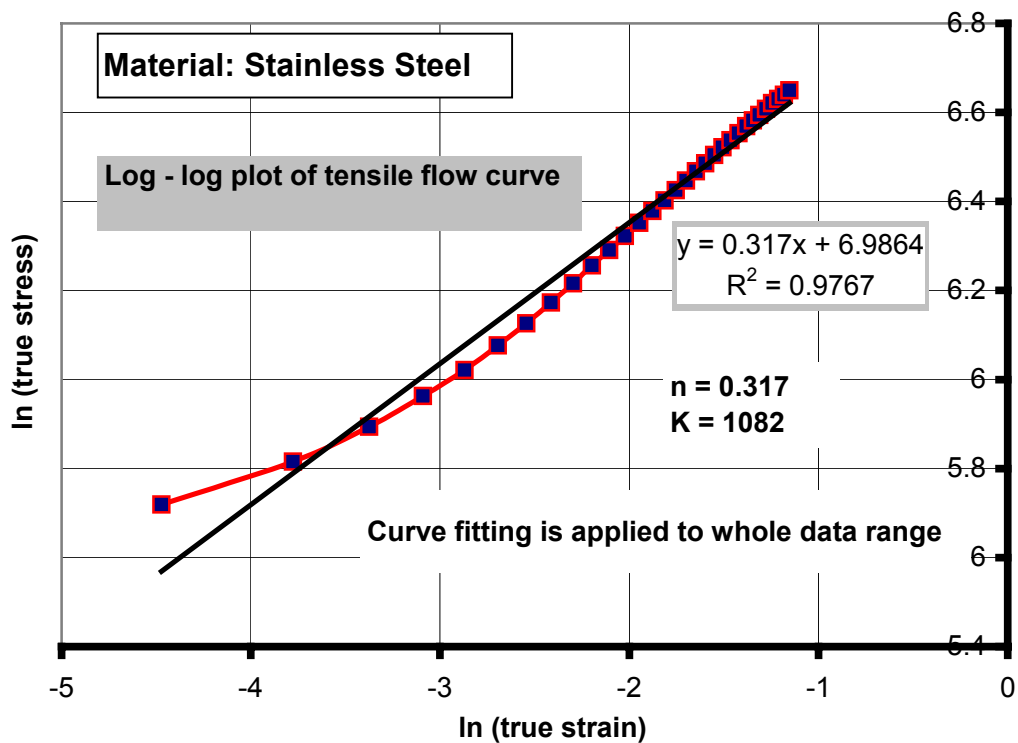
Figure 3.8 Determination of n and K from the whole tension flow data

$$m = n \qquad (3.11)$$

$$b = \ln(K) \rightarrow K = e^b \qquad (3.12)$$

This method is shown on Figure 3.8. Metals often fit to Ludwik's equation. But stainless steel (X5CrNiMo 1810) that is used in tension test shows a double linear behavior as illustrated in Figure 3.9.

From the Figure 3.9, it can be seen that K and n values change from region to region in which the fitting is done and Ludwik's relation fails to describe the plastic behavior at lower strains. The flow curve at lower strains is concaved up (Figure 3.10) when plotted in logarithmic coordinates and lies at higher stresses than those represented by the Ludwik relation at low strains as discussed in [61,62] (See also Section 2.4). At strains greater than about 0.069, the Ludwik relation represented the data adequately.
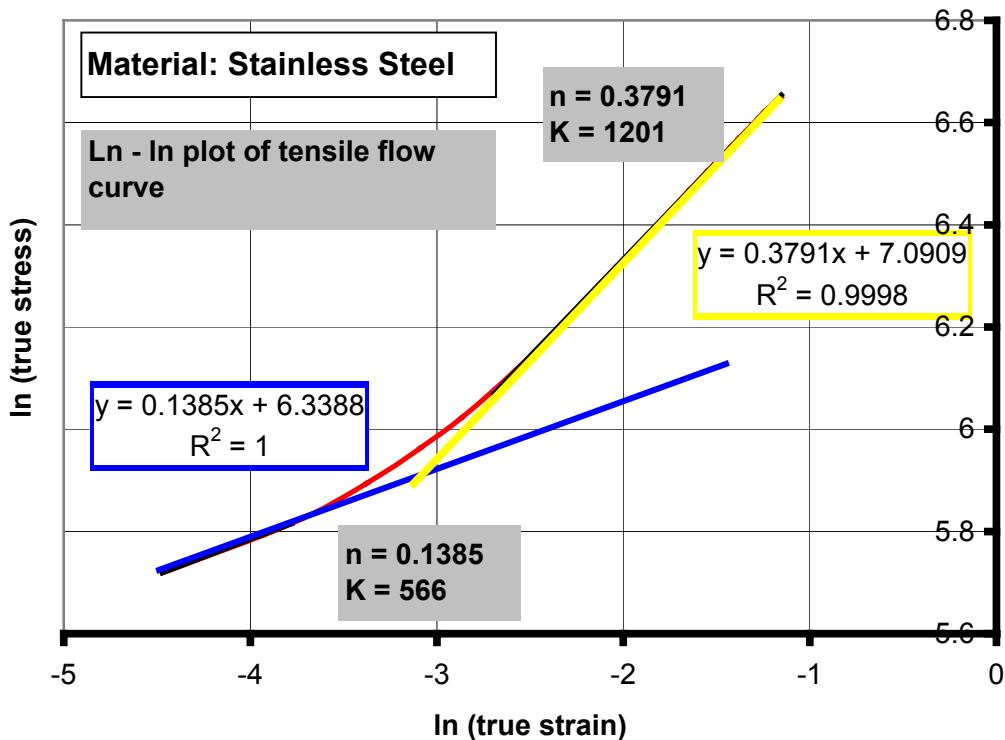
Figure 3.9 Determination of n and K from different regions

77
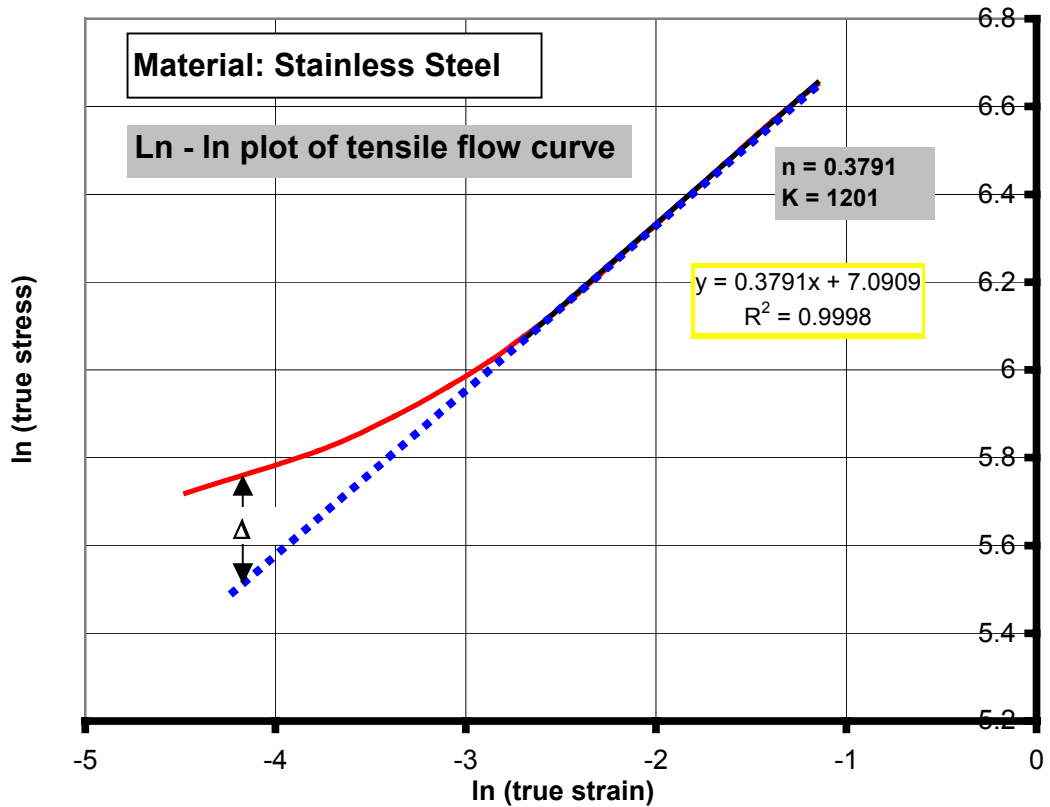
Figure 3.10 Representation of Δ on the logarithmic plot of the tension flow data.

Ludwigson relation can be applied to stainless steel as follows:

The difference between the observed true stress at low strains and the stress represented by the Ludwik relation extended to these low strains is termed Δ. In Figure 3.11 the logarithm of Δ was plotted against strain. This function can be represented as a linear function of strain:

$$\ln \Delta = K_2 + n_2 \varepsilon \qquad (3.13)$$

In this case K_2 and n_2 are constants. Their values for the case illustrated are 5.1451 and −54.139, respectively. Modified Ludwik's relation now can be written as

$$\sigma = 1201\varepsilon^{0.3791} + e^{5.1451} \cdot e^{-54.139\varepsilon} \qquad (3.14)$$

An additional parameter, ε_L, is defined by Ludwigson as the minimum strain above which the unmodified Ludwik relation reasonably represents the data. ε_L can be found as 0.069 when a value of $r = 0.02$ is selected.
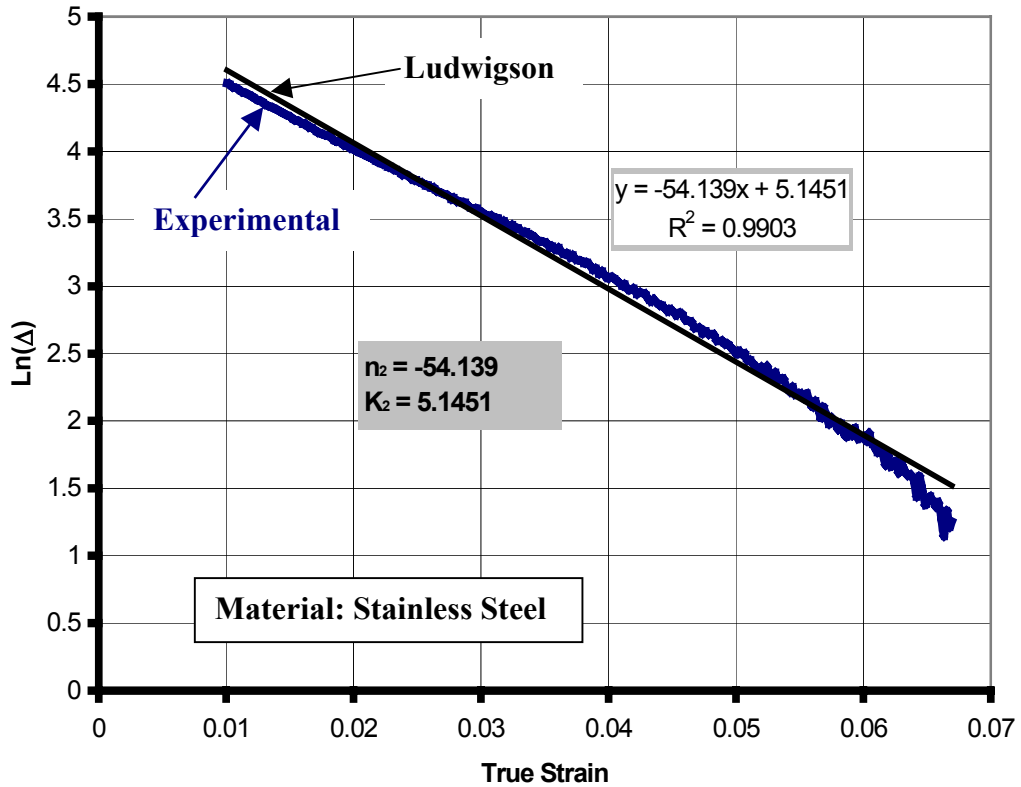
Figure 3.11 Determination of n_2 and K_2.

In Figure 3.12 Ludwigson fit and experimental flow curves of annealed stainless steel is shown. They seem on top of each other even at the low strains.

Another way to extrapolate may be to take initial part of the experimental flow curve and extrapolate the rest with n and K values obtained from second portion of the flow data. $\varepsilon_{pl} = 1.4$ is chosen as a last point of extrapolation because it is very near to the fracture strain in the tension test.
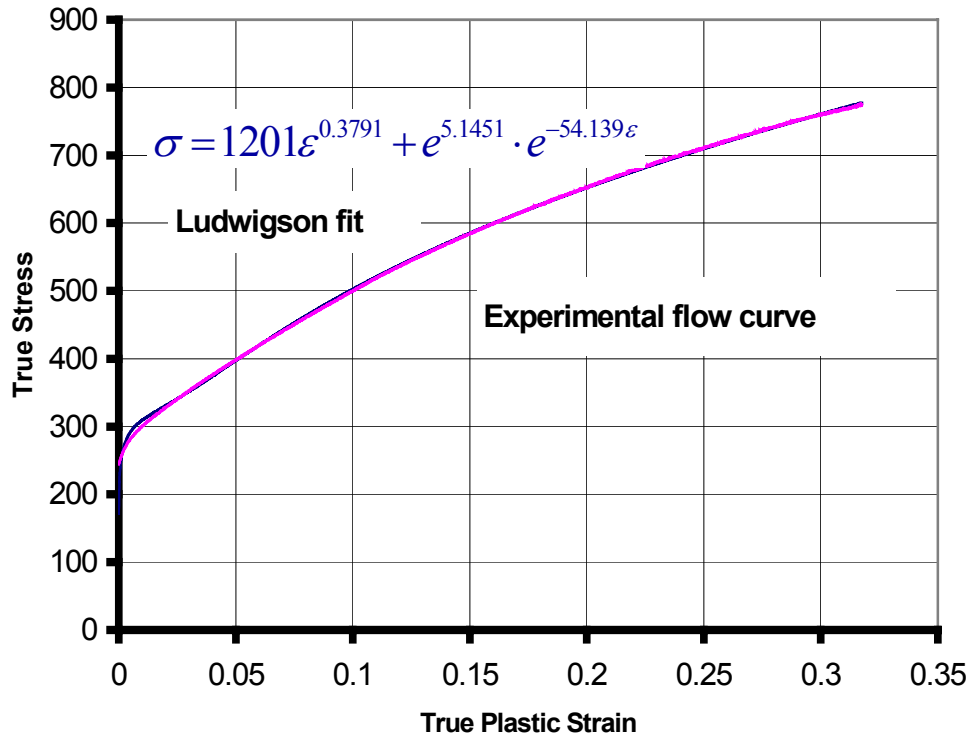
Figure 3.12 Comparison of Ludwigson fit wit experimental flow curve
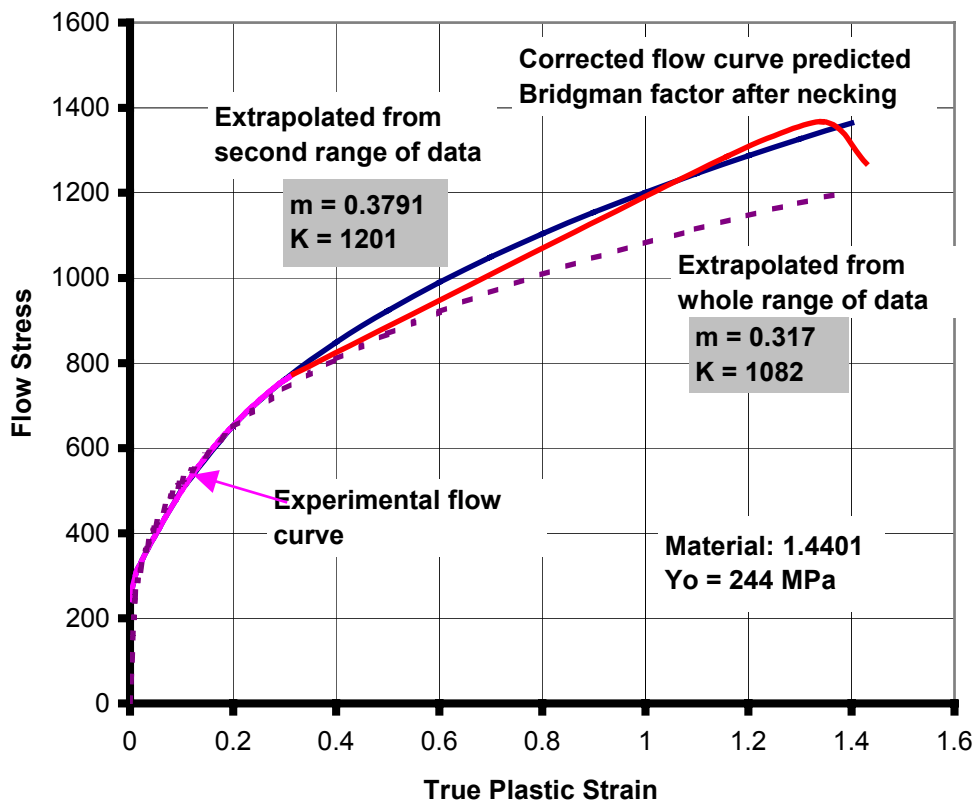
Figure 3.13 Comparison of corrected and extrapolated tension flow curves

The comparison of Bridgman corrected flow curve after necking and the Ludwik extrapolations of flow data before necking starts is done in Figure 3.13. It is seen that using last region of flow data for extrapolating after necking region is better in similarity and trend of hardening with experimental data when compared with the extrapolation of whole data. In Figure 3.13 also one can see that after necking corrected flow curve by predicted Bridgman factor has very near values when compared with this flow curve.

Tensile testing is also performed for the drawn state of the stainless steel. Figure 3.14 shows the comparison of annealed and drawn tensile flow curves. Although the specimen is workhardened there is no much shape change on the flow curve.

Flow curves obtained with different experiments at different states for the same material can be plotted in the same graph. Curves for the workhardened material should be shifted by an offset strain in order to adapt to zero-strain (annealed state) flow curve. Choosing theoretical strain at the center of the workpiece can be the first choice. It is a known value since initial and final areas are known. But also it should be noted that this strain value is the minimum strain value within the radial strain distribution of the workpiece. Mean strain of the strain distribution (found from FEM analysis) can also be taken as the offset strain.

In Figure 3.14 it is seen that offset strain 0.182 ($\varepsilon_{drawing}$) is not enough for the drawn flow curve to be on top of the annealed flow curve. This is accomplished if the offset strain is taken as 0.232. This is probably due to inhomogeneous strain distribution within the drawn workpiece. This value can be taken as mean equivalent plastic strain for the tension specimen. On the other hand this is not possible for compression flow curves because of the shape changes in flow curve.

81
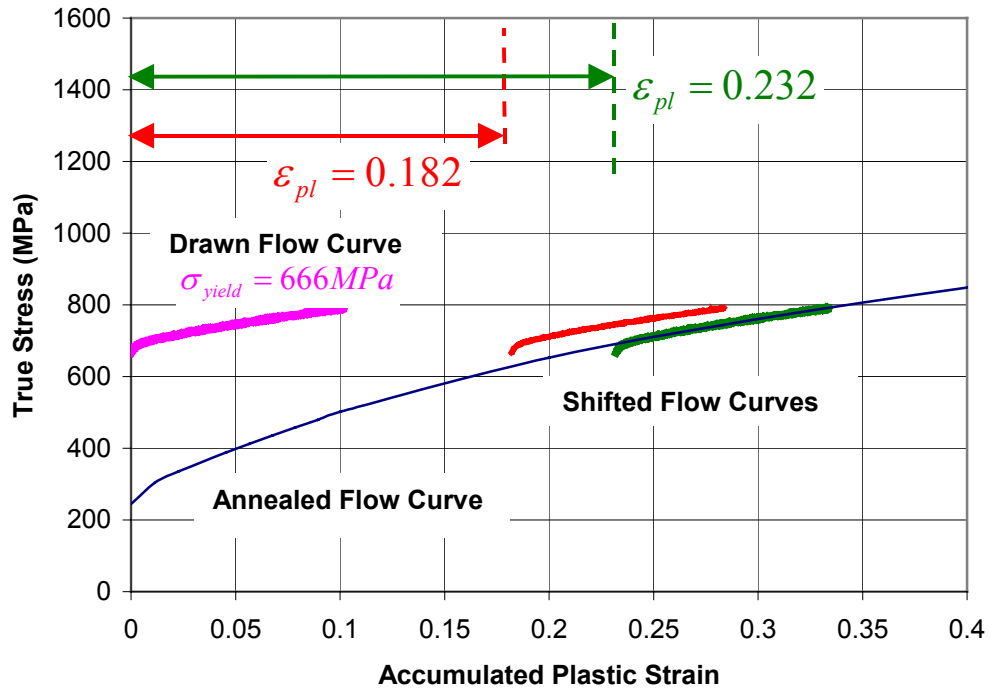
Figure 3.14 Shifting drawn tensile flow curve through the tensile flow curve

3.2.2 Compression Test Results

Standard compression tests, in which round specimens of 10 mm diameter and 15 mm height were employed, have been performed at an average strain rate of $2 \times 10^{-2} s^{-1}$, using 200 kN Zwick testing machine. Tests were repeated at least three times to obtain reliable results. Upper and lower surfaces were polished and molycote paste (MoS_2) is used as lubricant.

Interesting point in compression test is the elliptical shape that compressed specimen takes (Figure 3.15). This means that through out a loading in *z* direction, material deforms differently in *x* and *y* directions. This difference is about 6.7% which is not considered during the flow curve determinations.

Compression flow curves are assumed to give an average plastic behavior without making any correction including the anisotropic behavior of the material.
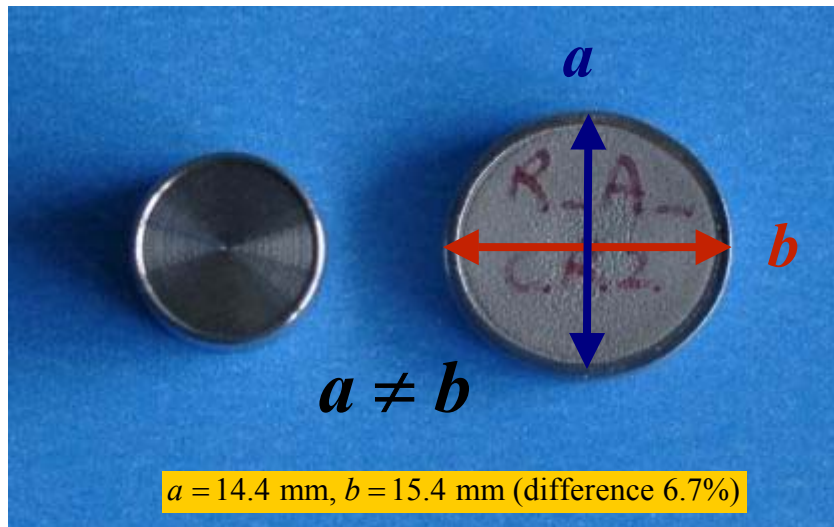
Figure 3.15 Elliptic shape of compressed Rastegaev test specimen.

Load-stroke data (Figure 3.16) can be converted to engineering stress – engineering strain data with the help of Eqs. (2.2), (2.3) and to true stress – true strain data with the help of Eqs. (2.27), (2.29).
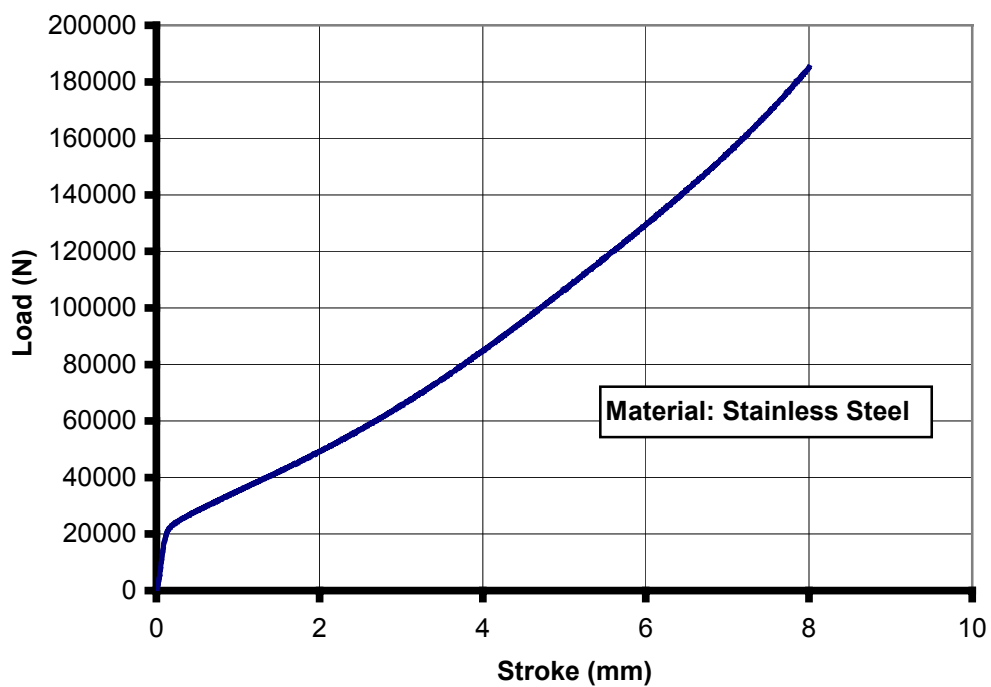
Figure 3.16 Load-stroke curve of stainless steel obtained from standard compression test

Yield stress is found by using 0.002 offset method which described in previous section. Engineering stress – strain curve gives the yield stress, $\sigma_0 = 283 MPa$ as illustrated in Figure 3.17. Slope of the line represented in Figure 3.17 is found to be 40700 MPa.

Load stroke data can easily be converted to engineering stress – engineering strain data (Figure 3.16) with the help of Equations (2.2), (2.4) and to true stress – true strain data with the help of Equations (2.29), (2.27). These curves are represented in Figure 3.18.
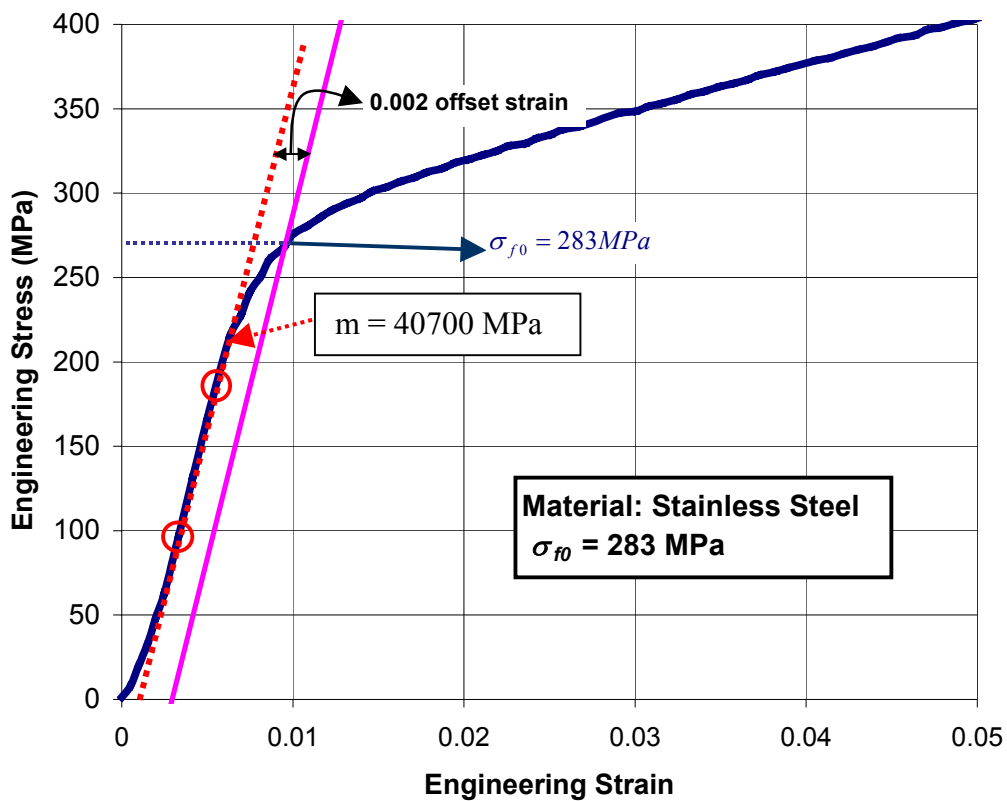
Figure 3.17 Yield point determination from engineering stress and strain curve of stainless steel obtained from tension test

From Figure 3.18 it can be seen that compression data is available up to $\varepsilon_{true} = 0.74$. This is twice of what obtained in tension test. Flow curve obtained by Equation (3.4) can be extrapolated in the same manner like for the tension test.
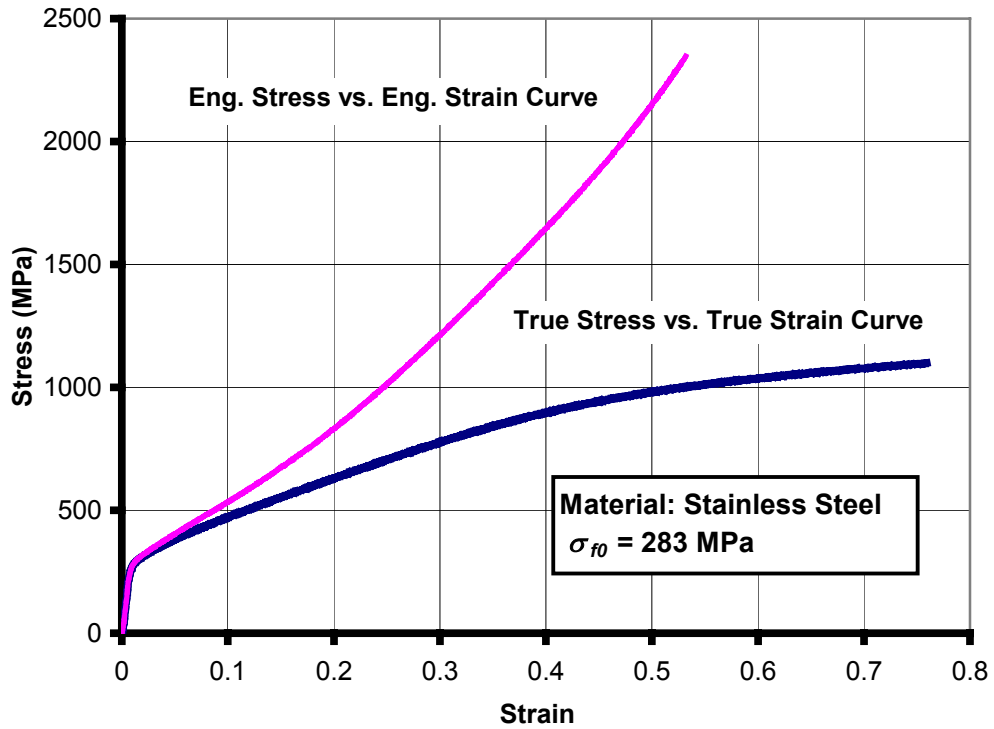
Figure 3.18 Stress and strain curve of stainless steel obtained from standard compression test
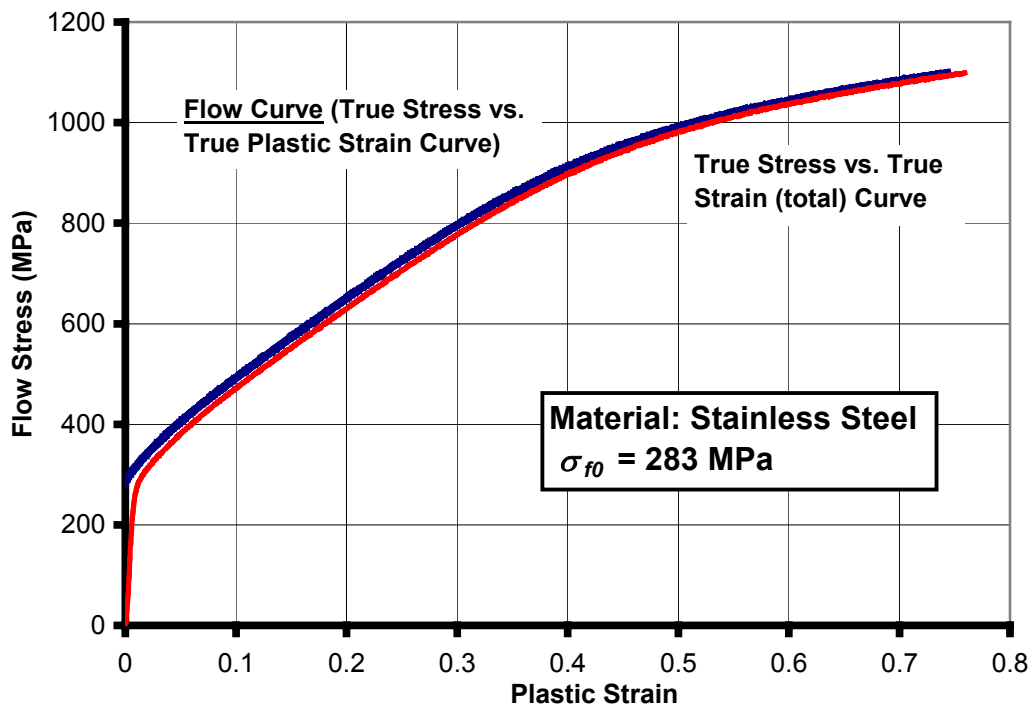
Figure 3.19 Flow curve and true stress – strain curve of stainless steel obtained from standard compression test

The yield stresses for the higher strain values can be obtained from the extrapolation of the experimental flow curves again by using Ludwik's equation.

By fitting this equation to whole range of flow data *n* and *K* values can be found as 0.3651 and 1232 MPa respectively as shown on Figure 3.20. Compression behavior of stainless steel shows a unique transition region between the initial and final regions in logarithmic scaled plot of stress-strain curve (Figure 3.21). This is somewhat different from tension flow curve of the material. By taking different regions in to account (Figure 3.22), different extrapolations can be done (Figure 3.23).
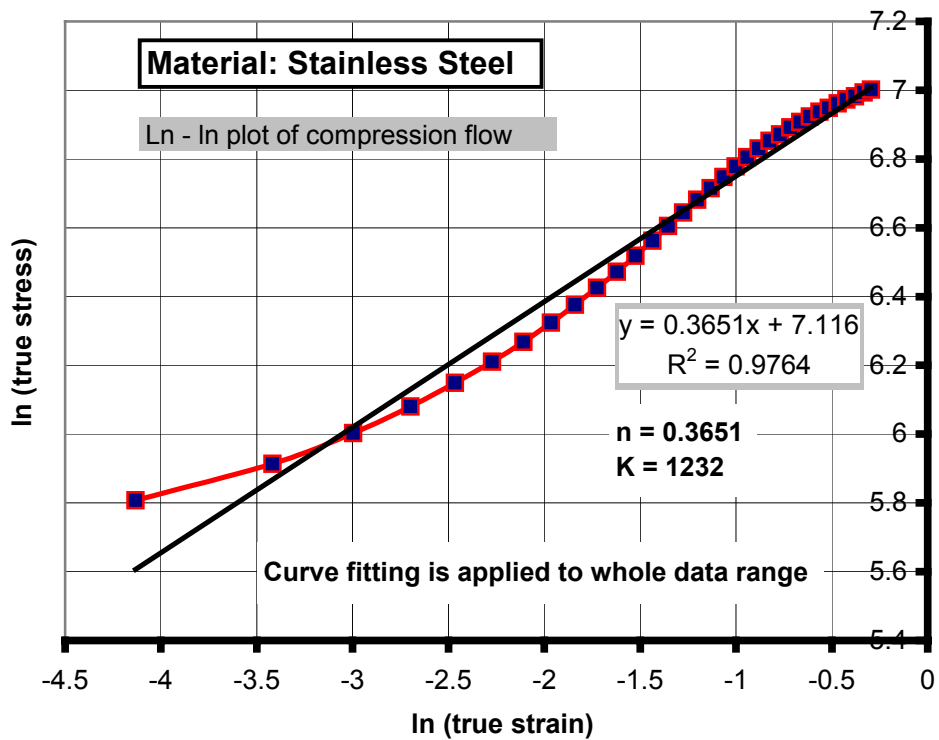
Figure 3.20 Determination of *n* and *K* from the whole compression flow data
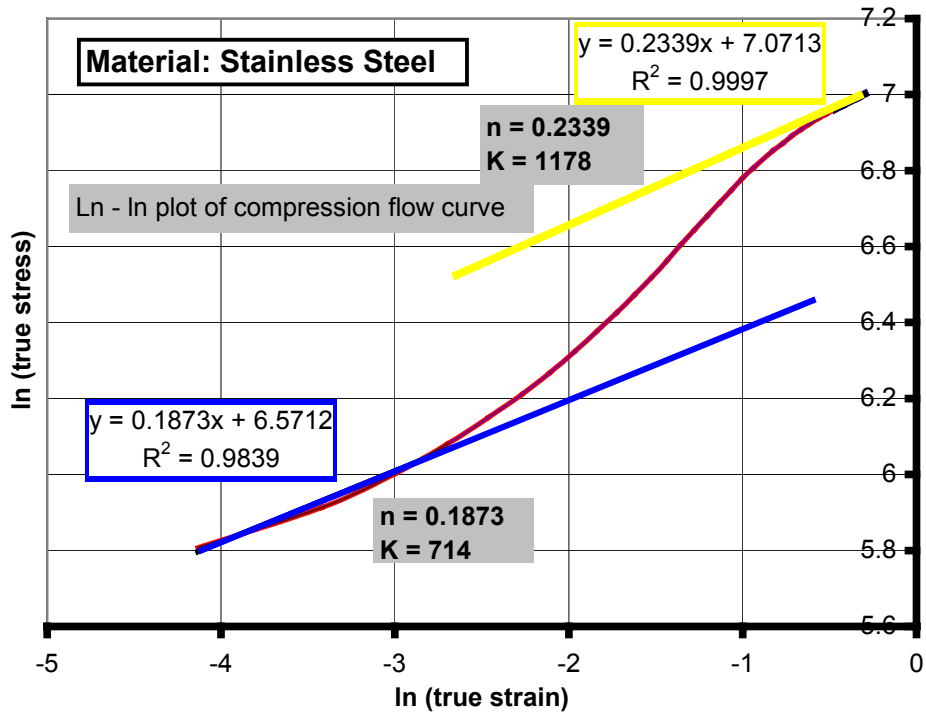
Figure 3.21 Determination of *n* and *K* from different regions of compression
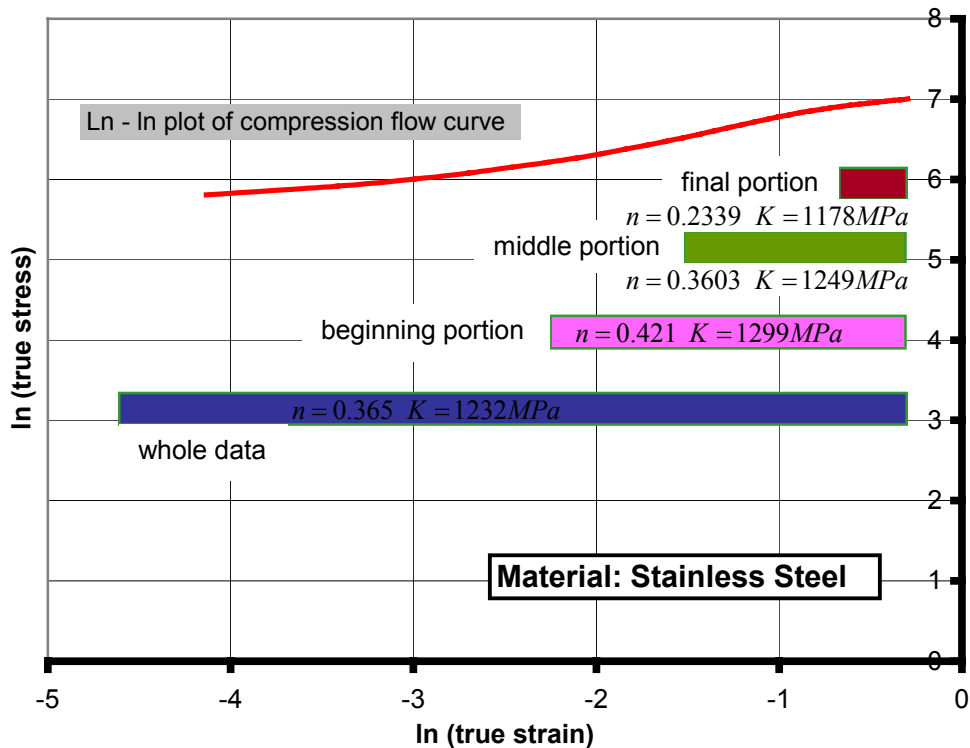
flow data

Figure 3.22 Regions used for determination of *n* and *K* of compression flow

data to be used in extrapolations of Figure 3.18

87
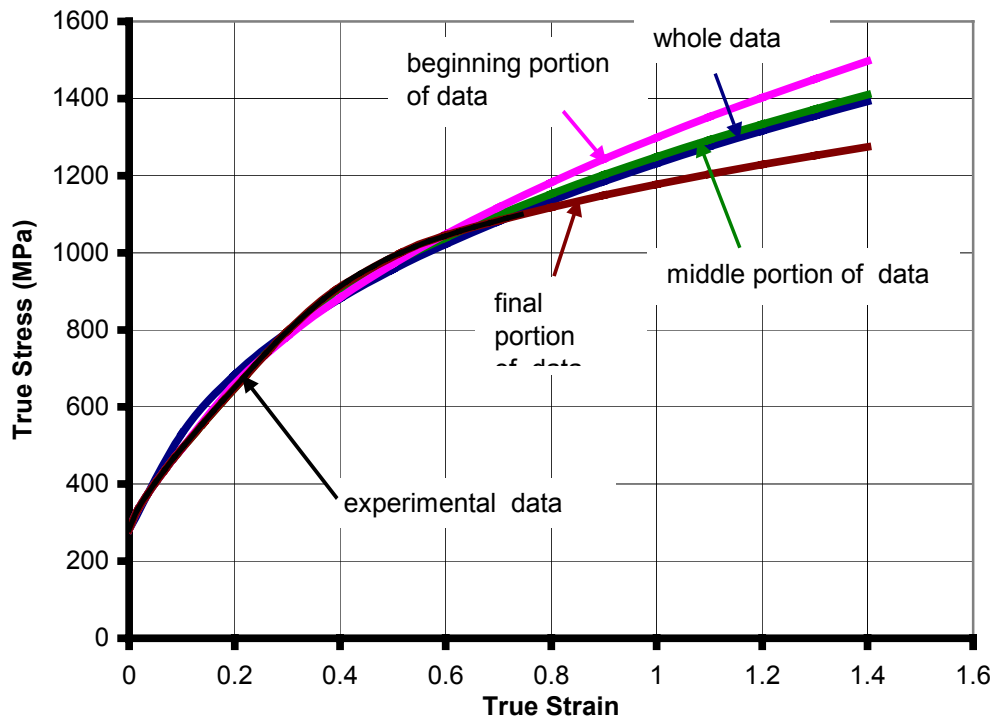
Figure 3.23 Extrapolations from different regions of compression flow data
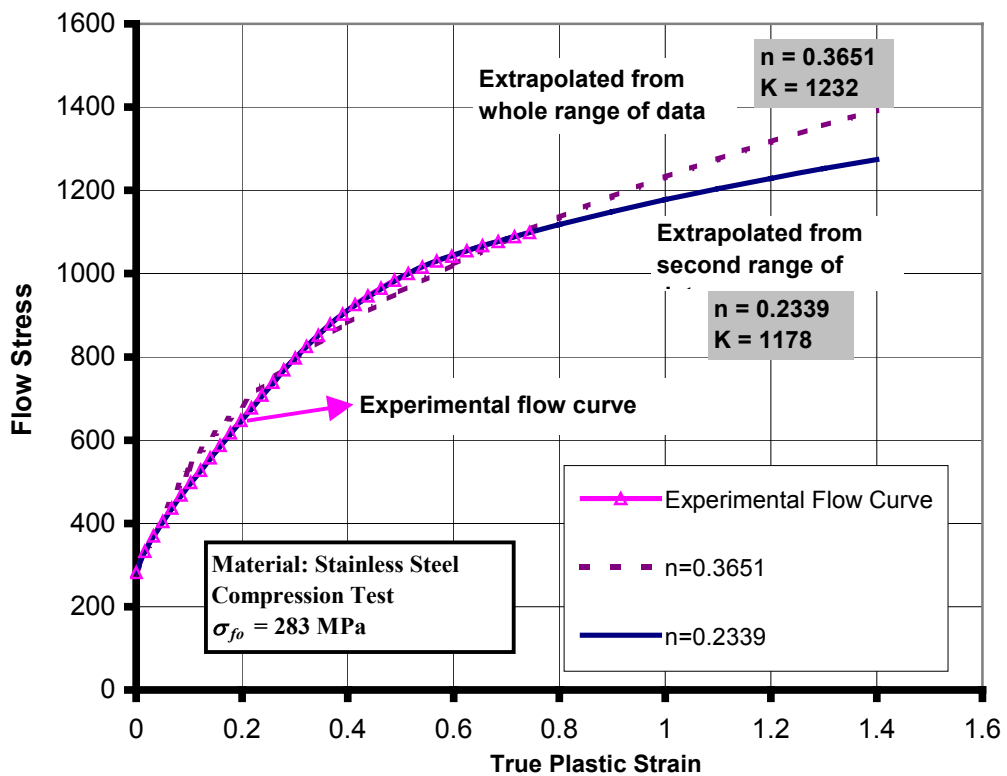
Figure 3.24 Comparison of extrapolated compression flow curves

From the Figures 3.21 and 3.22, it can be seen that K and n values change from region to region in which the fitting is done. The extrapolation is again done for the last region and the initial part is directly taken from experimental data. Along this study all the Ludwik extrapolations are made by this way. The comparison of Ludwik extrapolations of flow data is done in Figure 3.24. Fitting the last region of flow data gives best result in order to represent the experimental data and to show ongoing trend of the data.

In Section 2.1.2.1 it was discussed that this flow data contains some errors due to the nonhomogeneous deformation (barelling) as a result of the friction between compression specimen and dies (Figure 3.25). Correction of the flow data will be done by Siebel correction function and iterative FEM method. For both methods friction coefficient is needed. This data is obtained from another study as $\mu = 0.1$ (Couloumb friction) [50]. In this study ring test is used to determine friction coefficient. Simulation of compression test with $\mu = 0.1$ gave similar barreling diameters with experimental compression specimens.
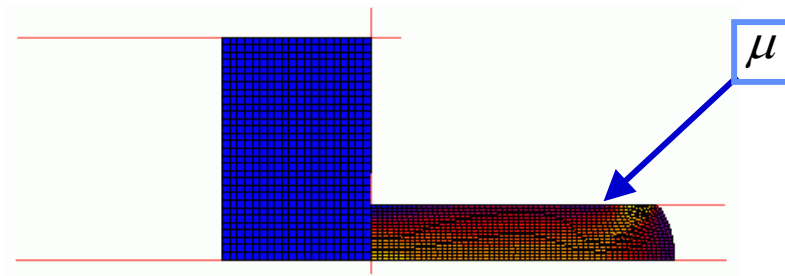
Figure 3.25 FEM modelling of compression test with barreling due to the friction

Due to the Siebel's [11] correction corrected stress can be written as:

$$\sigma_{siebel}\left(\varepsilon\right) = \frac{\sigma_{exp}\left(\varepsilon\right)}{c_{siebel}\left(\varepsilon\right)} \tag{3.15}$$

where $\sigma_{exp}\left(\varepsilon\right)$ is the average pressure and $c_{siebel}\left(\varepsilon\right)$ is Siebel's correction function. These variables can be given as function of strain:

$$\sigma_{\exp}(\varepsilon) = \frac{F(\varepsilon)}{\pi r^2(\varepsilon)} \tag{3.16}$$

$$c_{siebel}(\varepsilon) = \left(1 + \frac{2\mu r(\varepsilon)}{2h(\varepsilon)}\right) \tag{3.17}$$

Siebel's correction is very easy to apply; for low strain and friction coefficients it gives reliable results.

During this study for appling iterative FEM method some simplification are performed. The main idea of the method can be summarized with Eqs. (3.18) and (3.19). Correction function is defined as:

$$c^{i+1}{}_{FEM}(\varepsilon) = \frac{\sigma^{i+1}{}_{FEM}(\varepsilon)}{\sigma^{i}{}_{input}(\varepsilon)} \quad i = 0,1,2,... \tag{3.18}$$

$$\sigma^{i+1}{}_{input}(\varepsilon) = \frac{\sigma_{\exp}(\varepsilon)}{c^{i+1}{}_{FEM}(\varepsilon)} \quad i = 0,1,2,... \tag{3.19}$$

where $c^{i+1}{}_{FEM}(\varepsilon)$ is the correction function, $\sigma_{\exp}(\varepsilon)$ is experimental flow curve, $\sigma^{i}{}_{input}(\varepsilon)$ is input true stress-strain curve for FEM, $\sigma^{i+1}{}_{input}(\varepsilon)$ is corrected flow curve if the required precision is obtained, if not, input for FEM for the next iteration and $\sigma^{i+1}{}_{FEM}(\varepsilon)$ is true stress-strain curve obtained from FEM compression simulation performed with pre-assumed friction coefficient.

The process to determine the friction free flow curve by iterative FEM method is carried out as follows:

1.   The load-stroke curves of compressed specimen are determined by compression test and experimental flow curve $\sigma_{\exp}(\varepsilon)$ is obtained as described in above section.

2. $\sigma_{\exp}(\varepsilon)$ is input to the FEM program, then, a simulation of the former compression test is made with the same dimensions and pre-assumed friction coefficient and zero friction with the same number of increment. Load-stroke data is taken as output from FEM program and it is converted to the true stress – strain curve. Zero-friction model is run to be able to compare the stresses at the same strain due to difficulties of material dependent modeling (fitting) problems. Even it is not the case it will be not reliable to compare directly the experimental true stress – strain curve and simulated true stress – strain curve because of the extended elastic region in experimental true stress – strain curve due to deflection on the press. On the other hand simulated true stress – strain curve will have a very steep slope varying with the elastic-modulus entered to the FEM program.

3.   Calculation of correction function is done by dividing true stress values simulated with pre-supposed friction coefficient by true stress values simulated with no friction for the same strain values. Obtained curve is fitted to sixth order polynomial in order to apply it on the experimental flow curve.

4. $\sigma^{i+1}{}_{input}(\varepsilon)$ is calculated by dividing $\sigma_{\exp}(\varepsilon)$ by correction function. This flow curve can be assumed as friction free flow curve if the required precision is obtained. If this is not the case it will be input for FEM for the next iteration.

5.   Steps (2), (3) and (4) will be repeated until enough accuracy is obtained.

These steps of first iteration are represented as Eq. (3.20) and graphed on Figure 3.25.

$$\sigma^0_{input}(\varepsilon) = \sigma_{exp}(\varepsilon) \ (1^{st} \text{ Step})$$

$$\left.\begin{array}{l} \sigma^1_{FEM}(\varepsilon) : FEM\left(\sigma_{exp}(\varepsilon)\right)^{0.1 \text{ friction}} \\[2mm] \sigma^0_{input}(\varepsilon)^* : FEM\left(\sigma_{exp}(\varepsilon)\right)^{0 \text{ friction}} \end{array}\right\} (2^{nd} \text{ Step})$$

$$c^1_{FEM}(\varepsilon) = \frac{\sigma^1_{FEM}(\varepsilon)}{\sigma^0_{input}(\varepsilon)^*} \ (3^{rd} \text{ Step})$$

$$\sigma^1_{input}(\varepsilon) = \frac{\sigma_{exp}(\varepsilon)}{c^1_{FEM}(\varepsilon)} \ (4^{th} \text{ Step})$$

(3.20)
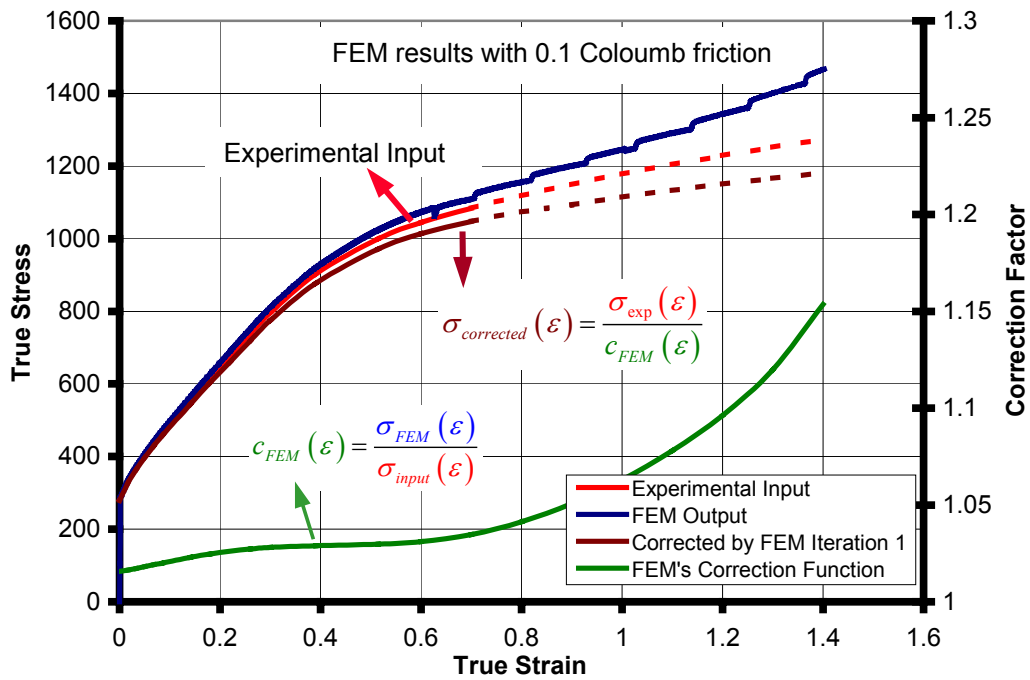
Figure 3.26 Application of iterative FEM method for first iteration

In Figure 3.26 dashed parts of experimental flow curve and corrected flow curve shows extrapolated parts of the curves. Correction function is used to correct experimental flow curve up to maximum compression strain (about 0.74). Reason for simulating the compression test for the correction function up to

strain of 1.4 is in order to correctly fit the general behavior of correction function.

Correction function is fitted to a sixth order polynomial as shown in Figure 3.27.
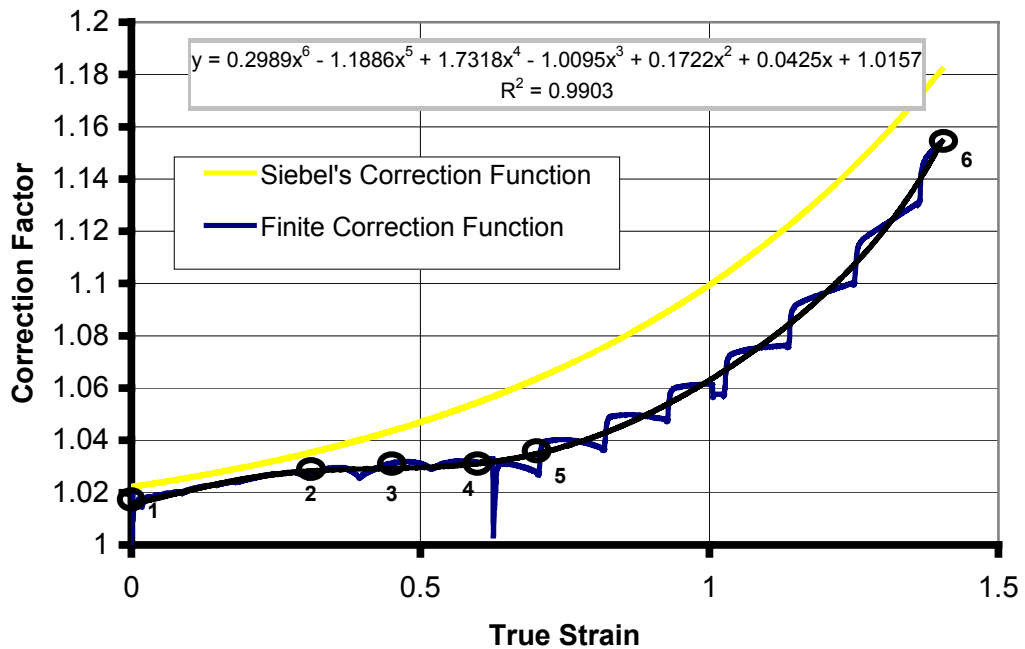
Figure 3.27 Fitting of iterative FEM method's correction function to a sixth order polynomial

Numbers shown on Figure 3.27 are representing the screen shots of simulation mesh of compression test on that strain. Screen shots are given in Figure 3.28.

Ongoing trend of the FEM correction function represented on Figure 3.27 about circles numbered 2, 3 and 4 is starting to deviate after number 5. In Figure 3.28 it can be seen that mesh in picture 5, starts folding besides sliding. This folding causes an increase on correction function due to increasing contact area.

Both correction functions of FEM and Siebel are presented in Figure 3.29 with experimental and corrected flow curves. Siebel correction curve has higher values for corresponding strain values, thus flow curve corrected by Siebel is below the flow curve corrected with iterative FEM method.
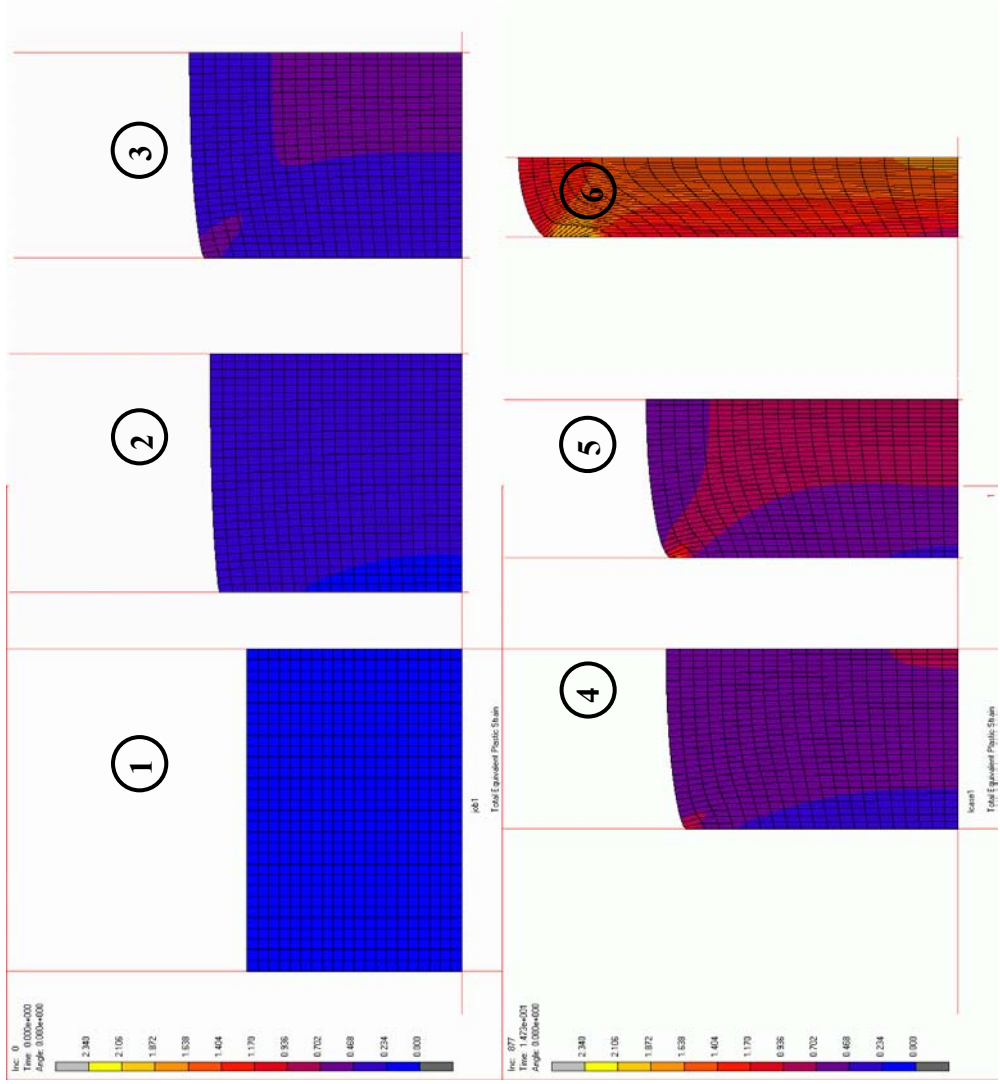
Figure 3.28 Screen shots of several increments of compression simulation numbered on Figure 3.27

94
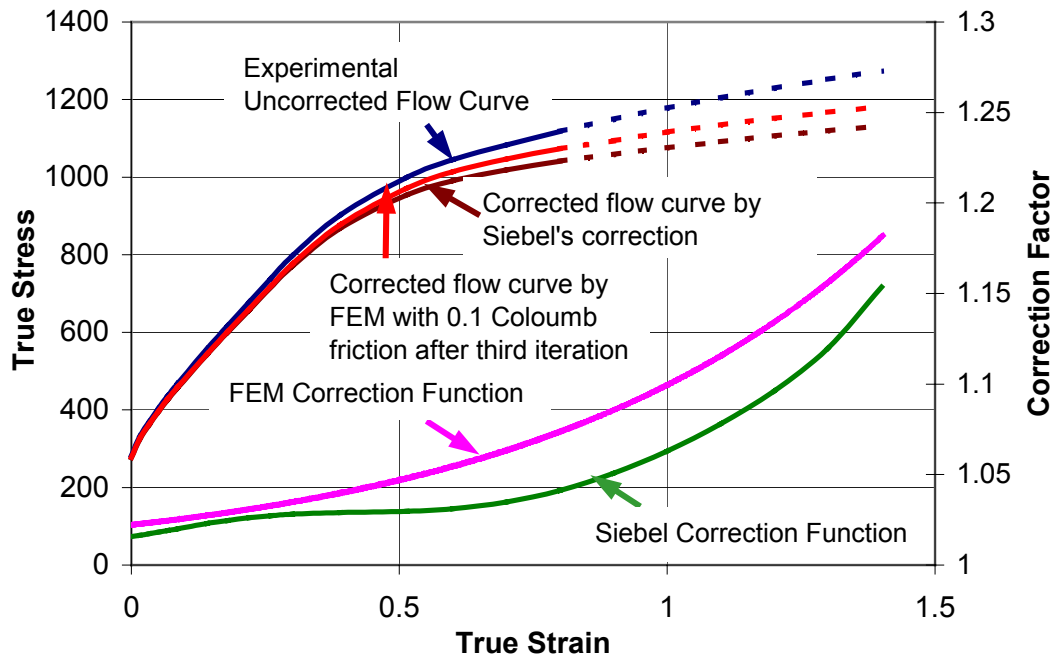
Figure 3.29 Corrected flow curves and correction functions of compression test of stainless steel
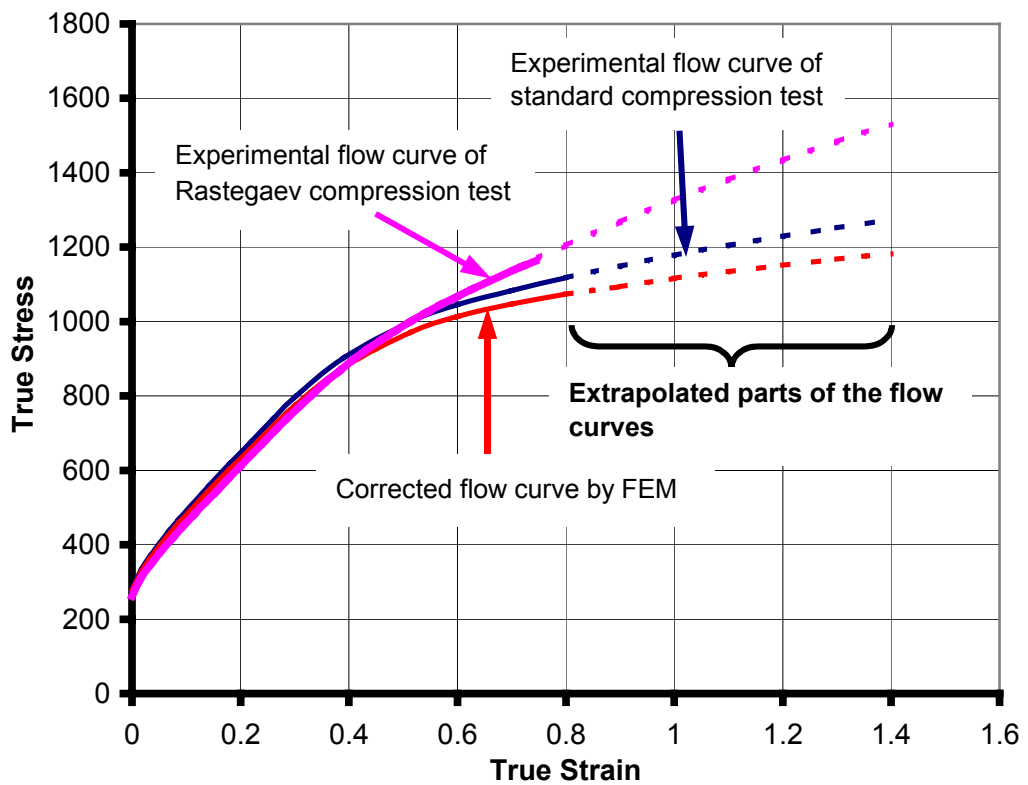
Figure 3.30 Rastegaev, standard and corrected standard compression flow curves of stainless steel

It is clear that during Rastegaev compression test measuring reduction of height instead of diameter change which is homogenous along the height of the specimen in this case, gives a big error after about 0.6 plastic strain. Figure 3.30 simply shows this difference when it is compared with experimental and corrected flow curves of standard compression test.

After this point of the study standard compression test results will be given as corrected flow curves by iterative FEM method.

Compression tests' results performed after drawing and extrusion processes and in annealed state are given in Figure 3.31. In this figure there is a big difference between Rastegaev and standard compression tests in drawn state, but in annealed and extruded states it seems to be similar up to 0.5 plastic strain and then difference becomes larger. The most interesting point in this graph is the lowering tendency of the hardening coefficient in the initial region of the flow curves for both tests. This lowering tendency increases with the following forming operations. This means this is less in annealed, more in drawn, and much more in extruded state. In the extreme case, extruded state, material behaves as it has constant yield stress (perfect plastic). This is commonly named as work-hardening stagnation in literature (see Section 2.5).
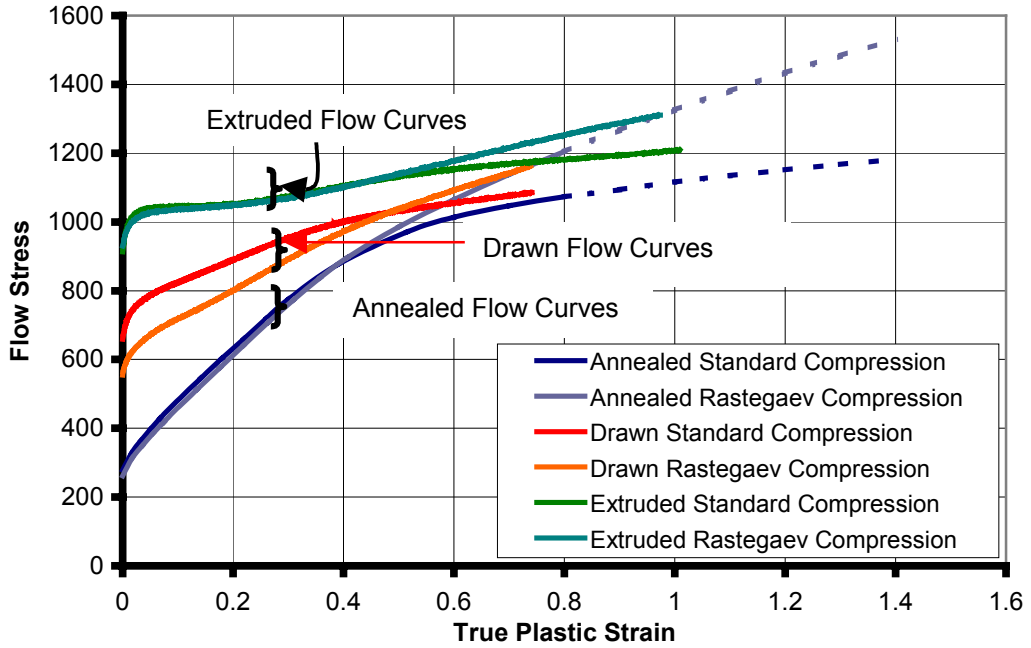
Figure 3.31 Rastegaev and standard compression flow curves of stainless steel in annealed, drawn and extruded state

In Figure 3.32 only the standard compression tests are shown. Compression flow curves of the drawn and the extruded states are shifted in order to compare them with the annealed flow curve. Shifting amount is taken as the equivalent plastic strain at the center of the drawn or extruded part. This is a known value, as the reduction ratio is known. The plastic strain can be found as follows,

$$\varepsilon_{pl} = \ln\left(\frac{A_0}{A}\right) = 2\ln\left(\frac{d_0}{d}\right) \tag{3.21}$$

where A_0 and d_0 are initial area and diameters respectively, A and d are formed area and diameters respectively. Although it is known that the plastic strain at the center is the minimum point on the radial distribution of plastic strain of a drawn or extruded part, this strain value is taken only to compare the work-hardened flow curves with the annealed one. Mean plastic strain calculations performed with FEM simulations will be presented in Chapter 4.

97
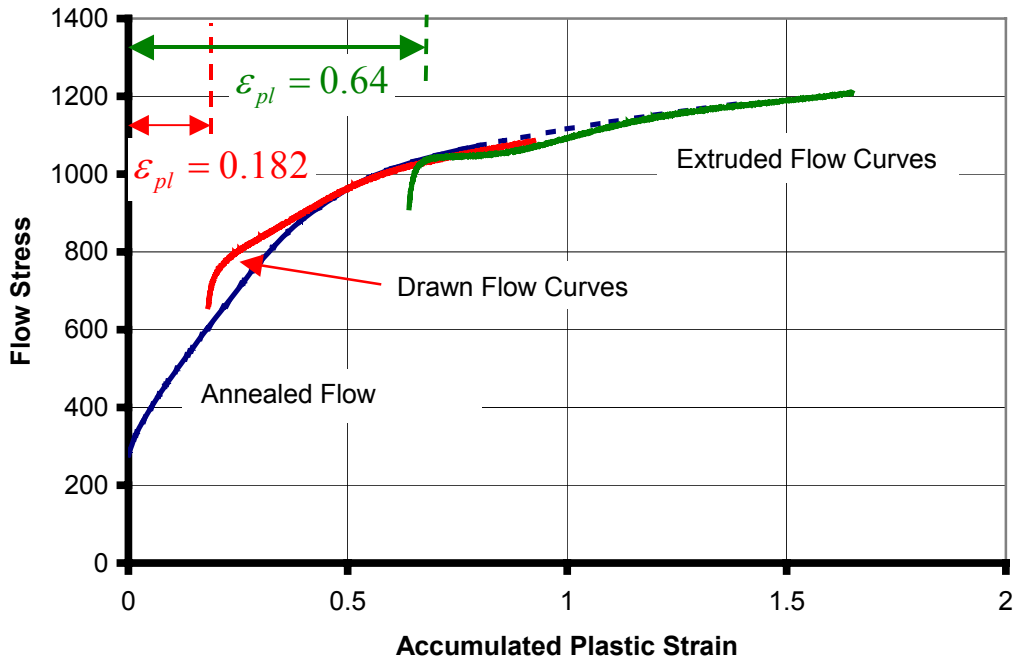
Figure 3.32 Standard compression flow curves of stainless in annealed, drawn and extruded state

In Section 3.2.1 it is shown that there is no shape change in tension flow curve of the same material in drawn state. But in compression flow curve of the drawn and extruded state there is an apparent shape change. It is also hard to say that this is because of the non-homogeneous strain distribution as it is not valid for tension flow curve.

Some more experiments were performed to investigate the Bauschinger effect.

Annealed tension samples were first pulled up to 10%, 20% and 36% (just before necking) elongation respectively and then cylinders were cut from the middle section without any radial machining. The obtained cylinders initially having an aspect ratio of 1.5 were compressed (Figure 3.33). The following Figures 3.34, 3.35, 3.36 represents the behavior of stainless steel after stress reversal with three different amounts of pre-strains.
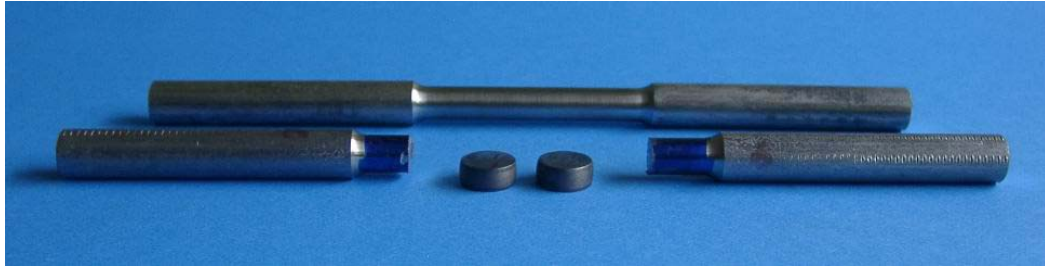
Figure 3.33 Compressed test specimen after being pre-strained by tension
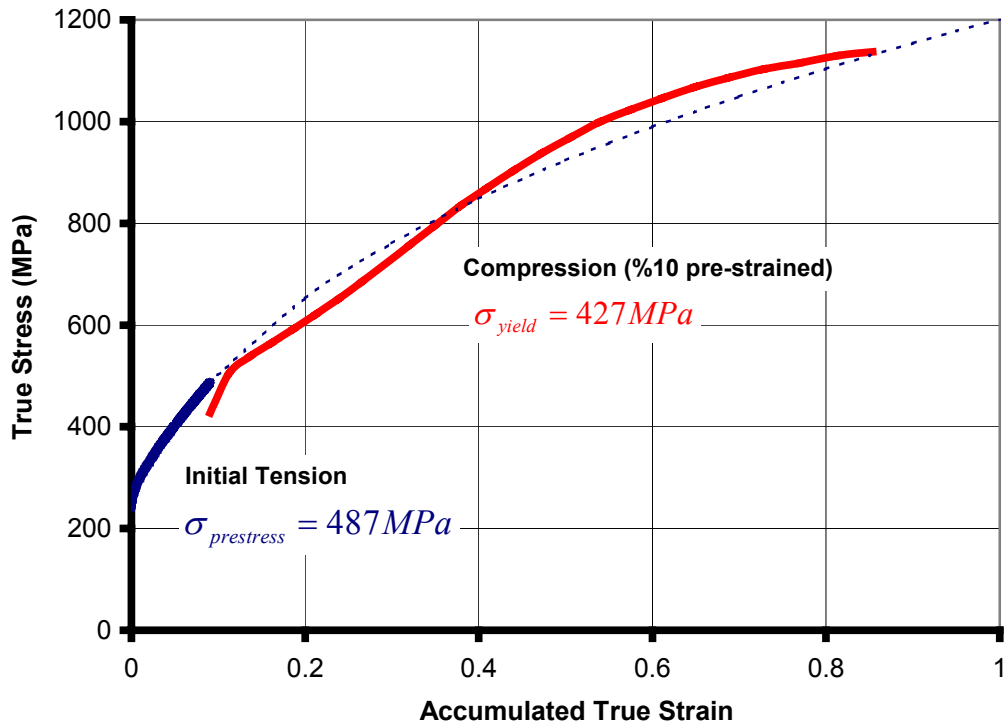
Figure 3.34 Stress reversal after ~0.09 plastic prestrain in tension

In Figures 3.34, 3.35, 3.36 it can be seen that with increasing prestrain, the difference between the initial yield point of the compression test and prestress, the highest flow stress applied in tension test, increases as well. This increasing difference shows that Bauschinger effect is increasing with increasing prestress (or prestrain). It can be seen that the reverse flow curve always stays below the monotonic one, and that after high prestresses tends to remain constant before beginning to rise again.
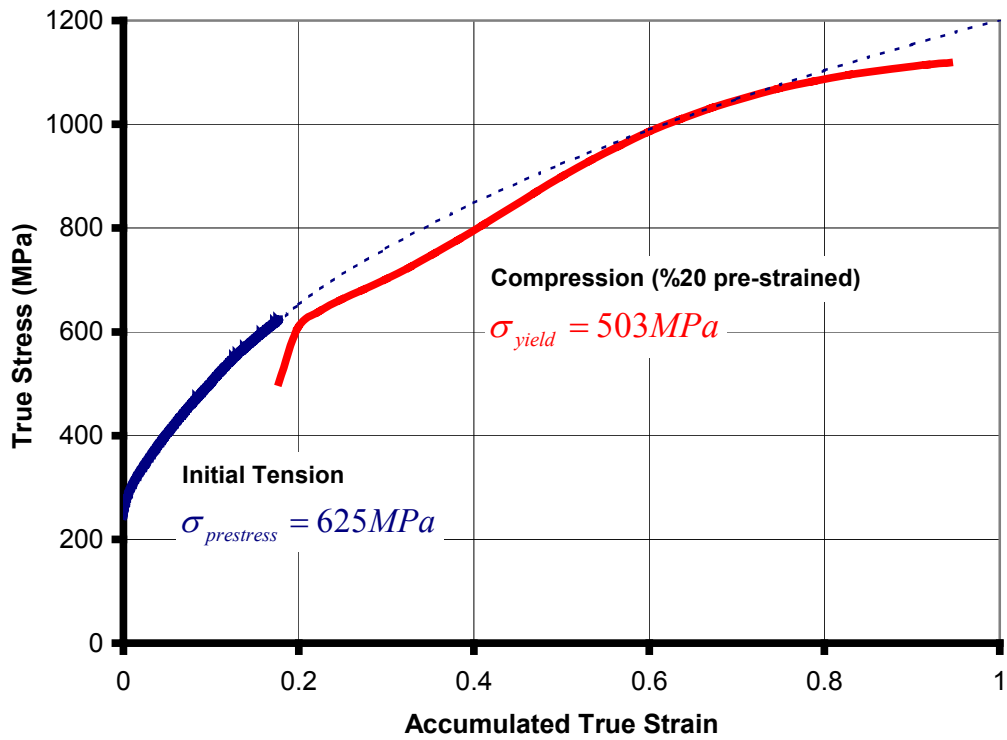
Figure 3.35 Stress reversal after ~0.177 plastic prestrain in tension
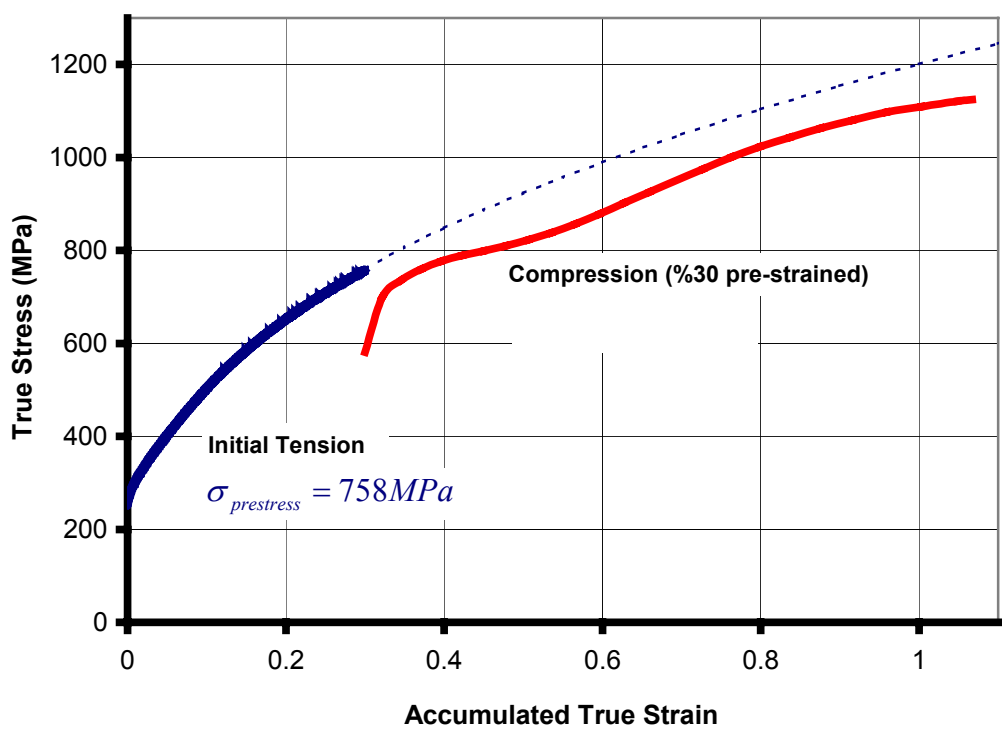
Figure 3.36 Stress reversal after ~0.3 plastic prestrain in tension
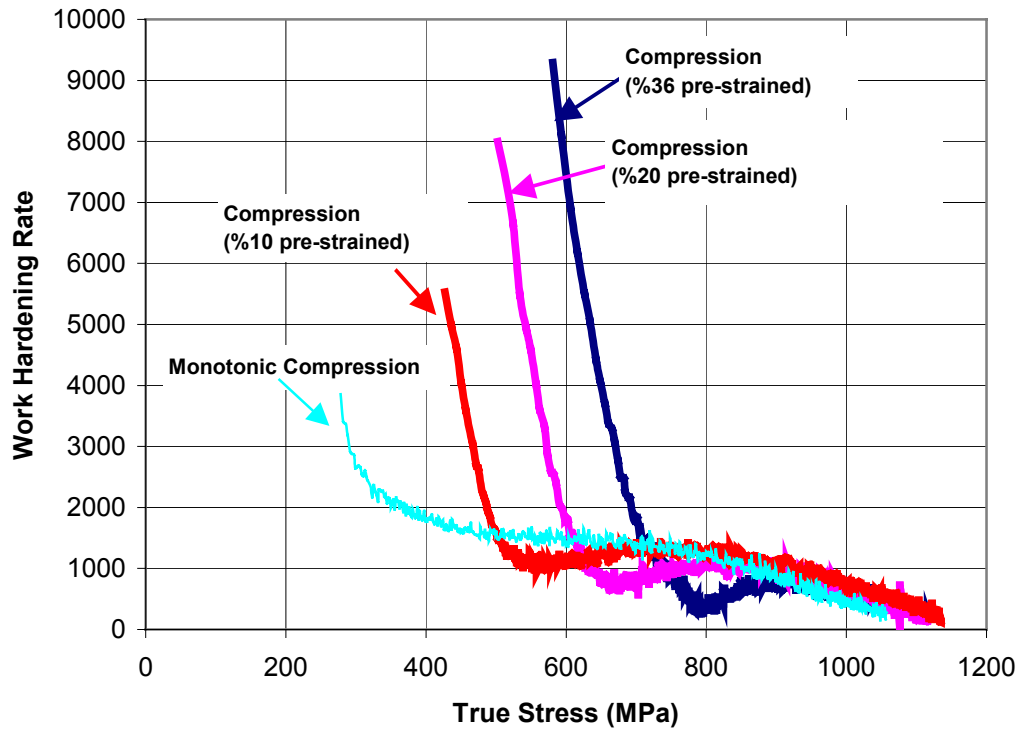
Figure 3.37 Dependence of the plastic work hardening rate on absolute stress during forward and reverse flow

Work hardening rate can be defined as

$$\theta = \frac{d\sigma_f}{d\varepsilon_{pl}} \tag{3.22}$$

From Figure 3.37 it is seen that initial work-hardening rate of reverse loading is much higher than the monotonic loading but decreasing rapidly. Beyond this initial stage θ_r, reverse work-hardening rate, drops below θ_f, forward work-hardening rate, for an extended period of stress (or strain) before becoming equal to θ_f at much higher flow stresses as also represented by Christodoulou [68]. But saturation in the Bauschinger effect is not observed.

101

3.2.3 Vickers Hardness Results

Hardness measurements are taken on radial and axial sections of the steel rod as shown in Figure 3.38.
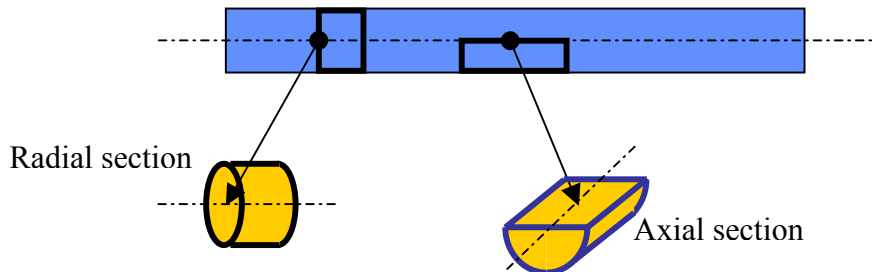
Figure 3.38 Schematic representation of radial and axial sections

Measurements can be classified as *radial* and *circumferential* measurements on radial sections (Figure 3.39(a)); *centerline* and *radial* measurements on axial sections (Figure 3.39(b)).
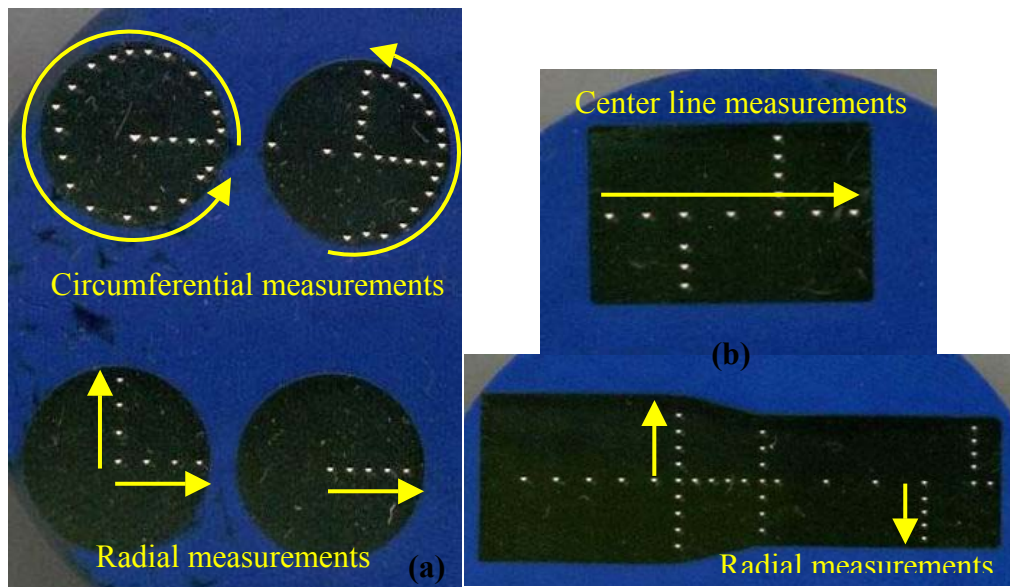
Figure 3.39 Representation of (a) radial and (b) axial sections

In annealed state it is expected that hardness distribution is constant. This can be said by only looking at the centerline measurements in Figure 3.40. But radial measurements on both axial (Figure 3.41) and radial (Figure 3.42) sections there

is a slight increase through outer region about 20 kg/mm^2. This hardening can be because of a drawing process done for the phosphating process.
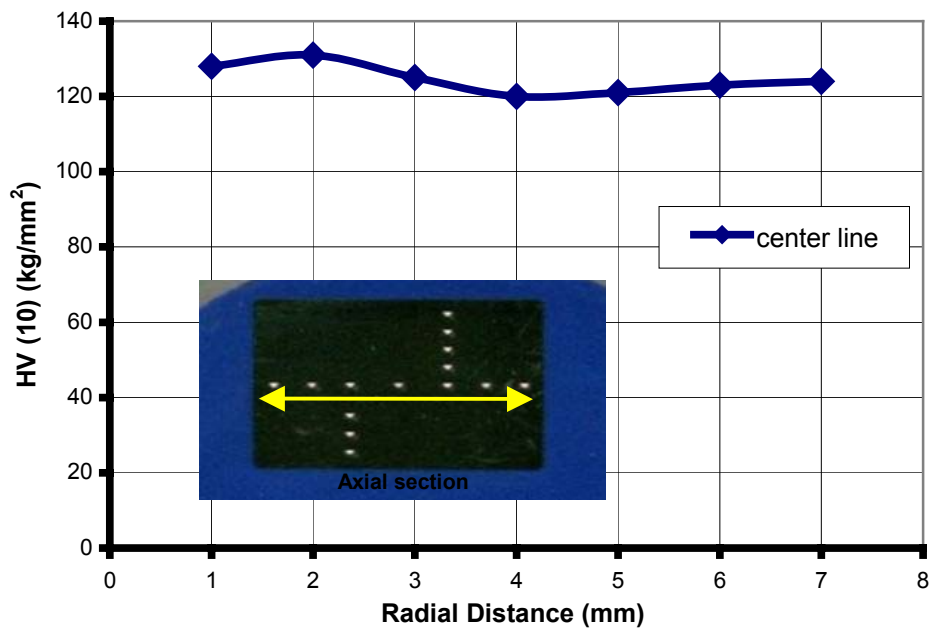
Figure 3.40 Representation of centerline measurements on axial sections of annealed stainless steel
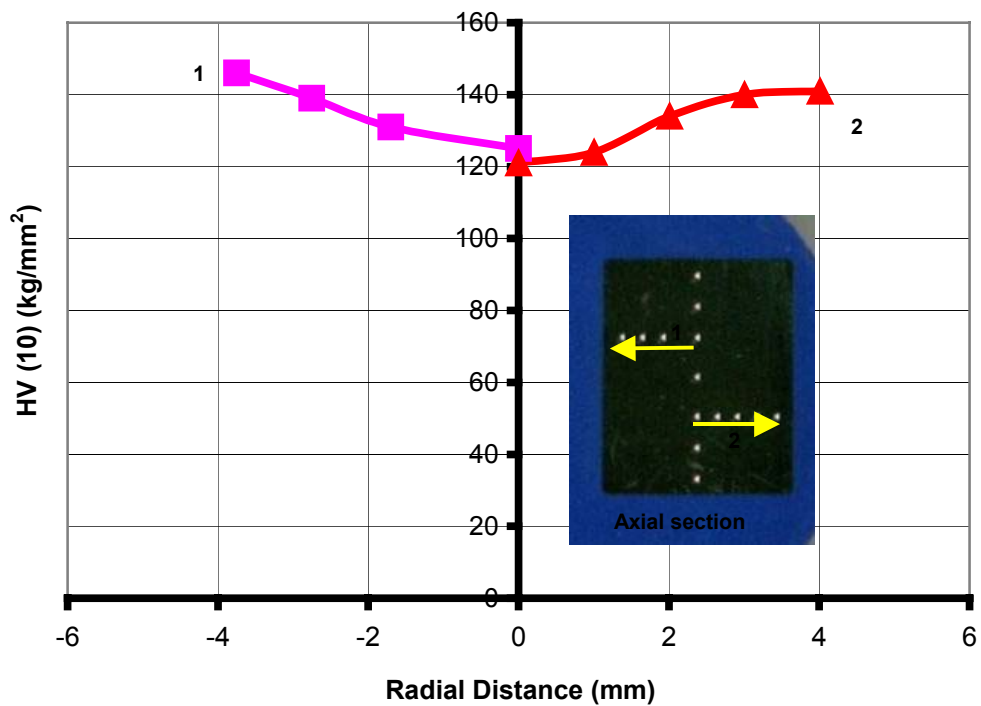
Figure 3.41 Representation of radial measurements on axial sections of annealed stainless steel
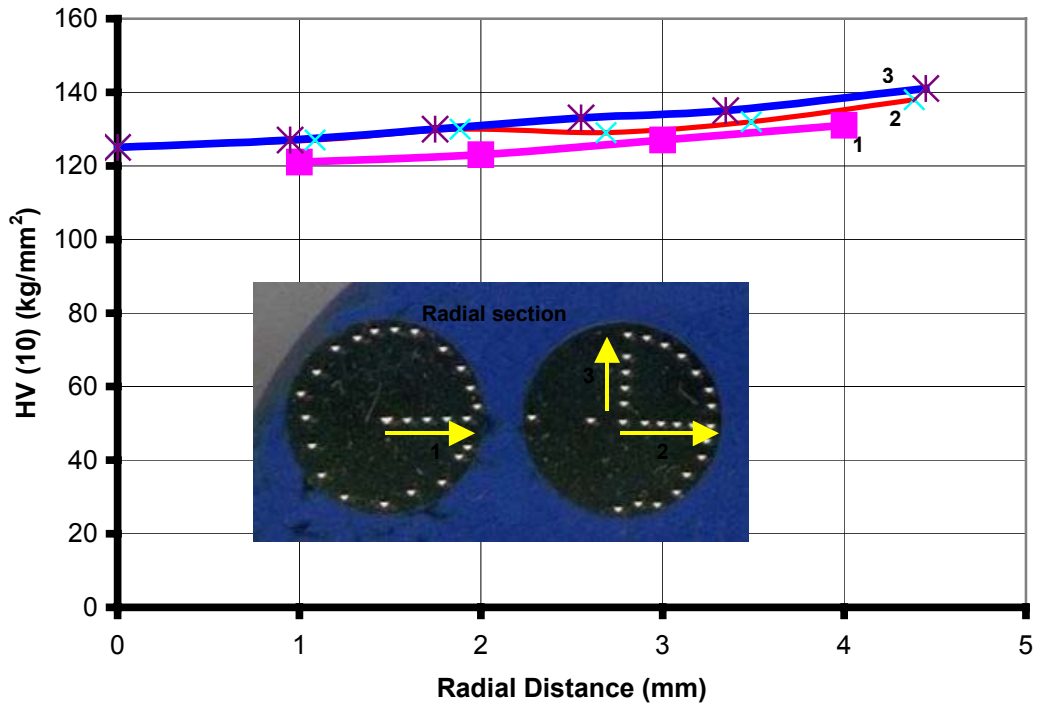
Figure 3.42 Representation of radial measurements on radial sections of annealed stainless steel
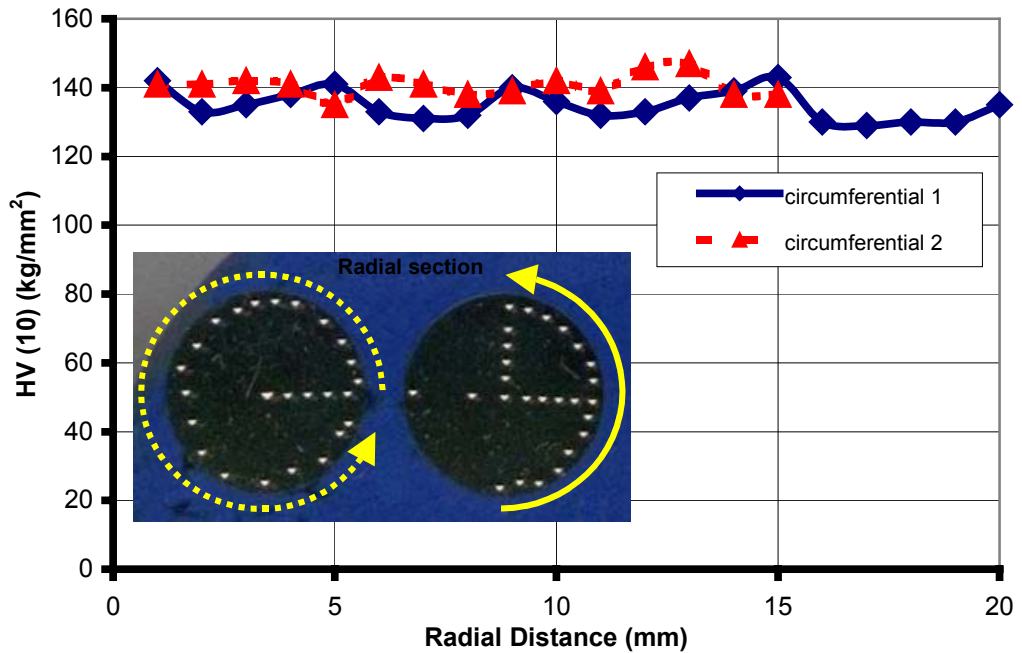
Figure 3.43 Representation of circumferential measurements on radial sections of annealed stainless steel

Circumferential measurements are taken on the radial section of annealed stainless steel in order to see two minimums and two maximums. This can be an indicator of anisotropy exhibited in compression test. But the circumferential hardness measurement's plot (Figure 3.43) is somewhat like a scatter changing from 129 to 143 kg/mm^2.
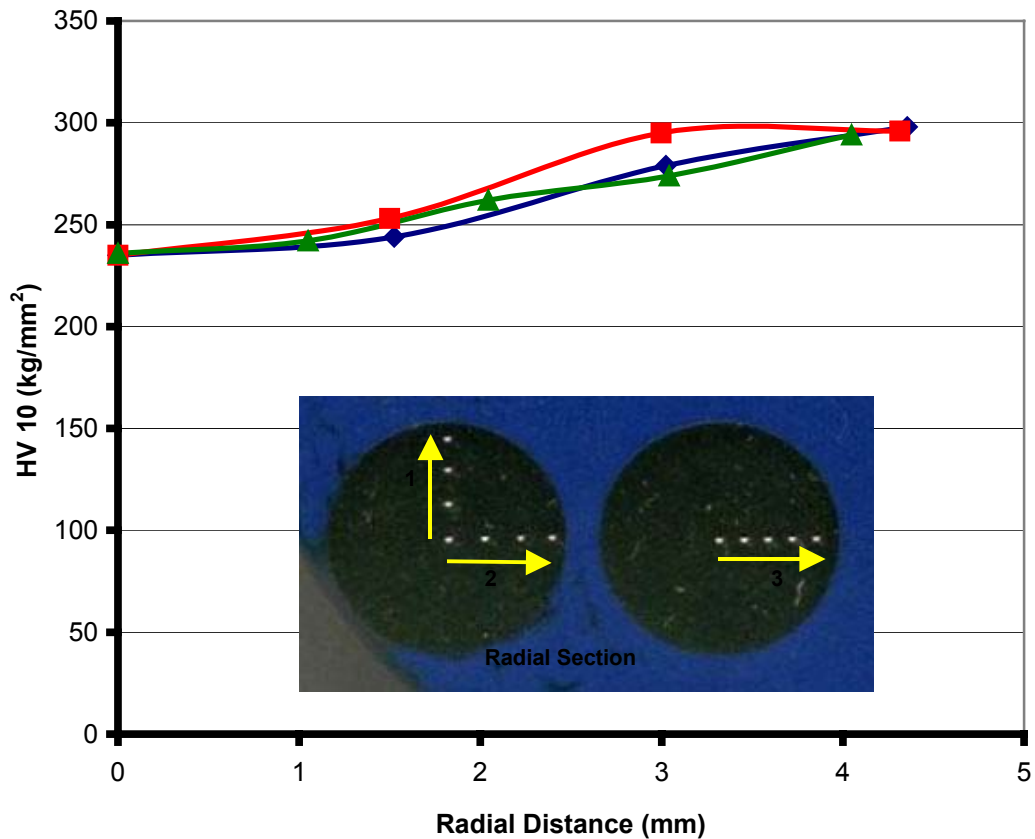
Figure 3.44 Representation of radial measurements on radial sections of drawn stainless steel

Figures 3.44 and 3.46 shows hardness distributions in radial and axial sections of drawn stainless steel. Radial distributions on radial section change 235 to 300 kg/mm^2 whereas this change is between 225 and 275 kg/mm^2 in axial section. But center hardness values seem to be about 230 kg/mm^2 for both sections.
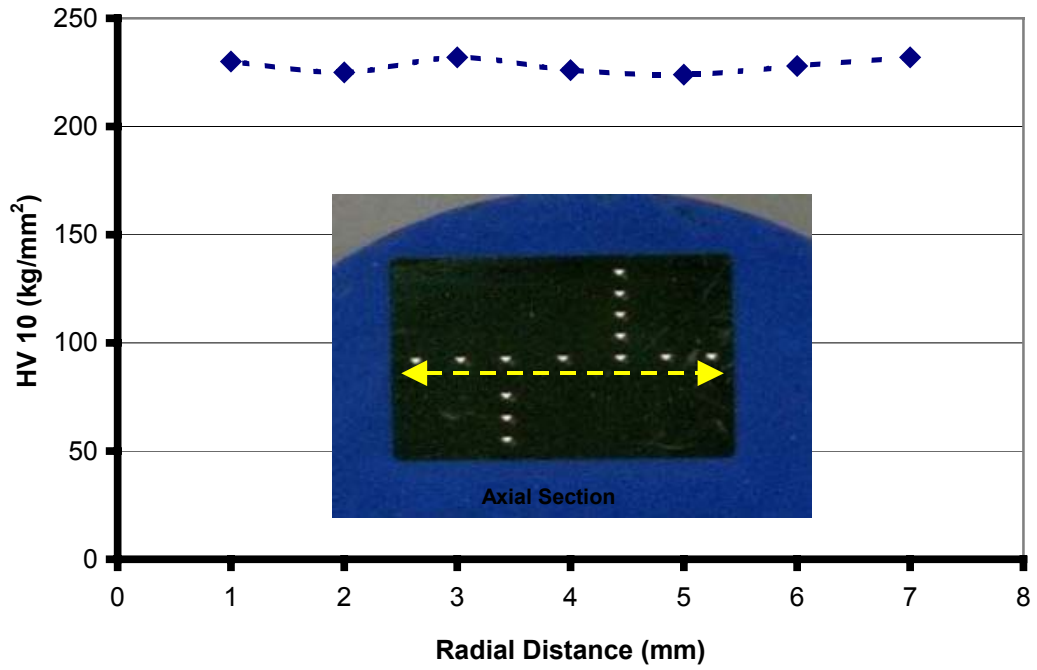
Figure 3.45 Representation of centerline measurements on axial sections of drawn stainless steel
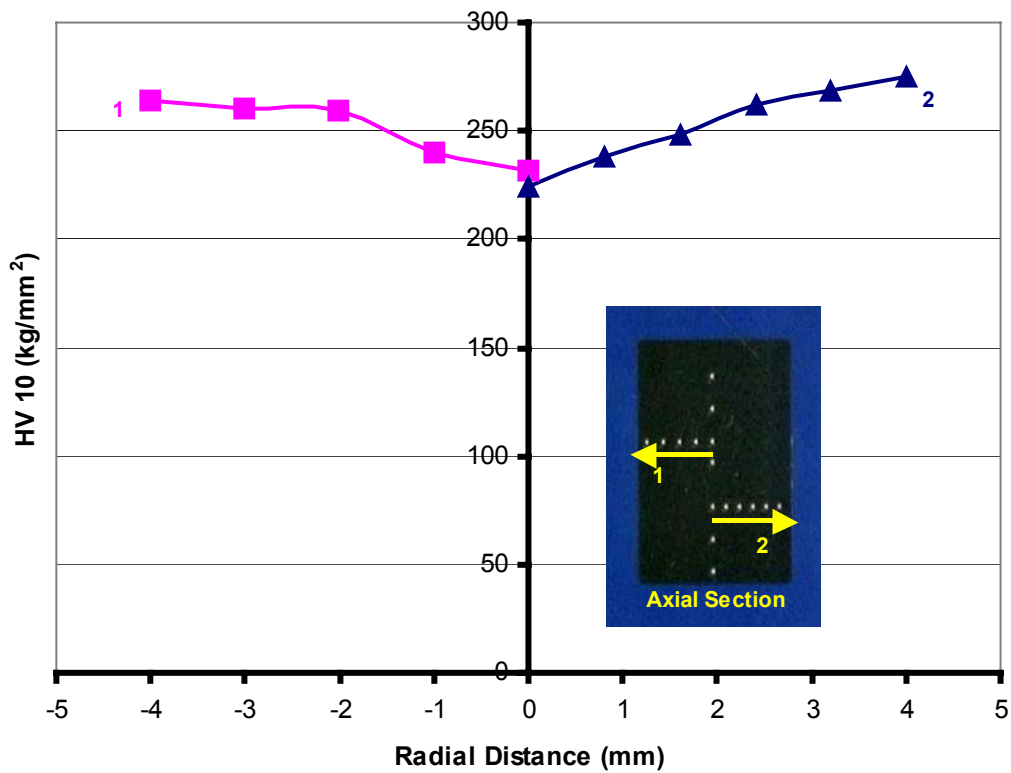
Figure 3.46 Representation of radial measurements on axial sections of drawn stainless steel
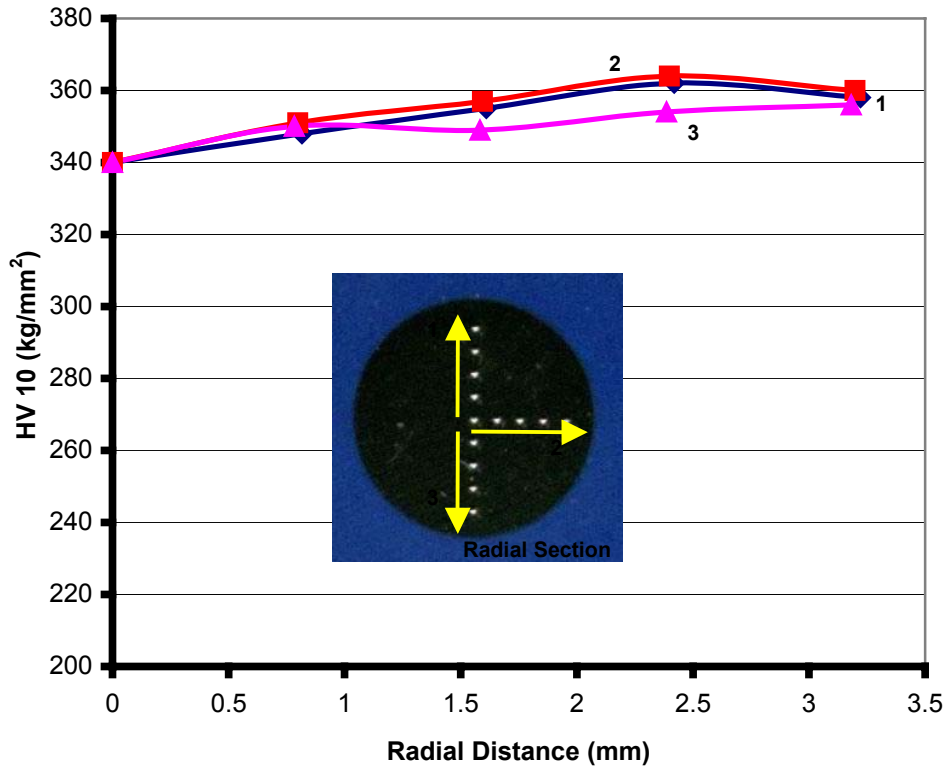
Figure 3.47 Representation of radial measurements on radial sections of extruded stainless steel
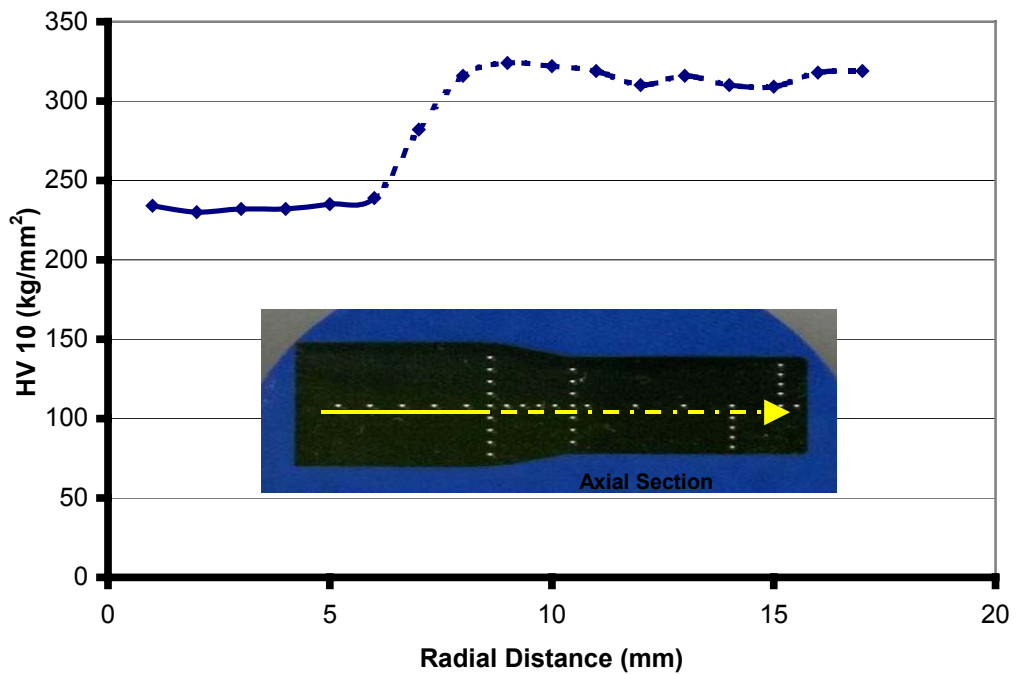
Figure 3.48 Representation of centerline measurements on axial sections of extruded stainless steel
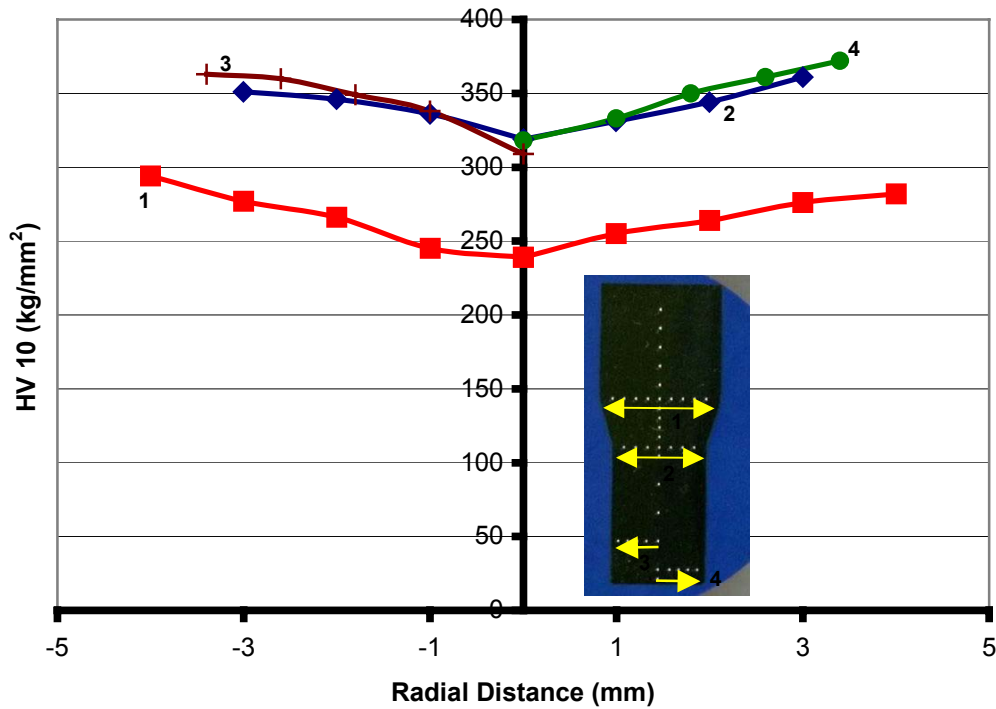
Figure 3.49 Representation of radial measurements on axial sections of extruded stainless steel

Figure 3.48 shows hardness distributions of billet side, deformation zone and extrudate side of axial section of an extruded specimen. Increasing hardness can be seen within the deformation zone. Billet side hardness radial distribution on axial section Figure 3.49 is very similar to that one in drawn specimen. In extrudate side hardness values changes between 318 and 372 kg/mm^2 in radial direction on axial section. On the other hand this 340 to 360 kg/mm^2 in radial section.

3.3   Carbon Steel

In this section experiments performed for carbon steel, their results and evaluations will be presented in detail. Load stroke curves, engineering stress-strain curves and determination of yield stresses will not be given as they are shown in previous sections. Load reversal experiments are investigated in Section 3.2.2.

3.3.1 Tensile Test Results

Tension tests, in which round specimens of 8 mm diameter and 40 mm gauge length were employed, were performed at an average strain rate of 1×10^{-3} s^{-1}, using 200 kN Zwick hydraulic testing machine. Tests were repeated at least three times to obtain reliable results.

For carbon steel specimen ultimate tensile strength can be taken as $\sigma_u = 615 MPa$, and necking strain as $\varepsilon_{eng}{}^{necking} = 0.1$, shown in Figure 3.50. Yield stress is also found by using 0.002 offset method.
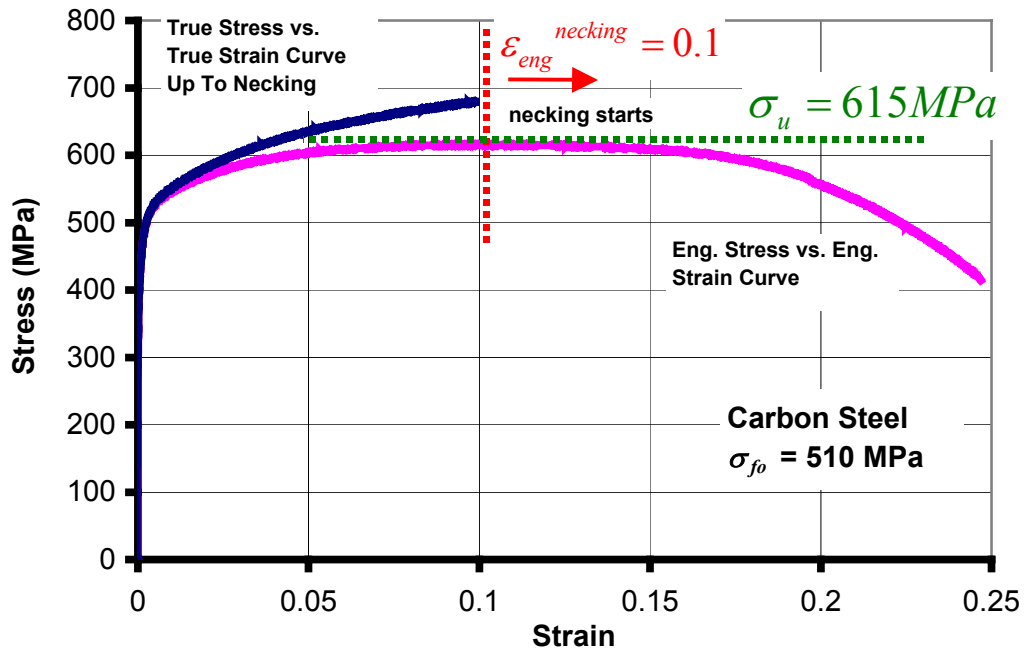
Figure 3.50 Stress and strain curve of carbon steel obtained from tension test

Flow curve can be obtained by plotting true stress values against equivalent true plastic strain values determined by the Eq. (3.5).

$$\varepsilon_{pl} = \varepsilon - \varepsilon_{el} = \varepsilon - \frac{\sigma_{f0}}{E} \qquad (3.5)$$

In this equation, ε_{pl} denotes the total equivalent plastic strain and ε_{el} is the total elastic strain at the point where σ_{f0} and E denotes the yield stress and modulus

of elasticity. Figure 3.51 shows the flow curve of carbon steel obtained from tension test without any extrapolation.
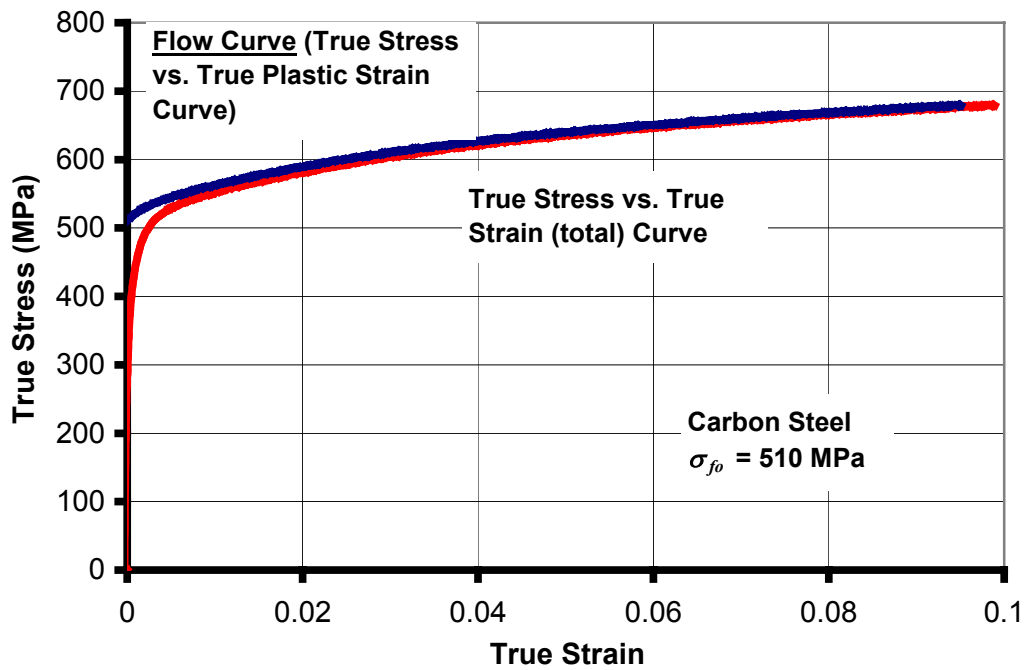
Figure 3.51 Flow curve and true stress – strain curve of carbon steel obtained from tension test

The yield stresses for the higher strain values can be obtained from Ludwik's extrapolation of the experimental flow curves. This method is described in previous sections. Carbon steel (18MnV5) that is used in tension test also shows some deviation from linear behavior as illustrated in Figure 3.52. But this deviation is valid for small plastic strain about 0.015, which corresponds to very small initial portion of the flow curve (Figure 3.53).
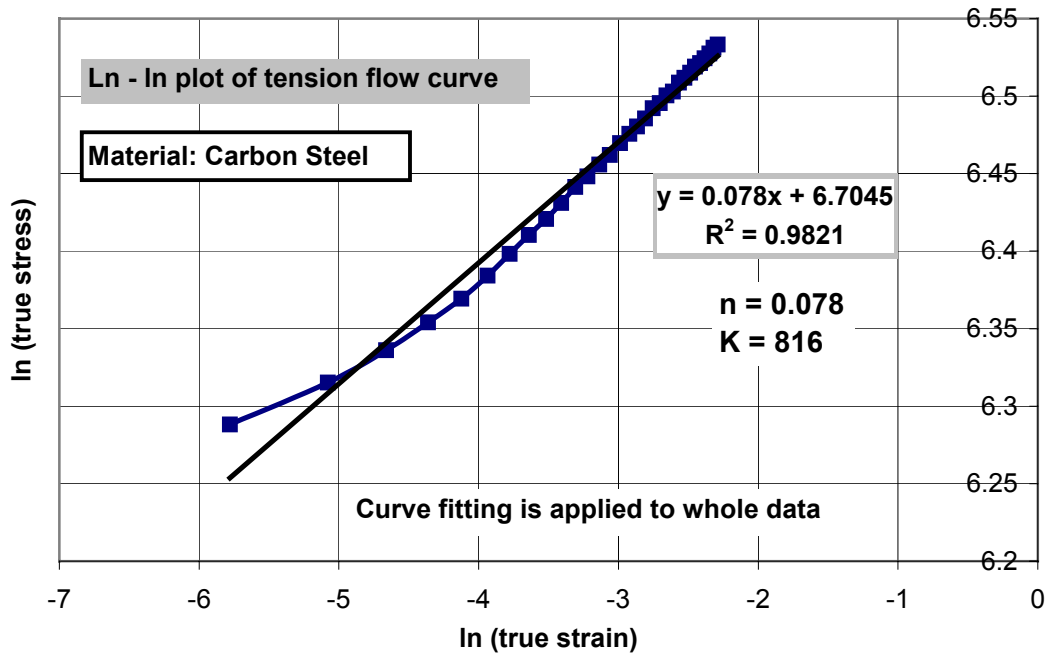
Figure 3.52 Determination of *n* and *K* from the whole tension flow data
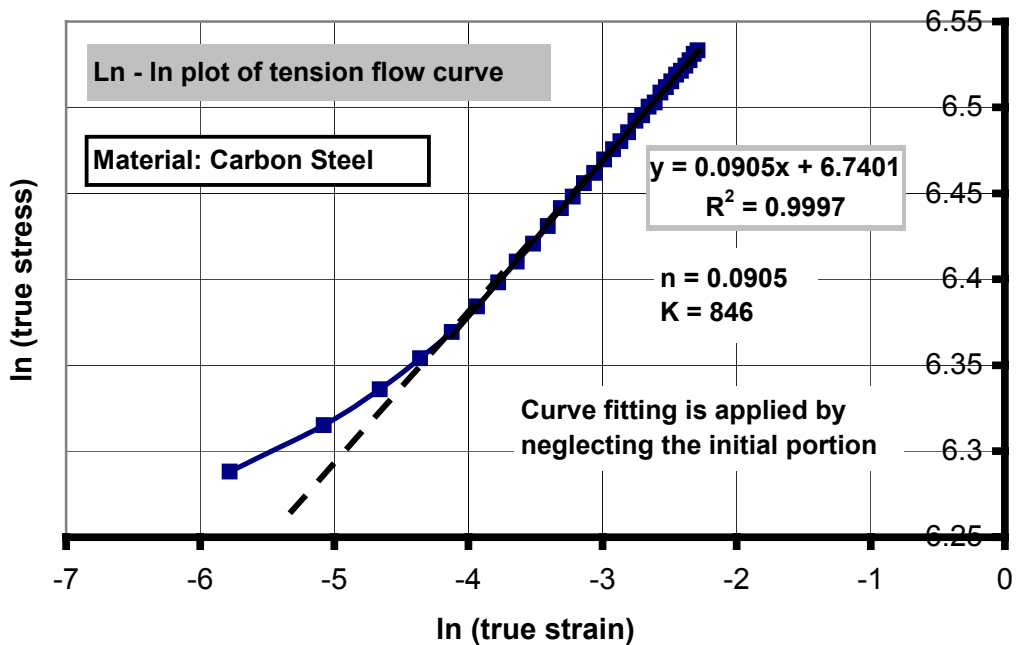
Figure 3.53 Representation of *n* value on the logarithmic plot of the tension

flow data by neglecting initial part

In Figure 3.54 Ludwik fit and experimental flow curves of rolled carbon steel is shown. This curve is obtained by taking initial part of the experimental flow

111

curve and extrapolating the rest with n and K values obtained from second portion of the flow data. $\varepsilon_{pl} = 1.1$ is chosen as a last point of extrapolation because it is very near to the fracture strain in the tension test.
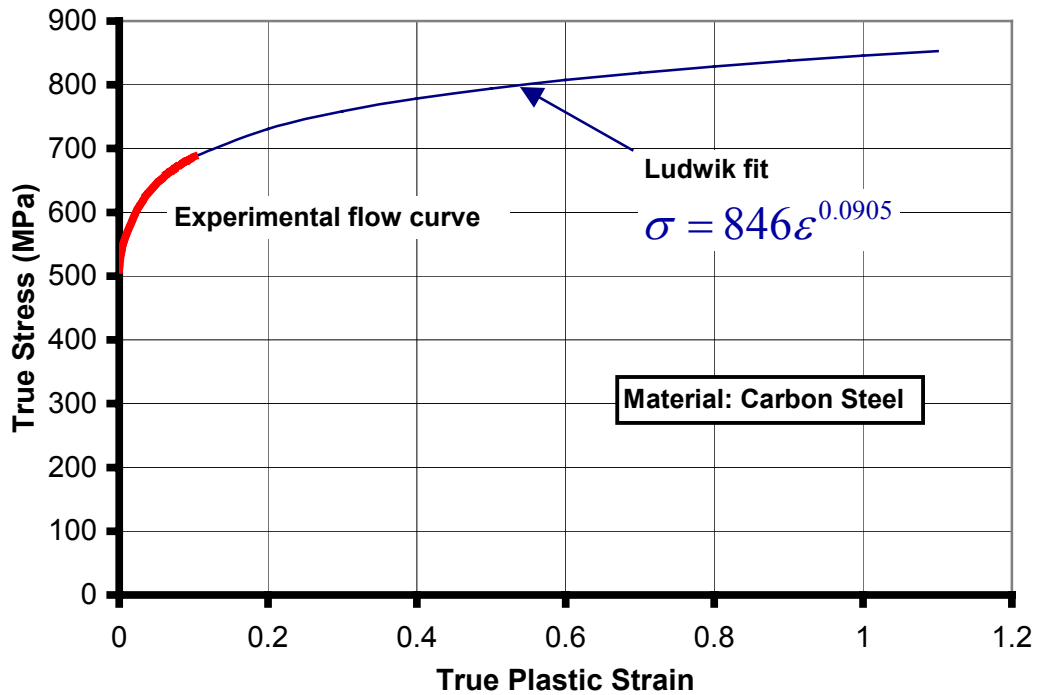
Figure 3.54 Comparison of Ludwik fit with experimental tension flow curve

Tensile testing is also performed for the drawn state of the carbon steel. Figure 3.55 shows the comparison of rolled and drawn tensile flow curves.

In Figure 3.55 it is seen that offset strain 0.178 ($\varepsilon_{drawing}$) is not enough for the drawn flow curve to be on top of the annealed flow curve. This is because the specimen directly starts necking (Figure 3.56). Drawing strain is higher than the necking strain in tension.
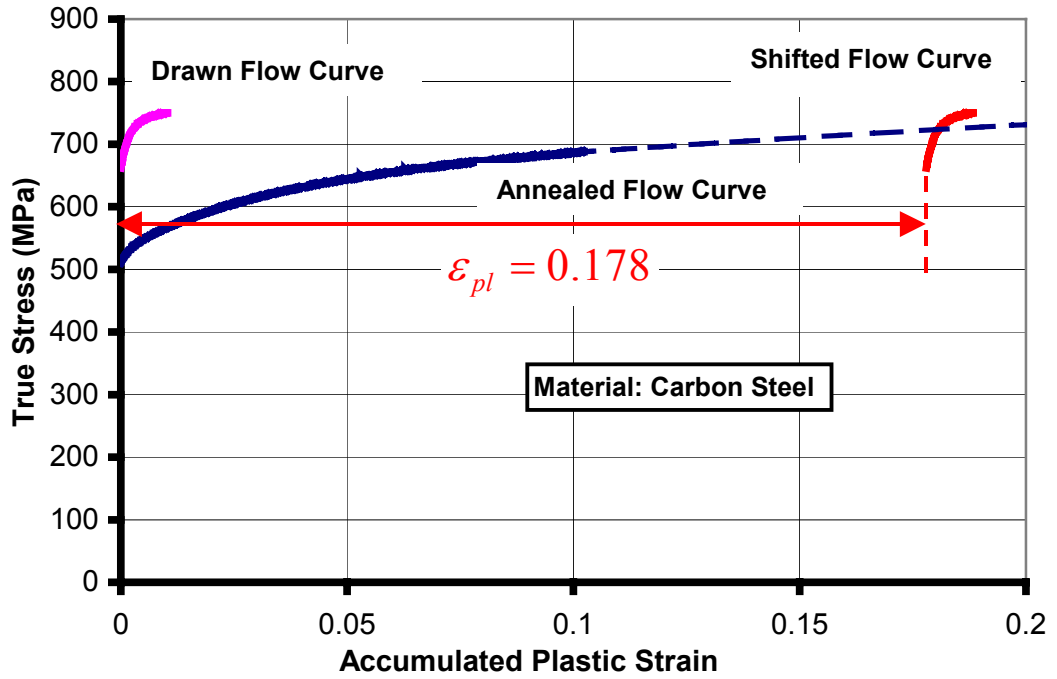
Figure 3.55 Shifting drawn tensile flow curve through the tensile flow curve
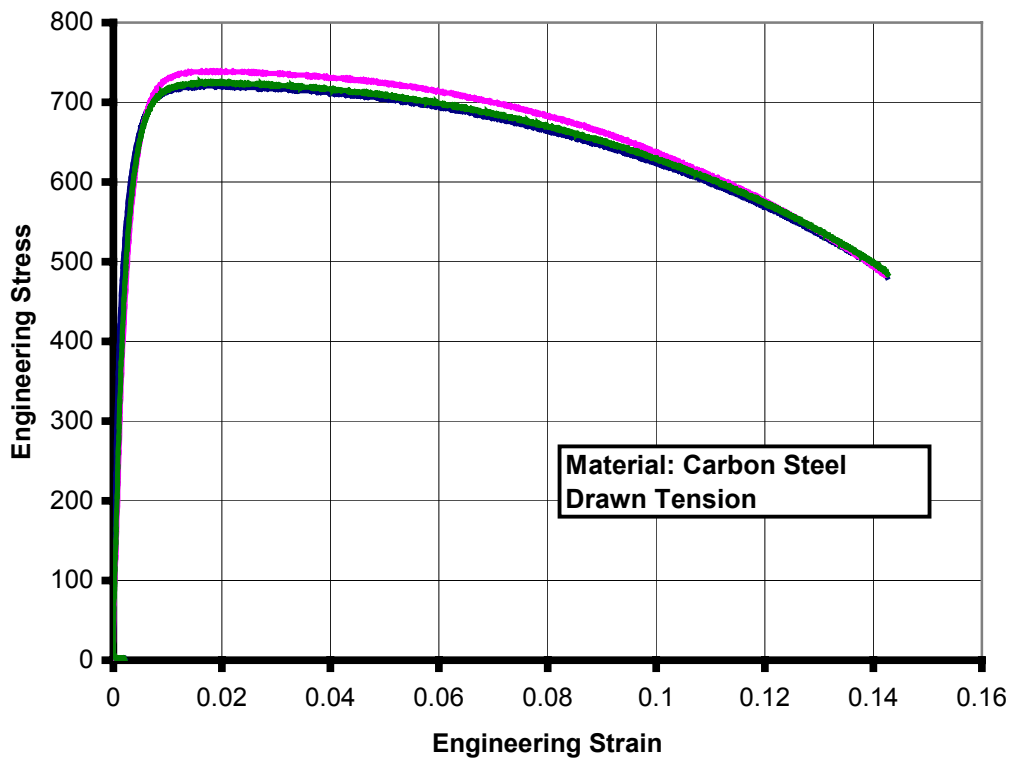
Figure 3.56 Engineering stress vs. strain curves of tension test for different three specimens of drawn carbon steel

3.3.2 Compression Test Results

Compression tests, in which round specimens of 10 mm diameter and 15 mm height were employed, were performed at an average strain rate of 2×10^{-2} s^{-1}, using 200 kN Zwick testing machine. Tests were repeated at least three times to obtain reliable results. Upper and lower surfaces were polished and molycote paste (MoS_2) is used as lubricant. Deformed carbon steel compression specimens preserved their circular shape unlike stainless steel (Figure 3.57).

Figure 3.57 Circular shape of compressed standard compression test specimen of carbon steel

Engineering stress – strain curve gives the yield stress, $\sigma_0 = 491 MPa$ by using 0.002 offset method which described in previous section. From Figure 3.58 it can be seen that compression data is available up to $\varepsilon_{plastic} = 0.74$. Flow curve obtained by Equation (3.4) can be extrapolated in the same manner with tension test.
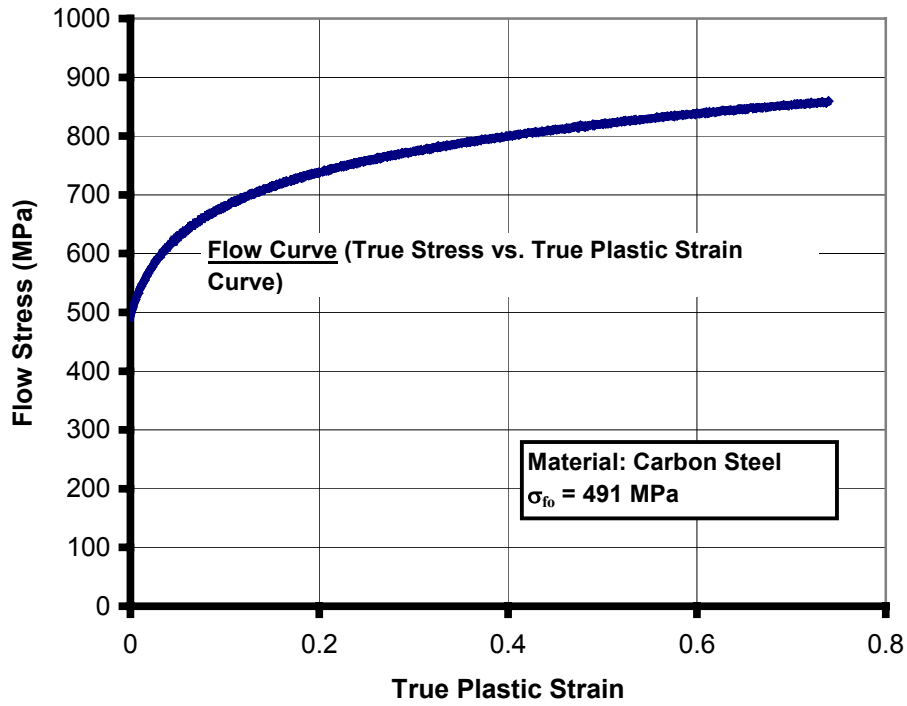
Figure 3.58 Flow curve and true stress – strain curve of carbon steel obtained from compression test
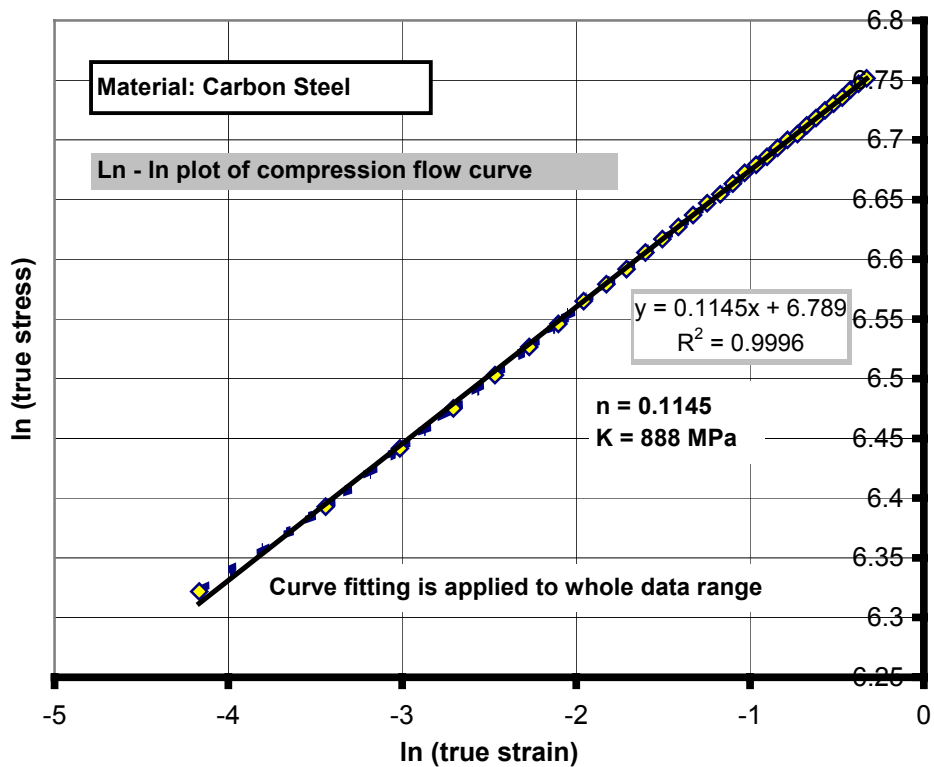
Figure 3.59 Determination of *n* and *K* from the whole compression flow data

115
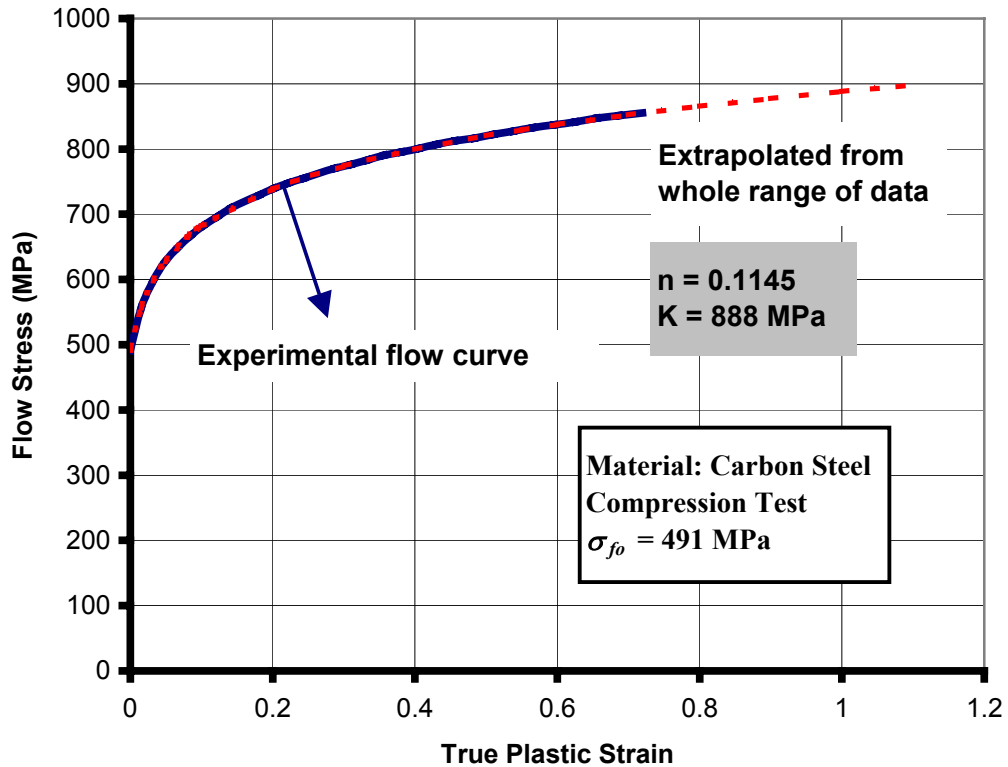
Figure 3.60 Extrapolations from different regions of compression flow data

From the Figure 3.59, it can be seen that compression flow curve of the rolled carbon steel perfectly fits the Ludwik's equation. The extrapolation is done for the whole experimental data. The comparison of Ludwik extrapolations of flow data is done in Figure 3.60. Ludwik's fit seems to represent the exact behavior of the experimental data.

In Section 2.1.2.1 it was discussed that this flow data contains some errors due to the non-homogeneous deformation (barelling) as a result of the friction between compression specimen and dies. Correction of the flow data will be done by Siebel correction function and iterative FEM method. For both methods friction coefficient is needed. This data is obtained from another study as $\mu = 0.06$ (coulomb friction) [50]. In this study ring test is used to determine friction coefficient. Figure 3.61 shows the FEM results for different Coulomb friction factors. Internal diameter change vs. stroke comparison with the experimental measurements indicates the correct friction coefficient. The deviation of the last

experimental data can be due to the extreme deformation of the ring specimen and change of the friction coefficient.
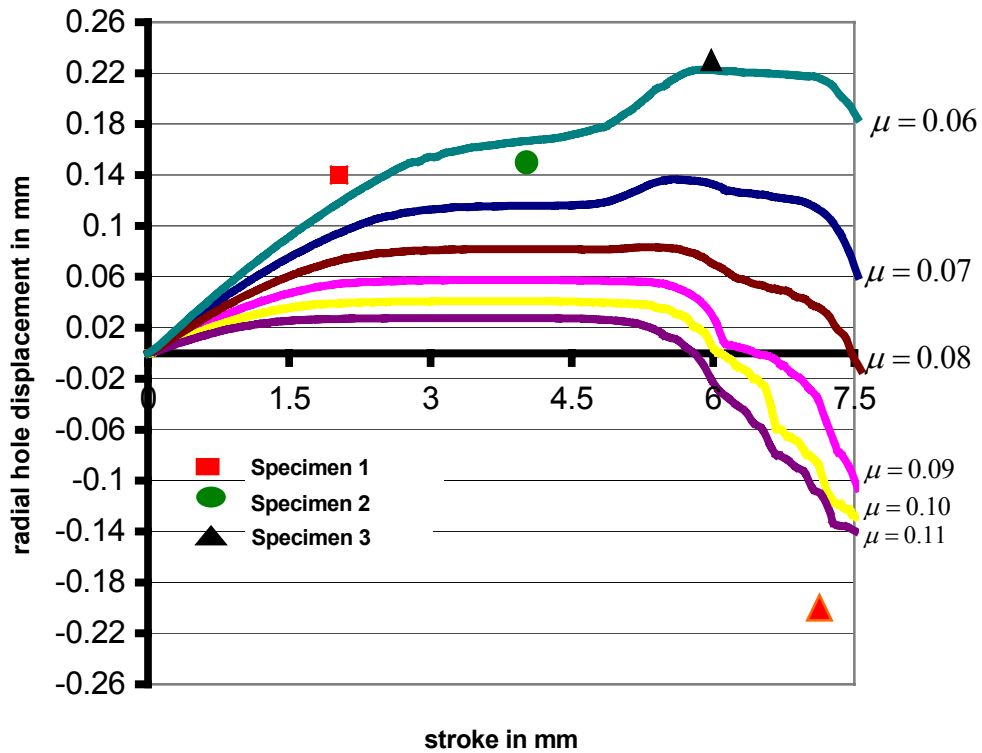
Figure 3.61 Determination of Coulomb's friction coefficient from ring compression test
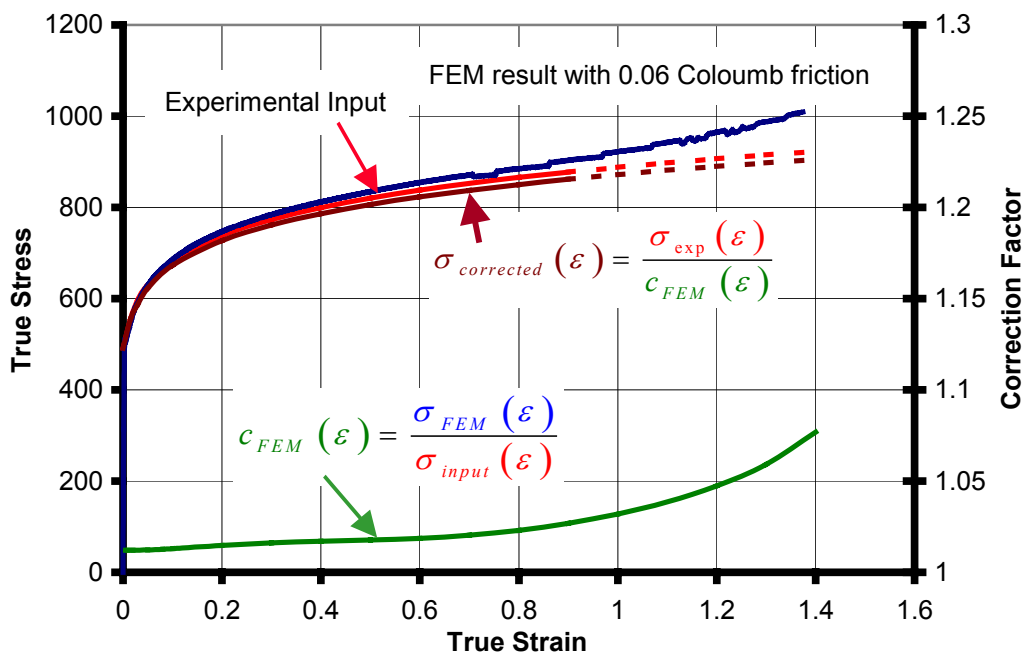
Figure 3.62 Application of iterative FEM method for first iteration

In Figure 3.62 dashed parts of experimental flow curve and corrected flow curve shows extrapolated parts of the curves. Correction function is used to correct experimental flow curve up to maximum compression strain (about 0.74). Reason for simulating the compression test for the correction function up to strain of 1.4 is in order to correctly fit the general behavior of correction function.

Correction function is fitted to a sixth order polynomial as shown in Figure 3.63.
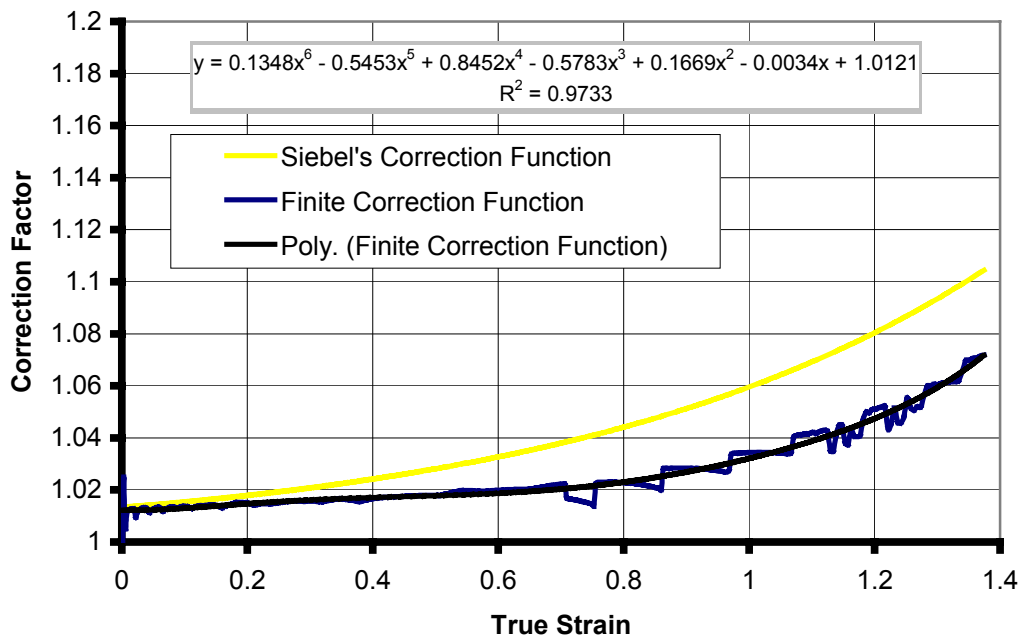
Figure 3.63 Fitting of iterative FEM method's correction function to a sixth order polynomial

Both correction functions of FEM and Siebel are presented in Figure 3.64 with experimental and corrected flow curves. Siebel correction curve has higher values for corresponding strain values, thus flow curve corrected by Siebel is below the flow curve corrected with iterative FEM method.
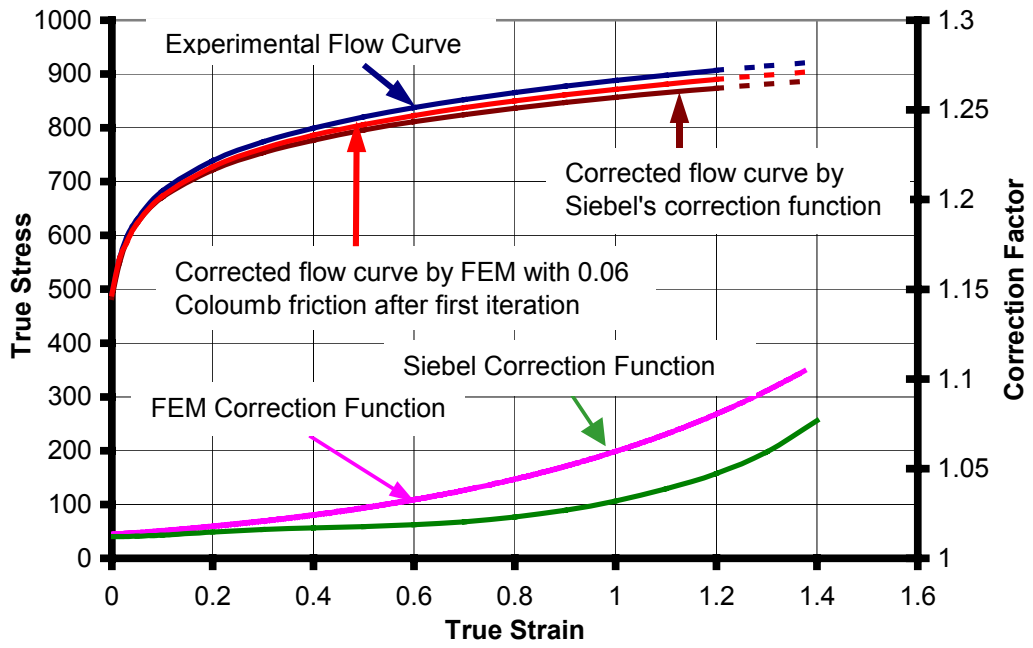
Figure 3.64 Corrected flow curves and correction functions of compression test of rolled carbon steel (18MnV5)
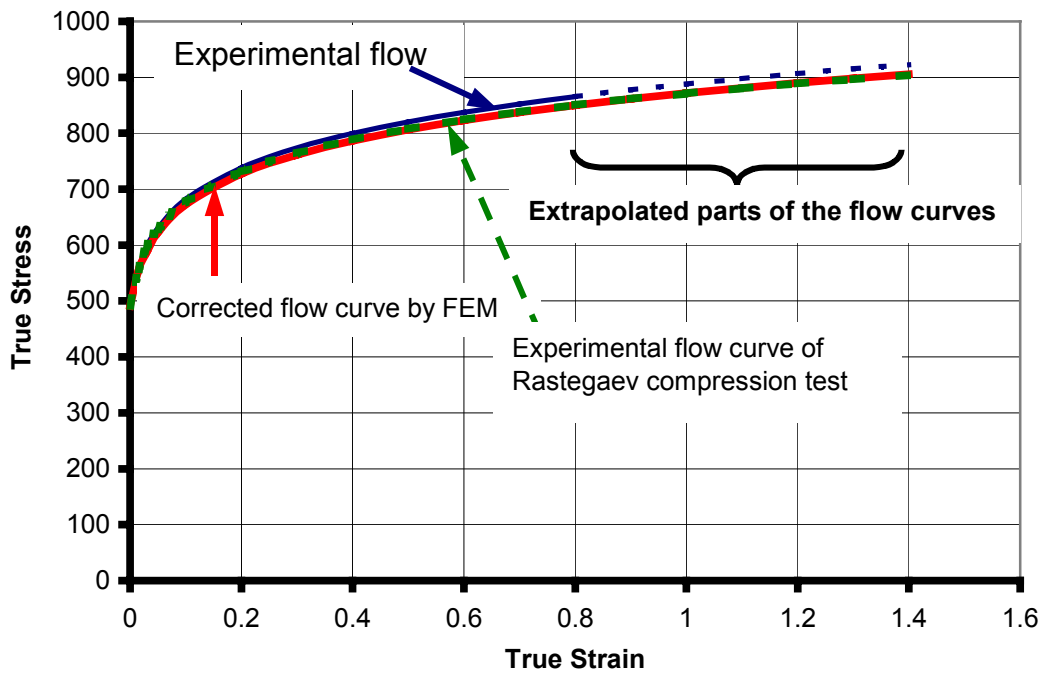
Figure 3.65 Rastegaev, standard and corrected standard compression flow curves of rolled carbon steel

Figure 3.65 shows that corrected flow curve of standard compression test is almost same with flow curve Rastegaev compression test even in the extrapolated region. After this point of the study standard compression test results will be given as corrected flow curves by iterative FEM method.

Compression tests' results performed after drawing and extrusion processes and in rolled is given in Figure 3.66. In this figure there is no difference between Rastegaev and standard compression tests in rolled and extruded states, but in drawn state there is a difference of 20 MPa between the flow curves of standard compression and Rastegaev compression. In extruded state carbon steel also exhibits workhardening stagnation.
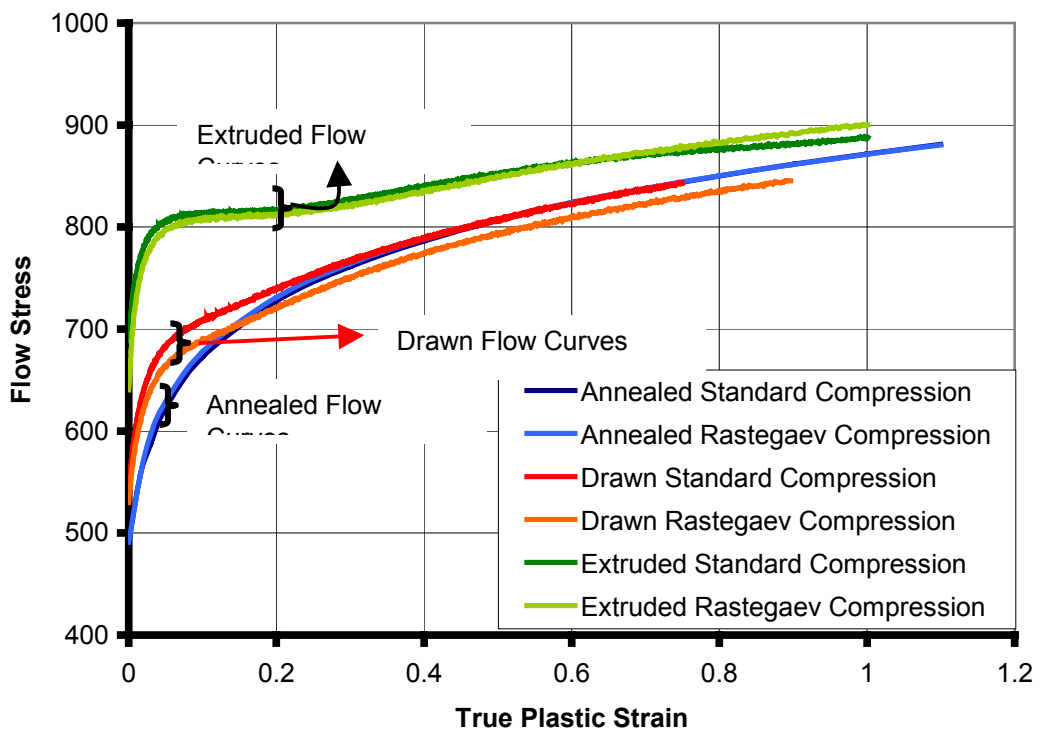
Figure 3.66 Rastegaev and standard compression flow curves of carbon steel in annealed, drawn and extruded state.

In Figure 3.67 only the standard compression tests are shown. Compression flow curves of the drawn and the extruded states are shifted in order to compare them with the annealed flow curve. Shifting amount is taken as the equivalent plastic

strain at the center of the drawn or extruded part. This is a known value, as the reduction ratio is known. The plastic strain can be found as follows,

$$\varepsilon_{pl} = \ln\left(\frac{A_0}{A}\right) = 2\ln\left(\frac{d_0}{d}\right) \tag{3.23}$$

where A_0 and d_0 are initial area and diameters respectively, A and d are formed area and diameters respectively. Although it is known that the plastic strain at the center is the minimum point on the radial distribution of plastic strain of a drawn or extruded part, this strain value is taken only to compare the work-hardened flow curves with the annealed one. Mean plastic strain calculations performed with FEM simulations will be presented in Chapter 4.
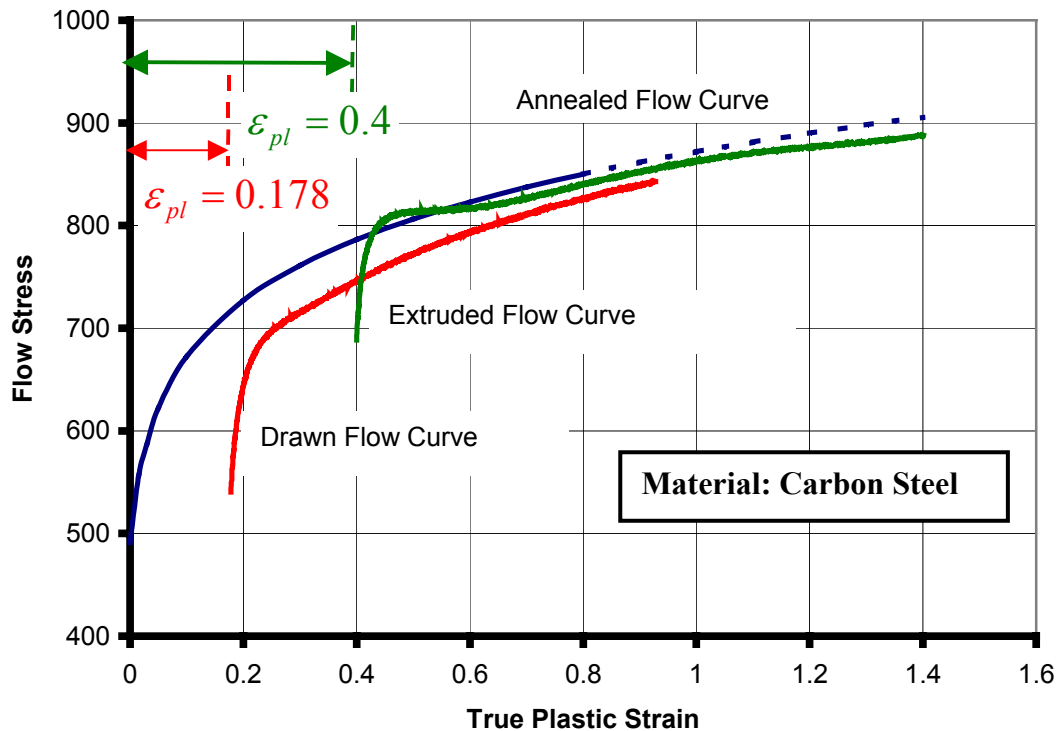
Figure 3.67 Standard compression flow curves of carbon steel in annealed, drawn and extruded state

In compression flow curve of the drawn and extruded state there is an apparent shape change in their initial regions with respect to the rolled state. On the other hand last regions seem to be similar.

Some more experiments were performed to investigate the Bauschinger effect.

Annealed tension sample were first pulled up to 11.2% (just before necking) elongation and then cylinders were cut from the middle section without any radial machining. Then the cylinders having aspect ratio of 1.5 are compressed. The following Figure 3.68 represents the behavior of carbon steel after stress reversal after 11.2% pre-strain.
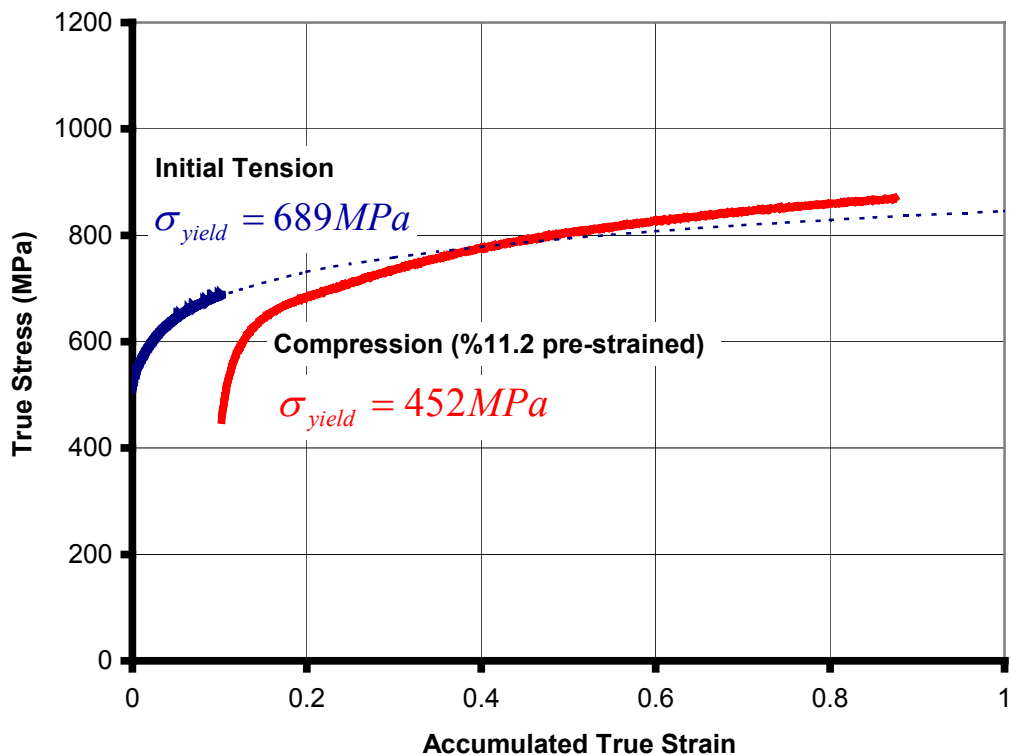
Figure 3.68 Stress reversal after ~0.09 plastic prestrain in tension

In Figures 3.68 it can be seen that with a prestrain, the initial yield strength of the following compression test goes below the initial yield strength of the rolled compression test. This decrease in yield strengths indicates an obvious Bauschinger effect like stainless steel. Because of low necking strain of carbon steel only one prestrained compression test is performed.

3.3.3 Vickers Hardness Results

In this section experimental Vickers hardness distributions will be presented. In Chapter 4 this data will be compared with predicted hardness numbers.

In annealed state it is expected that hardness distribution is homogeneous. Center measurements on axial section give an average Vickers hardness number of 198 kg/mm^2 (Figure 3.69). Radial measurements on axial section (Figure 3.70) change from 190 to 200 kg/mm^2 and radial measurements on radial section are about 192 kg/mm^2.
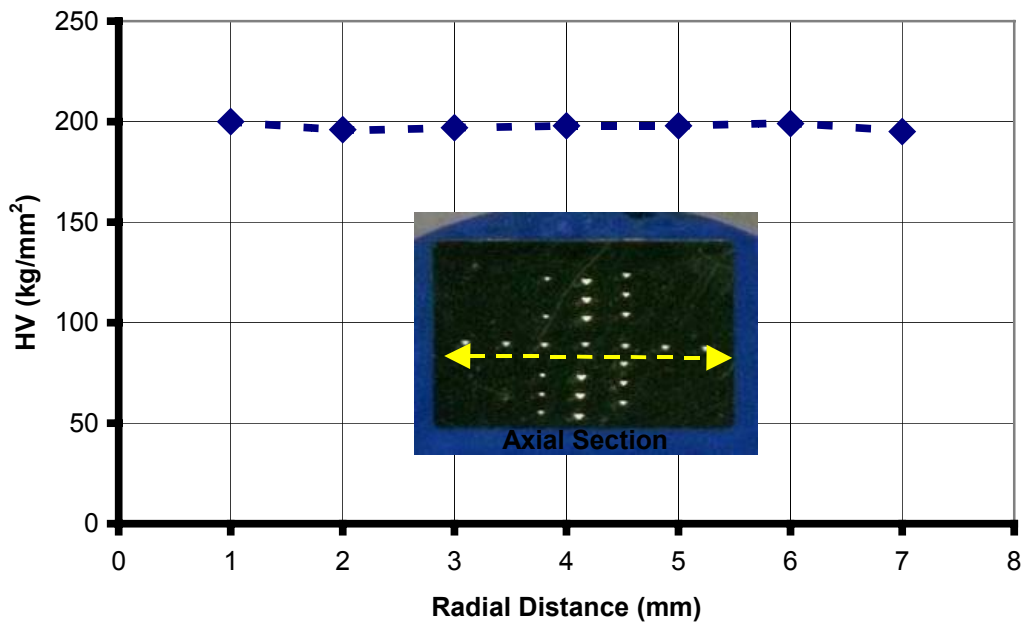
Figure 3.69 Representation of centerline measurements on axial sections of rolled carbon steel
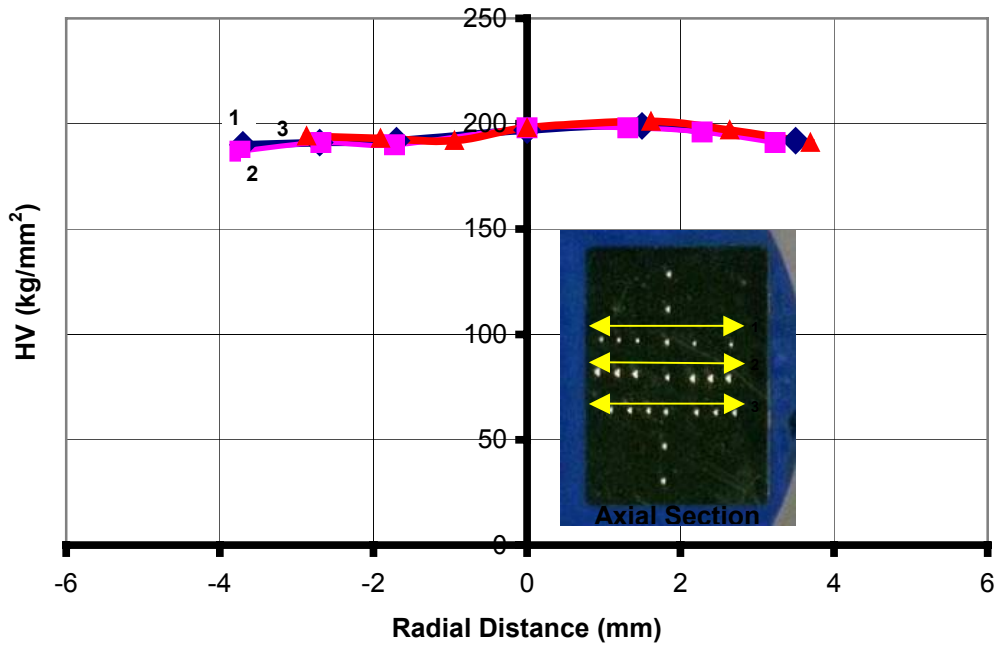
Figure 3.70 Representation of radial measurements on axial sections of rolled carbon steel
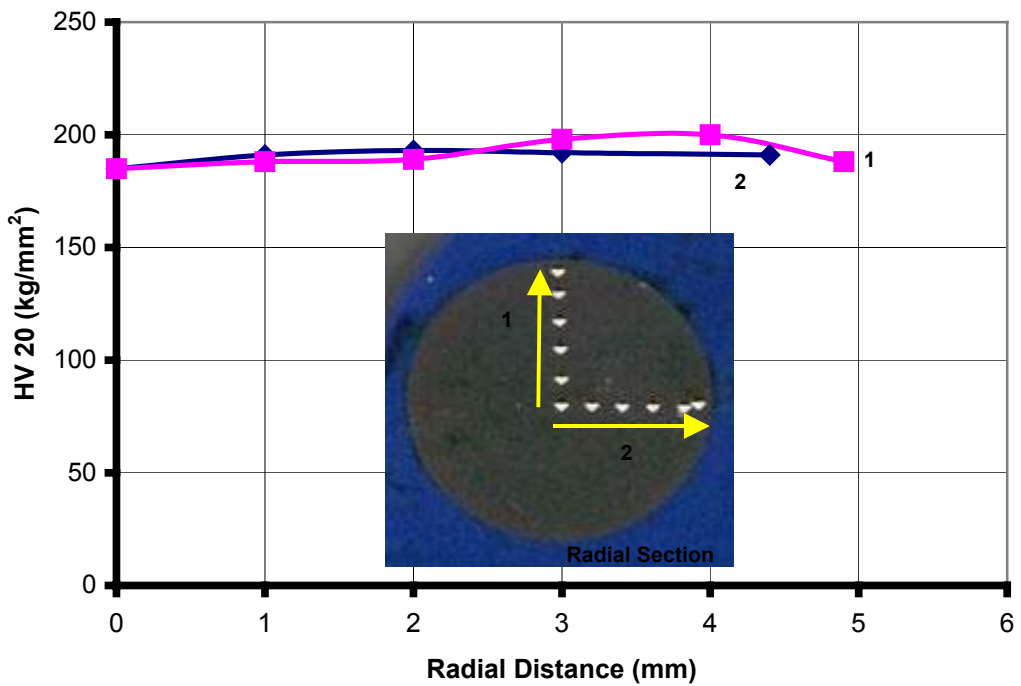
Figure 3.71 Representation of radial measurements on radial sections of rolled carbon steel

Figures 3.72 and 3.74 show radial hardness distributions in radial and axial sections of drawn carbon steel. Radial distributions on radial section change from 218 to 234 kg/mm^2 and this change is between 223 and 230 kg/mm^2 in axial section. Center measurements on axial section give an average Vickers hardness number of 222 kg/mm^2 (Figure 3.73) These values are much smaller when compared with stainless steel because of stainless steel's high hardening coefficient. Although carbon steel has high initial yield strength it has low hardening coefficient. Hence the hardness difference between its strain-hardened states is small.
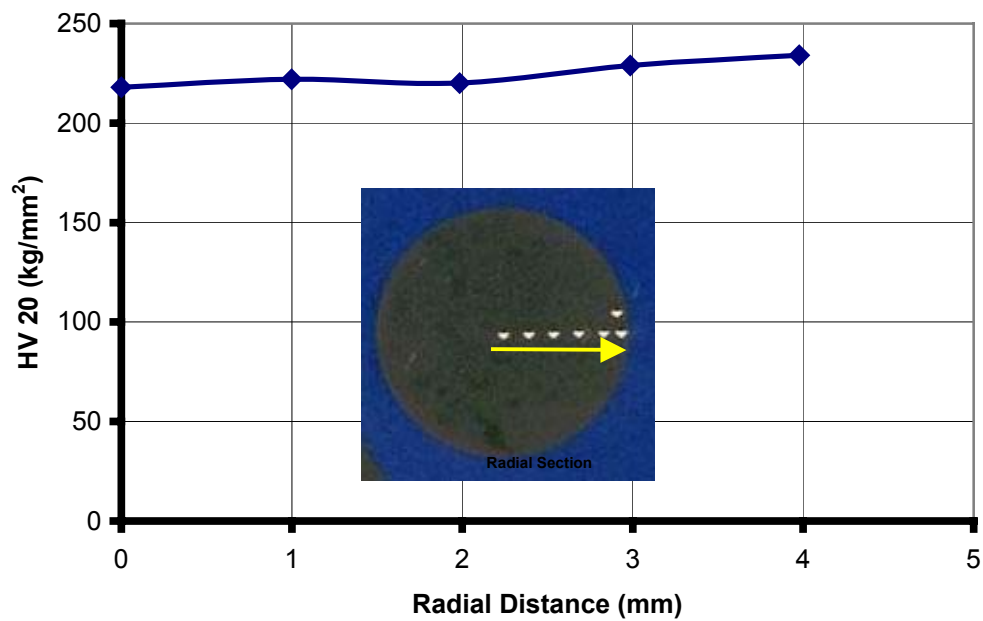
Figure 3.72 Representation of radial measurements on radial sections of drawn carbon steel
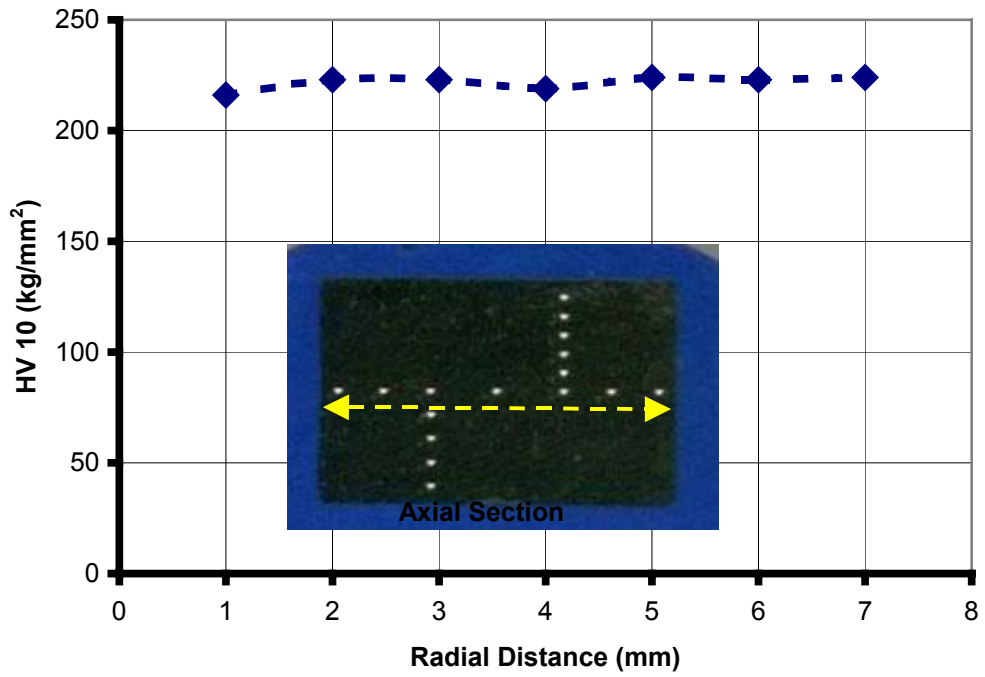
Figure 3.73 Representation of centerline measurements on axial sections of drawn carbon steel
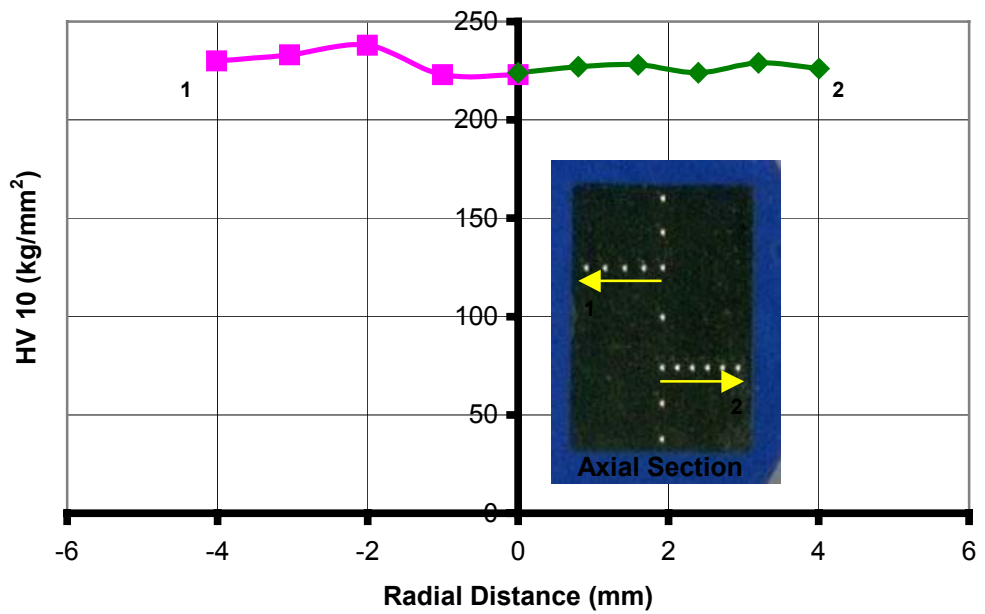
Figure 3.74 Representation of radial measurements on axial sections of drawn carbon steel

126
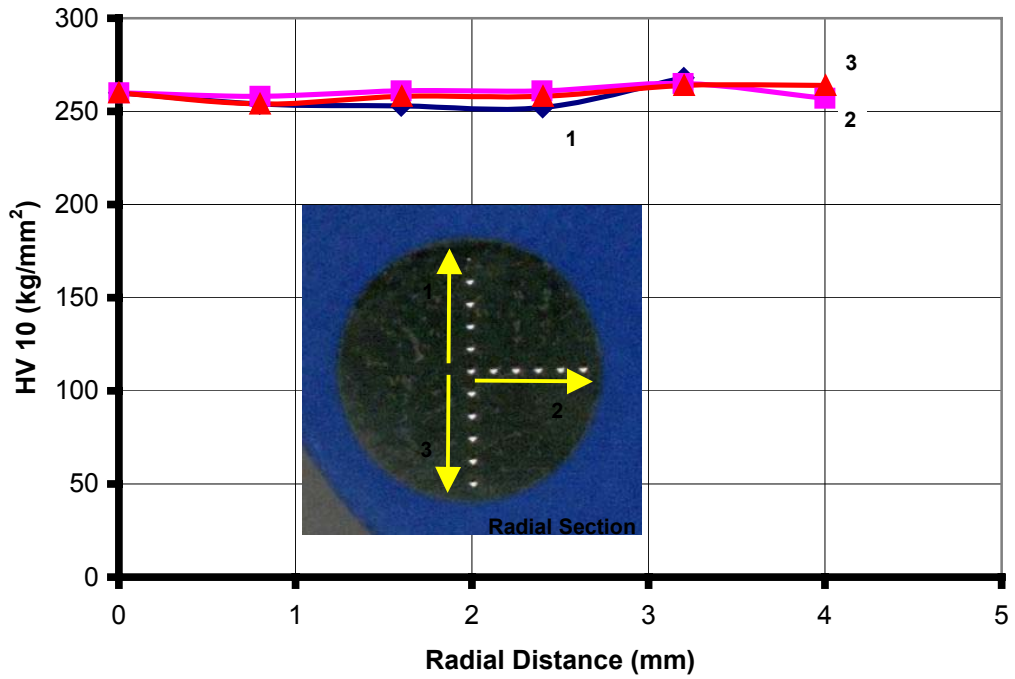
Figure 3.75 Representation of radial measurements on radial sections of extruded carbon steel
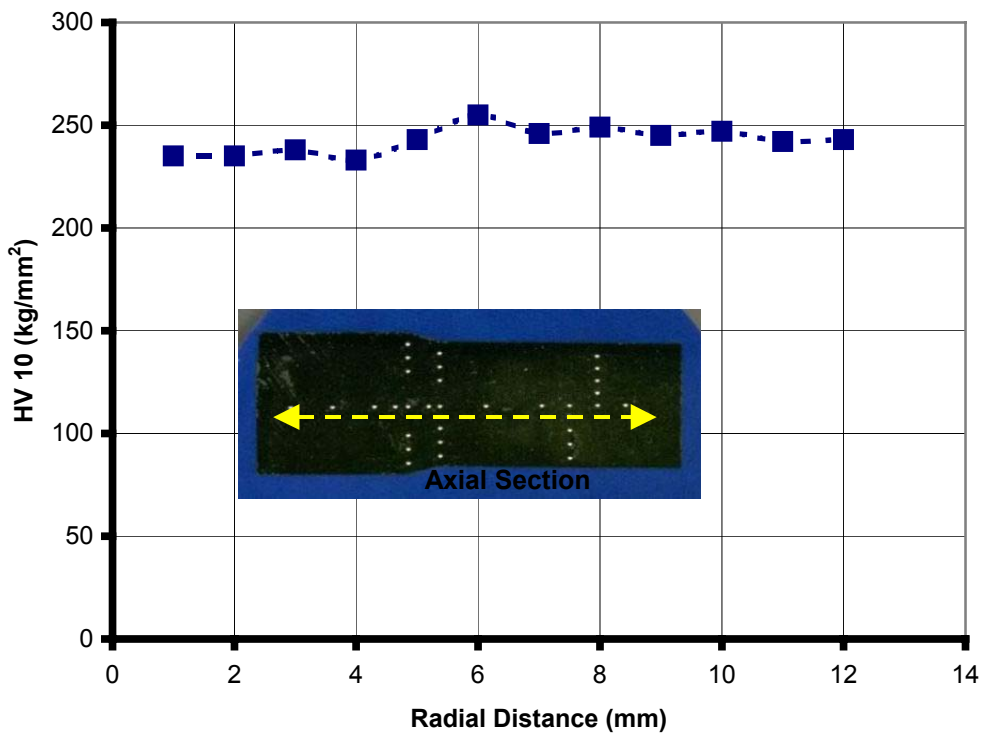
Figure 3.76 Representation of centerline measurements on axial sections of extruded stainless steel
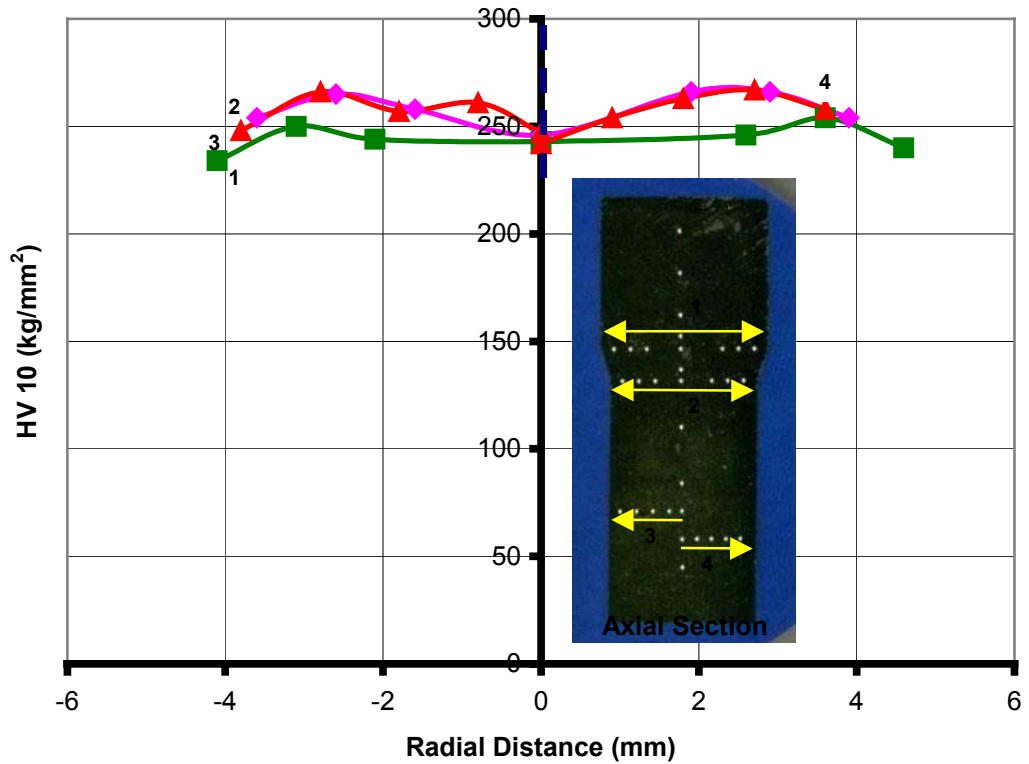
Figure 3.77 Representation of radial measurements on axial sections of extruded carbon steel

Figure 3.76 shows hardness distributions of billet side, deformation zone and extrudate side of axial section of an extruded specimen. Increasing hardness can be seen within the deformation zone. But this increase is very small with respect to stainless steel. For carbon steel the reduction ratio is smaller. Center hardness values change from 235 to 245 kg/mm^2 for centerline on axial section (Figure 3.76). In extrudate side hardness values changes between 242 and 267 kg/mm^2 in radial direction on axial section (Figure 3.77). On the other hand this is about 260 kg/mm^2 in radial section (Figure 3.75).

CHAPTER 4

MODELING OF EXPERIMENTS AND FORMING PROCESSES

4.1   Finite Element Modeling of Forming Processes

In this section finite element modeling of forming processes for production of anchors with two different geometries and material properties will be presented. Although production of an anchor has many forming operations (eg. drawing, extrusion, heading, rolling) only drawing and extrusion will be modeled. Differences between the stainless steel anchor and the carbon steel one are the dimensions of the dies and the material behaviors. The geometry, boundary conditions, material properties used in modeling of two processes will be presented separately.

4.1.1 Geometry

In constructing the geometry of drawing and forward rod extrusion process, a FEM model made by HILTI and the measured dimensions are used. The models for drawing and extrusion are given in Figure 4.1 and 4.2 respectively. Geometry variables like billet diameter (d_{billet}), half die angle (α), die entrance diameter

(d_0), die exit diameter (d_1), fillet radii (r_i) are given in Table 4.1 for drawing and in Table 4.2 for extrusion.
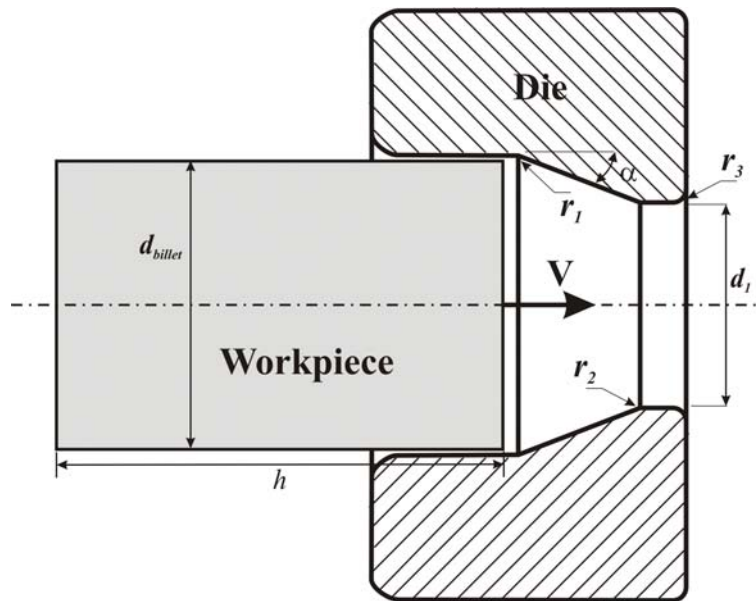
Figure 4.1 Geometry of the wire drawing process

Table 4.1 Material dependent geometry parameter for wire drawing process

Material	α	d_{billet} (mm)	d_1 (mm)	r_1 (mm)	r_2 (mm)	r_3 (mm)	h (mm)
Stainless Steel	10^0	11.5	10.5	0.2	0	0.3	50
Carbon Steel	10^0	11.5	10.61	0.2	0	0.3	50
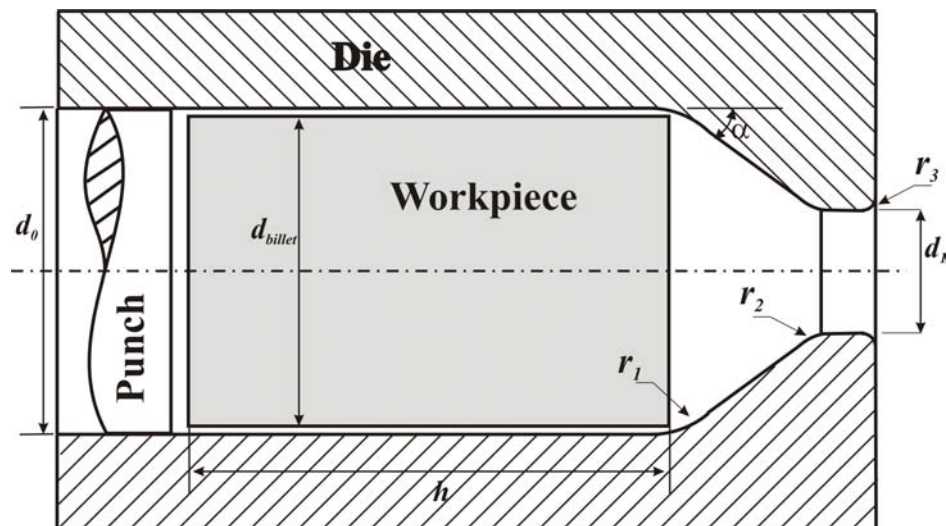
Figure 4.2 Geometry of the extrusion process

Table 4.2 Material dependent geometry parameter for extrusion process

Material	α	d_{billet} (mm)	d_0 (mm)	d_1 (mm)	r_1 (mm)	r_2 (mm)	r_3 (mm)	h (mm)
Stainless Steel	13^0	10.5	10.58	8.34	1.5	0.4	0.3	35
Carbon Steel	15^0	11.61	10.7	9.4	0.2	0.1	0.3	35

Both processes can be modeled as axisymmetric since geometries and loadings are rotational around x-axis. This simplification reduces the model size and number of elements in a great amount as given in Figure 4.3 and 4.4.
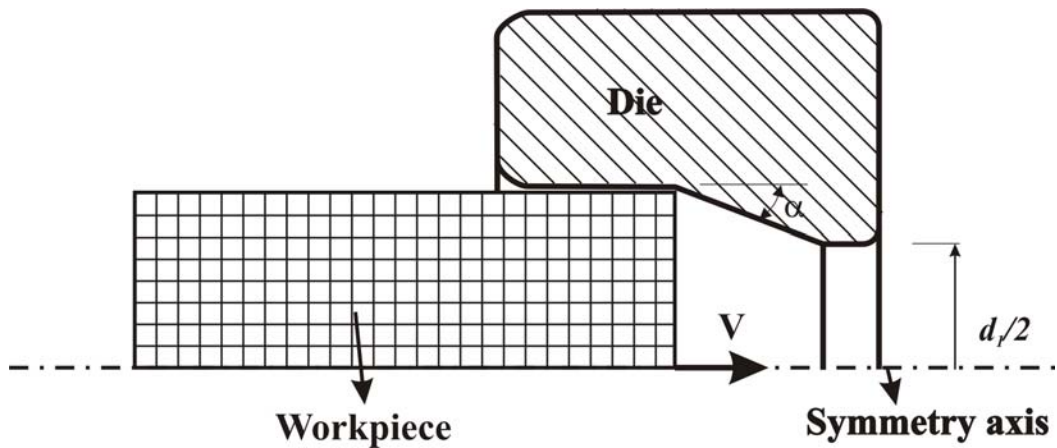
Figure 4.3 Geometry of the drawing process as modeled in MSC/Superform
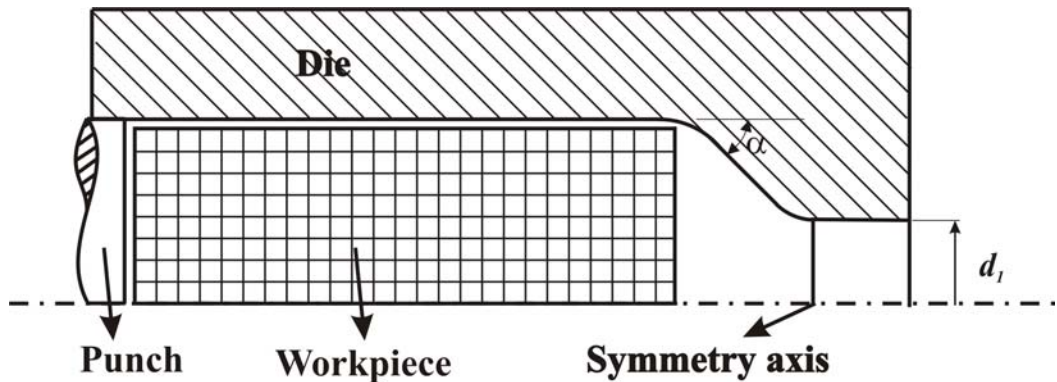
Figure 4.4 Geometry of the extrusion process as modeled in MSC/Superform

4.1.2 Boundary Conditions

Boundary conditions of drawing and extrusion processes are given in Figure 4.5 and 4.6. The workpiece is deforming plastically under the action of prescribed

131

velocities on the surface portion A_v and deforming plastically under the action of prescribed forces on the surface portion A_f. For drawing (Figure 4.5) the surface portion A_{v4} has the velocity V. Surface portions A_{v1}, A_{v2}, A_{v3} have zero velocity in the normal direction to rigid die surface. For extrusion (Figure 4.6) the surface portion A_{v1} has the velocity V_{tool}. Surface portions A_{v2}, A_{v3}, A_{v4} have zero velocity in the normal direction to rigid die surface. Surface portions A_f have zero force.
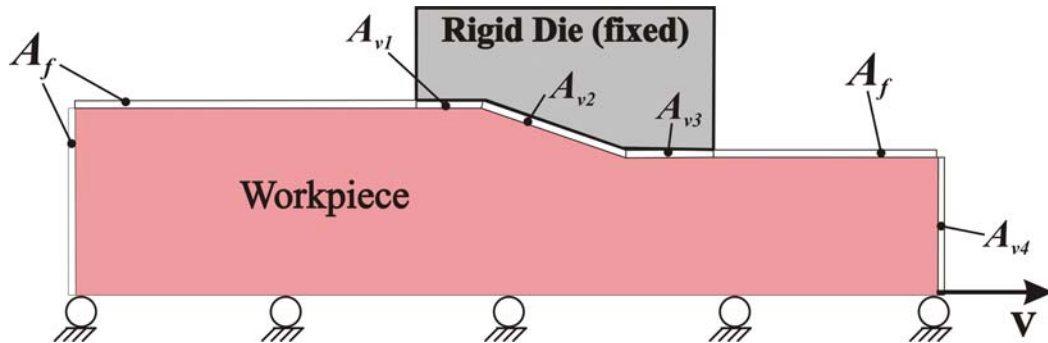
Figure 4.5 Boundary condition of drawing process
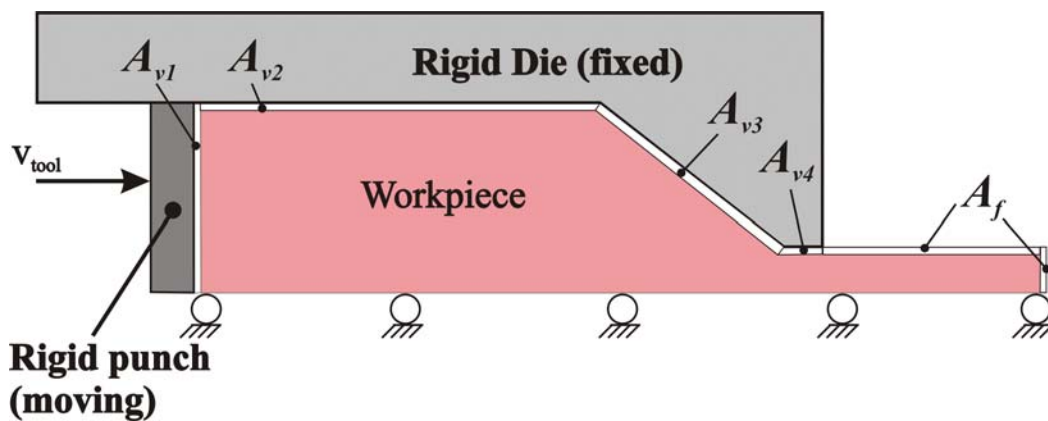
Figure 4.6 Boundary condition of extrusion process

Equivalent plastic strains attained during the drawing process are the initial conditions of the workpiece at the beginning of the extrusion process.

During the simulations Coulomb friction is used. Preliminary studies that were performed by HILTI showed that friction factor is about 0.03-0.04. For the simulations friction factor for drawing is taken as 0.03 and for extrusion is taken as 0.04.

4.1.3   Material Properties

While modeling the axisymmetric drawing and extrusion process, material is assumed to exhibit isotropic hardening and yielding. In the simulations elasto-plastic material model was used. True stress versus plastic strain values are used as the flow stress data of the material in the simulations. Since extrusion results in large deformation and hence large strains, it is necessary to have the flow stress to large values of plastic strain. For stainless steel and carbon steel there are two different flow curves that can be used. These are friction corrected compression and tension flow curves for each material as given in Figure 4.7 and 4.8. They are experimentally obtained curves that are discussed in Chapter 3. In each graph represented compression flow curves are friction corrected flow curves.

The graph shows flow stress versus plastic strain with the following labels:

- **Compression Flow Curve**, $\dot{\overline{\varepsilon}}_{compression} = 2 \times 10^{-2} s^{-1}$
- **Tension Flow Curve**, $\dot{\overline{\varepsilon}}_{tension} = 1 \times 10^{-4} s^{-1}$
- **Stainless Steel Annealed**

Axes: Flow Stress (MPa) versus Plastic Strain
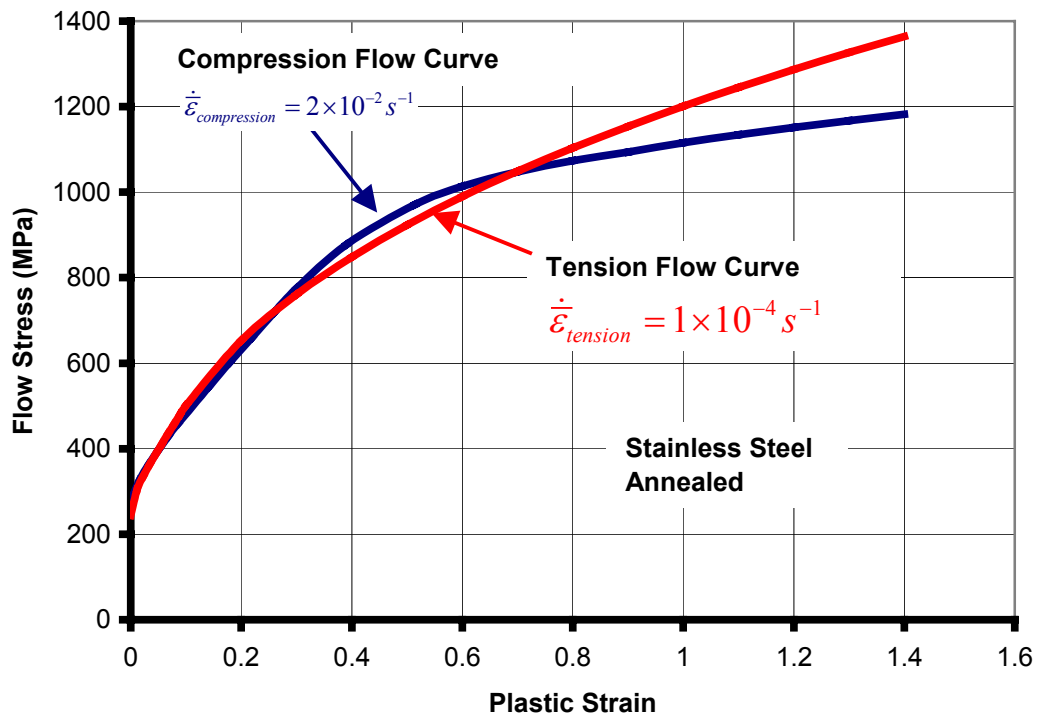
Figure 4.7 Compression and tension flow curves for annealed stainless steel
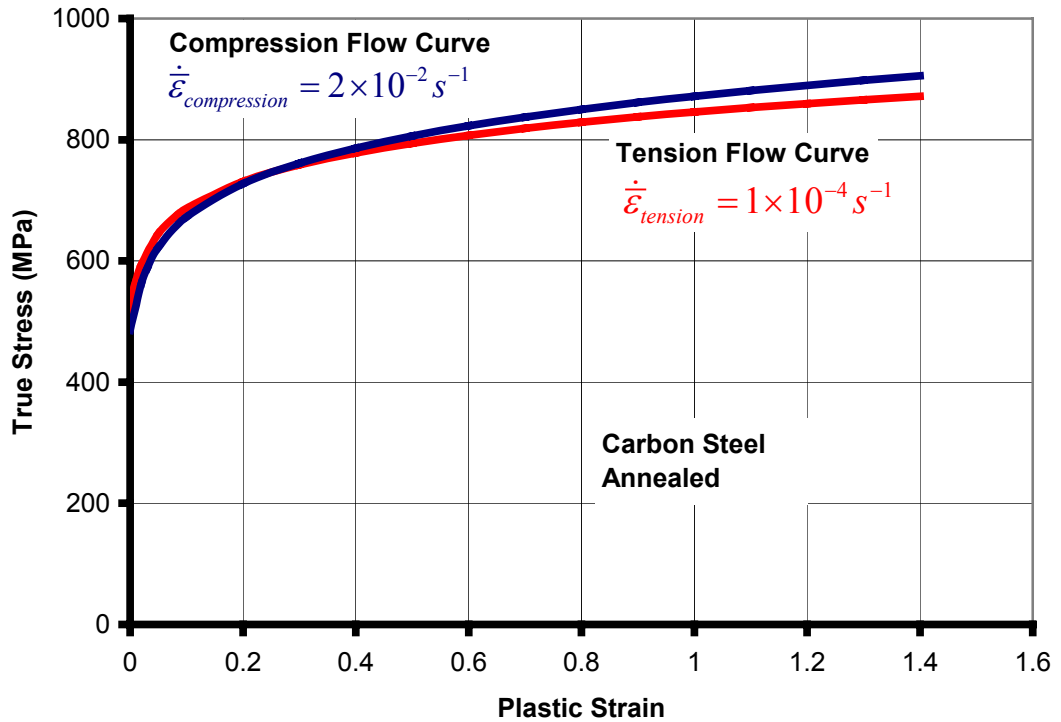
Figure 4.8 Compression and tension flow curves for annealed carbon steel

From Figure 4.7 it can be seen that compression flow curve of stainless steel is going below the tensile flow curve after plastic strain of 0.7. In Figure 4.8 compression and tension flow curves of carbon steel seem to be very close although they are getting apart from each other with increasing strain.

4.1.4 Simulation Results for Stainless Steel

In this section general course of operation used in the model will be presented and radial distribution of equivalent plastic strain will be given. A general view of model of the drawing and extrusion process can be seen in Figure 4.9.
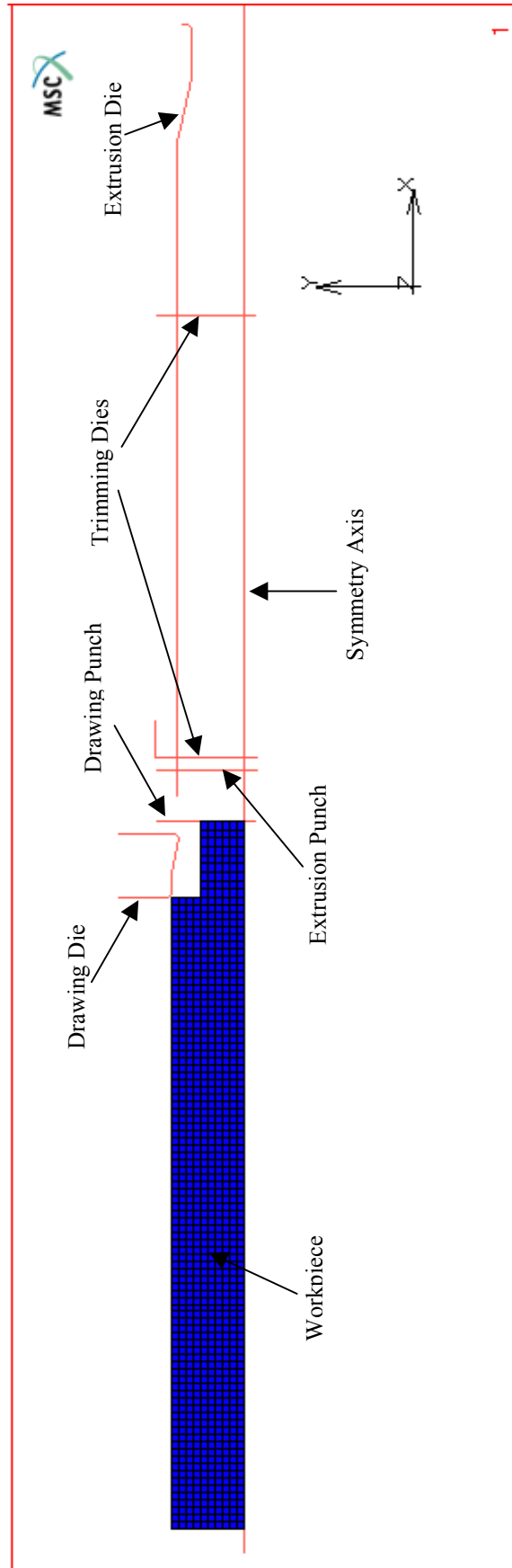
Figure 4.9 Axisymmetric model of extrusion after drawing in MSC/Superform

Extrusion Die

Trimming Dies

Drawing Punch

Drawing Die

Extrusion Punch

Symmetry Axis

Workpiece

Drawing punch is fixed to the out-going surface of the workpiece as shown in Figure 4.9. This is primarily done in order to take punch force as an output for the comparison with real forces. But this comparison could not be possible since real forces are not available. Fixing a rigid die instead of giving a displacement boundary condition to each node on the pulling side will provide ability of remeshing the workpiece. Dies and punches used in simulations are modeled as rigid tools. A constant velocity of 1 mm/s is given to both drawing and extrusion punch. Figure 4.10 (a) and (b) shows the final shape and strain distribution after drawing and extrusion process respectively for stainless steel. Also in the same figure geometric strain values on the center of the workpiece are given. This strain value is the minimum value within radial distribution of equivalent plastic strains. Maximum strain is located on the surface or near to the surface.

These simulations are performed by using both compression and tension flow curve. But both simulations gave the same strain distribution for the drawn and extruded workpiece. Radial distribution of equivalent plastic strain on the reduced section of drawn and extruded workpiece are given in Figure 4.11.

Figure 4.11 shows that compression and tensile material flow data is not affecting the strain distribution. The major variables for strain distribution is geometry of the die and the coefficient of friction and those are same for both flow curves. These data will be the primary data to obtain hardness values with the related correlation formulas and compare them with the experimental ones. In Figure 4.11 average plastic strain values of the radial distribution are also shown. This will be compared with the amount of shifting the strain-hardened experimental flow curve data, and as well as the simulated data. Three methods are used for obtaining average of equivalent plastic strain distribution. These are arithmetical average, area based average and volume based average. Arithmetical average can be given as

$$\frac{\sum \varepsilon_i}{\# \text{ of data}} \tag{4.1}$$
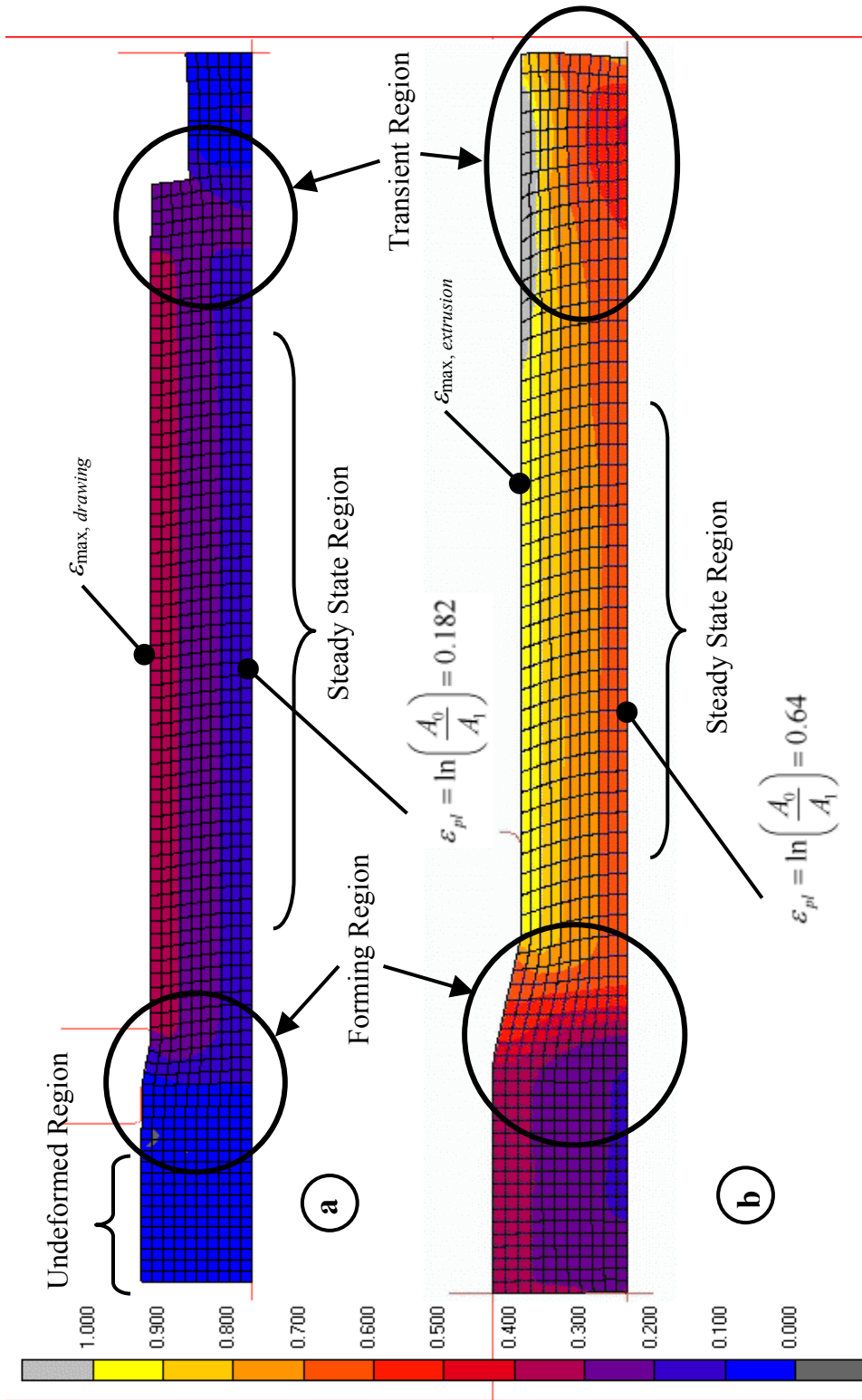
Figure 4.10 Final equivalent plastic strain distribution and regions of workpiece after (a) drawing and (b) extrusion process for stainless steel

Area based average values are calculated by the below formula

$$\frac{\int \varepsilon_{pl}(r)dr}{r_{max}} \qquad (4.2)$$

This is also similar for volume based average which can be represented by

$$\frac{\int \varepsilon_{pl}(r)dA}{A_{max}} \qquad (4.3)$$

Through out the study area based average values will be represented on the graphs.
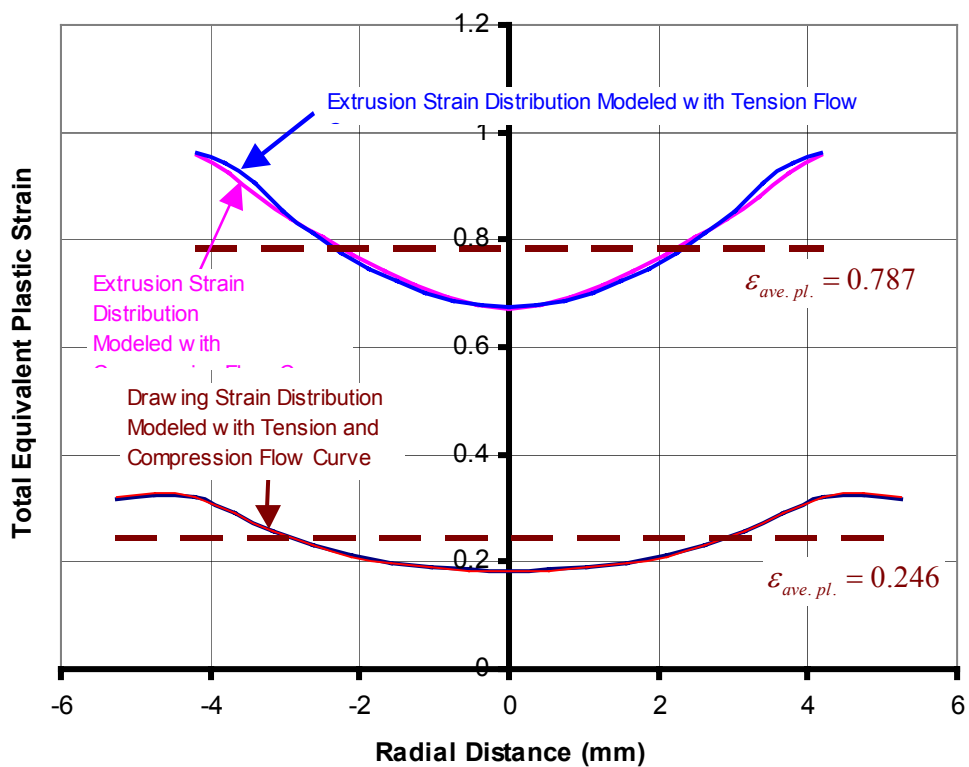
Figure 4.11 Radial distribution of equivalent plastic strain in the drawn and extruded cross-sections for stainless steel

In real case the drawn workpiece are cut into predefined lengths for the process of extrusion. In the model this is done by a trimming process, which is a defined option in MSC/Superform. This tool is basically designed for removing flash like unwanted material without giving any plastic strain for the following process. In

our model it is used for obtaining preferable geometry for extrusion after drawing and desired workpiece dimensions for compression and tension tests after forming processes. Figure 4.12 shows the trimming process on the drawn part. It can be seen that there is no plastic strain change on the trimmed workpiece. Used trimming option does not allow complex geometries of trimming dies so this process can be performed by two trimming operations (Figure 4.12 (b) and (c)). After two trimming operations the workpiece is ready for extrusion process (Figure 4.12 (d)).

Major parameters used for finite element simulations of drawing and extrusion processes are given in Table 4.3. Relative residual check is used as a convergence criterion for all simulations.

Table 4.3 Parameters of FEM for drawing and extrusion processes of stainless steel

	Process	
	Drawing	**Extrusion**
Number of Elements	924	770
Step Size (mm)	0.1	0.08
Convergence Limits	0.05	0.05
Element Edge Length (mm)	0.5	0.45

4.1.5   Simulation Results for Carbon Steel

Model used for carbon steel is principally the same as used for stainless steel. The differences are in die dimensions and flow curves used. So this changes the strain distribution. These models also give the same strain distribution for compression and tension flow curve of compression flow curve as represented in Figure 4.13. Reduction in stainless steel is larger especially in extrusion so strains are larger than carbon steel.

Major parameters used in finite element simulations of drawing and extrusion processes are given in Table 4.4.
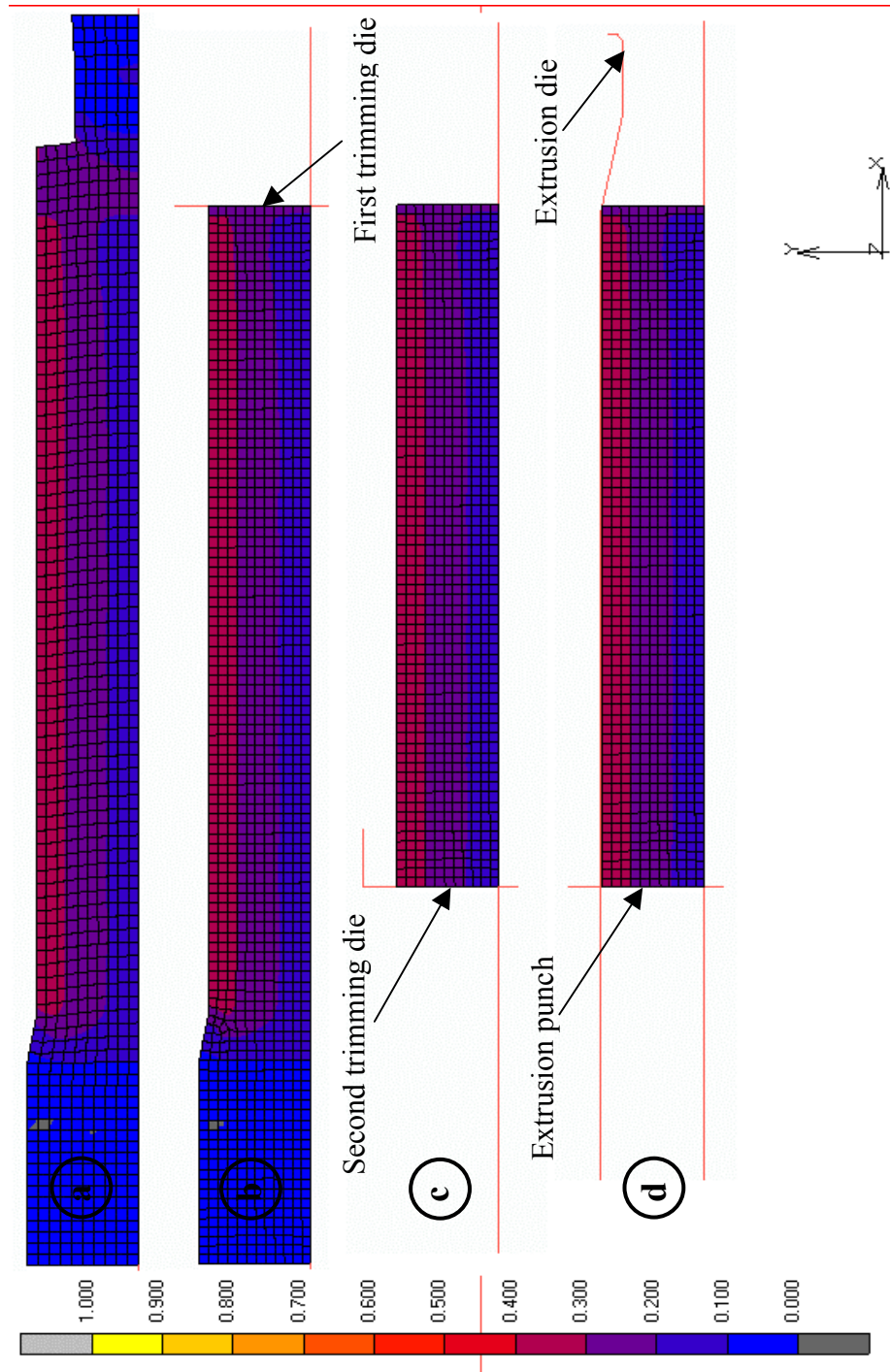
Figure 4.12 Two trimming processes of drawn workpiece for extrusion process for stainless steel

Table 4.4 Parameters of FEM for drawing and extrusion processes of carbon steel

	Process	
	Drawing	**Extrusion**
Number of Elements	924	770
Step Size	0.1	0.1
Convergence Limits	0.05	0.05
Element Edge Length	0.5	0.45
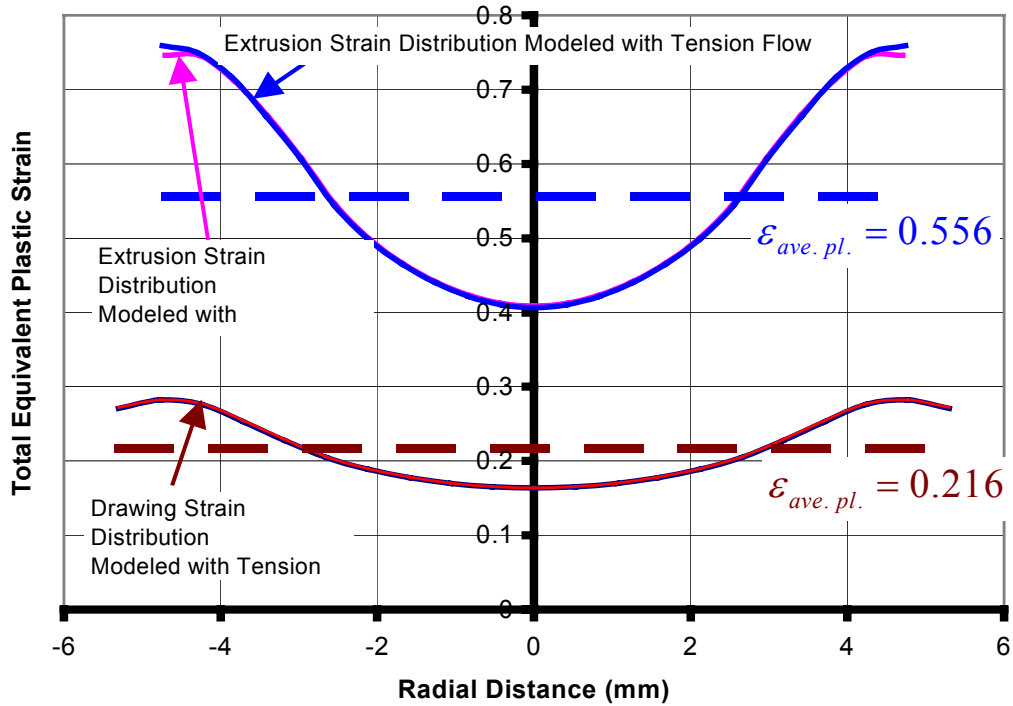
Figure 4.13 Radial distribution of equivalent plastic strain in the drawn and extruded cross-sections for carbon steel

4.2 Finite Element Modeling of Experiments After Forming Processes

Modeling of standard compression and tension tests after forming processes is done in order to compare experimental flow curves with flow curves obtained from simulations. FEM will also provide us the shifting amount of the non-homogenously strain-hardened specimen's flow curve in order to compare it with the annealed flow curve. One other reason for modeling is to see whether there

will be a shape change in the flow curve because of the non-homogenous strain distribution. The results will also represent the difference between perfectly isotropic material in yielding and hardening and a real material that may be both anisotropic in yielding and hardening. The models of the experiments that are performed are tabulated in Table 4.5 for both materials.

Table 4.5 shows that each experiment model uses its own flow curve. This means that for a compression experiment model compression flow curve is used but the former processes can be modeled with either tension or compression flow curve. Table 4.5 contains experiment numbers that are used in this section to refer the experiment with former processes and material flow curves tabulated in the table.

Table 4.5 Experiments modeled after drawing and extrusion processes with different flow curves

	Model	Process	Experiment after forming process		Process	Experiment after forming process
		Drawing	Compression	Tension	Extrusion	Compression
Material Data Used	1	Tension	Compression	-	-	-
	2	Tension	-	Tension	-	-
	3	Compression	Compression	-	-	-
	4	Compression	-	Tension	-	-
	5	Tension	-	-	Tension	Compression
	6	Compression	-	-	Compression	Compression

After forming process for obtaining the test specimen geometry again trimming is used. For tension modeling quarter geometry of the workpiece is used as seen on the Figure 4.14. Two boundary conditions are given to the workpiece: One is zero velocity in x direction to the nodes on the left surface of the workpiece and the other is 1 mm/s velocity in x direction to the nodes on the right surface of the specimen. As there is no punch in the model, force data is collected as a sum of the reaction forces of the nodes on the right surface of the specimen.
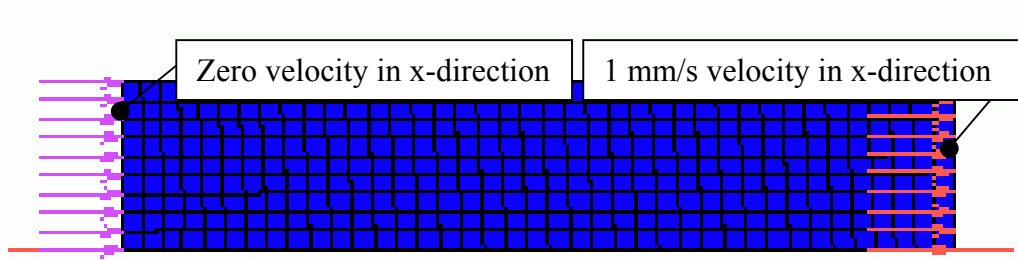
Figure 4.14 Boundary conditions of tension test for stainless steel

For compression modeling in axisymmetric model of full geometry of the workpiece is used as seen on the Figure 4.15 shows the deformed shape and strains of the workpiece between dies having friction coefficient of 0.1 for stainless steel. For carbon steel this friction factor is taken as 0.06. These are experimentally obtained value from ring compression tests as discussed in Chapter 3.
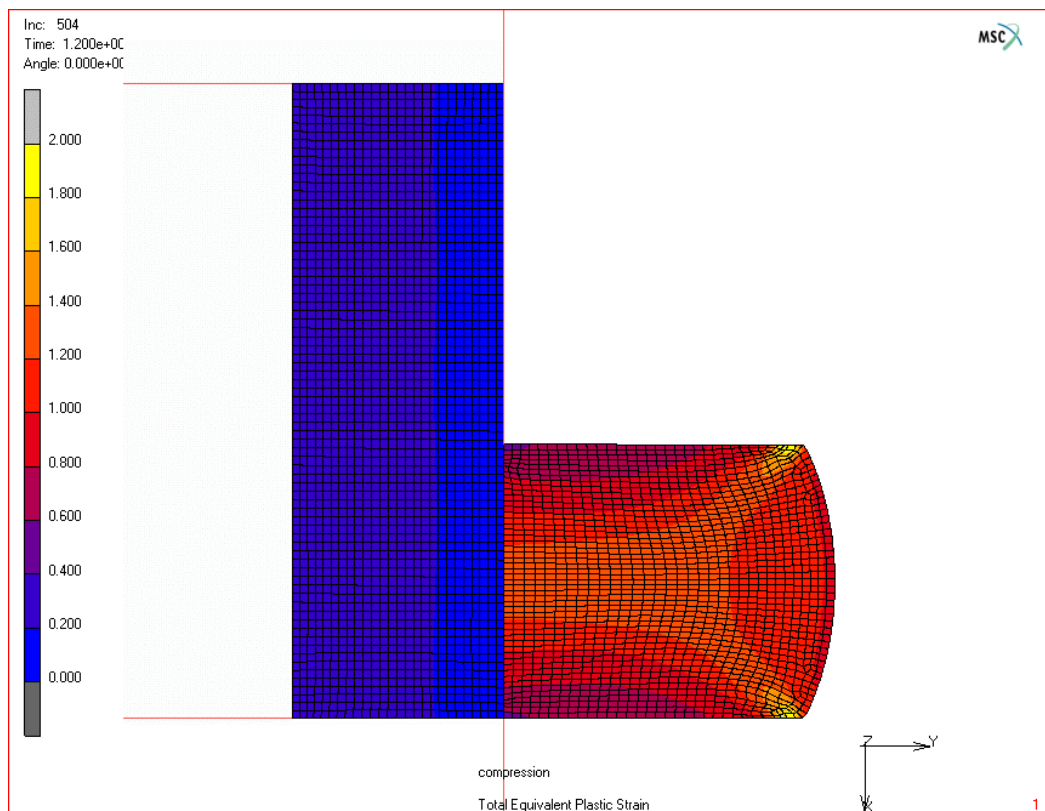
Figure 4.15 Undeformed and deformed compression workpiece after drawing process for stainless steel

4.2.1 Stainless Steel Results

In the previous section it is shown that the radial strain distribution is same although different material flow curves are used. This is why first and third experiments results are same. And similarly this is true for second and forth experiments and fifth and sixth experiments as plotted in Figure 4.16. Initial region of the flow curves plotted in Figure 4.16 seem to be smooth. There is no observable shape change as there is in the experimental flow curves. Simulated compression flow curves plotted on Figure 4.16 are not friction corrected flow curves and they will be compared with not friction corrected experimental compression flow curves through out this chapter.
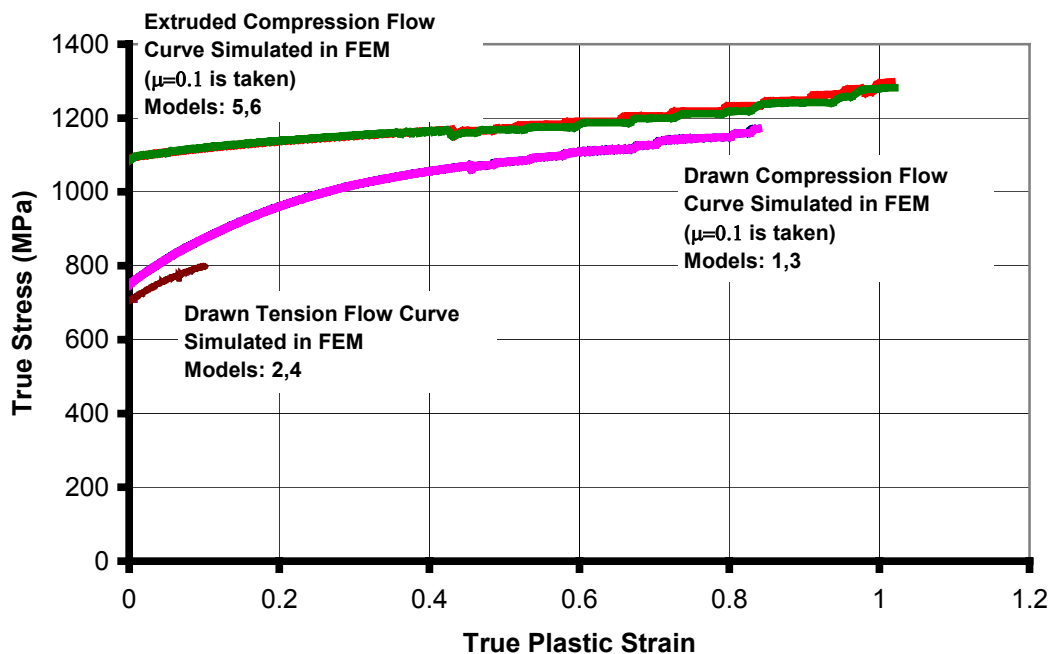
Figure 4.16 Results of flow curves obtained from compression and tension experiments modelled with FEM

Figure 4.17 shows the radial distribution of the equivalent plastic strain on the undeformed workpieces for compression and tension experiments modeled in FEM and area based average plastic strain of this strain distribution. This average strain distribution will be compared with simulations.

144

Major parameters for finite element simulations of compression and tension tests after drawing and extrusion processes are given in Table 4.6.

Table 4.6 Parameters of FEM for compression and tension tests after drawing and extrusion processes of stainless steel

	Process		
	Compression After Drawing	**Tension After Drawing**	**Compression After Extrusion**
Number of Elements	1950	351	1302
Step Size	Adaptive Stepping	0.025	Adaptive Stepping
Convergence Limits	0.01	0.01	0.01
Element Edge Length	0.2	-	0.2

Figure 4.18 compares the simulated compression flow curve of drawn stainless steel with the experimental one. At the very beginning of the experimental flow curve effect of Bauschinger can be seen. After this low yielding experimental flow approaches to the simulated curve and then a deviation from simulated curve appears. Through the end of the curve this deviation decreases and curves approaches to each other.
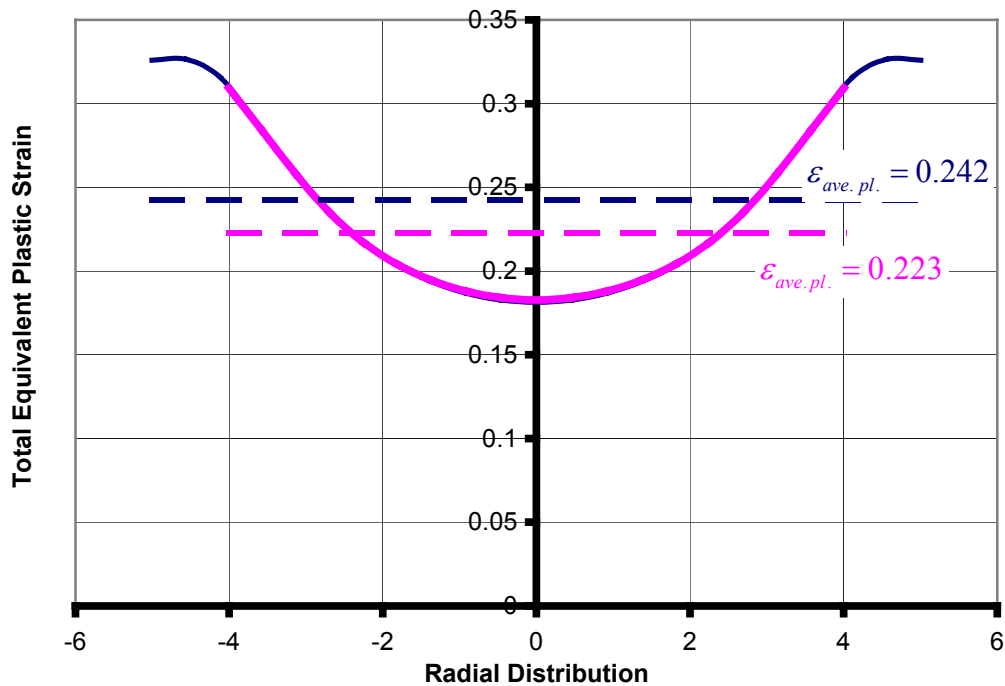
Figure 4.17 Radial strain distribution of the undeformed compression and tension specimens after drawing for stainless steel

145

Figure 4.19 shows that for stainless steel the amount of shifting of the drawn compression flow curve should be $\varepsilon_{pl} = 0.275$ in order to compare it with the annealed flow curve. This shifting is basically done by moving the workhardened flow curve in x-direction until its first point touches the annealed flow curve.

Figure 4.20 shows the simulated tension flow curve of drawn stainless steel with the experimental one. Both curves are parallel with each other. Simulated flow curve is 12 MPa higher than the experimental one. This can be logical because flow directions of both process (drawing and tension) is similar, so it is not surprising not to see the effect of anisotropic hardening. The little deviation may be a result of misjudgment of friction on the dies.

Figure 4.21 shows that for stainless steel the amount of shifting of the drawn tension flow curve should be $\varepsilon_{pl} = 0.243$ in order to compare it with the annealed curve. This value is nearly same with the experimentally found value ($\varepsilon_{pl} = 0.232$) in Chapter 3.
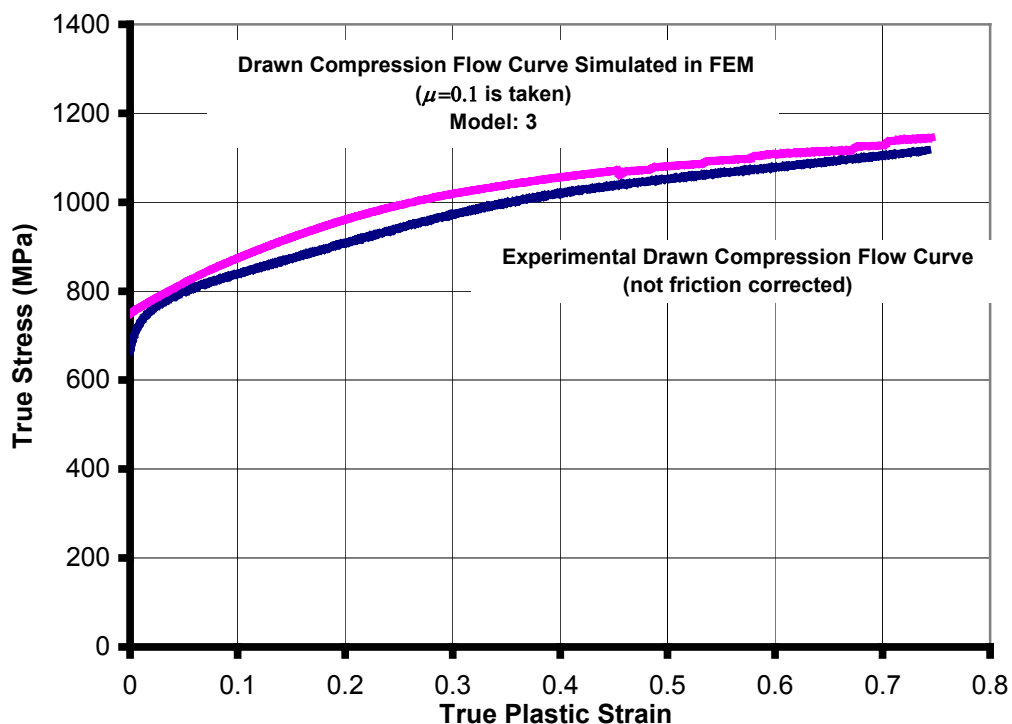
Figure 4.18 Experimental and simulated results for drawn compression test of stainless steel

Figure 4.19 Shifted drawn compression flow curve obtained from FEM for stainless steel
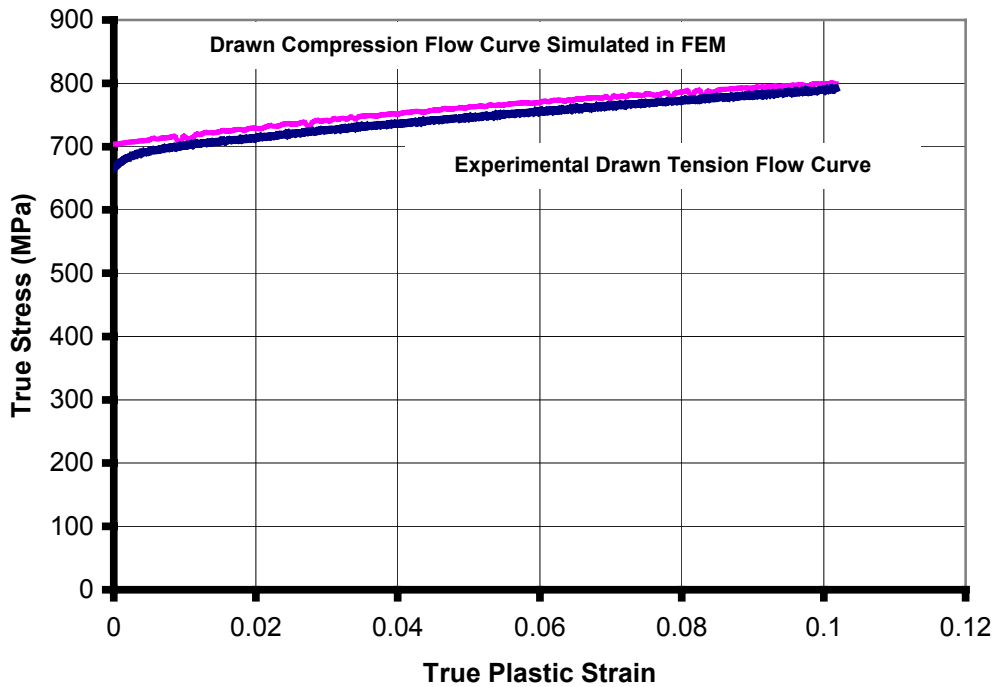
Figure 4.20 Experimental and simulated results for drawn tensile test of stainless steel

147
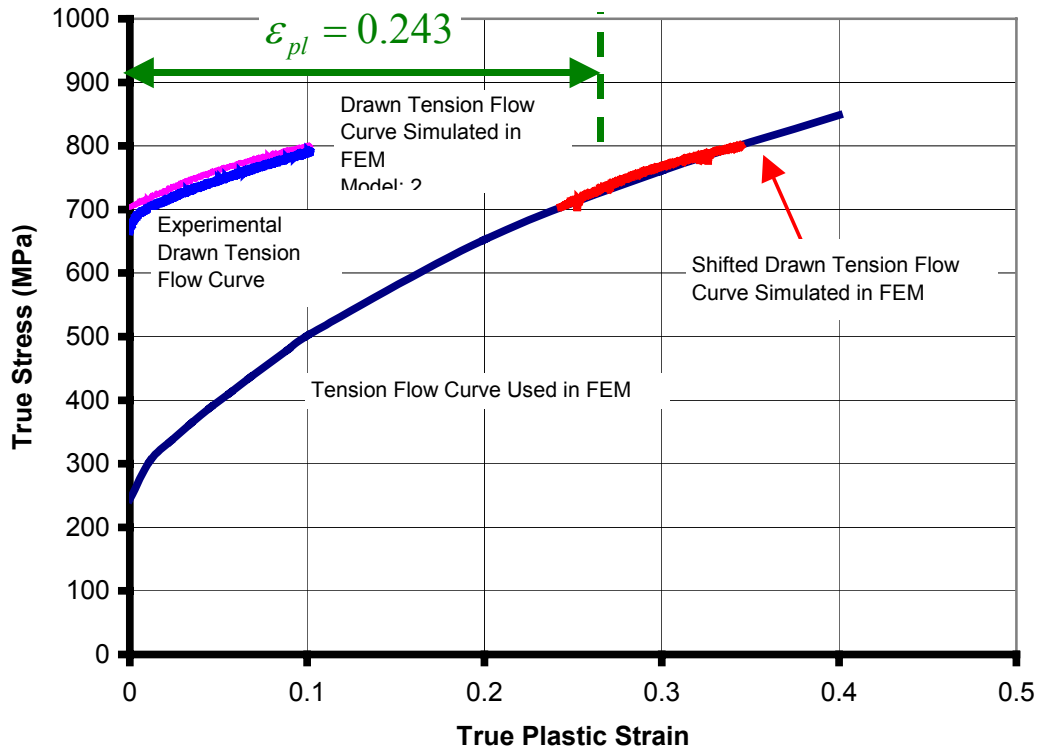
Figure 4.21 Shifted drawn tension flow curve obtained from FEM for stainless steel

Figure 4.22 shows the simulated compression flow curve of extruded stainless steel with the experimental one. In this state it possible to see the exaggerated form of the drawn state. At the beginning of the curves it should be noted that with increasing amount of deformation the difference between the simulated and the experimental flow curves increases. This means that Bauschinger effect increases. Through the end of the curves experimental flow curve also approaches to simulated one like in drawn state.

Figure 4.23 shows that for stainless steel the amount of shifting of the extruded compression flow curve should be $\varepsilon_{pl} = 0.84$ in order to compare it with the annealed curve.
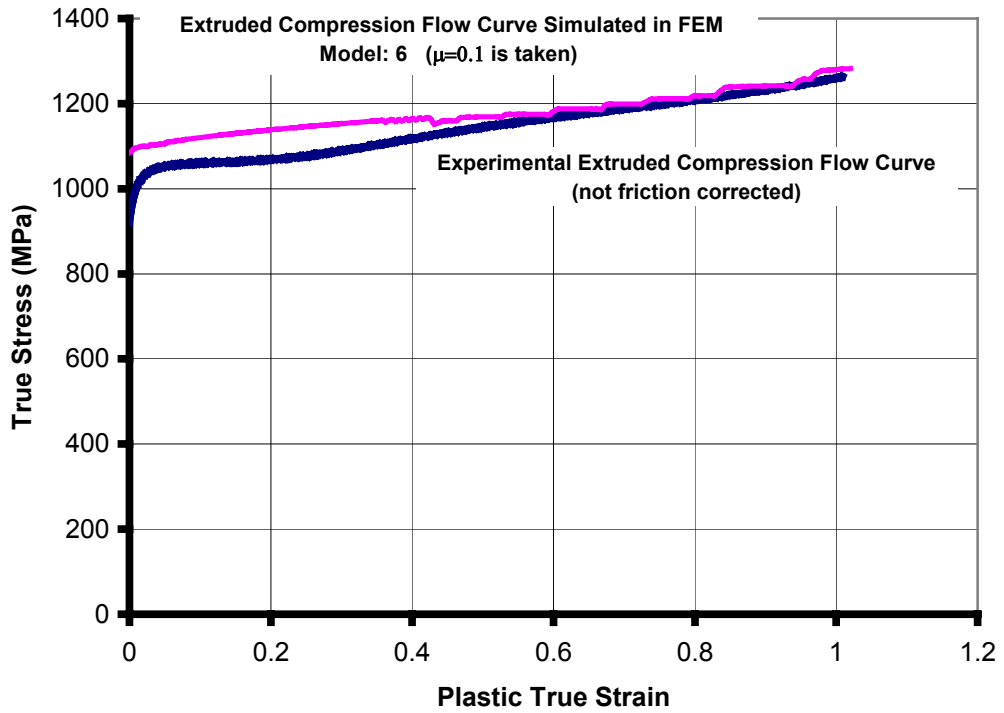
Figure 4.22 Experimental and simulated results for extruded compression test of stainless steel
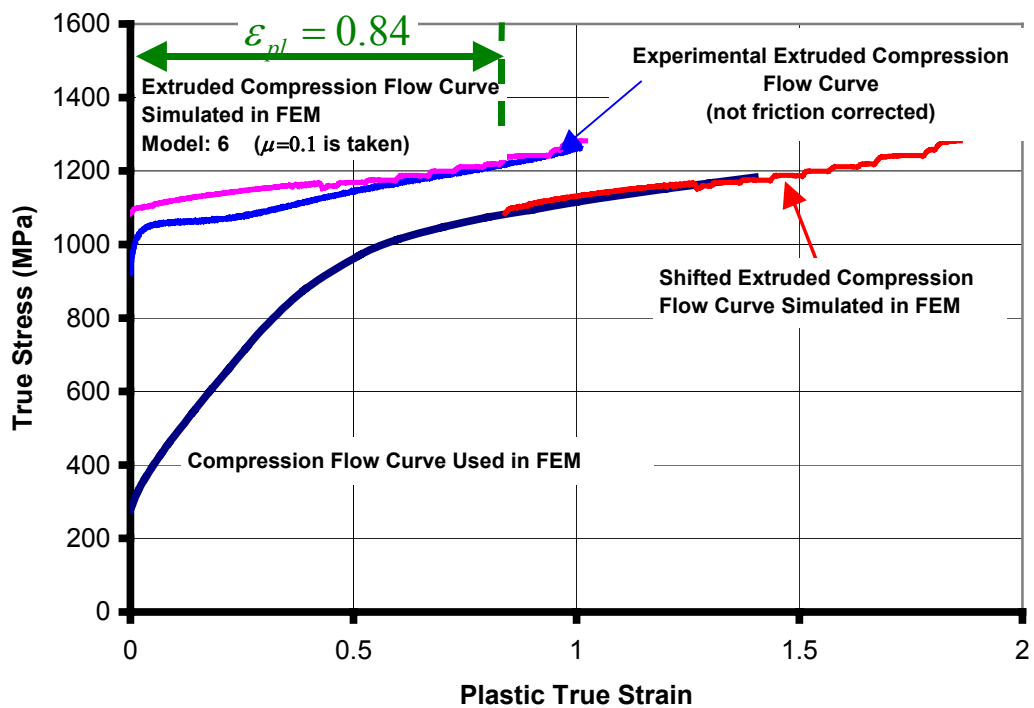
Figure 4.23 Shifted extruded compression flow curve obtained from FEM for stainless steel

Table 4.7 gives a general comparison of three different types of average values with the shifting strain required to locate simulated flow curve for the related test on the annealed flow curve. The average values are obtained from the graphs plotted on Figures 4.11 and 4.17. From Table 4.7 it can be seen that volume based average is similar with simulation results. This is not surprising since the pressure on compression test is inversely proportional with area under it.

Table 4.7 Average of radial distribution of equivalent plastic strain on undeformed compression and tension specimens at different states for stainless steel

	Specimen		
	Drawn Compression	**Drawn Tension**	**Extruded Compression**
Geometric Strain $\left(\ln\left(A_0/A\right)\right)$	0.182	0.182	0.64
Arithmetical Average	0.244	0.226	0.789
Area Based Average	0.242	0.223	0.787
Volume Based Average	0.272	0.244	0.836
Shifting Required in Simulation	0.275	0.243	0.84

4.2.2 Carbon Steel Results

As already discussed in previous sections changing material flow curve doesn't change strain distribution much. So using compression or tension flow curve doesn't change simulated compression flow curves as shown in Figure 4.24. Also there is no observable shape change as there is in the experimental flow curves for carbon steel.

Figure 4.25 gives the radial strain distribution of the undeformed workpiece for compression experiment modeled in FEM and average plastic strain of this strain distribution. This average strain distribution will be compared with simulations.
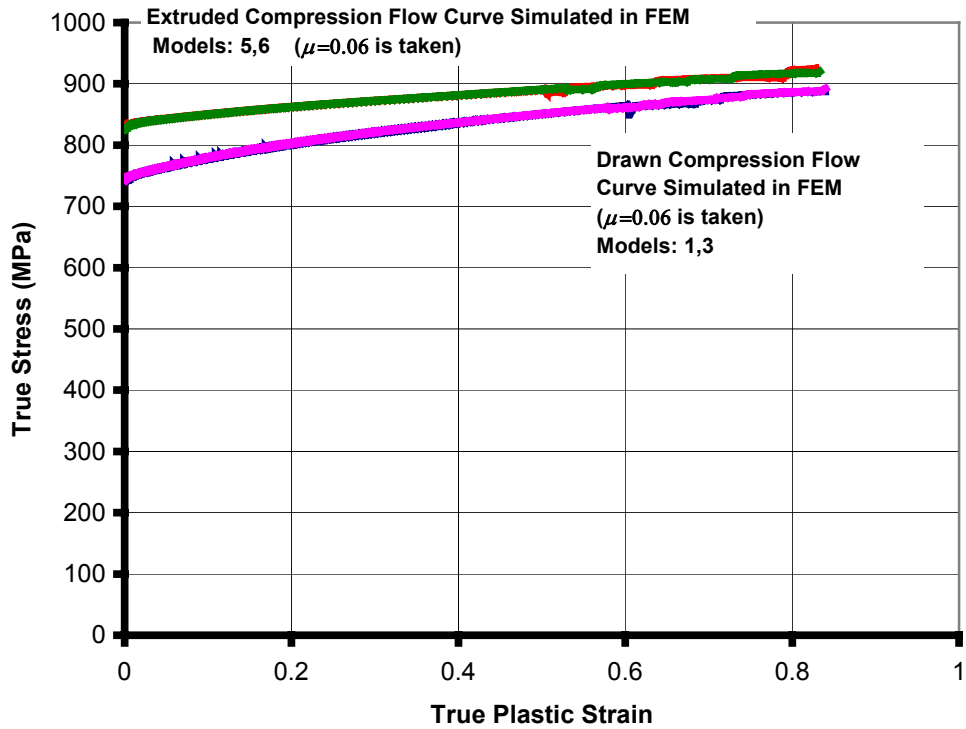
Figure 4.24 Results of flow curves obtained from compression and tension experiments modeled with FEM
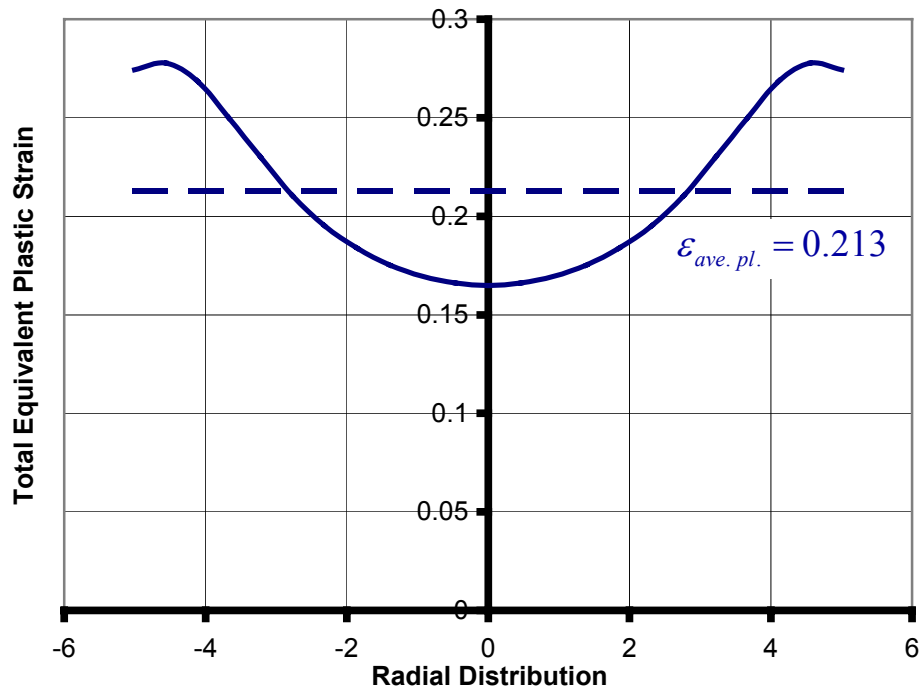
Figure 4.25 Radial strain distribution of the undeformed compression specimens after drawing for carbon steel

Major parameters for finite element simulations of compression tests after drawing and extrusion processes for carbon steel are given in Table 4.8.

Table 4.8 Parameters of FEM for compression tests after drawing and extrusion processes of carbon steel

	Process	
	Compression After Drawing	**Compression After Extrusion**
Number of Elements	1950	1680
Step Size	Adaptive Stepping	Adaptive Stepping
Convergence Limits	0.01	0.01
Element Edge Length	0.2	0.2

Figure 4.26 shows the simulated compression flow curve of drawn carbon steel with the experimental one. Carbon steel also shows similar behavior with stainless steel. At the very beginning of the experimental flow curve effect of Bauschinger can be seen. Through the end of the curves experimental flow curve approaches to the simulated flow curve.
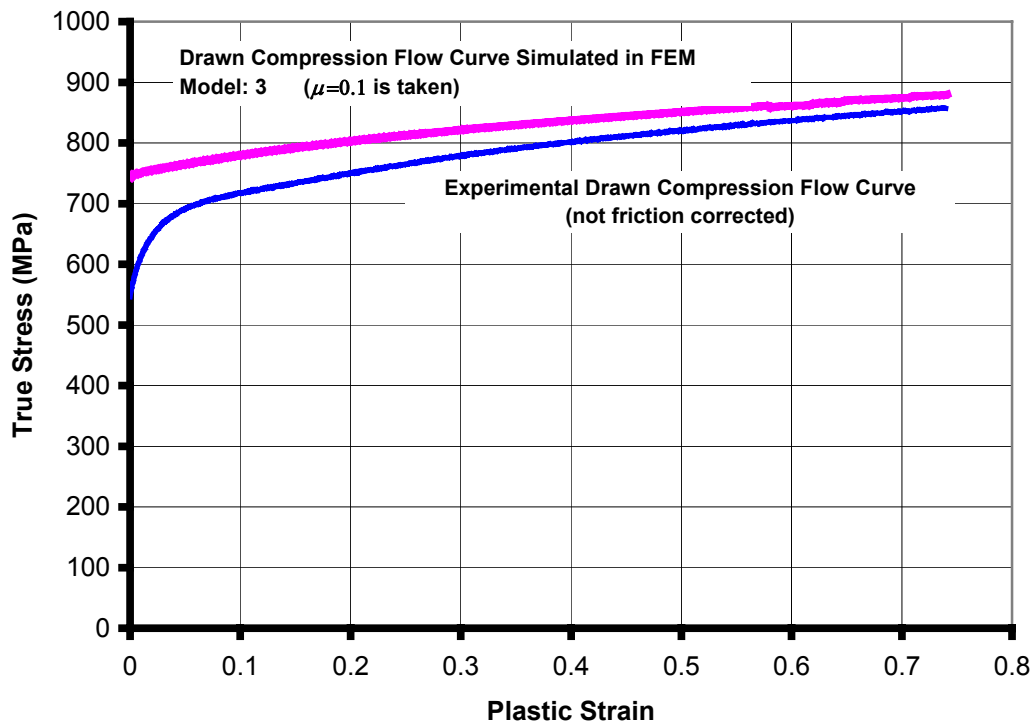
Figure 4.26 Experimental and simulated results for drawn compression test of carbon steel

Figure 4.27 shows that for carbon steel the amount of shifting of the drawn compression flow curve should be $\varepsilon_{pl} = 0.24$ in order to compare it with the annealed curve.

Figure 4.28 shows the simulated compression flow curve of extruded stainless steel with the experimental one. Carbon steel shows same behavior with stainless steel in extruded state. Amount of shifting of the extruded compression flow curve should be $\varepsilon_{pl} = 0.62$ in order to compare it with the annealed curve as shown in Figure 4.29.

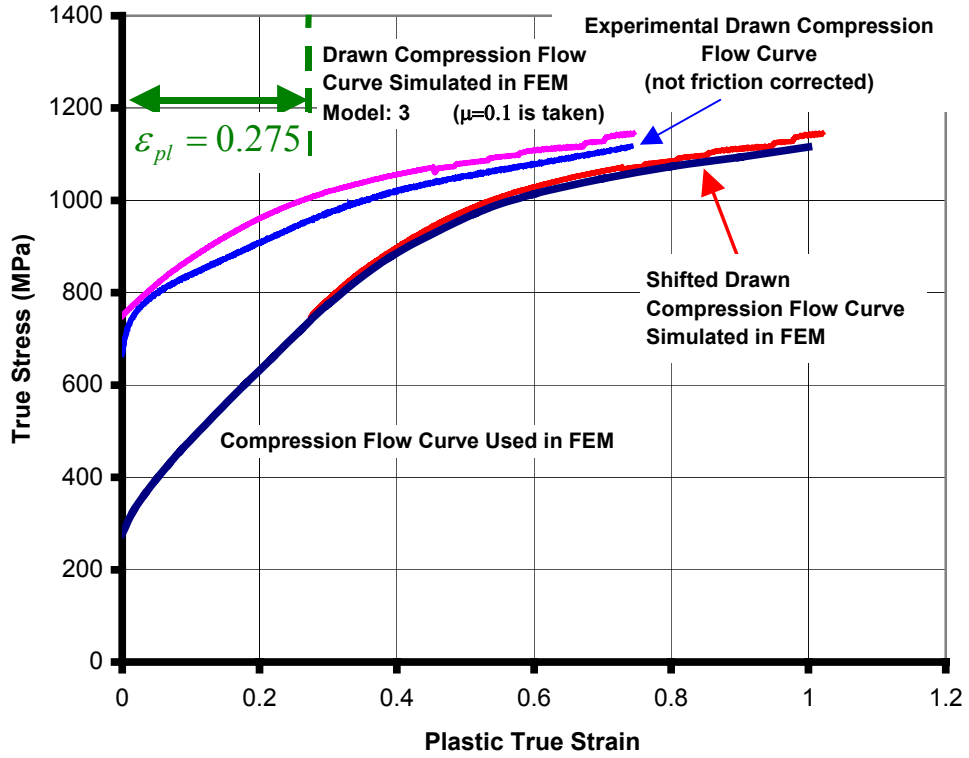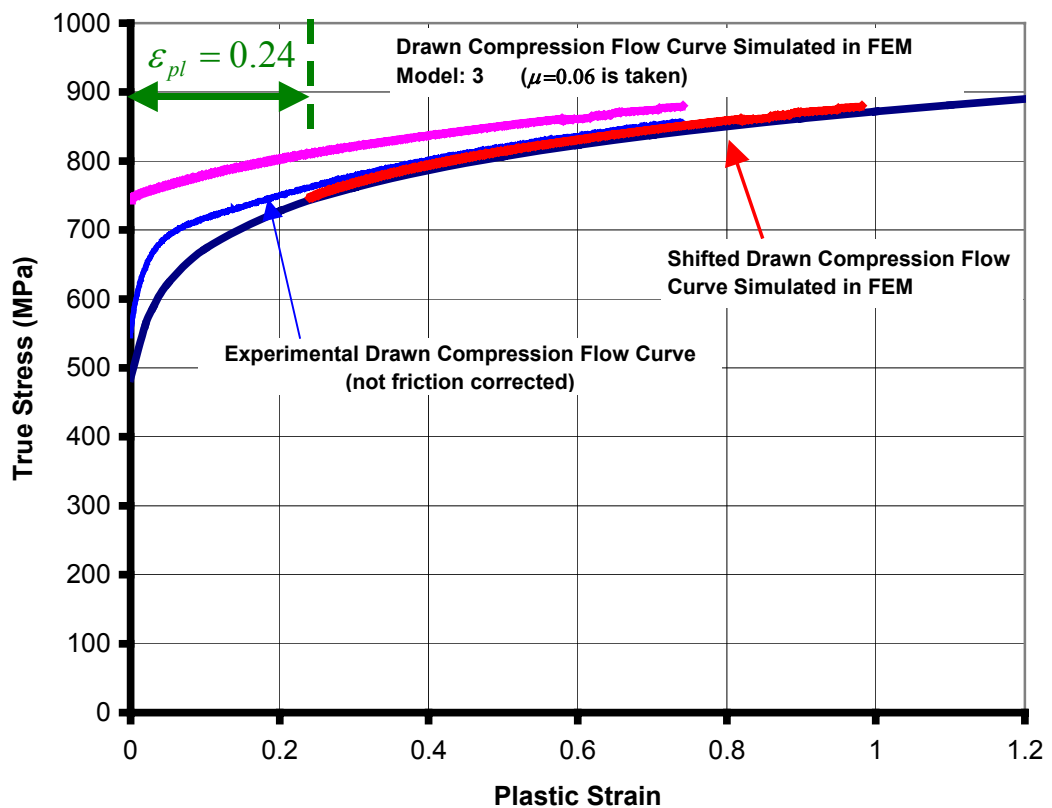**Figure 4.27** Shifted drawn compression flow curve obtained from FEM for carbon steel
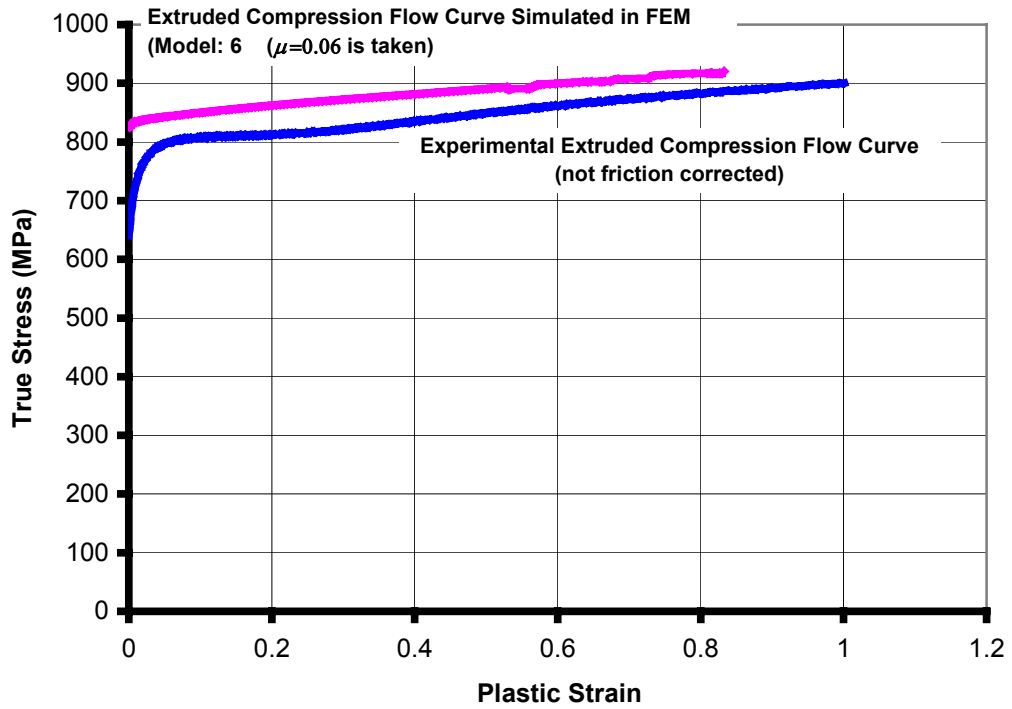
Figure 4.28 Experimental and simulated results for extruded compression test of carbon steel
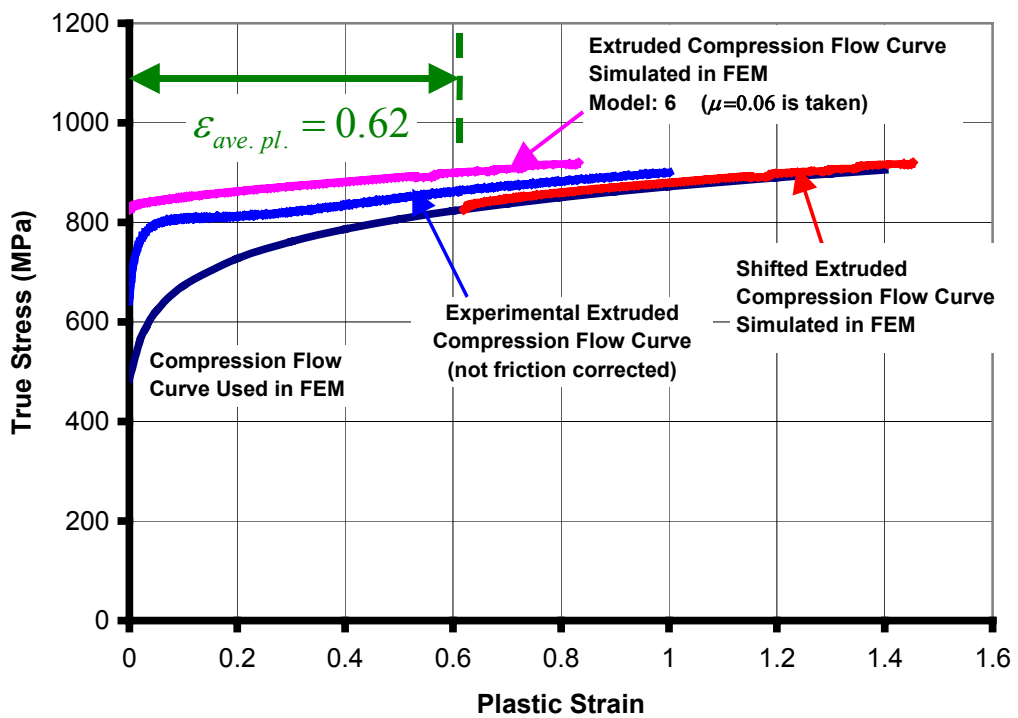
Figure 4.29 Shifted extruded compression flow curve obtained from FEM for carbon steel

154

Table 4.9 gives a general comparison of three different types of average values with the shifting strain required to locate simulated flow curve for the related test on the annealed flow curve. The average values are obtained from the graphs plotted on Figures 4.13 and 4.25. In Table 4.9 results are similar to those in stainless steel.

Table 4.9 Average of radial distribution of equivalent plastic strain on different compression and tension specimens at different states for carbon steel

	Specimen	
	Drawn Compression	**Extruded Compression**
Geometric Strain $\left(\ln\left(A_0/A\right)\right)$	0.178	0.40
Arithmetical Average	0.214	0.556
Area Based Average	0.213	0.556
Volume Based Average	0.235	0.625
Shifting Require in Simulation	0.24	0.62

4.3 Vickers Hardness Distribution Prediction

This section presents the results of Vickers hardness number predictions by using some relations between yield stress and Vickers hardness described in Section 2.1.3. Although these relations are stated to predict the yield strength, in this study they are used to predict hardness numbers to verify these relations for further usage of this method. On the other hand, it should be noted that these relations uses single flow curve and they assume the material as isotropic. In the previous chapter it is seen that work-hardened material have smaller yield strength than it is expected for both materials. So assumption of isotropic material is not valid in this case.

For the hardness prediction of the center points, where the equivalent plastic strain is exactly known, six equations are used for the prediction. These equations are tabulated in Table 4.10.

Table 4.10 Relations between Vickers hardness and yield strength used in this study

	Relation
Tabor	$HV = 2.9\ Y$ *(at equivalent plastic strain of 0.08)*
Tekkaya	$HV = 2.475\ Y$ *(at equivalent plastic strain of 0.112)*
Tekkaya & Yavuz 1	$HV = 2.527 \cdot Y$ *(at an offset strain of 0.120)*
Tekkaya & Yavuz 2	$HV = 2.528 \cdot Y$ *(at an offset strain 0.130)* **for** $0.00 < \varepsilon_{pl} < 0.50$ $HV = 2.520 \cdot Y$ *(at an offset strain 0.230)* **for** $\varepsilon_{pl} \geq 0.50$
Tekkaya & Yavuz 3	$HV = 2.50 \cdot Y$ *(at an offset strain 0.118)* **for** $0.00 < n < 0.10$ $HV = 2.52 \cdot Y$ *(at an offset strain 0.116)* **for** $0.10 \leq n < 0.20$ $HV = 2.54 \cdot Y$ *(at an offset strain 0.135)* **for** $n \geq 0.20$
Tekkaya & Yavuz 4	$HV = 2.51 \cdot Y$ *(at an offset strain 0.140)* **for** $K < 800 \cdot MPa$ $HV = 2.51 \cdot Y$ *(at an offset strain 0.130)* **for** $K \geq 800 \cdot MPa$

4.3.1 Hardness Prediction for Stainless Steel

In this section comparison of predicted hardness values and experimental ones at the center of the workpiece are done. Also radial distribution of best predicting equation will be compared with experimental distribution.

Figure 4.30 shows average experimental Vickers hardness values on center of radial and axial cross-sections of annealed, drawn and extruded workpieces. Beside of these experimental values predicted Vickers hardness values are also given in this figure. In annealed state all equations work well, especially Tekkaya's equation. But in drawn and extruded states the difference between experimental values and predicted values found with Tekkaya's equation and Tekkaya & Yavuz 1-4 is increasing with increasing deformation. On the contrary this is not the case for the hardness values predicted with Tabor's equation. The percent errors between predicted values and experimental values on axial cross-

section are given in Table 4.11. Percent errors in predicted values are not bigger than 15%. Tabor's equation shows good conformity with experimental values.

Table 4.11 Percent errors between experimental hardness values and predicted values on center of the axial cross-sections of stainless steel

	% - Error					
	Tabor	**Tekkaya**	**Equation1**	**Equation2**	**Equation3**	**Equation4**
Annealed	7	1	6	9	11	8
Drawn	-6	-15	-12	-11	-10	-12
Extruded	-1	-15	-13	-11	-12	-13

Figure 4.31 shows the difference between predicted hardness values by using different flow curves. These flow curves are experimental (not friction corrected) compression flow curve, corrected compression flow curve and tension flow curve. For drawing correcting the compression flow curve decreases the predicted hardness values for an amount of 3% and using tension flow curve instead of corrected compression flow curve decreases the predicted hardness values up to 4.4%. For extrusion correcting the compression flow curve decreases the predicted hardness values for an amount of 3.8% to 5.8% and using tension flow curve instead of corrected compression flow curve decreases the predicted hardness values from 1.5% up to 7.8%.

Figures 4.32 and 4.33 show comparison of experimental and predicted radial hardness values for drawn and extruded stainless steel. From Figure 4.31 it is seen that best predicting equation is Tabor's equation and in Figures 4.32 and 4.33 this equation's results are compared.

Figure 4.30 Comparison of predicted Vickers hardness values and experimental hardness values on the center of the annealed, drawn and extruded workpiece

158

Figure 4.31 Radial distribution of predicted Vickers hardness values on drawn and extruded stainless steel

Figure 4.32 Comparison of experimental radial distribution of Vickers hardness values on axial cross-section of drawn stainless steel with predicted hardness values by using both corrected compression and tension flow curve

159

Figure 4.33 Comparison of experimental radial distribution of Vickers hardness values on axial cross-section of extruded stainless steel with predicted hardness values by using both corrected compression and tension flow curve

For both distributions Tabor's equation seems to be successful on predicting center and outer region hardness values. On the other hand the general distribution from center to outer diameter is not similar and while corrected compression flow curve gives better results in drawing, tension flow curve gives better results for extrusion. So the success of Tabor's prediction may be a coincidence.

4.3.2 Hardness Prediction for Carbon Steel

In this section comparison of predicted hardness values and experimental ones at the center of the carbon steel workpiece are done. Also radial distribution of best predicting equation will be compared with experimental distribution.

Figure 4.34 shows average experimental Vickers hardness values on center of radial and axial cross-sections of annealed, drawn and extruded carbon steel

workpieces. Beside of these experimental values predicted Vickers hardness values are also given in this figure. In all states only Tabor's equation is successful in predicting the Vickers hardness values. In rolled, drawn and extruded states the difference between experimental values and predicted values found with Tekkaya's equation and Tekkaya & Yavuz 1-4 is increasing with increasing deformation. On the contrary this is again not the case for the hardness values predicted with Tabor's equation. The percent errors betwee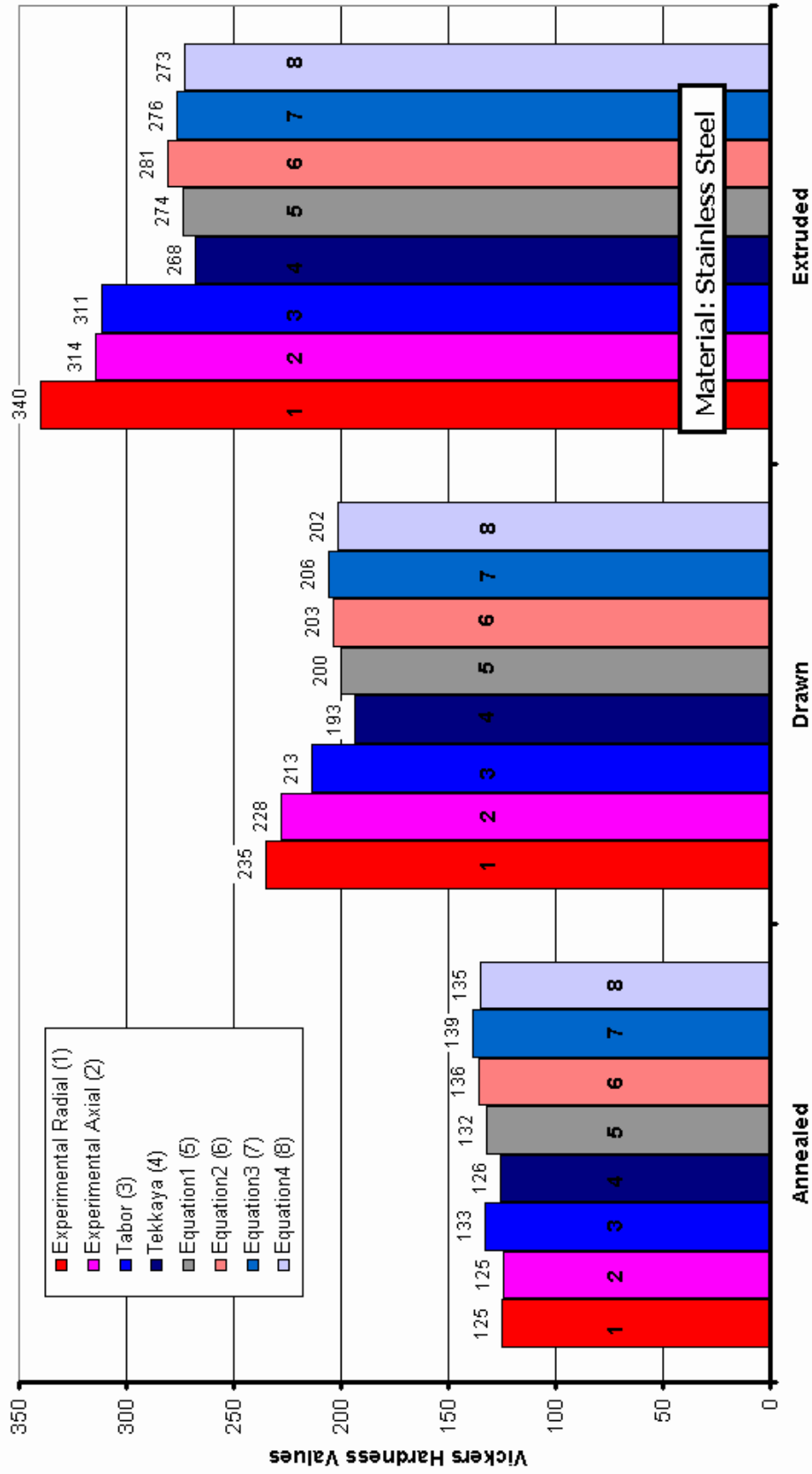n predicted values and experimental values on axial cross-section are given in Table 4.12. Percent errors in predicted values are not bigger that 17% for all equations. Tabor's equation shows good conformity with experimental values with an error less than 3.3%.

Table 4.12 Percent errors between experimental hardness values and predicted values on center of the axial cross-sections of carbon steel

	% - Error					
	Tabor	**Tekkaya**	**Equation1**	**Equation2**	**Equation3**	**Equation4**
Rolled	-2	-13	-11	-10	-12	-11
Drawn	-0	-14	-12	-11	-13	-12
Extruded	-3	-17	-15	-15	-16	-15

Figure 4.35 shows the difference between predicted hardness values by using different flow curves. These flow curves are experimental (not friction corrected) compression flow curve, corrected compression flow curve and tension flow curve. For drawing correcting the compression flow curve decreases the predicted hardness values for an amount of 1.7% and using tension flow curve instead of corrected compression flow curve decreases the predicted hardness values up to 0.8%. For extrusion correcting the compression flow curve decreases the predicted hardness values for an amount of 1.8% and using tension flow curve instead of corrected compression flow curve decreases the predicted hardness values from 1.5% up to 2.7%.
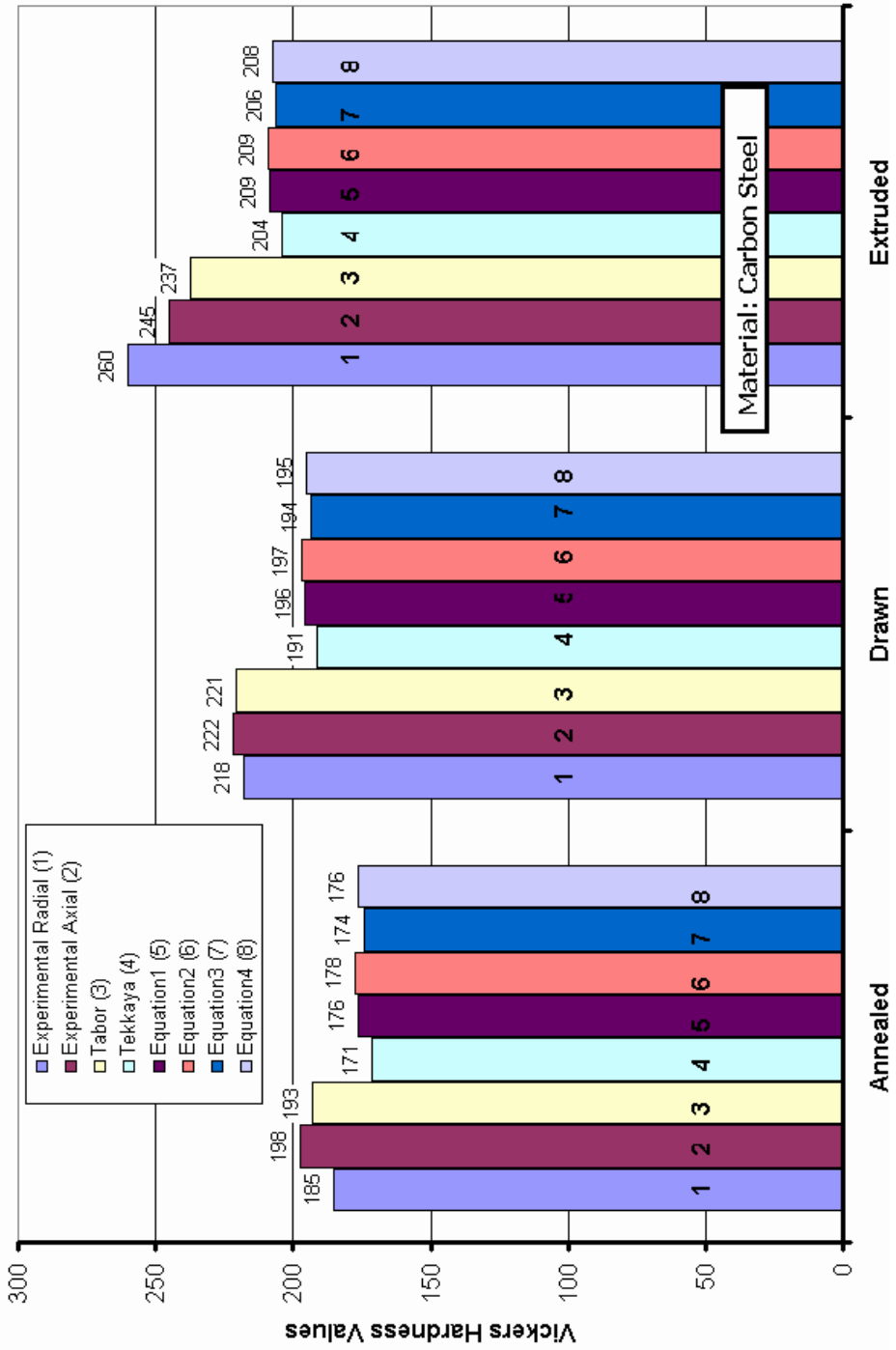
Figure 4.34 Comparison of predicted Vickers hardness values and experimental hardness values on the center of the annealed, drawn and extruded carbon steel workpiece
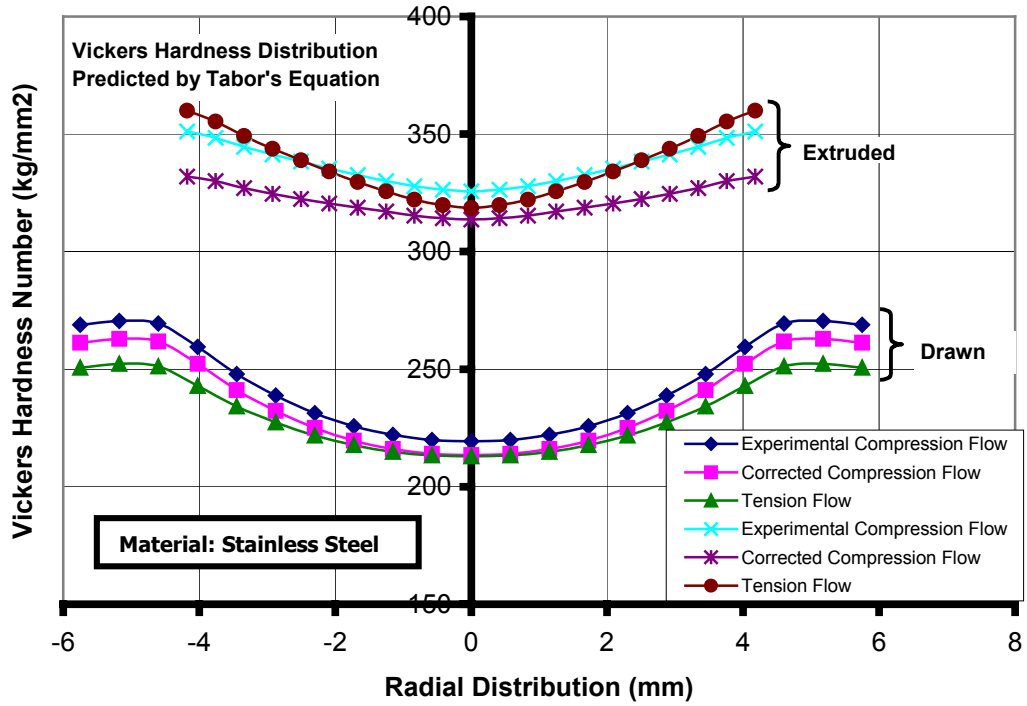
162

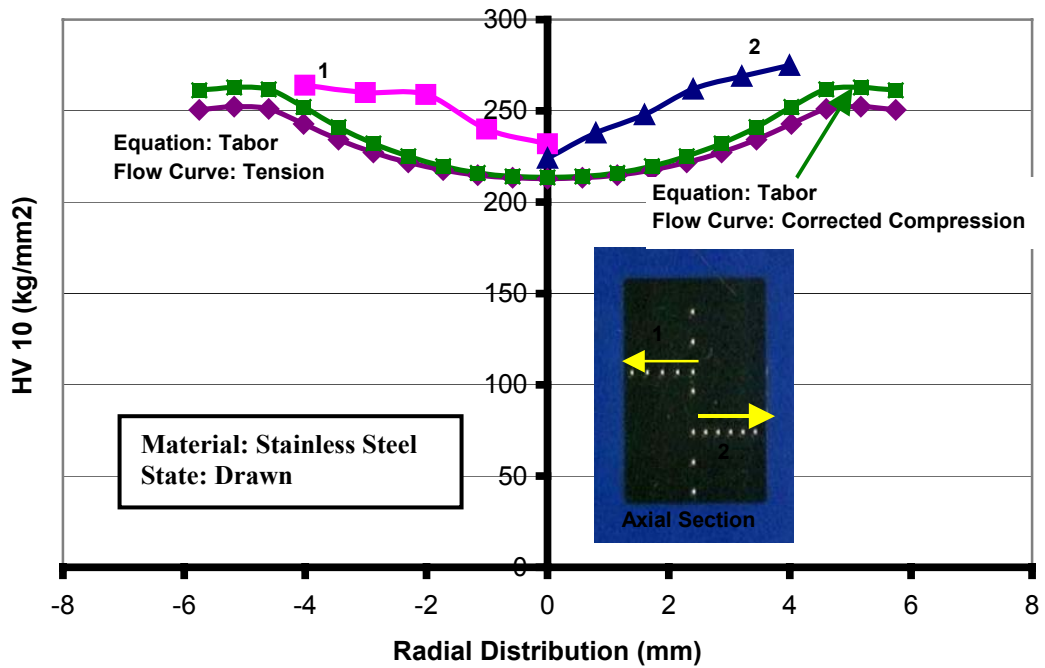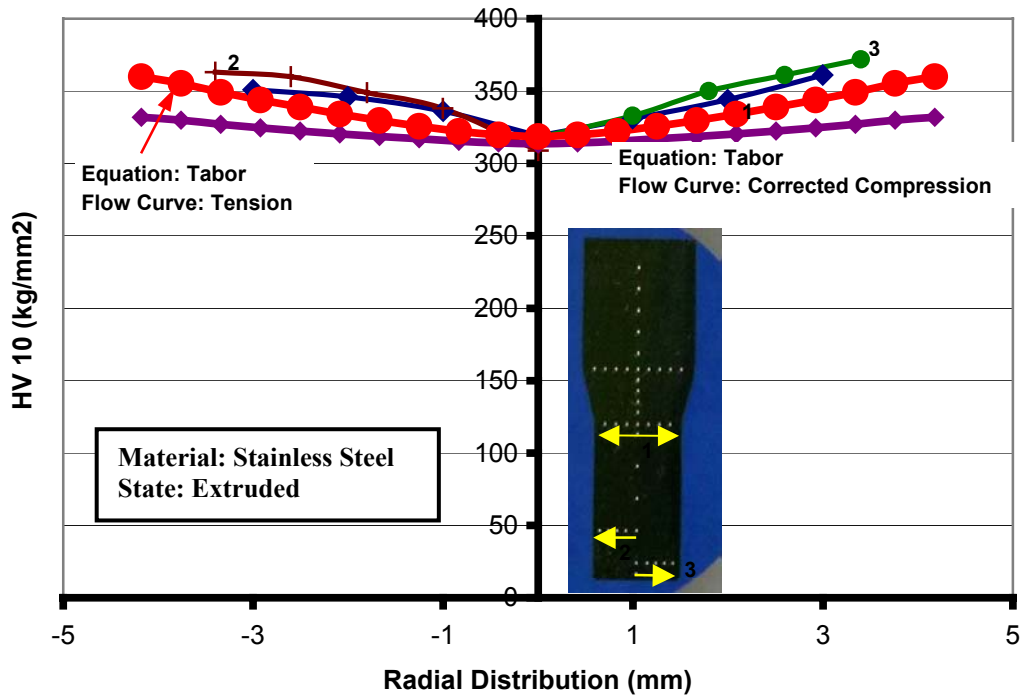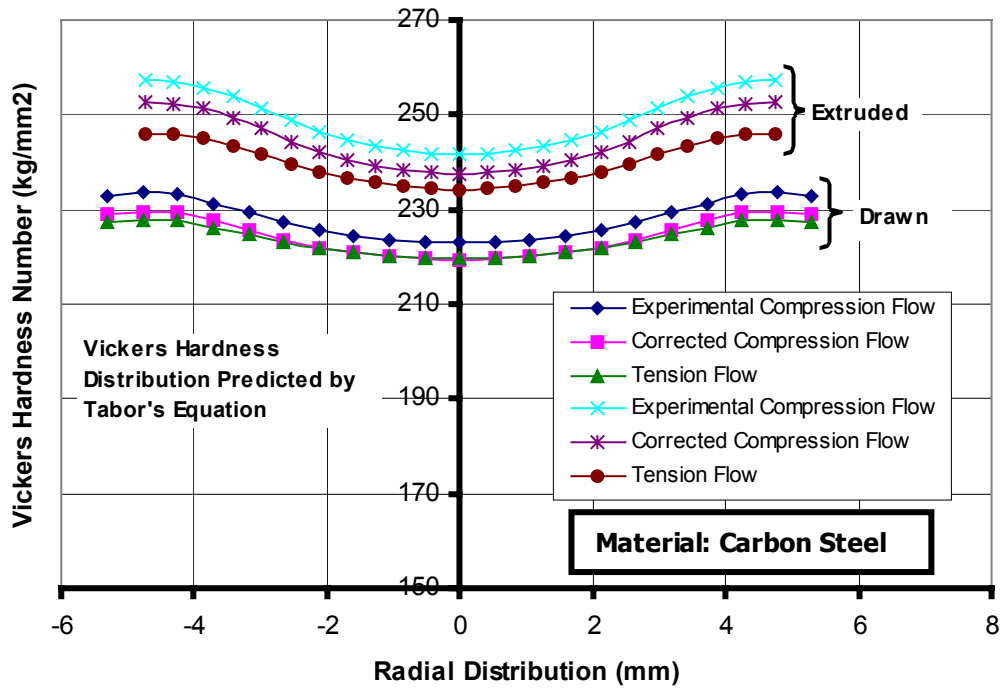**Figure 4.35** Radial distribution of predicted Vickers hardness values on drawn and extruded carbon steel
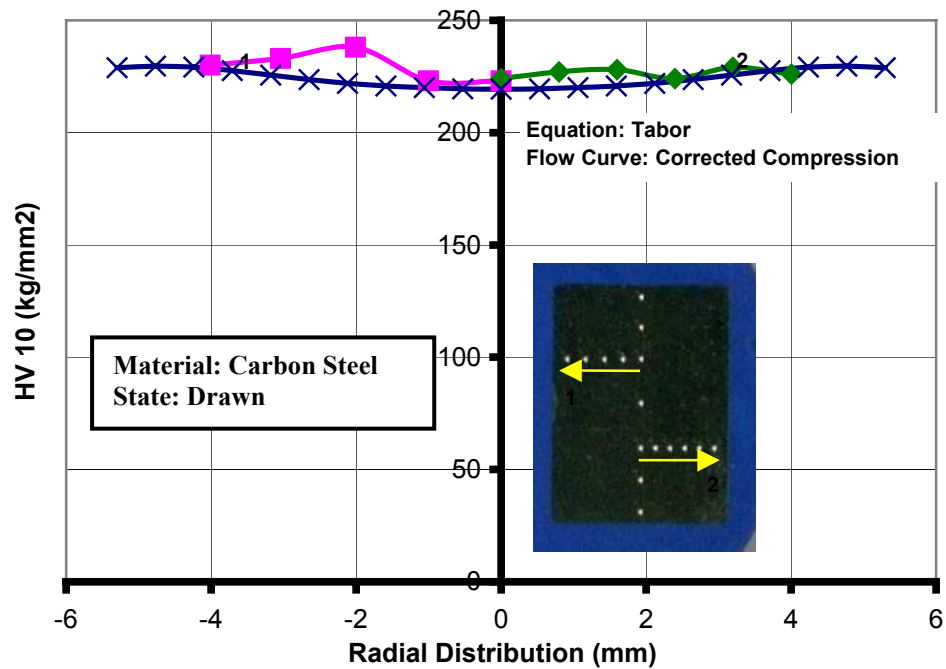
Figure 4.36 Comparison of experimental radial distribution of Vickers hardness values on axial cross-section of drawn carbon steel with predicted hardness values by using both corrected compression and tension flow curve

Figures 4.36 and 4.37 show comparison of experimental and predicted radial hardness values for drawn and extruded stainless steel. From Figure 4.35 it is seen that best predicting equation is Tabor's equation and in Figures 4.36 and 4.37 this equation's results are compared.
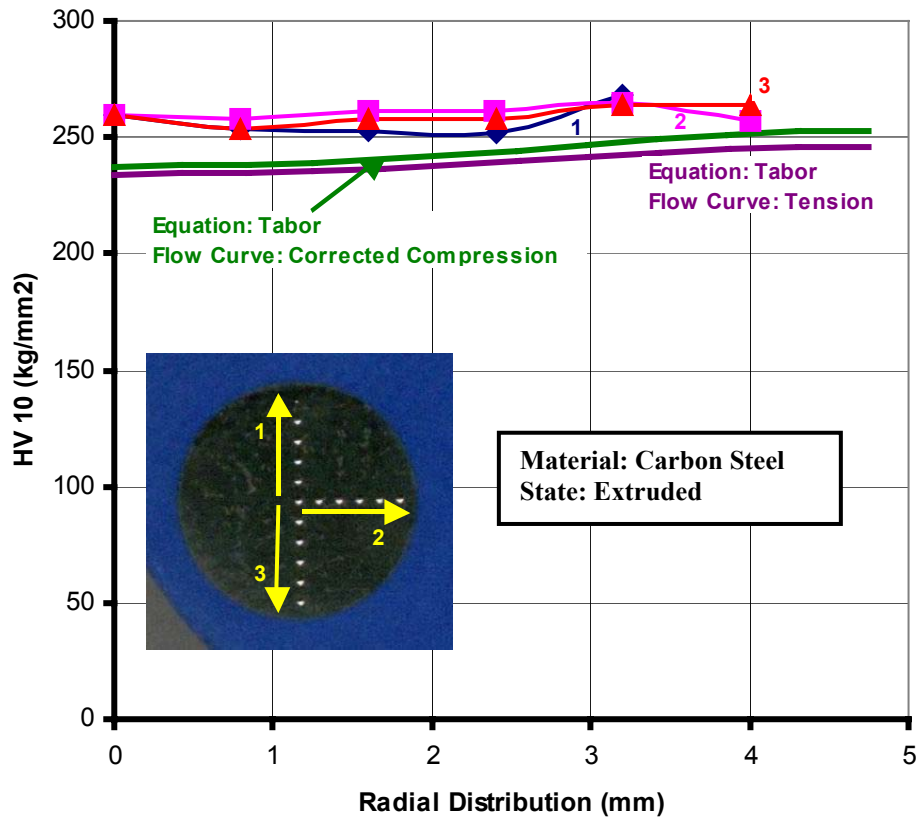
Figure 4.37 Comparison of experimental radial distribution of Vickers hardness values on axial cross-section of extruded carbon steel with predicted hardness values by using both corrected compression and tension flow curve

Especially for drawing Tabor's equation seems to be successful on predicting center and outer region hardness values. On the other hand the general distribution from center to outer diameter is not similar and while corrected compression flow curve gives better results for extrusion.

When the anisotropic behavior of both carbon and stainless steel is thought it cannot be expected to take good results from Tekkaya's equation. But the success of Tabor's prediction does not convenience completely.

CHAPTER 5

3D COMPRESSION TEST MODELING FOR ANISOTROPY CONSTANTS PREDICTION

During the compression and tension tests the development of elliptical cross section in initially round test pieces of stainless steel makes it necessary to model in FEM. Commercial FEM program MSC.Marc will be used for modeling. MSC.Marc uses Hill's quadratic yield function for anisotropic materials.

In MSC.Marc, Hill's yield function (Eq. 2.68) is defined from user input consisting of different ratios of yield stress in different directions with respect to a reference stress. In the FEM models used in this study, z-axis is taken in the direction of compression as illustrated in Figure 5.1.
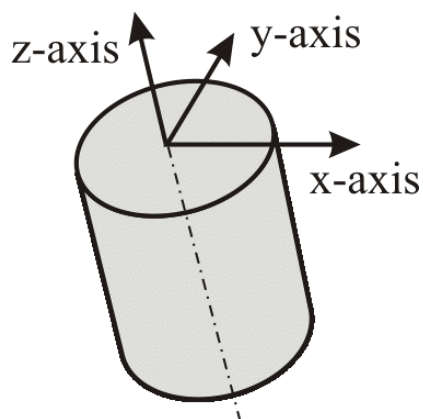
Figure 5.1 Stress directions defined for FEM model

Corrected compression flow curve is taken as reference stress. Therefore, the yield stress ratio in z-axis can be taken as 1.0, $Z = \sigma_z / \sigma_f = 1.0$. The yield stress ratios in the x and y directions, X and Y, have been changed to reflect different material anisotropy. Other stress ratios can be found as follows

$$X = \frac{\sigma_x}{\sigma_f}, \quad Y = \frac{\sigma_y}{\sigma_f}, \quad R = \frac{\sigma_{yz}}{\sigma_f / \sqrt{3}}, \quad S = \frac{\sigma_{xz}}{\sigma_f / \sqrt{3}}, \quad T = \frac{\sigma_{xy}}{\sigma_f / \sqrt{3}} \qquad (1.1)$$

When the yield stress ratios have been defined, Marc/Mentat will calculate the anisotropy parameters according to the following equations

$$
\begin{aligned}
F &= \frac{1}{2}\left(1 + \frac{1}{Y^2} - \frac{1}{X^2}\right), \\
G &= \frac{1}{2}\left(1 + \frac{1}{X^2} - \frac{1}{Y^2}\right), \\
H &= \frac{1}{2}\left(\frac{1}{X^2} + \frac{1}{Y^2} - 1\right), \\
L &= \frac{1}{2R^2}, \quad M = \frac{1}{2S^2}, \quad N = \frac{1}{2T^2}
\end{aligned}
\qquad (1.2)
$$

In FEM model Z, R, S, T parameters are taken as 1. By predicting X and Y values the barrel diameters (Figure 5.2) in x and y directions are tried to be found. Barrel diameters are measured at the end of the compression experiment.
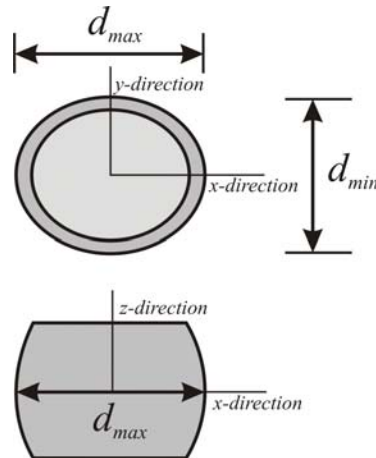
Figure 5.2 Maximum and minimum barrel diameters of deformed standard compression specimen

Table 5.1 shows dimensions of the deformed and undeformed compression specimen. Dimensions of undeformed specimen will also be the initial geometry for our FEM model. Final barrel diameters of the simulated compression test with pre-assumed X and Y values will be compared with experimental results. Comparing barrel diameters are thought to be more consistent when compared with the minimum and maximum diameters on contacting surfaces of compression specimens. Because contacting surface diameters can differ from each other and they are difficult to measure. Also deformed specimens do not form an exact ellipse shape.

Table 5.1 Dimensions of the deformed and undeformed compression specimen

	h	d_{max}	d_{min}	% difference
Undeformed	15.04	10.02	10.02	0
Deformed	7.11	15.35	14.4	6.6

1/8 of the workpiece is modeled because of the symmetry. Snapshot of the model is given in Figure 5.3. Because of the symmetry three symmetry planes normal to *x, y, z* directions are used. Punch has a velocity of -0.2 mm/s in *z*-direction with a friction coefficient of 0.1. 1264 elements are compressed with 0.2 mm step size and 0.01 convergence tolerance with varying X and Y values. During this study convergence testing of relative residual force and eight-noded hexahedral element is used. No remeshing is performed. As seen from the illustrated Figure 5.2 specimen is wanted to be deformed more in *x*-direction. This is possible by giving a higher *Y* value than *X*. The final diameters simulated by taking Y as 1 and decreasing the X value from 1 to desired value to obtain elliptic dimensions of the experiment. The results are tabulated in Table 5.2.

Table 5.2 Values of d_{max} and d_{min} with varying X value

	X	Y	Z	d_{max}	d_{min}	*% difference*
Experimental	-	-	-	15.35	14.4	6.6
Simulation 1	1	1	1	14.84	14.84	0
Simulation 2	0.99	1	1	15.06	14.62	3.01
Simulation 3	0.98	1	1	15.29	14.38	6.31
Simulation 4	0.975	1	1	15.41	14.26	8.08
Simulation 5	0.979	1	1	15.32	14.36	6.66
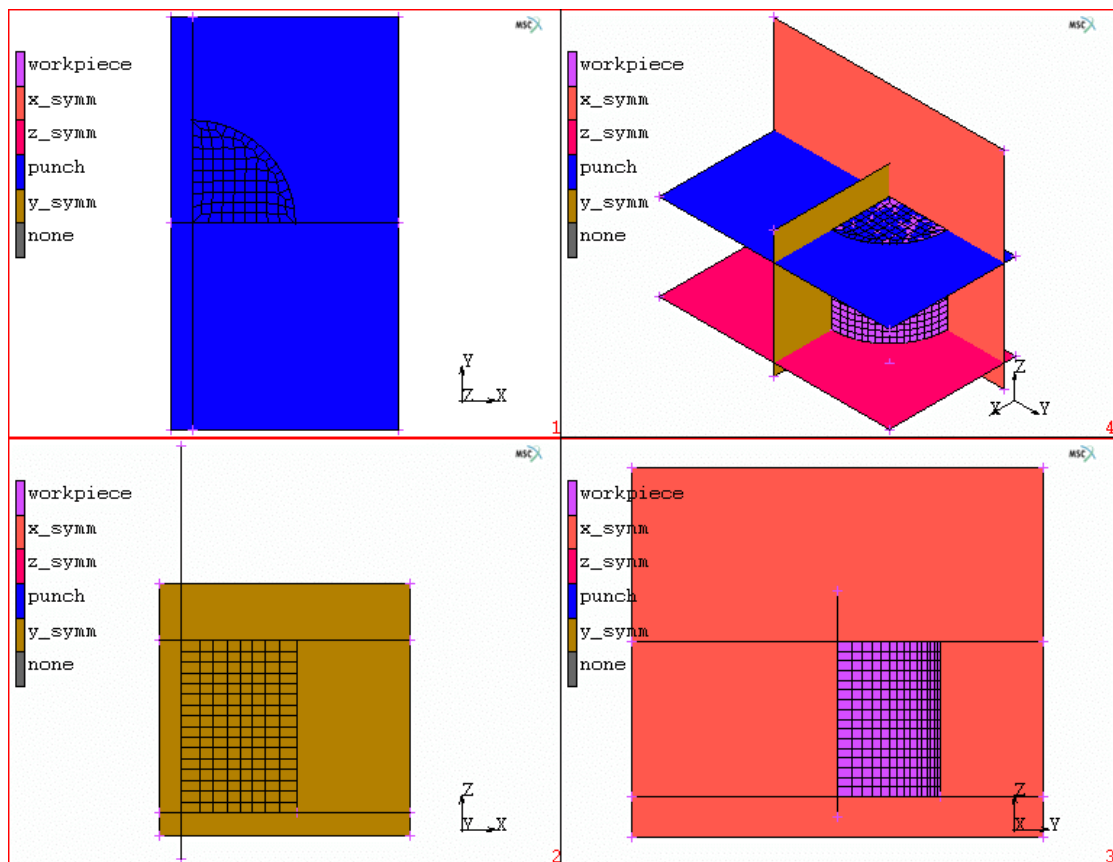
Figure 5.3 Snapshots of the 3D compression model with 4 views

Table 5.2 shows that decreasing X value down to 0.979 and keeping Y and Z constant similar elliptic dimensions can be obtained. Simulation 5 is shown in Figure 5.5 with different displacements in x and y directions.

Similar study can be made by only increasing Y value, or decreasing X and increasing Y value simultaneously. Table 5.3 shows that with Y of 1.1 and X of 0.989 similar deformation can be obtained.

Table 5.3 Values of d_{max} and d_{min} with varying X and Y value

	X	Y	Z	d_{max}	d_{min}	% difference
Experimental	-	-	-	15.35	14.4	6.6
Simulation 1	1	1	1	14.84	14.84	0
Simulation 6	0.99	1.1	1	15.27	14.42	5.92
Simulation 7	0.989	1.1	1	15.29	14.40	6.25

It should also be noted that changing X and Y values does not change the simulated flow curve unless Z value is changed. Figure 5.4 shows that experimental and simulated are same for X=0.989 and Y=1.01.
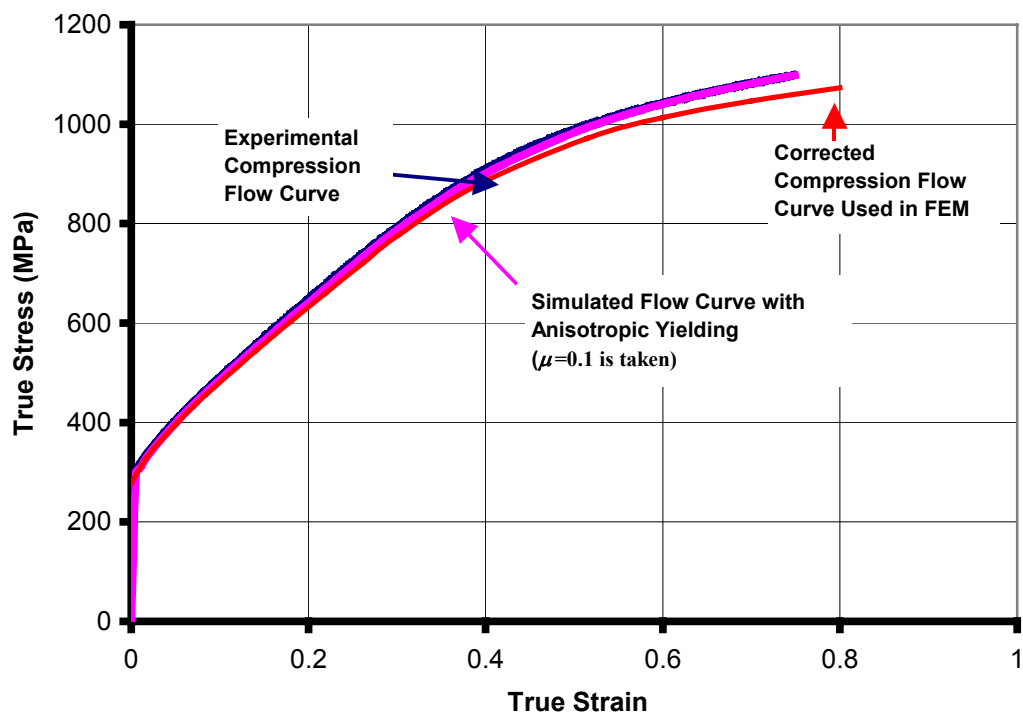
Figure 5.4 Comparison of simulated compression flow curve with anisotropic yielding with experimental flow curve
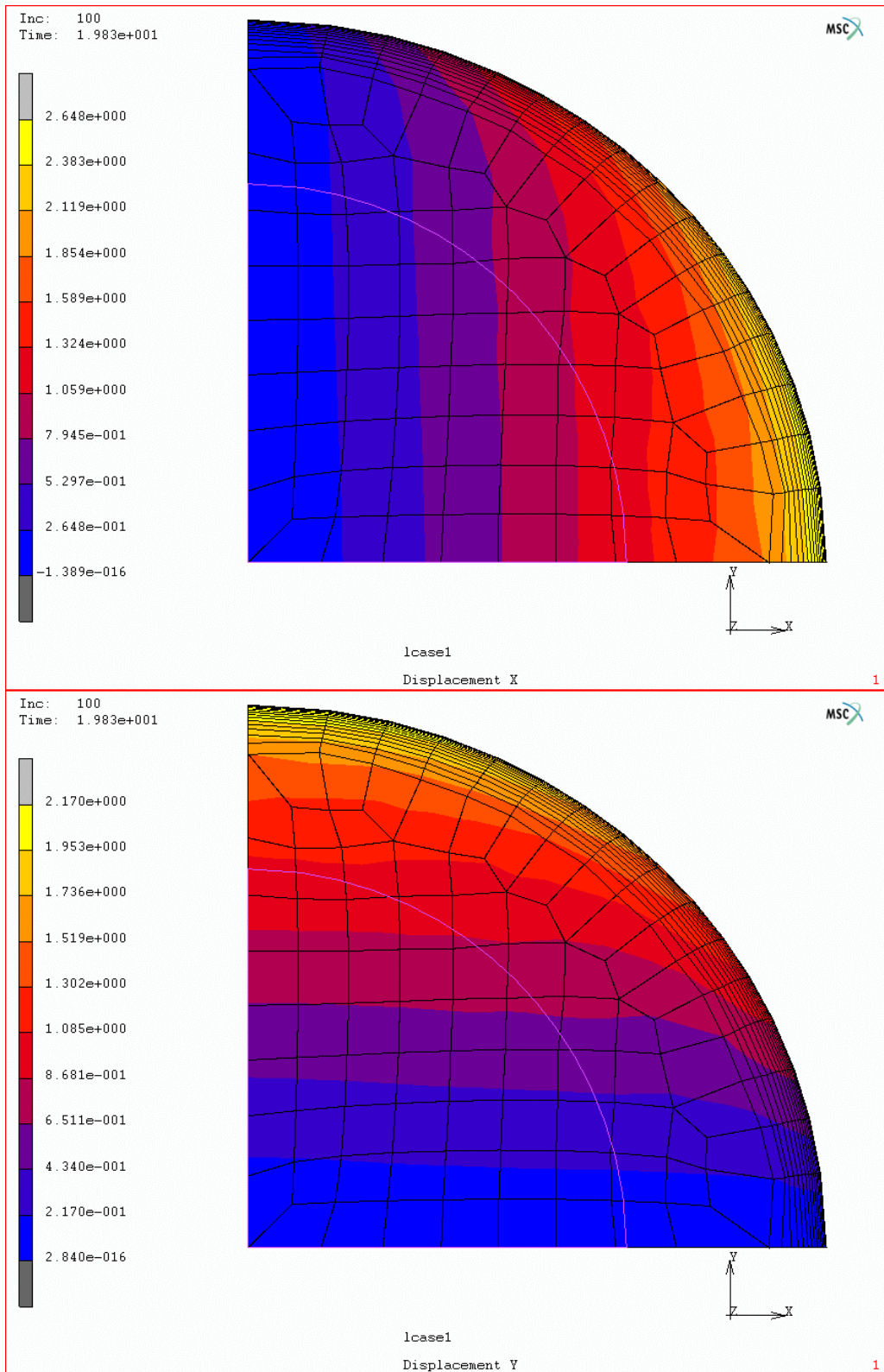
Figure 5.5 Simulated compression specimen having different displacements in different directions

CHAPTER 6

CONCLUSIONS AND FURTHER RECOMMENDATIONS

In this study mechanical properties of stainless steel and carbon steel before and after forming operations are investigated by performing standard compression, Rastegaev compression and tensile tests. Two forming operations are studied. These are drawing and afterwards extrusion, which are at least suitable for compression testing.

During evaluation of the compression test results iterative FEM method is used in order to obtain friction free flow curve and it is seen that this correction is quite compatible for carbon steel when compared with Rastegaev compression test results. Iterative FEM method is used through out the study. Deviation from Ludwik's fit is observed for stainless steel. For stainless steel Ludwigson's fit is successfully applied to the tension flow curve. Also Bridgman correction factor is used to correct the tensile test data after necking starts. This gave a similar result with extended tensile flow curve using Ludwik's fit.

First motivation of this study is the large difference between compression and tensile flow curves of stainless steel, obtained from HILTI. This difference is shown in the below graph.
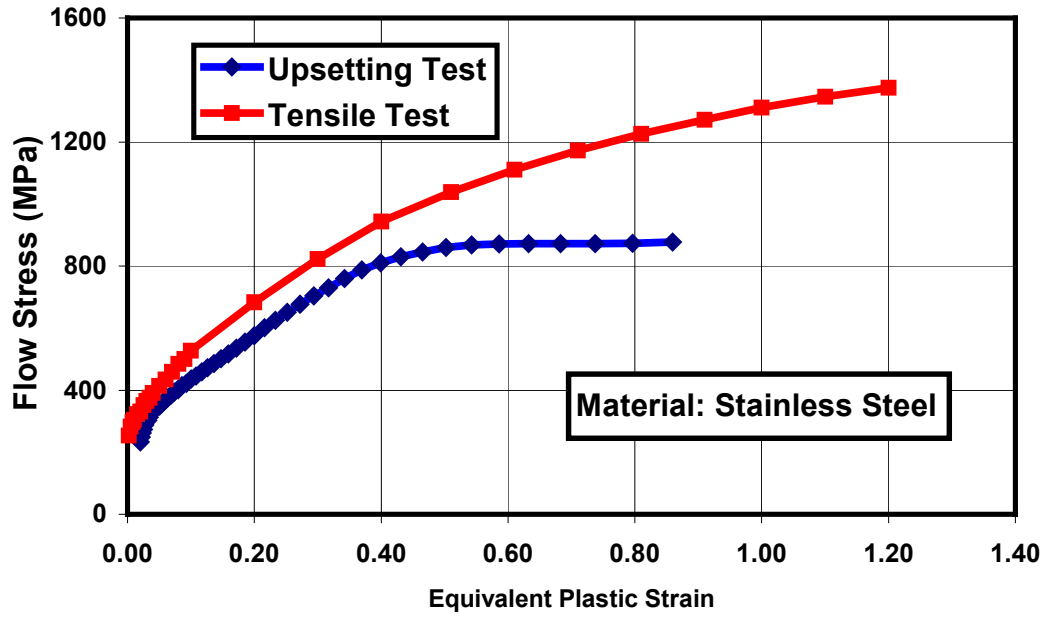
Figure 6.1 Compression and tension flow curves of stainless steel supplied by HILTI
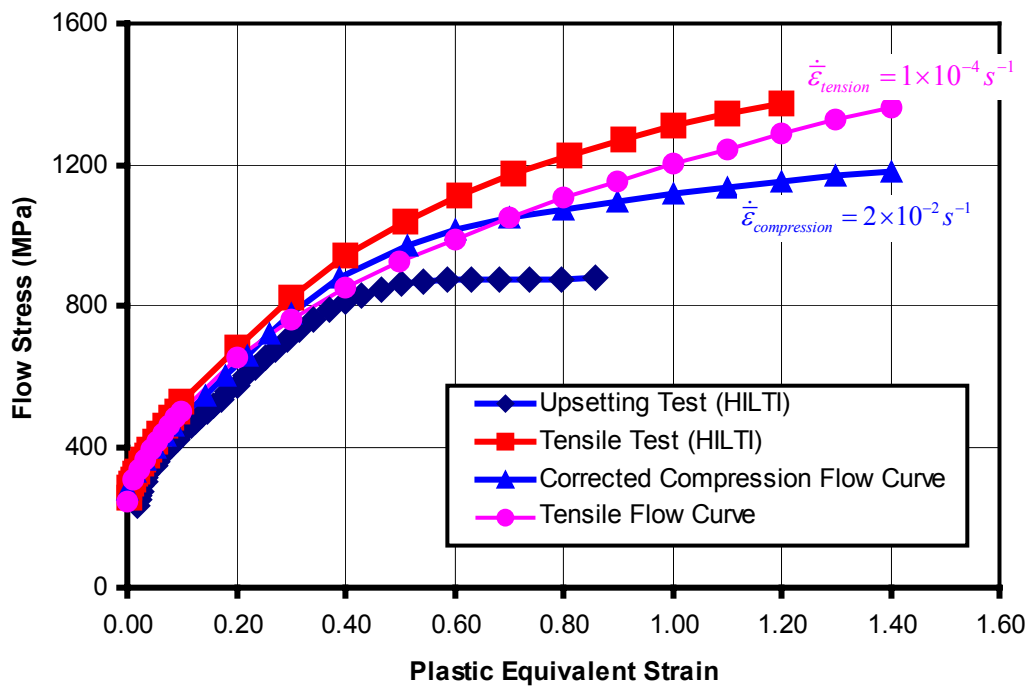
Figure 6.2 Compression and tension flow curves of stainless steel supplied by HILTI and results of this study

172

However performed experiments in this study showed that up to 0.7 equivalent plastic strain compression and tensile flow curves are similar with each other and located between compression and tensile flow curves obtained by HILTI (Figure 6.2). Although it is known that HILTI has three material suppliers for stainless steel it can be thought that this difference can be a result of strain-rate dependence of the material.

Anisotropic hardening can be thought to be a cause of the difference between the loading directions. For this purpose some large strain load reversal experiments performed for both material. These are the standard compression experiments conducted after pre-strained by tension. The results showed that beside lower yield stresses there is lowering tendency in the slope of the initial part of the flow curves as shown in Figure 6.3. It is observed that with increasing pre-strain fall in yield stress (Bauschinger effect) increases more in the new flow curve.

Same effect is seen in compression flow curves performed after drawing and extrusion processes. Comparison of these flow curves should be done with annealed compression flow curve to see if there is any Bauschinger effect or not. Shifting the workhardened flow curves with an amount of geometric strain (equivalent plastic strain on the center of the workpiece) is the first choice. This is presented in Figure 3.31. Workhardened flow curves attract attention with their initially high work hardening rates. After this region especially in extruded compression flow curve workhardening stagnation is observed. Then workhardening rate starts to increase. This is probably because of sub-boundary instabilities resulted from load reversals. Load reversal term may seem to be irrelevant when the case is compression after extrusion process. But the grain elongation directions of extrusion and tension are in the same direction. Simply flow directions of both processes are same. This also explains the unchanged behavior of drawn tension flow curve shown in Figure 3.14.
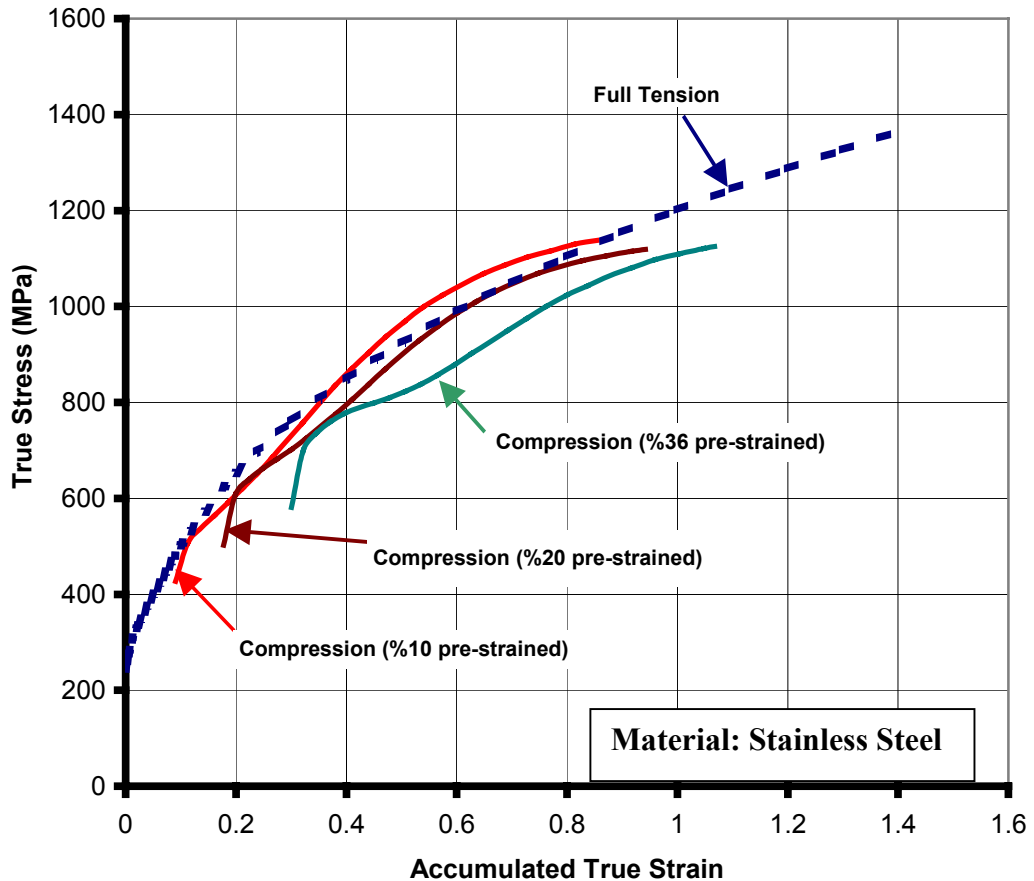
Figure 6.3 Monotonic tension flow curve and friction corrected tension pre-strained compression flow curves of stainless steel

Another problem arises from comparison point of view. Workhardened flow curves are firstly shifted by an amount of equivalent plastic strain at the center of the specimen. But this is the minimum plastic strain on the drawn compression test specimen. FEM simulations results (Chapter 4) based on elasto-plastic and isotropic material showed that shifting strain value must be larger. In Chapter 4 it is also indicated that volume-based average of equivalent plastic strain distribution gave the same shifting strain value with finite element simulations. By using the new shifting strain values compression flow curves can be compared as in Figure 6.4. All the compression flow curves used in Figure 6.4 are friction corrected. This figure shows general deviation of stainless steel from an isotropic material behavior. Bauschinger effect and workhardening stagnation shows itself similar to large strain load reversal experiments. Both drawn and

extruded compression flow curves converge to annealed compression flow curve with increasing strain.
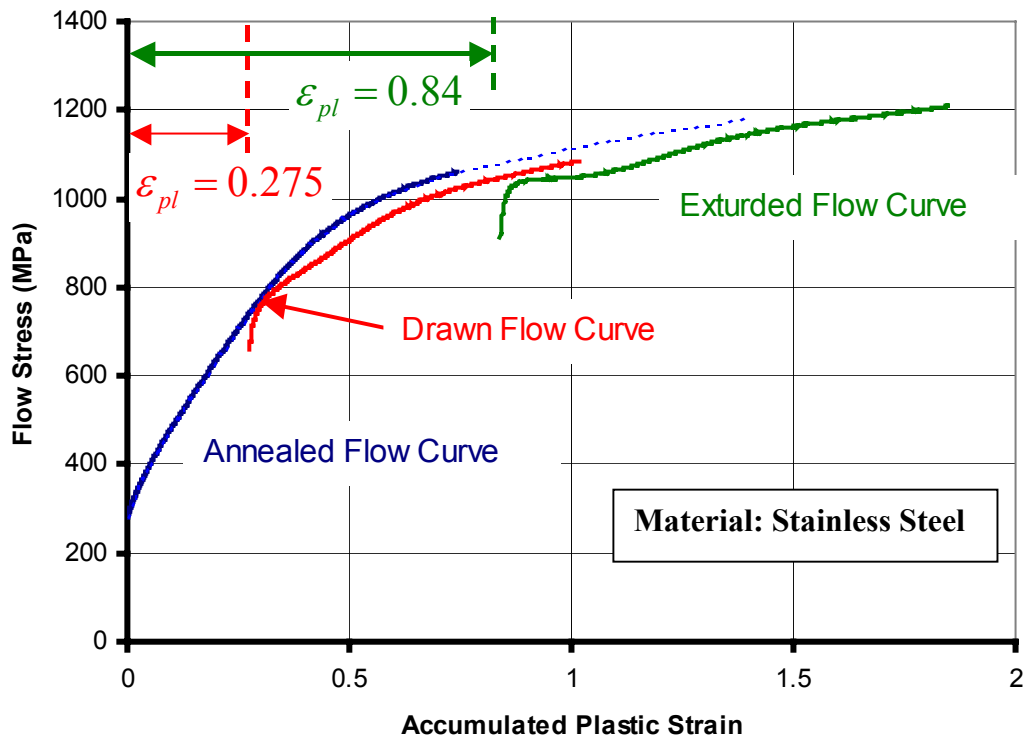
Figure 6.4 Comparison of annealed compression flow curve with drawn and extruded compression flow curves of stainless steel

Hardness measurements were performed to predict yield strength distribution within the workpiece by using relations of Tabor and Tekkaya, which are assuming material as isotropic. During this study Vickers hardness numbers are predicted by using these relations and available annealed flow curves.

In spite of Bauschinger effect seen in workhardened flow curves, predicted Vickers hardness numbers are lower than experimental values. The best predicting relation is seen to be Tabor's one. But the hardness values in radial and axial sections seem to be different from each other. Besides, this relation is only able to get closer to the center values of hardness on axial section but not the general radial distribution. Difference between hardness numbers on radial and axial sections shows that anistropic hardening occurs within material, but

available relations used for correlating hardness number to yield strength are not able to predict this difference. In this case although Tabor showed consistency with center values of axial sections for both materials, none of these relations are enough accurate to predict general disturbance of yield strength of an anisotropic material.

Finally anisotropic yielding in radial direction for stainless steel is modeled by using quadratic equation of Hill. MSC/Mentat is used for the modeling. The parameters for Hill's equation are found by using the final dimensions of the deformed compression specimen. Also it is shown that by using Hill's yield criteria the compression flow curve simulated is consistent with the experimental one.

Results obtained from various mechanical tests shows that predicting product properties with available hardening models by means of FE simulations cannot represent the exact material behavior.

As the recommendation for the further studies, below comments can be done.

The load reversal characteristics of both steels should be investigated further. This could be performed with torsion test, which is a more popular way for this kind of experiments. Tension test after compression should also be investigated. Also unloading characteristics is important for load reversal experiments and anisotropic materials in point of pre-yielding.

TEM (transmission electron microcopy) study is needed for investigating sub-grain hardening mechanisms, especially for describing workhardening stagnation and pre-yielding (Bauschinger effect).

Although there are several kinematic and combined hardening models, it is difficult to explain workhardening stagnation with these methods. For designing a convenient relation between yield strength and hardness by using finite element simulations first of all a convenient anisotropic model should be developed.

REFERENCES

[1]   **Lange K.:** Handbook of Metal Forming, McGraw-Hill (1985)

[2]   **Pöhlandt K**.: Materials Testing for the Metal Forming Industry, Springer (1989), pp. 2-41.

[3]   **Dowling, N.A.:** Mechanical Behavior of Materials, Prentice-Hall, 1993.

[4]   **Banabic, D.; Bunge, H.-J.; Pöhlandt, K.; Tekkaya, A.E.:** Formability of Metallic Materials, Springer-Verlag 2000.

[5]   **Dieter, G.E.:** Mechanical Metallurgy, McGraw-Hill, 1976.

[6]   **Tekkaya A.E.:** ME 453 Lecture Notes, METU, ANKARA (2001).

[7]   **Johnson, W.; Mellor, P.B.:** Engineering Plasticity, Van Nostrand Reinhold Company, 1973.

[8]   **Siebel, E.; Schwaigere, S.:** Mechanichs of Tensile Test (in German), Arch. Eisenhüttenwes., 19 (1948), pp. 145-152.

[9]   **Bridgman, P.W.:** The Stress Distribution at the Neck of a Tension Specimen, Transactions of American Society for Metals, Vol. 32, 1944, p. 553.

[10] **Thomsen, E.G.; Shabaik, A.H.; Sohrabpour, S.:** A Direct Method for Obtaining an Effective Stress-Strain Curve from a Tension Test, Manufacturing Engineering Transactions, SME, 1977, pp. 139-143.

[11] **Siebel E.; Pomp A.:** Determination of Flow Stress and Friction with the Upsetting Test (in German), Mitt. KWI Eisenforsch. 9 (1927), pp. 157-171.

[12] **Avitzur, B.:** Handbook of Metal-Forming Processes, John Wiley & Sons (1983) pp. 907-940.

[13] **Wiegels, H.; Herbertz, R.:** Upsetting Test on Cylindrical Test Pieces with High Friction for Determining Flow Stress (in German), Stahl und Eisen 99 (1979), pp. 1380-1390.

[14] **Schey, J.A. et al.:** The Effect of Friction on Pressure in Upsetting at Low Diameter to Height Ratios, J. Mech. Work. Technol. 6 (1982), pp. 23-24.

[15] **Osakada, H. et al.:** A Method Determining Flow Stress under Forming Conditions, Annls of the CIRP 30/1 (1981), 99.135-138.

[16] **Sachs, G.:** Z. Metallkde. 16 (1924), p. 55.

[17] **Sato, Y.; Takeyama, H.:** An extrapolation Method for Obtaining Stress-Strain Curves at High Rates of Strain in Uniaxial Compression, Tech. Rep. Tohoku Univ. 44 (1980), pp. 287-302

[18] **Polakowski, N.H.:** The Compression Test in Relation to Cold Rolling, J. Iron Steel Inst. 163 (1949), pp. 250-276.

[19] **Pöhlandt, K.:** Contribution to the Recording of Flow Curves at High Natural Strain (in German), Seminar "Neuere Entwicklungen in der Massivumformung", Forschungsgesellschaft Umformtechnik mbH., Sttutgart, 26.-27.6.1979.

[20] **Chen F.K.; Chen C.J.:** On the Nonuniform Deformation of the Cylinder Compression Test, Transactions of the ASME, Vol. 122, April 2000, pp. 192-197

[21] **Rastagaev, M.V.:** New Method of Homogeneous Upsetting of Specimens for Determining the Flow Stress and the Coefficients of Inner Friction (in Russian), Zav. LAb. (1940), pp.354.

[22] **Parteder E.; Bünten R.:** Determination of Flow Curves by Means of a Compression Test under Sticking Friction Conditions Using an Iterative Finite-Element Procedure, Journal of Materials Processing Technology, 74 (1998), pp. 227-223.

[23] **Xinbo L.; Fubao Z.; Zhiliang Z.:** Determination of Metal Material Flow Stress by the Method of C-FEM, Journal of Materials Processing Technology, 120 (2002), pp. 227-223.

[24] **Tabor D**.: The Hardness and Strength of Metals, J. Inst. Metals, Vol.79, pp.1-18, 1951.

[25] **Tabor D**.: A Simple Theory of Static and Dynamic Hardness, Proc. Roy. Society Series A., Vol.192, pp.247-274, 1948

[26] **Dannenmann, E., Wilhelm, H., Steck, E.:** "Uber den Zusammenhang zwishen Eindringharte und Umformgrad bei Kaltumformvorgangen", Bander Bleche Rohre, (1968), pp 368-394.

[27] **Ramaekers, J.A.H.:** 1970, Harte und Verformung metallischer Werkstoffe. Dr.-Ing. Dissertation, Technische University Eindhoven, Eindhoven.

[28] **Wilhelm, H.:** 1969, Untersuchungen über den Zusammenhang zwischen Vickersharte und Vergleichsformanderung bei Kaltumformvor-gangen. Berichte aus dem Institut für Umformtechnik der Universitat Stuttgart, Essen: Girardet.

[29] **Kim, H.; Lee, S.-M.; Altan, T.:** J. Mat. Proc. Techn. 59 (1996), pp.113-121.

[30] **Srinivasan, K.; Venugopal, P.:** J. Mat. Proc. Techn. 95 (1999), pp. 185-190.

[31] **Tekkaya A.E.:** Hardness Measurements on Cold-Formed Workpieces, Advanced Technology of Plasticity, Vol.II, Proceedings of the 6th ICTP, 1999.

[32] **Tekkaya A.E.:** An Improved Relationship between Vickers Hardness and Yield Stress for Cold Formed Materials and its Experimental Verifications, Annals of the CIRP, Vol.49, 2000.

[33] **Yavuz B.**; **Tekkaya A.E.:** Correlations between Vickers Hardness Number and Yield Stress of Cold-Formed Products, 9th Intermational Conference on Machine Design and Production - UMTIK 2000, 13-15 Sept. 2000.

[34] **Avitzur B., Kohser R.A.:** Quantitative Friction Determination Through Forging – A New Approach, Manufacturing Engineering Transactions, SME, 1976, pp. 123-129.

[35] **Tan X.:** Comparisons of Friction Models in Bulk Metal Forming, Tribology International, 35 (2002), pp. 385-393.

[36] **Von Karman Th.:** On the theory of rolling. Z. angew. Math. Mech.1925;5:139–41.

[37] **Kunogi M.:** On plastic deformation of hollow cylinders under axial compressive loading, Rep. Sci. Res. Inst., Tokyo 1954; 2(30), pp. 63–92 (in Japanese).

[38] **Kudo, H.:** Some analytical and experimental studies of axi-symmetric cold forging and extrusion, Int J Mech Sci, 1960–61; Part I: 2:102–27; Part II: 3:91–117.

[39] **Siebel, E.:** Resistance and deformation and the flow material during rolling, Stahl und Eisen 1930;50:1769–75.

[40] **Orowan, E.:** Section V. A simple method of calculating roll pressure and power consumption in hot flat rolling. Iron Steel Inst.: Spec. Rep. 1946;34:124–46.

[41] **Sims, R.B.:** The calculation of roll force and torque in hot rolling mills. Proc. Instn. Mech. Engrs. 1954;168:191–200.

[42] **Alexander, J.M.:** A slip line field for the hot rolling process. Proc. Instn. Mech. Engrs. 1955;169:1021–30.

[43] **Nadai, A.:** The force required for rolling steel strip under tension. J. Appl. Mech. 1939;(June) 6 (Transactions of the ASME):A54–A62.

[44] **Orowan, E.:** The calculation of roll pressure in hot and cold flat rolling. Proc. Instn. Mech. Engrs. 1943;150:140–67.

[45] **Tselikov, A.I.:** Present state of theory of metal pressure upon rolls in longitudinal rolling. Stahl 1958;18(5):434–41.

[46] **Unksov, E.P.:** An engineering theory of plasticity. London: Butterworths, 1961.

[47] **Bay N, Gerved G.:** Friction and pressure distribution in disk forging. Presented at: 17th International Cold Forging Group Plenary Meeting, Nagoya, Japan, September 1984.

[48] **Van Rooyen G.T., Backofen W.A.:** A study of interface friction in plastic compression. Int. J. Mech. Sci. 1960;1:1–27.

[49] _____, MARC Mentat Manual.

[50] **Koçak, Ö.**: "Formability Analysis of Metals" METU, ANKARA (to appear soon)

[51] **Hill, R.:** A User-Friendly Theory of Orthotropic Plasticity in Sheet Metals, Int. J. Mech. Sci., Vol. 35,25 (1993), No. 1, p. 19

[52] **Hosford, W.F.:** Comments on Anisotropic Yield Criteria, Int. J. Mech. Sci. 27 (1985), pp. 423-427.

[53] **Barlat, F.:** Yielding Description for Solution Strengthened Aluminum Alloys, Int. J. Plasticity, 13 (1997), p. 185

[54] **Karafillis, A.**P.; Boyce, M.C.: A General Anisotropic Yield Criterion Using Bounds and a Transformation Weighting Tensor, J. Mech. Phys. Solids, 41 (1993), pp. 2285-2294.

[55] **Banabic, D.; Pöhlandt, K.:** Yield Criteria for Anisotropic Sheet Metal, UTF Science, 2 (2001), pp. 19-27.

[56] **Ziegler, H.:** A Modification of Prager's Hardening Rule, Quarterly of Applied Mathematics, Vol. 17, 1959, pp. 55-65.

[57] **Mollica, F.; Rajagopal K.R.; Srinivasa, A.R.:** The Inelastic Behavior of Metals Subject to Loading Reversals, International Journal of Plasticity, 17 (2001), pp. 1119-1146.

[58] **Khan, A.S.; Jackson, K.M.:** On the Evolution of Isotropic and Kinematic Hardening with Finite Plastic Deformation, Part I: Compression/Tension Loading of OFHC Copper Cylinders, International Journal of Plasticity, 15 (1999), pp. 1265-1275.

[59] **Low, J.R.; Garofalo, F.:** Proc.Soc. Exper. Stress Analys., 1947, 44, 16.

[60] **Ludwigson D.C.; Berger J.A.:** Plastic Behaviour of Metastable Austenitic Stainless Steels, Journal of The Iron and Steel Institute, January 1969, pp.63-69.

[61] **Ludwigson D.C.:** Modified Stress-Strain Relation for FCC Metals and Alloys, Metallurgical Transactions, Vol.2, October 1971, pp. 2825-2828.

[62]   **Mannan S.L.; Samuel K.G.; Rodriguez P.:** Stress-Strain Relation for 316 Stainless Steel at 300 K, Scripta Metallurgica, Pregamon Press, Vol. 16, 1982, pp. 255-257.

[63]   **Ulvan E.; Koursaris A.:** The Effect of Grain Size on the Bulk Formability and Tensile Properties of Austenitic Stainless Steel Types 304 and 316, Metallurgical Transactions A, Vol. 19A, September 1988, pp. 2287-2298.

[64]   **Bauschinger, J.:** Mitt. Mech. –Tech. München, 13 (1881) 1.

[65]   **Hasegawa, T.; Yakou, T.; Karashima, S.:** Deformation Behavior and Dislocation Structures upon Stress Reversal in Polycrystalline Aluminium, Materials Science and Engineering, 20 (1975), pp. 267-276.

[66]   **Hasegawa T. Yakou T. and Kocks U. F.:** "A Unified Representation of Stress-Strain Curves in Reversed Direction of Prestrained Cell-Forming Metals", Transactions of the Japan Institute of Metals, Vol. 27, No.6 (1986), pp. 425 to 433.

[67]   **Takahashi, H.; Shiono I.:** "Bauschinger Curves and Reloading Curves At Large Strain", Advances In Constitutive Laws for Engineering Materials (1989), Volume I, pp.208-211.

[68]   **Christodoulou N.; Woo O.T.; and MacEwen S.R.:** "Effect of Stress Reversals On The Work Hardening Behaviour of Polycrystalline Copper", Acta Metall., Vol. 34, No. 8, 1986, pp. 1553-1562.

[69]   **Stout M.G. and Rollett A.D.:** "Large-Strain Bauschinger Effects in Fcc Metals and Alloys", Metallurgical Transactions A, Vol. 21A, December 1990, pp. 3201-3213.

[70]   **Hu Z.; Rauch E.F. and Teodosiu C.:** "Work-hardening Behavior of Mild Steel Under Stress Reversal at Large Strains", International Journal of Plasticity, Vol. 8, 1992, pp. 839-856.

[71] **Hu Z.:** Work-Hardening Behavior of Mild Steel under Cyclic Deformation at Finite Strains, Acta Metall., 42, 1994, pp. 3481-3491.

[72] **Yoshida F.; Uemori T.:** A Model of Large-Strain Cyclic Plasticity Describing the Bauschinger Effect and Workhardening Stagnation, International Journal of Plasticity, 18 (2002), pp. 661-686.

[73] **Mroz, Z.**: On the Description of Anisotropic Work-Hardening, J. Mech. Phys. Solids, 15 (1967), 163.

[74] **Dafalias, Y.F.; Popov, E.P.:** A Model of Nonlinearly Hardening Materials for Complex Loading, Acta Mecanica, 21 (1975), p. 173.

[75] **Krieg, R.D.:** A Practical Two-Surface Plasticity Theory, J. Appl. Mech., Trans. ASME, 42 (1975), p. 641.

[76] **Chaboche, J.L., Rousselier, G.:** On the Plastic and Viscoplastic Constitutive Equations, Parts I and II, Trans. ASME, J. Press. Vessel Technol., 105 (1983), 153.

[77] **Mroz, Z.:** Hardening and Degradation Rules for Metals Under Monotonic and Cyclic Loading, Trans. ASME, J. Eng. Mater. Technol., 105 (1983), p. 113.

[78] **Hu, Z.; Hwang, K.; Zhou, C.:** Constitutive Relations of Metallic Materials Under Cyclic Loading, Acta Mecanica Sinica, 21 (1989), p. 705.

[79] **Ekici, Ö:** Java Application for Relative Coordinate Determination, 2000